THE HANDBOOK OF X-RAY SINGLE-BOUNCE MONOCAPILLARY OPTICS, INCLUDING OPTICAL DESIGN AND SYNCHROTRON APPLICATIONS

A Dissertation

Presented to the Faculty of the Graduate School

of Cornell University

in Partial Fulfillment of the Requirements for the Degree of

Doctor of Philosophy

by

Sterling W. Cornaby

May 2008

THE HANDBOOK OF X-RAY SINGLE-BOUNCE MONOCAPILLARY OPTICS, INCLUDING DESIGN OF THE OPTICS AND SYNCHROTRON APPLICATIONS

Sterling W. Cornaby, Ph.D.

Cornell University 2008

This dissertation is a reference book and a comprehensive look at single-bounce monocapillary x-ray optics, covering their uses, function, design, fabrication, evaluation, and applications for microfocusing on synchrotron beam lines. The single-bounce monocapillary optics are elliptically shaped pieces of hollow glass capable of focusing x-ray beams to a spot size between 5 and 50 μm, with gains in intensity ranging from 10 to 1000, and divergences ranging from 1 to 10 mrad. This dissertation also includes many successful experimental applications for which the optics have been used for the past three years. Experiments include high pressure powder diffraction, high resolution micro-diffraction (μXRD), micro-x-ray fluorescence (μXRF), confocal x-ray fluorescence on antiquity paintings (confocal μXRF), confocal x-ray fluorescence with "football" monocapillaries, micro protein crystallography, Laue protein crystallography, micro small angle x-ray scattering (μSAXS), time resolved powder diffraction of reactive multilayer foils, miniature toroidal mirrors, and a comparison between the single bounce monocapillary optic and Kirkpatrick-Baez (KB) mirrors. Background information is given on x-ray sources, detectors and x-ray optics for which monocapillary optics are often designed. A comparison to other available microfocusing x-ray optics is given. An explanation is given of the basic physical principles of monocapillary optics and different optical modeling methods. The theoretical and present fabrication limitations are discussed. The fabrication and design of the optics is explained, along with examples of the design process. Information is

given on the fabrication and design of the glass puller, which is used to make the optics, and on auxiliary equipment used to align and tailor the x-ray beam from the single bounce monocapillary optics. Thus, I attempt to summarize everything we presently know about single-bounce monocapillary optics.

Additionally, Chapter 8 gives a description of silicon nitride x-ray mirrors. They are 300 nm thick, and 0.6x85 mm in size. X-ray transmission mirrors function as high-pass energy filters with a sharp energy cutoff, which is adjustable by the angle of the mirror, in a wide-bandwidth synchrotron x-ray beam. The energy cut-off can be adjusted from 8 to 12 keV at angles of 0.26º to 0.18º respectively.

BIOGRAPHICAL SKETCH

Sterling William Cornaby was born in Logan Utah, in 1974 to Dale and Cheri Cornaby. He grew up in the farming community of Lake Shore, Utah, on his father's 400-acre farm and 2000-acre ranch. He graduated from Spanish Fork High School in 1992. After high school, he spent one year at the University of Utah. He then spent two years serving a mission for The Church of Jesus Christ of Latter-Day Saints, in Mississippi, Louisiana and Texas. He returned to Utah and finished his B.S. degree in physics at Brigham Young University in December of 1998. He completed a M.S. degree in physics at Brigham Young University in August of 2000, under Dr. Larry V. Knight with a thesis entitled "Using a CCD to Gather XRF and XRD Information Simultaneously". He married Sherilee Phillips in October of 2000. From 2000 to 2002 he continued working on the XRF/XRD CCD instrument at MOXTEK Inc. In the fall of 2002 he moved to Ithaca, New York to attend Cornell University, and to work at CHESS. While in Ithaca New York, he had two children, Arianna (born in October of 2003) and Lucas (born in January 2006).

ACKNOWLEDGEMENTS

The single-bounce monocapillary optics at CHESS is an encompassing project. It has many players, who have played a major role for just the past few years. Many people have worked on developing the optics both before and currently with me. Don Bilderback, the assistant director of CHESS and my acting advisor, is the founder and leader of the microfocusing monocapillary optics used at CHESS. He has always given me full support in my efforts with the optics, of which I have been thankful. I have appreciated his support. Tom Szebenyi has been another major support for this project, pulling a vast majority of the optics, spending most of his time building and tuning the new capillary puller. A large amount of chapter 6 in this dissertation is based on his efforts. Rong Huang (now at APS), while I did not directly work with him, laid a very sound base for me to begin at when I started on the project. Section 3.2.2 is his work on the design capillary program, and all of chapter 3 is based on the design tools that he developed for the monocapillary project. A few others have spent time directly on the capillary project. Aaron Mauer, an undergraduate student who developed the spike reduction program (section 6.3.3), and reprogrammed the capillary furnace file program into LabVIEW. Robert Santavicca, an RET visiting high school teacher who pulled a number of optics and helped to make furnaces. Courtney Couvreur, another RET, who made the first far-field simulations in Matlab, comprised in section 6.4.3. Heung-Soo Lee, a visiting scientist from the Pohang Accelerator Laboratory in Korea, who performed the bending tests in section 7.3.

In addition to the help on the monocapillary optics fabrication and development, there has been a lot of collaboration on CHESS's beam-lines as well. I have been able to work with all of the CHESS scientists and staff, and most of the MacCHESS scientists

and staff, all of whom I thank for their help and friendship. I would like to thank Sol Gruner, the director at CHESS and my official adviser, for allowing me the freedom to pursue my interests at CHESS. In my time working on the microfocusing optics, I have been involved on every beam-line. Because of the number of people involved in these different projects, I have chosen to acknowledge them in each of the sections of Chapter 9, by individual projects.

I would like to acknowledge my funding sources while at CHESS. My first year at Cornell University I received the G-line Fellowship, which allowed me the freedom to start working at CHESS from my first semester at Cornell in the fall of 2002. Since that time, I have been funded by CHESS, which is supported by the National Science Foundation and NIH-NIGMS via NSF award DMR-0225180.

In closing, I would like to thank my family. My parents, Dale and Cheri Cornaby, and my wife's parents Jim and Jan Phillips who have been supportive. Most of this dissertation was written in my in-law's home in Oklahoma. I really appreciate my dear wife, Sherilee, who has always been supportive of me and who helped me proofread my dissertation, and my children Arianna and Lucas, who do not care at all what I do, just as long as I play with them and read to them. Sherilee deserves recognition and thanks, from me and the people I have helped at CHESS, because she has spent many nights home alone, taking care of our family without me while I have tended to the needs at the synchrotron. Last of all I would like to show appreciation to God who gave us this wonderful universe to enjoy and explore.

TABLE OF CONTENTS

LIST OF FIGURES

LIST OF TABLES

Chapter 1 Basics of X-ray Sources, Detectors, and Optics

This chapter gives an overview of sources, detectors and optics that frequently cross paths with monocapillary optics in experiments. It is impossible to use and design monocapillary optics separately from other elements in the beam, especially the x-ray source. This chapter also gives some background information on other types of microfocusing x-ray optics, which both augment and compete in x-ray beam applications with single-bounce monocapillary optics. This handbook summarizes information on sources, detectors, and other x-ray optics to give a place to start when questions arise about x-ray experiments involving capillary optics, and the equipment surrounding them. It is vital to have some background on each component because all of the components in an x-ray microbeam experiment interact with each other in order to make a particular measurement feasible.

1.1 Introduction to X-rays

Optics is the study of the natural properties of light and the manipulation of light with optical components for the best experimental advantage. The electromagnetic spectrum spans many orders of magnitude in wavelength, from hundreds of kilometers (radio waves) to femtometers (Gamma rays) in wavelength. There are many disciplines in optics, with each discipline focusing on a range of wavelengths. They include radio waves, microwaves, infrared, visible light, ultra violet, x rays and gamma rays. Figure

1.1 shows the electromagnetic spectrum with markers giving units in wavelength, frequency, and energy. Experts in the different optical fields each prefer different units, so having this figure is often very useful while reading or discussing electromagnetic waves among the different branches. Conversions between the different units are made with two relations: the dispersion relation in vacuum and the Planck-Einstein equation, in the following forms:

$$c = f\lambda \rightarrow \lambda[m] = \frac{3\times10^{8}}{f[Hz]} \qquad E = hf \rightarrow \lambda[nm] = \frac{1239.8}{E[eV]} \tag{1-1}$$

Where 'c', 'f', 'λ', and 'h' are the speed of light, the frequency, the wavelength, and Planck's constant, respectively:

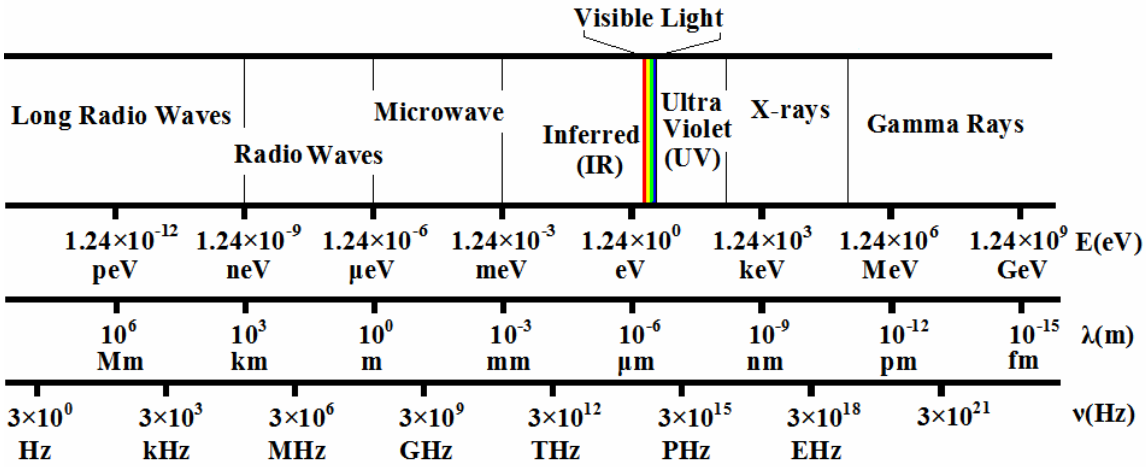

Figure 1.1 The electromagnetic spectrum over several magnitudes. Units are given in wavelength (m), Energy (eV) and frequency (Hz).

The range of the spectrum used in this dissertation is the x-ray range, from about 1 to 70 keV. X rays were discovered in 1895 by W.C. Röntgen [1]. Since that time, they have become one of the major tools utilized to probe structures in matter. Right from the beginning, the medical field used x rays to see internal structures, such as bones in the

body. In the scientific community, x rays have proven to be an exceptional tool in probing matter in an endless array of materials. X rays can probe very large objects, such as a person or a suitcase, or the very smallest of structures, such as the positions of atoms in DNA, or protein molecules. X rays are especially good at unearthing internal structures of materials because of their penetrating nature. They are extremely useful for obtaining molecular or atomic structure of materials. The theoretical framework that explains how x rays interact with matter, in its large range of forms, is well established today. Presently, x-ray science is in a mode of exploring what we know about x rays to reveal information from an ever growing field of matter with unknown structures, unknown materials, unknown dynamics, etc [1].

Advances in x-ray sources, x-ray detectors and x-ray optics enhance the usefulness of x rays for probing matter. For every advance made in one of these areas, there follows an advance in the materials that can be investigated. Below, I will be giving an overview of sources, detectors, and optics.

1.2 X-ray Sources

To demonstrate what role optics play in an experiment, I would like to present what would constitute a "perfect source". For a perfect source, you could specify anything that you wanted, without limitations. A list of attributes used to specify for source include:

1. The x-ray energy or wavelength.
2. The spread in energy - the bandwidth $\Delta E/E$.
   Narrow energy spreads increase the temporal or longitudinal coherence.
3. The angular distribution.

The angular range can be a full 4π steradian to a perfectly collimated beam.

4. The size of the source - radiation coming from everywhere or from a point source.

   The smaller the source, the better the spatial coherence becomes.

5. The power or spectral brightness of the beam.

   How many photons exist in time, angle, energy, and space.

6. Time variations.

   This includes pulses in time (such as pulses at a kHz rate), the pulse width (such as a nanosecond width pulse) to a continuous source in time.

7. The polarization of the light.

   The polarization could be random, linearly polarized or circularly polarized, etc.

If we could dial up any of the conditions above, the source would never limit the experiment. With a perfect source could provide anything: a source with high spatial and temporal coherence, like a laser beam, or a bright wide-bandwidth beam, like a flood light. A source that can have all attributes is not real, but sources that can most emulate an ideal tunable source are very valuable. The way to get a source close to an ideal source is to have a source with a broad range of characteristics. Optics can then select the characteristics out of the source that are desired, and/or change one characteristic feature from the source into another more desired property.

Example of selecting a characteristic: A Bragg reflection from a silicon crystal picks out a narrow 0.01% bandwidth of energy from a broadband wiggler x-ray beam. The energy is selected by adjusting the angle of the crystal in reference to the incoming x-ray beam. The conjunction of a broad bandwidth source and a silicon crystal allow for a tunable, narrow bandwidth x-ray source.

Example of changing a characteristic: A focusing optic, such as a single bounce mono-capillary optic, can increase the x-ray intensity in an x-ray beam. The focusing optic changes a collimated beam into a diverging beam of a few mrad. At the focus of the optic, there will be a higher x-ray intensity, on the order of 50 to 1000 times larger than the collimated beam. In this case, the collimation of the beam was sacrificed to increase the intensity of the beam in a small focal spot.

Tailoring an x-ray beam requires understanding the source of radiation. Functionally, there are two main sources for x rays, an x-ray tube and a synchrotron; I will briefly describe these sources, giving their basic functions and limitations. There are other sources of x rays that are not as commonly used, such as plasma sources, soft x-ray lasers, and high harmonic laser generation, as seen in the references [2-4].

1.2.1 X-ray Tubes

X-ray tubes have been used since 1895, since the very beginning of x-ray science. A common design for the x-ray tubes consists of a cathode and an anode separated by a distance in a vacuum. The cathode generates free electrons, typically from a hot tungsten filament. The anode is typically a metal target. A high voltage, measured in many kV, is placed between the cathode and anode. Free electrons accelerate from the cathode toward the anode, which hit the anode and produce x-rays. The energy of radiation given off by x-ray tubes comes in two categories. The first is very specific, narrow lines of energy, with a bandwidth of $\Delta E/E \sim 0.05\%$. The narrow lines are called K or L x-ray emission lines, with the energy of the lines corresponding to the elemental composition of the anode. The second is a very broad bandwidth bremsstrahlung or braking radiation caused by the quick deceleration of the electrons entering the anode

[1,2]. Other features of an x-ray tube consist of a leaded housing to block radiation, since the x-rays are harmful, and a window used to let the x-rays out at desired locations (Figure 1.2). These windows are often made of out of beryllium because it has a high transmission coefficient for x-rays.

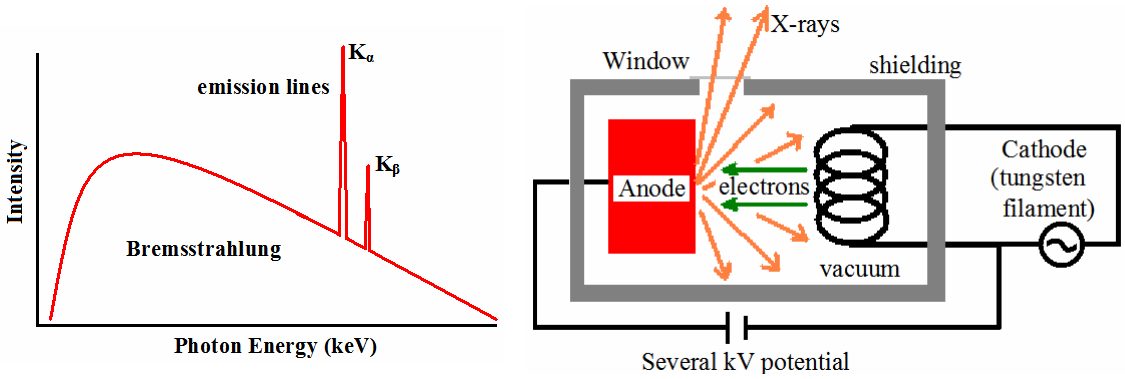

Figure 1.2 On the left is a typical spectrum from an x-ray tube showing both the bremsstrahlung and emission lines. On the right is a simple diagram of the major parts of an x-ray tube.

The major limitation for an x-ray tube is that it can only go so high in radiative power. The heat load that the anode can take from the electron beam sets the radiative limit. Exceeding this limit melts the anode and destroys the x-ray tube. Only about ½ % to ¼ % of the energy put into the x-ray tube converts into x rays; most of the energy converts into thermal energy. Many engineering tricks help improve the performance of x-ray tubes. Two common ways of reducing the effects of heating are water cooling the anode and rotating the anode to spread out the heat load.

X-ray tubes are also limited in their spectral brightness '*photons/s/mrad^2/mm^2/0.1%BW*' (alternately called brilliance). X-ray tubes are capable of emitting about 10^7 photons/s/mrad^2/mm^2/0.1% bandwidth for stationary anodes and about 10^{10} photons/mrad^2/mm^2/0.1% bandwidth for rotating anodes in the narrow bandwidth K_α lines. Spectral brightness is a very effective unit in comparing sources, because it does

not change with optical techniques. For a perfect optical system, with no losses due to absorption, aberrations etc, the spectral brightness is a conserved quantity from the source plane into the image plane.

A useful place to start when estimating the flux of the Cu K_α line from an x-ray tube with a copper anode is [5]:

$$Flux \approx 3 \times 10^{13} [\frac{photons\ (CuK_\alpha)}{kW \cdot second \cdot steradian}] \quad (1\text{-}2)$$

From this equation, a rough estimate of the number of photons collect from an x-ray tube can be made, given the voltage is larger than 20 kV, and the power the tube is known. If you know the size of the spot on the anode, you can include that as well (section 1.5.3).

Even with the limitations in flux, there is plenty of ongoing work to tune some of the other characteristics, such as generating smaller spot sizes, timing schemes, etc. Below is list of x-ray tube attributes, including some comments about the advantages and limitations.

1. The energy or wavelength.

   X-ray tubes have energies from 1 keV to about 200 keV.
2. The spread in energy - the bandwidth $\Delta E/E$.

   X-ray tubes have higher power, narrow energies corresponding to the K and L emission lines of the anode material, and lower power, broad Bremsstrahlung energies.
3. The angular distribution.

X-ray tubes have 2π steradian spread in radiation; this is good for doing medical x-ray imaging. Collimated beams are achieved by selecting a very small solid angle, which causes a large loss in power and x-ray counts in the beam.

4. The size of the source - radiation coming from everywhere or from a point source.

   X-ray tubes have a source size ranging from a few centimeters down to a fraction of a millimeter. Some newer commercial x-ray tubes have micro-source sizes down to about 20 μm.

5. The power or spectral brightness of the beam.

   X-ray tubes have higher power, narrow energies corresponding to the K and L lines of the anode material, from 1×10^{10} to 1×10^{8} photons /sec/mm^2/mrad^2/0.1% and lower power, broad Bremsstrahlung energies from 1×10^{6} to 1×10^{2} photons /sec/mm^2/mrad^2/0.1% [6].

6. Time variations.

   X-ray tubes range from continuous to producing x-ray flashes of about 100 nanoseconds [7].

7. The polarization of the light.

   X-ray tubes produce random polarization.

1.2.2 Synchrotron X-ray Sources

Synchrotron radiation is the generic term used for radiation produced by accelerated charged particles (electrons and positrons) traversing on curved paths at relativistic speeds. The photons are emitted in a narrow cone, in the same direction of the particle beam, tangent to the curved path. The energy range of the radiation spans from the infrared to x-rays. Synchrotron radiation was first observed in 1947 at GE [8]. It was

initially viewed as a negative attribute in circular particle accelerators because the radiation caused power loss in the particle beam. In time, it was realized that synchrotron radiation could be a very good source for x-rays and much more powerful than x-ray tubes. Synchrotron radiation is much more brilliant than x-ray tubes. A 3rd generation synchrotron undulator line has a spectral brightness 10^{10} higher than the K_α line emitted from a rotating anode tube [1]. Synchrotron radiation has a large array of capabilities that are not possible with x-ray tube sources because of the dramatic increase in power. The first accelerator dedicated to synchrotron radiation started at the Synchrotron Radiation Source in Daresbury around 1970 [9]. There are now around 70 synchrotron facilities in the world and 14 in the United States. Seven facilities in the United States use the x-ray spectrum produced.

In the following sections I will describe the three insertion devices synchrotrons use to bend the particle beam path in storage rings to produce radiation. All of them use magnetic fields to bend the particle beam. The three insertion devices are bending magnets, wigglers, and undulators. I will give a description of each.

1.2.2.1 Bending Magnets

A bending magnet bends the path of the electron or positron particles around a storage ring to follow a closed orbit. Because it curves the particle beam, the bending magnet causes the beam to emit synchrotron radiation. The synchrotron radiation emitted from the bending particle beam has several characteristics. The beam is small, narrow, and has a wide range of energies (Figure 1.3). The source size, which is the cross section of the particle beam profile, can range from 0.05 mm to 3-4 mm, depending on the size of particle beam in the storage-ring bending magnet. The instantaneous angular spread of

radiation from the bending magnet lies within a cone of $1/\gamma$ (see Figure 1.3 and equations (1-3) and (1-4) below). This angle is typically around 0.1 mrad (0.006º). In practice, the divergence of the x-ray beam in the vertical direction is $1/\gamma$. In the horizontal direction, or in the plane of the storage ring, the angle of radiation is larger than $1/\gamma$ (called the instantaneous angular width). A segment of the particle beam arc is viewed, not just a single point along the arc. The segment of the particle beam arc has a larger angular spread, and beam-defining slits set the viewable angle in the horizontal direction.

Below I give a list of some useful formulas for both the angular spread and the critical energy of the bending magnet radiation.

$$\gamma = \frac{E_e}{m_e c^2} \tag{1-3}$$

$$\theta_r = \frac{1}{\gamma} \tag{1-4}$$

$$\rho[m] = \frac{3.3E_e[GeV]}{B[T]} \tag{1-5}$$

$$E_c[keV] = 0.665E_e^2[GeV]B[T] \tag{1-6}$$

Equation (1-3) gives the value for 'γ' (the Lorentz factor), where 'E_e' is the energy of the particle beam and 'm_e' is the mass of the particles in the beam. Equation (1-4) gives the angular opening for the radiation cone from a bending magnet. Equation (1-5) gives either the radius of the particle beam's bend 'ρ', or the magnetic field strength, 'B' in practical units. Equation (1-6) gives the critical energy of the radiation emitted by the bending magnet, in practical units [1,2,6]. The critical energy is defined as the

photon energy that divides the emitted beam power into equal halves. The values needed to generate the bending magnet spectral brightness curves for D-line at CHESS (which is very similar to C-line) are given below, with the resulting spectral curves given in Figure 1.3:

E_e=5.3 GeV, B=0.55 T

Source's spot size = 1.49(H) x 1.18(V) mm^2 FWHM

Source's divergence = 4.5(H) x 0.1 (V) $mrad^2$

Distance from source to center of the hutch =13.3 m

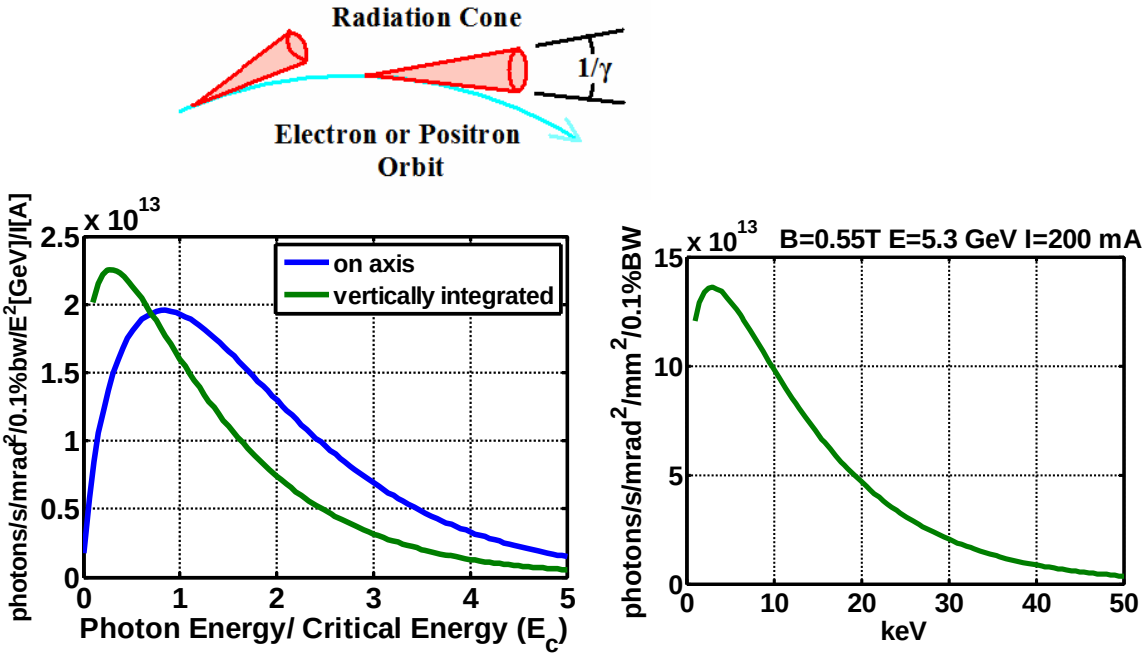

Figure 1.3 Above shows a sketch of the synchrotron radiation cone from a relativistic particle beam. The left graph is the energy spread of a bending magnet, normalized to the square of the electron energy and the beam current, for both the on-axis x-ray beam (blue) and the vertically integrated x-ray beam (green). The vertically integrated curve has been divided the D-line vertical divergence, to give both curves the same units. The right graph shows the vertically integrated spectrum of a bending magnet, with inputs for D-line at CHESS. Again, vertically integrated curve has been divided by D-line's vertical divergence, to give the curve's units in photons/s/$mrad^2$/mm^2/0.1% BW (close to, but not quite spectral brightness, because of the vertical integration).

With the information above for the bending magnets at C and D lines at CHESS, we can generate the spectral brightness curves for D-line[1] (Figure 1.3) [10,11]. We must pay careful attention when using programs that generate bending magnet curves. Some programs use the photon counts that come from just the on-axis beam, and others use the photon counts that come from a vertical integration of the beam. The left graph in Figure 1.3, which is a normalized curve of bending magnet radiation, shows the difference between the spectrums of an on-axis and vertically integrated beam; the x-ray beam's energy spectrum has angular dependence in the vertical direction. I prefer using the vertically integrated beam profile, because it represents the energy profile found within an experimental hutch, over a finite slit size. The right graph of Figure 1.3 shows the vertically integrated spectral brightness for the D-line bending magnet, which is divided by D-line's vertical beam divergence to give it the same units as spectral brightness[2]. Using this figure for D-line, with a 1x1 mm^2 slit 13 m from the source, we can calculate 7.1×10^{12} photons/sec/100mA, with a 1.5% bandwidth multilayer at 10 keV. This value is an overestimate, which neglects the windows, attenuators, and reflection coefficients of the optics in the beam line. The value quoted on the D-line web page is 1×10^{12} photons/sec/mm^2/100mA at 10 keV. Because this calculation is full of potential pitfalls in its calculation, I have used it as an example in section 1.5.3 which covers spectral brightness.

[1] Or alternatively in many other flux/intensity based units.
[2] Vertical integration gives units of '*photon/s/mrad/mm^2/0.1% BW*'. I want the units to be in '*photon/s/mrad^2/mm^2/0.1% BW*' for comparisons between bending magnets, undulators, and wigglers. This is close to, but not exactly the true spectral brightness.

1.2.2.2 Wigglers and Undulators

Another way to produce synchrotron radiation is to veer the particle beam back and forth in a series of alternating arcs, thereby wiggling the beam. In essence, a wiggler is a bunch of bending magnets right next to each other. Both wigglers and undulators work on this principle, the difference being how hard the beam is wiggled. The parameter used to separate wigglers and undulators is 'K', undulators have a 'K' close to one and wigglers have a 'K' much greater than one, on the order of ten or higher.

$$K = 0.934\lambda_u[cm]B_0[T] \tag{1-7}$$

Where 'λ_u' is the period of the oscillation in the alternating magnetic field and 'B_0' is the strength of that field. Different values of 'K' have quite a profound effect on the energy spectrum they produce (Figure 1.4). Wigglers have a continuous spectrum, and typically have a higher total flux than both bending magnets and undulators.

Undulators have a series of peaks, which ultimately come from constructive interference of the radiation emitted from the charged particles passing each pole of the magnetic array, generating a series of harmonic energies. The energy of these harmonics can be shifted if needed by slightly changing the 'K' value by moving magnets closer together or further apart, which changes the peak magnetic field strength 'B_0'. Undulators have a spectral brightness 100 to 10000 times larger than wigglers, because the intensity is concentrated in a series of peaks, and the source sizes are typically much smaller. In addition, an undulator has a spatial distribution for each harmonic peak. For example, the peak power of the first harmonic is on-axis with the particle beam, and the higher order harmonics have peak powers that are off axis [1,2,6]. Figure 1.4 gives the on-axis spectral brightness of the undulator beam, not the

spectral brightness integrated over an aperture size [2]. In addition, many of the programs do not give spectral brightness directly, so care is needed to get into the right units, knowing the source size, and divergence.

Wigglers and undulators also differ in the divergence of the radiation that they produce. Wigglers have a divergence of '$1/\gamma$' in the vertical (same as a bending magnet) and 'K/γ' in the horizontal. Undulators have a divergence smaller than both wigglers and bending magnets.

$$\theta_{horz} = \frac{K}{\gamma} \qquad \theta_{vert} = \frac{1}{\gamma} \qquad \text{Divergence for wigglers} \quad (1\text{-}8)$$

$$\theta_{horz,vert} = \frac{1}{\sqrt{N}\gamma} \qquad \text{Divergence for undulators} \quad (1\text{-}9)$$

All of the 'θ's' are the angles of divergence, 'K' is defined in equation (1-7) and 'N' is the number of poles, or oscillations in the electron beam.

To give some examples of the spectral brightness of both a wiggler and an undulator, I chose the G-line wiggler at CHESS and an imaginary undulator that is very similar to the G-line wiggler. The parameters needed to generate the spectral brightness curves are given below, with the resulting spectral curves given in Figures 1.4 and 1.5 [11].

G line Wiggler:

λ =12 cm B = 0.8 T (K = 9), N = 49, E_e=5.3 GeV

Source's spot size= 3.6(H) x 1.1(V) mm^2

Measured source divergence = 1.6(H) x 0.1(V) $mrad^2$, calculated from a 40(H) x 2.5(V) mm burn 25m from source, June 2007.

Calculated source divergence = 0.9(H)x0.1(V) mrad^2

Distance from source to the G1 hutch front wall = 33.5 m

Imaginary G-line undulator:

λ = 12 cm B = 0.13 T (K = 1.5), N = 49, E_e=5.3 GeV

Source's spot size = 0.3(H) x 0.1 (V) mm^2 (10x smaller then G line)

Source's divergence = .025(H) x .015(V) mrad^2

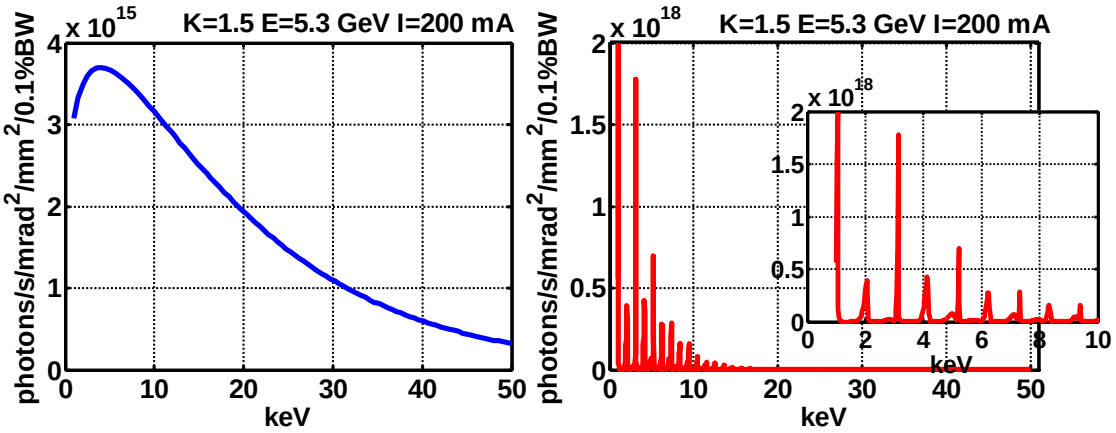

Figure 1.4 The left graph shows the vertically integrated spectrum of the G-line wiggler and the right graph shows the on-axis spectral brightness of an imaginary G-line undulator. The vertically integrated wiggler curve in the left graph has been divided by G-line's vertical divergence, to give both the curves the same units for comparison (the wiggler curve is not quite the spectral brightness).

From Figure 1.4 we can see the large differences between the spectral brightness between wigglers and undulators. As the '*K* ' value increases in an undulator, the harmonics get closer together, and the amount of radiation in the higher order harmonics increases. The wiggler spectrum is the limit of this effect where the harmonic peaks cross and are washed out into a continuous spectrum. Figure 1.5 shows the spectral brightness of the D-line bending magnet, the G-line wiggler, and the imaginary G-line wiggler all on one plot. From this figure, it is easy to see that the

undulator has a spectral brightness over 200 to 1600 times larger than the wiggler in the harmonic peaks, and the wiggler has a spectral brightness over 20 to 80 times larger than the bending magnet.

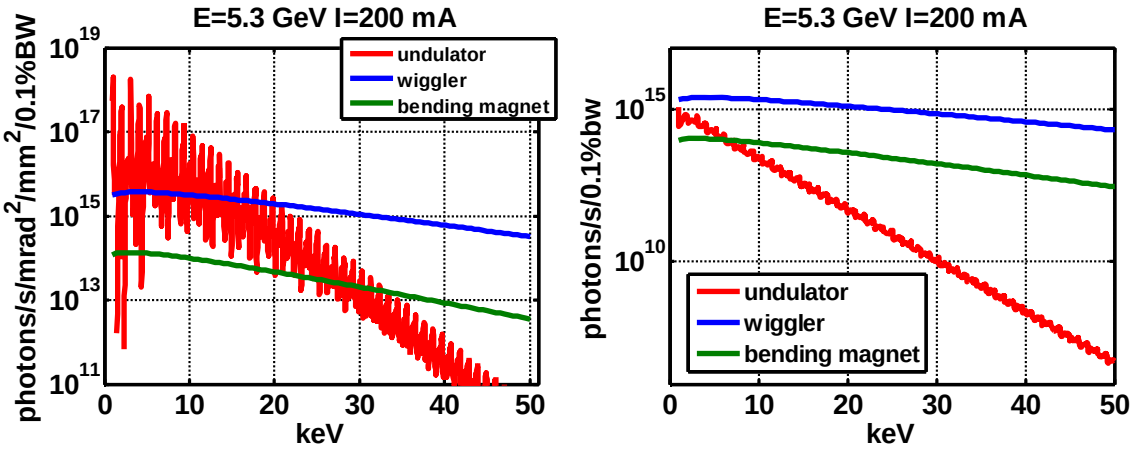

Figure 1.5 The left graph shows the spectral brightness of the D-line bending magnet, the G-line wiggler, and the imaginary G-line undulator. The right graph shows power, in photons per second per 0.1% BW, of the bending magnet, wiggler and undulator (integrated over all the harmonics). This shows that the wiggler has a highest number of photons, or a highest power x-ray beam.

The undulator wins out in spectral brightness, but this is not the whole story; the wiggler wins out in raw power, or in the total number of photons in the beam. In addition, wigglers tend to have a higher spectral brightness at higher energies. The left graph in Figure 1.4 shows the total flux in the beam taking into account the sources' respective beam sizes and energy distribution. The wiggler has a higher total photon count over both the undulator and the bending magnet. The key for the undulator is its placement in space of the x rays it produces. Ten meters away from each example source, the beam size is 0.6(H) x 0.3(V) mm^2 for the imaginary G-line undulator, 20(H) x 2(V) mm^2 for the G-line wiggler, and 45(H) x 2(V) mm^2 for the D-line bending magnet. For the undulator, the photons are concentrated into a smaller area. The wiggler has a larger total number of photons spread out over a much larger area.

In any case, overall a synchrotron is an unsurpassed x-ray source. Between the bending magnet, undulator, and wiggler, there are many uses for this remarkable x-ray source. Below I have summarized their attributes.

1. The energy or wavelength

   Very broad from less than an eV (Infrared) to over 100 keV

2. The spread in energy - the bandwidth $\Delta E/E$.

   Can be very broad or narrow, ΔE can be several keV to 1 eV or less, depending on optics.

3. The angular distribution.

   Very narrow cones of radiation, from 0.01 mrad to 5 mrad.

4. The size of the source - radiation coming from everywhere or from a point source.

   Small sources, from a few mm to tens of microns. Smaller sources have a good spatial coherence.

5. The power or spectral brightness of the beam.

   From 1×10^{19} to 1×10^{12} photons /sec/mm^2/mrad^2/0.1% bandwidth [6]. They are the brightest sources of x rays we have.

6. Time variations.

   Continuous to about 500 MHz pulse rate, down to 40 ps pulse width [2,12]. The Energy recovery Linac (ERL), a newly proposed accelerator can get above a GHz pulse rate with ~1 ps pulse width [13].

7. The polarization of the light.

   The polarization is linear on the same plane as the electron beam. The x-rays become more circularly or elliptically polarized when they are off this plane.

For the previous sections about synchrotron radiation I have drawn heavily from of the X-ray Data Booklet and the Center for X-ray Optics website. The radiation curves were generated by X-ray Oriented Programs (XOP) [6,10,11,14].

1.3 X-ray Detectors

A detector collects scattered x-rays after they have interacted with a sample. By collecting the scattering events, we can investigate the structure, dynamics, composition, etc. of that sample. The detector used for an experiment very often needs specific attributes from the source in order to detect useful information. Optics, including single bounce monocapillary optics, are often chosen to select attributes from the source that the detector cannot select. For example, CCD's gather position information, but do not usually gather energy information. When a CCD is used in protein crystallography, the x-ray beam is set to a very specific x-ray energy by the optics, mostly because the CCD cannot discriminate the energy. If an area detector could measure energy in addition to position, the energy selection optics would not necessarily be needed[3]. Below is a master list of attributes a detector may measure from scattered x-rays, which give information about the sample.

- The number of the photons.
- The timing of the photons, or when the photons arrive at a detector.
- The energy or wavelength of the scattered light.
- The position and/or direction of the scattered light in space.
- The polarization of the light.

The phase of light is another attribute often wanted in scattering experiments. A photon of light does not intrinsically possess a phase, and therefore the detector cannot directly

[3] An energy sensitive area detector would profoundly change protein crystallography methods.

measure the phase. The phase arises as a phase difference occurs between two photon events, therefore measuring the phase requires a reference. The reference phase can be created in several ways. One way involves changing the wavelength of the x rays around an absorption edge in the material, such as in multi-wavelength anomalous dispersion (MAD). Another way includes splitting the x-ray beam with a beam splitter, and using one of the beams as a phase reference. Still another way is referencing the phase of the un-scattered beam with the phase of the scattered beam, by placing the detector at an optimum location from a sample, with an appropriately small source, as in phase contrast imaging [15-17].

A perfect detector gives the time, position, direction, wavelength, and polarization of every scattered photon from a sample. Such an extraordinary detector would allow for limitless scattering experiments. In reality, most detectors available effectively collect information for one or two of the above attributes, and the rest in a very limited way. Several terms describe a detector's limits:

- Count Rates: the upper limit to the number of photons detected per unit time.
- Energy Range or Dynamic Range: the range of photon energies the detector senses.
- Dynamic range or Intensity Range: the range and gradation to which a storage detector can hold information, i.e. if the film is over exposed, its dynamic range has been exceeded.
- Quantum Efficiency: the detected events divided by the total events, measured in a percentage. Real detectors do not measure 100% of the photons impingent on them.
- Energy Resolution: the detector's limit in uniquely distinguishing two closely spaced photon energies.

I have very briefly summarized some x-ray detectors with a few of their basic characteristics in Table 1.1. The table gives a very brief description of the detectors used commonly at CHESS, with the upper bounds of what each detector can do. The detectors fall into two broad categories, counting detectors, some of which have an energy resolution, and area detectors.

The counting detectors possess two major modes of operation, pulse mode and current mode. In pulse mode, the timing and energy of each event can be recorded, and in current mode, very large intensities can be measured [18][4]. Optics advantageously limits the events that counting detectors can detect. Counting detectors can work in conjunction with optics or apertures to refine the energy resolution, such as in wavelength dispersive spectrometers, or to enhance the positional or angular resolution. Enhancing the energy resolution, and/or the positional resolution decreases the number of photons detected in a set amount of time. This increases the time it takes to do an experiment.

Area detectors include CCD's, film, storage-phosphor image plates[5], burn paper, and the pixel array detector. Area detectors cannot typically count individual x-ray events, but they can sample many points in space with a large number of individual pixels. They integrate all the counts in each pixel element over a period of a second or more. At the end of an exposure, the detector records the overall intensity in each pixel. Area detectors typically do not discriminate among different energies.

[4] The book by G. Knoll (reference [18]) is an excellent source of information on radiation detectors.
[5] Specifications for the Mar345 image plate detector (used at CHESS) can be found at www.marresearch.com (marUSA Inc. 1880, Oak Ave, Evanston Il, 60201).

Table 1.1 A brief list of x-ray detectors used at CHESS with a range of attributes.
***For CCD's you can only get energy resolution with single x-ray events directly hitting a pixel.**
**** This is a very unique area detector, because of the extremely fast frame rate.**

Detectors (counting)	**Energy Range (keV)**	**Energy Resolution (keV)**	**intensity (cps)**	**Position (mm^2)**
Ion Chamber (gas) [18]	1 to 3000 keV	None (current mode)	Up to ~1×0^{13} cps (current mode)	~ 10 to 10000 mm^2
Scintillators (many kinds of materials) [18]	2 to ~3000 keV	limited 40-700 keV (typically 30% of photon energy)	Up to ~3×10^6 cps (Pulse mode)	~ 1 to 50 mm^2 (one to a few elements)
Si (Li) [18] (energy dispersive)	0.5 to ~20 keV	~0.15 to 0.3 keV FWHM	Up to ~6×10^5 cps (Pulse mode)	~ 1 to 50 mm^2 (one to a few elements)
Ge (Li) [18] (energy dispersive)	2 to ~1000 keV	~0.1 to 2.0 keV FWHM	Up to ~1×10^5 cps (Pulse mode)	~ 1 to 50 mm^2 (one to a few elements)
Photodiodes (energy dispersive) [18]	1 to ~20 keV	~0.15 to 0.3 keV (Pulse mode) None (Current mode)	Up to ~1×10^{13} cps (Current mode)	~ 1 to 50 mm^2 (one to a few elements)
Detector (area)	**Energy Range (keV)**	**Energy Resolution (keV)**	**Frame rates**	**Pixel size (µm) and array size**
CCDs [19,21]	1 to 100 keV (higher than 10 keV needs a phosphor)	None or ~0.15 to 0.3 keV (Very limited)*	Minutes to a few msec. Read out is typically 60 to 1 sec.	5 to 100 µm arrays of 1×10^4 to $4x10^7$ pixels
image plates (phosphor plates) [f. note 5]	keV	None	Minutes to a few sec. Read out is typically a 100 to 30 sec.	40 to 150 µm arrays of $1x10^5$ to 8×10^7 pixels
pixel array detector** [22]	1-10 keV	None in analog form	Very fast, ~1 µsec for 8 frames. Read out is a few sec.	150 µm pixels in an array of ~$1x10^4$ pixels

A few area detectors can run outside normal operations. A CCD can gather energy information running in the very limited mode of gathering single pixel x-ray events [19-21][6]. The pixel array detector can take eight frames with a frame rate in the microsecond time scale, making it a very unique area detector [22].

1.4 X-ray Optics

X-ray optics tailor x-ray beams to have the qualities most desired for an experiment. Optics change the x-ray beam from the source to match the needs of the sample or the detector. They change the size, divergence, bandwidth, flux density, and direction of the beam. Section 1.4.1 gives a brief description of beam line optics commonly used at CHESS. Single-bounce monocapillary optics are commonly used with these other optics. Section 1.4.2 gives a brief description of an assortment of x-ray microbeam optics, with a brief description of how they function, their advantages, limitations and how they compare to single-bounce monocapillary optics.

1.4.1 Beam Line Optics

Synchrotron beam lines usually have optics that can handle the full synchrotron power, which contains the full energy spread, called the white beam. Optics select the bandwidth desired for an experiment, and often they provide a focus in the vertical direction, the horizontal direction, or sometimes both simultaneously. Table 1.2

[6] The book by J. Janesick (reference [19]) is an excellent source of information on CCD's.

outlines the white beam optics commonly used at CHESS. I will give a brief description of each optic.

Monochromator crystals are optics that can operate in the white x-ray beam. They are commonly large and very close to perfect silicon or germanium crystals. The most common configuration is the two-crystal offset geometry (Figure 1.6). The beam Bragg reflects from the first crystal, and then Bragg reflects again from the second crystal, which offsets the output monochromatic beam and makes it parallel to the white beam. The energy width of the Bragg reflection off the crystal defines the energy spread, with bandwidths typically around 0.01%. In this configuration, the crystals are flat and do not focus the beam. Other configurations use a sagittal bent crystal, which focuses the x-ray beam in the horizontal direction [23]. Basic ray optics equations can estimate the magnification factors of these optics in the parallax approximation. With these optics, the magnifications typically range between 1 to 1/3 (see equation 2-2).

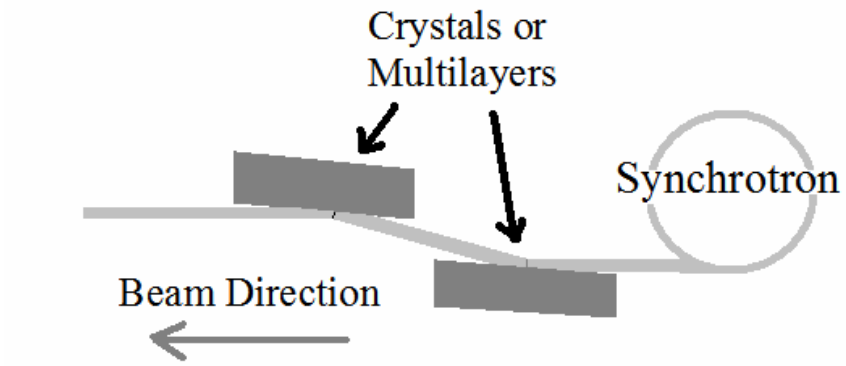

Figure 1.6 This sketch shows the two crystal offset geometry, which is very common for multilayers, crystals, and mirrors. The reflections set the bandwidth of the beam, and make the input and output beams parallel.

Table 1.2 A list of white beam optics used at CHESS.

	Materials	**focusing**	**Energy range**	**Bandwidths ΔE/E**
monochromator crystals	Silicon, Germanium	none, vertical horizontal	1 to 100 keV	~0.01%
Multilayer optics	Typically W or Mo with B_4C	none, vertical, horizontal	1 to 30 keV	0.1 % to 10% 0.5% to 2% (Typical)
Total reflection mirrors	Silicon, copper coated with Rh	none, vertical	Cut of energy from 1 to 40 keV	Low band pass filter

Another commonly used optic is a multilayer. They also typically use the two-crystal offset geometry (Figure 1.6). The energy width of the Bragg reflection off multilayers is 10 to 100 times wider than crystal optics. Multilayer optics typically have a bandwidth of around 0.5% to 2%. Above 30 keV, multilayer optics act more like total external reflection mirrors, because at high energies, the angle of the reflection is too low. The first multilayer is typically flat and provides no focusing. The second multilayer may be shaped to provide some focusing [24]. Two shapes of multilayer optics can focus the beam. A cylindrical multilayer optic provides horizontal focusing, and a toroidal multilayer optic provides both vertical and horizontal focusing. CHESS uses flat and cylindrical multilayer optics. The multilayer optics have magnifications that typically range between 1 to 1/3 (see equation 2-2).

A reflection mirror is another commonly used optic. It functions as a low band-pass energy filter, which reduces the heat load on other downstream components in the beam line. Reflection mirrors suppress the higher energy harmonic x-rays that pass through

monochromatic crystals. Adjusting the mirror to the appropriate grazing incident angle, ranging from 1 to 5 mrad (0.05º to 0.3º), sets the reflection's characteristic cut-off energy (see section 2.1). Slightly bending the reflection mirror can focus or collimate the x-ray beam.

1.4.2 Microfocusing Optics

X-ray microfocusing optics have made incredible advances in the past fifteen to twenty years. Advances in x-ray optics have come in all three major categories of optics: reflective optics, refractive optics, and diffractive optics. Many of the first working types of microfocusing hard x-ray optics emerged between 1988 and 1996; including Fresnel zone plates (diffractive) [25-31], polycapillaries (reflective) [32-35], multi-bounce monocapillaries (reflective) [33,36-38], elliptically shaped single-bounce monocapillaries (reflective) [39-41], and x-ray refractive optics [42-45]. Kirkpatrick-Baez (KB) mirrors (both reflective and diffractive) and other shaped mirrors and multilayers have been around for much longer [46]. KB mirrors continue to compete very well with these other microfocusing methods, by improving their qualities [46,47]. Still others methods for microfocusing have come a little later, such as x-ray waveguides (reflective) [48-50].

Over the last ten to twelve years, the applications and designs of microfocusing optics has greatly expanded. Combining the different optical methods together enables new developments, which ultimately result in new microfocusing optics, such as Fresnel lenses, Bragg-Fresnel lenses, and Fresnel-Laue lenses [51-53]. In the years to come crossover will continue to occur between microfocusing ideas, making microfocusing x-ray optics a truly rich field of study.

The assortments of different microfocusing optics all have their own advantages and limitations. A few basic attributes define the quality of microfocusing x-ray optics. The spot size primarily defines the quality of a microfocusing x-ray optic because a smaller spot size allows for a higher resolution of features within a sample. Other metrics include the divergence, numerical aperture, gain, efficiency, working length, aberrations, fabrication limits, theoretical limits, energy range etc. These attributes are important, depending on the particular experiment.

Table 1.3 highlights various x-ray microfocusing optics and their attributes. This table gives ranges on attributes, not necessarily typical values or extraneous values achieved by various optics. For example, single-bounce monocapillaries typically have a spot size ranging from 5 to 20 μm, but they have achieved a spot size down to 250 nm [54]. The table demonstrates one overall trend: optics that produce the smallest spots also have the highest gains. Table 1.3 captures most of the functional highlights, but it does not capture how each optic functions or highlights their particular advantages and limitations.

The index of refraction for x-rays, which is slightly less than 1 by a factor of about 10^{-5}, determines the functionality of every optic in the table above (section 2.2). Figure 1.7 gives a simple sketch of each of these optics with some rays traced out in blue showing their focusing.

Table 1.3 A list of x-ray microfocusing optics outlines some of the metrics and capabilities of each of the optics listed.
***this very small one dimensionally focused beam was created by a Fresnel-Laue Lens , which is very similar to a zone plate.**

	Spot Size (μm)	**Divergence**	**Gain**	**Efficiency**	**Working length**	**limitations**
Single-Bounce Monocapillaries	100 to 0.25	10 to 1 mrad	2 to 10^3	99% to 90%	0.2 to 150 mm	Aperture size, Slope errors
Multi Bounce Monocapillaries	50 to 0.09	10 to 1 mrad	2 to 10^3	20% or less	a few μm	Focus at optic's tip
Polycapillaries	100 to 10	Up to 20º	100 to 10^4	40% to 20%	2 to 100 mm	Limited spot size
Fresnel Zone Plates	30 to 0.03*	Over 20º, down to 0.1 mrad	2 to 10^6	40% to 10%	A few mm to meters	Aperture size, chromatic aberration
Refractive lenses	30 to 0.25	10 to 0.1 mrad	2 to 4000	90% to 10%	a few mm to meters	Aperture size, chromatic aberration
KB mirrors	0.09 and larger	A few degrees to 0.1 mrad	3 to 10^6	95% to 40%	A few cm to meters	Slope errors
Waveguides	0.03 and larger	10 to 1 mrad	2 to 4000	20% or less	a few μm	Focus at optic's tip

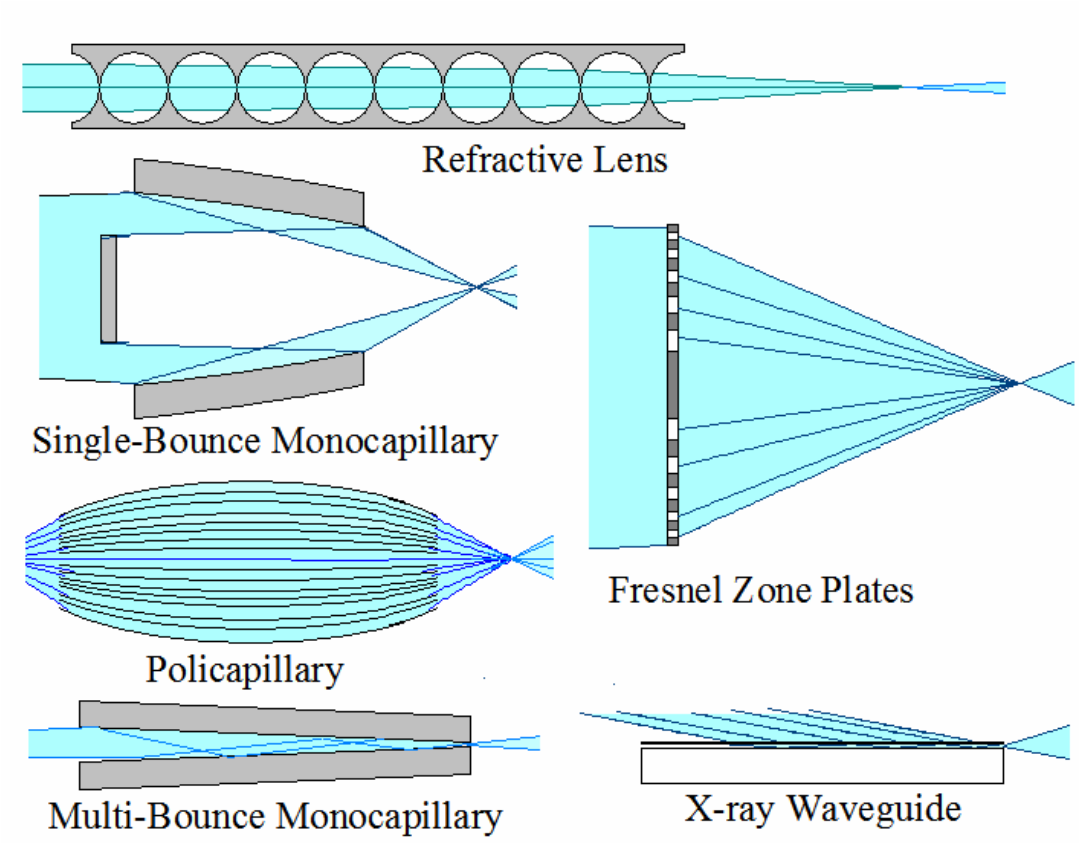

Figure 1.7 A sketch of various microfocusing optics (not to scale). Reflective optics, which use total external reflection include single-bounce monocapillaries, multi-bounce monocapillaries, polycapillaries, and x-ray waveguides. Fresnel zone plates are diffractive optics. Each carefully placed ring in the plate produces a pi phase shift in the x-rays, thereby setting up a maximum point of constructive interference at the focus. The refractive lenses are made of many concave lenses to focus the x-ray beam, because the index of refraction is slightly less than one.

Single-bounce monocapillaries

Advantages: They have a controlled divergence, they are achromatic, they are almost 100% efficient, and they are able to focus to high energies, up to 80 keV.

Limitations: The most serious limitations are the figure slope errors, which limit the spot size. They are not imaging optics, but they can be, using a two bounce design [55].

Multi-bounce monocapillaries

Advantages: They can have a very small spot size, which does not depend on the source size.

Limitations: The largest disadvantage is their working distance. A sample needs to be within a few microns of the optic. They are also are not extremely efficient.

Polycapillaries

Advantages: They can collect a very large solid angle, up to 20º, which results in very high gains, and makes them a natural fit to flux limited X-ray tubes.

Limitations: spot sizes are larger than 10 μm and they are non-imaging. The spot size is energy dependent, getting larger at lower energies (see section 9.4).

Zone Plates

Advantages: These are excellent optics for creating very small focal spot sizes, resulting in very high gains. They can create images with high spatial resolution.

Limitations: They have chromatic aberration. Their efficiency and resolution drop quickly at higher energies (15-20 keV and above). Their fabrication limits their aperture size. (Section 9.10 gives an example of zone plates at A2)

Refractive lenses

Most often these lenses have one dimensional focusing. Two are often used in series to get two dimensional focusing. Some refractive optics can focus in two dimensions.

Advantages: They have very small spot sizes and can focus energies up to 100 keV.

Limitations: The absorption in the lenses' material limits the aperture size, they also have chromatic aberration.

Kirkpatrick-Baez mirrors

These mirrors are often two bendable cylinder shapes with surfaces at 90º with respect to each other and through which X-rays bounce successively. Ideally, they want to be shaped like a section of an ellipsoid, just like the single-bounce monocapillary optic. They can either be a reflective optic, or have a multilayer reflection.

Advantages: They can create very small spot sizes, with extremely well-controlled figures and slope errors. They are achromatic.

Limitations: These mirrors are expensive and often must be kept in a vacuum chamber to keep the multilayers clean. They also are limited in achieving very short focal lengths, which would allow for higher magnifications.

Waveguides

Advantages: They can have a very small spot size, which does not depend on the source size.

Limitations: The largest disadvantage is their working distance. A sample needs to be within a few microns of the optic. They are also non-imaging and not extremely efficient.

This gives a glimpse of what is out there in the realm of microfocusing optics. Again, with all the optics available, and all the variations that could be tried, it is not always clear what the best microfocusing optic is for a particular experiment. Single-bounce monocapillaries can be compared directly to other optics, or can work in conjunction with these other optics. In sections 9.9 and 9.10 I give two examples of a single bounce monocapillary compared to both a zone plate at CHESS's A2 beamline and a KB mirror at APS's 18ID line. Single-bounce monocapillaries can work in conjunction with other

microfocusing optics. Examples include Xradia's x-ray microscopes[7], which use a single-bounce monocapillary to focus the beam from the x-ray tube onto a sample, and then a zone plate images the sample at a high resolution. Another example uses a zone plate to focus to a small spot, and then uses a single bounce monocapillary to further de-magnify the zone plate image to get a very small, 250 nm spot size from the single-bounce monocapillary [54]. The possibilities for endless combinations of optical configurations grow with each new improvement made.

1.5 General Units Notes

There are units of measurement that are very useful for synchrotrons. They are so often used by beam line scientists that newcomers to the community are somewhat baffled by what they are talking about. I have included this section because of its usefulness; especially to anyone not intimately familiar to what a beam line scientist does and for a reference for an exhausted beam line scientist, running late at night.

1.5.1 The Milliradian Angular Unit

The milliradian (mrad) unit is very useful in a wide array of basic synchrotron applications. The mrad unit quickly verifies the resolution, divergence, placement of beam line components, etc. on the beam line.

[7] From discussions with Dr. Wenbing Yun, founder of Xradia (5052 Commercial Circle Concord, CA 94520, URL: www.xradia.com). The company makes single-bounce capillary optics, but exact products or methods of using the single-bounce monocapillary optics are undisclosed information. The information above is my best guess of where they would be used in advertised products.

$$\theta_d[mrad] \cong \frac{l_{x,z}[mm]}{l_y[m]} \tag{1-9}$$

Where 'θ' is an angle, '$l_{x,z}$' is a distance measured in the horizontal or vertical direction respectively, perpendicular to the x-ray beam, and 'l_y' is a distance measured along the x-ray beam. Equation 1-9 is valid for small mrad sized angles, satisfying the small angle approximation. The key to the equation 1-9, and the equations below is using the right units: angles in milliradians, path lengths in meters (alternatively millimeters), and distances perpendicular to the path in millimeters (alternatively microns). If a slit is open by 'x' mm and it is one meter from a point source, the divergence of the beam is 'x' mrad. Another form of the small angle approximation estimates the size of a beam along its path.

$$s_e^2 \cong s_s^2 + \left(l_y \theta_d\right)^2 \tag{1-10}$$

$$s_e \approx l_y \theta_d \tag{1-11}$$

Where 's_e' is the estimated beam size, 's_s' is the source or slit size, 'l_y' is the estimated beam size's distance from the source or slit, and 'θ_d' is the beam's divergence. Equation 1-10 estimates the size of the beam along its path. Equation 1-11 is often adequate, especially in the horizontal direction, and in practice often equivalent to equation 1-9. Below are two examples of applying the equations above, which quickly calculate beam line problems.

Example 1: What surface area does the multilayer optics need to have at D-line to collect the entire beam 10 meters from the source? D-line has a source size of 1.49(H)x1.18(V) mm^2 and a divergence of 4.5(H)x0.1(V) $mrad^2$. Ten meters down

stream, using equation 1-11, the beam size horizontally is ~(10m*4.5 mrad) or 45 mm; the multilayer needs to be ~ 50 mm wide. In the vertical direction, using equation 1-11, the beam is $((\sim 1mm)^2 + (10m*0.1\ mrad)^2)^{1/2}$, or 1.4 mm in the vertical direction; the multilayer needs to intersect about 2 mm of the beam. If the mirror reflects the beam at 1º (17 mrad), the multilayer needs to be 0.117 m long to collect the entire beam vertically (equation 1-9 gives l_y = 2mm/17mrad = 0.117 m). The multilayer should be about 50 mm wide and about 120 mm long.

Example 2: A detector with a 100 by 100 array of 150 μm^2 square pixels, (15 by 15 mm^2 area) sits 55 mm away from the sample. A single-bounce monocapillary optic produces an x-ray beam with a 50 μm spot and an 8 mrad divergence on the sample. What is the angular resolution and how wide in pixels is a diffracted beam? The angular resolution will be 8 mrad (0.46º), or the same as the capillary divergence. The size of diffraction spot 55 mm away from the sample is $((40\ \mu m)^2 + (55mm*8\ mrad)^2)^{1/2}$, or 440 μm, which is about 3 pixels wide. The optics and not the detector limit the resolution. What is the angular resolution if the divergence of the capillary optic is 2 mrad (0.12º)? The size of diffraction spot now is $((40\ \mu m)^2 + (55mm*2\ mrad)^2)^{1/2}$, or 120 μm, which is about 1 pixels wide. At this point, the detector will limit the resolution; we could move the detector further from the sample to improve the resolution, if desired.

From the two examples above, we can see the mrad unit is extremely useful for quickly figuring out sizes of optics, resolution, etc. on the x-ray beam lines. Equations 1-9, 1-10 and 1-11 are extremely useful in many beam line applications. These basic equations are used repeatedly on the beam lines and with the single-bounce monocapillary optics.

1.5.2 Resolution and Structural Sizes

In x-ray experiments there are two basic questions that come up repeatedly, especially when someone wants to use focusing optics. They are, "What is the largest structure size we can resolve?" and "What is the smallest observable peak shift?"

The question "What is the largest structure size we can resolve?" comes up in both SAXS and protein crystallography. The x-ray beam's divergence sets the upper limit on the measurable unit cell size in crystallography, or a molecule size in SAXS. The two equations below are derived from Bragg's law, they give the divergence required to see to a certain feature size.

$$d_{\max} = \frac{\lambda}{2\sin\theta_{div}} \cong \frac{\lambda}{2\theta_{div}} \qquad q_{\min} = \frac{4\pi\sin\theta_{\min}}{\lambda} \cong \frac{4\pi\theta_{\min}}{\lambda} \qquad (1\text{-}12)$$

In the equations above 'd_{max}' is the upper size limit measurable with a beam divergence of 'θ_{div}' at a wavelength of 'λ'. In inverse units 'q_{min}' is the lower inverse size limit. For example, a beam divergence of ~ 1.0 mrad or smaller is needed to see feature sizes up to 500 Å (0.0126 $Å^{-1}$ in momentum "q" space) in a 10 keV beam.

The question "What is the smallest observable peak shift?" comes up in diffraction experiments, where small changes in the lattice spacing of the samples happen for a multitude of reasons. In order to be able to distinguish a shift or a split in a peak, the shift or spilt has to be around 1/10 to 1/20 of the FWHM for the peak, assuming good counting statistics.

$$\Delta\theta \le \frac{\theta_{div}}{20} \qquad \Delta d \approx \left| \frac{\lambda}{2\sin(\theta_{peak} + \Delta\theta)} - \frac{\lambda}{2\sin(\theta_{peak})} \right| \qquad (1\text{-}13)$$

In the equations above 'θ_{div}' is the divergence of the beam '$\Delta\theta$' is the observable peak shift in angle, 'θ_{peak}' is the peak position at a wavelength of 'λ' and 'Δd' is the smallest observable lattice spacing shift. For example, for a beam with a divergence of 2 mrad, the minimum observable shift in angle would be ~0.1 mrad (0.006º). At a 'θ_{peak}' of 5º at 10 keV, 'Δd' would be approximately 0.009 Å. At a 'θ_{peak}' of 10º at 10 keV, 'Δd' would be approximately 0.002 Å.

1.5.3 Spectral Brightness (or Brilliance)

For synchrotrons, the unit used to compare sources is spectral brightness, also often called brilliance. Spectral brightness has units of '*photons /sec/mm^2/mrad^2/0.1% bandwidth*'. Optics do not change the spectral brightness, which makes the unit useful for directly comparing x-ray sources. Other useful units, such as total flux '*photons/sec*', or flux density '*photons/sec/mm^2*' can be calculated from the spectral brightness. Spectral brightness is not a unit particularly useful for experiments; it needs to be changed into other units such as flux or flux density, which are more applicable to experiments.

To convert the spectral brightness of an x-ray source into other units, other effects must be known, such as the divergence and size of the source, and the effects of other optics in the beam. Careful attention must be made to convert spectral brightness into other units; the conversions are full of pitfalls. For spectral brightness, the '*mm^2*' refers to a

source size, not the size of an aperture down stream from the source. For spectral brightness, the '*mrad*^{2}' refers to a beam size down stream from the source. The flux density's area in '*mm*^{2}' is calculated from the spectral brightness's '*mrad*^{2}' divergence.

To help clarify how to use spectral brightness, I will calculate the flux density at D-line using the spectral brightness curves in Figure 1.3. The D-line web page quotes a flux density of 1×10^{12} photons/sec/mm^2/100mA at 10 keV in the hutch. For Figure 1.3, the curve is not quite spectral brightness, it has already been vertically integrated; it gives 9.4x10^{13} photons /sec/mm^2/mrad^2/0.1% bandwidth, for a 200 mA current at 10 keV. To compare the quoted flux density with the calculated vertically integrated flux, the units need to be changed into a flux density. The source size is 1.18x1.49 mm^2. D-line uses a multilayer with a 1.5% bandwidth. The flux density is estimated at 13 meters from the source (in the hutch) at a positron current of 100 mA. Below is given the units conversion:

$$\begin{aligned} Flux_D &= 9.4\times10^{13}\left[\frac{photons}{s\cdot mm^s(source)\cdot mrad^2(source)\cdot 0.1\%BW\cdot 200mA}\right]\cdot\ 1.76[mm^2(source)] \\ &\quad\cdot 5.7\times10^{-3}\left[\frac{mrad^2(source)}{mm^2(hutch)}\right]\cdot 15[0.1\%BW]\cdot 0.5\left[\frac{200mA}{100mA}\right] \\ &= 7.1\times10^{12}\left[\frac{photons}{s\cdot mm^2(hutch)\cdot 100mA}\right] \end{aligned} \tag{1-14}$$

The estimated flux density '*Flux$_D$*' is 7.1x10^{12} photons/s/mm^2/100mA. Units seem to just disappear and reappear too conveniently, for the calculation above. The '*5.7×10^{-3} mrad^2/mm^2(hutch)*' converts the divergence in '*mrad*^{2}' to a flux density area in units of '*mm*^{2}' in the hutch. This conversion comes from the divergence of a imaginary 1 mm slit at a distance of 13 meters (0.076 mrad), and then squaring it to get the second dimension (0.0057 mrad^2). The '*15*' bandwidth conversion is from the 1.5% multilayer

bandwidth. The change from 200 mA to 100mA is a linear relation, which is evident in the units in the left graph in Figure 1.3. To get it into units of 100 mA, the flux density needs to be divided by two[8]. The measured value is 1×10^{12} photons/sec/mm/100mA at 10 keV quoted on the D1 web page. This value is an overestimate, which neglects the windows, attenuators, and reflection coefficients of the optics in the beam line. Again, I use this example to stress that the units used vary, and care must be used to convert the units correctly.

[8] Disappearing and reappearing units are common in flux-based unit conversions.

Chapter 2 Basics of Single-Bounce Monocapillary Optics

X-ray single-bounce capillary optics have the same function as refractive lens in visible light optics. They redirect rays of light to a focus. This chapter covers some basic optics equations, useful for capillary optics. This chapter also covers the two basic principles needed to understand how single-bounce monocapillaries function. The principles are how x rays reflect from a surface and how ellipsoidal shapes focus a beam.

2.1 Optic Basics

Single-bounce monocapillary optics follow the basic ray optics equation in the parallax approximation:

$$\frac{1}{i}+\frac{1}{o}=\frac{1}{f} \tag{2-1}$$

This familiar "thin-lens" equation has 'f' as the focal length of the optic, 'o' as the object-to-optic distance, and 'i' as the image-to-optic distance (Figure 2.1). For monocapillaries on synchrotron beam lines, object distances are typically much longer than the image distances. Object distances range from 1 to 30 meters and image distances range from 20 to 150 mm. In this limit, the image distance is almost the same as the focal length, so often with monocapillaries the image distance and the focal length are the same. Some other useful quantities are the magnification of the beam, the

divergent angle of the beam, and the numerical aperture, given in equations (2-2), (2-3) and (2-4), respectively.

$$M = \frac{i}{o} = \frac{s_i}{s_o} \tag{2-2}$$

$$\theta_{div} = \frac{D}{i} \tag{2-3}$$

$$NA = n \sin\left(\frac{\theta_{div}}{2}\right) \approx \frac{\theta_{div}}{2} \tag{2-4}$$

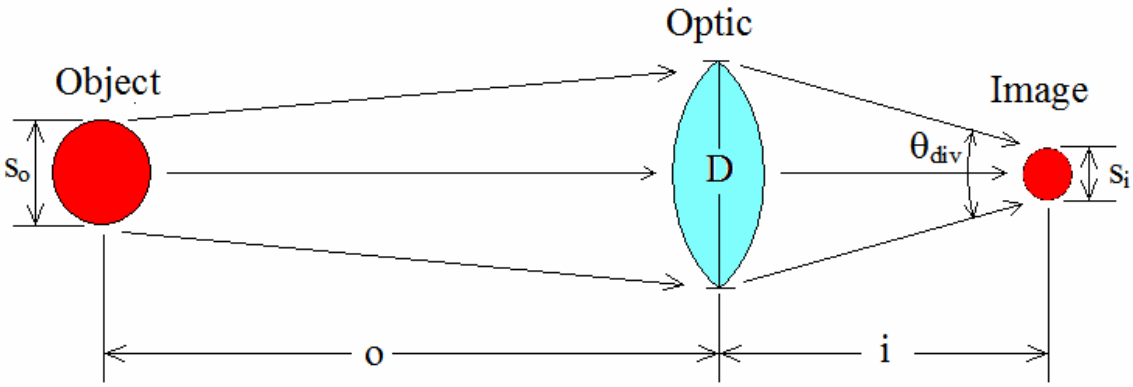

Figure 2.1 This diagram shows all parameters in the basic ray optics equation, the magnification, and the divergence of the beam.

For the equations above 'M' is the magnification, 's_o' is the object size, 's_i' is the image size, 'θ_{div}' is the full divergence from the optic, 'D' is the optics diameter, 'n' is the index of refraction and 'NA' is the numerical aperture. All of these equations can be used with the monocapillary optics. The magnification of monocapillary optics can range from 1/50 to 1/100000 in practice and produce x-ray spot sizes from 5 to 50 μm, on synchrotron beam lines. The divergence of single-bounce monocapillary optics range from 2 to 10 mrad; this gives a numerical aperture of 0.005 to 0.001. For x-ray optics, 'n' is very close to 1 and 'θ_{div}' is small, therefore 'NA' equals '$\theta_{div}/2$'.

Another useful concept is gain. The gain is simply the ratio of intensity at the focal spot with and without the optic.

$$G = \frac{I_{in}}{I_0} \tag{2-5}$$

Where 'G' is the gain, 'I_{in}' is the intensity through the pinhole at the optic's focus, and 'I_0' is the intensity through the pinhole without the optic in the x-ray beam. In order to measure the gain, a pinhole is placed at the focal position, and the intensity of radiation is measured with and without the optic. The pinhole should be smaller than the optic's spot size, by at least a factor of two.

2.2 Total External Reflection of X-rays

One of the key concepts in understanding all x-ray reflection optics, including single-bounce monocapillary optics is total external reflection. X-rays are not easily reflected, they only reflect from surfaces at grazing incident angles, typically at less then 1º. This effect is explained by applying the index of refection for x rays to Snell's law. The index of refraction for x rays in all materials is slightly less than one, often expressed in the form:

$$n = 1 - \delta + i\beta \tag{2-6}$$

Where 'δ' is the real part often called the decrement, or phase variation term of the index of refraction, and 'β' is the imaginary part, or the absorption term of the index of refraction [1,2]. With most materials, the 'δ' is approximately 10^{-5}. 'β' can vary depending on the material and wavelength, but is usually a factor of 10 to 100 smaller

than 'δ', away from atomic absorption edges. Snell's law, measured with angles from the surface, has the form:

$$n_1 \cos\theta = n_2 \cos\theta' \tag{2-7}$$

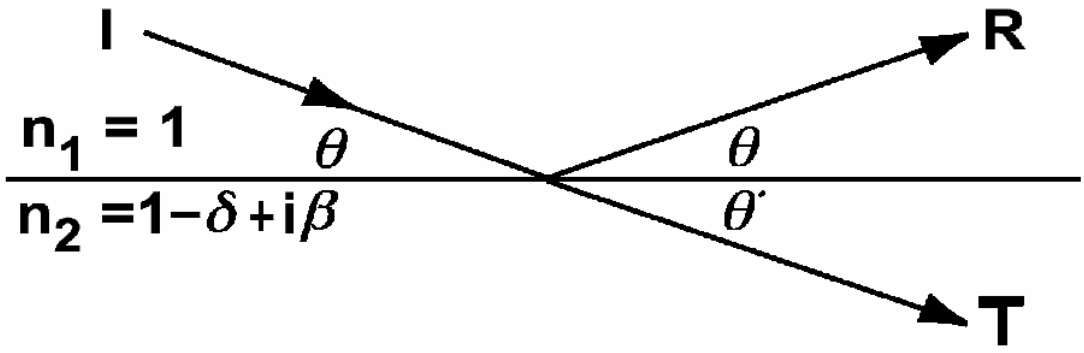

Figure 2.2 A schematic view of the quantities used in Snell's law at grazing incidence.

Where 'θ' is the angle between the surface and the beam, 'n_2' is the index of refraction of the material, 'n_1' is the index of refraction of vacuum, which is 1 (Figure 2.2). Total external reflection occurs because 'n_2' is less than 'n_1'. This allows the angle of the transmitted beam, 'θ'' to reach zero, thereby eliminating any transmitted beam into the surface. Eliminating the transmitted beam leaves only the reflected beam. The critical angle for this transition is:

$$\cos\theta_c = \frac{n_2}{n_1} \tag{2-8}$$

$$\theta_c \cong \sqrt{2\delta} \tag{2-9}$$

The second form of this equation is achieved making the small angle approximation and by Taylor expanding the cosine. So for 'δ' of approximately 10^{-5}, the critical angle is 4.4 mrad (0.25º). The critical angle is proportional to the wavelength of the scattered x

rays and is proportional to the square of the scattering material's atomic number 'Z'. This can be shown by expanding 'δ' out into its scattering parameters [2].

$$\theta_c \propto \lambda\sqrt{Z} \tag{2-10}$$

This shows that higher 'Z' (larger atomic number) materials and longer wavelength (lower energy) x-ray beams have larger critical angles.

Single-bounce monocapillaries are generally made of glass. Figure 2.3 gives the reflectivity of glass, SiO_2, at an angle of 2 mrad (0.11º) as a function of energy. For glass at an angle of 2 mrad, x-ray energies under 16 keV (0.77 Å wavelength) efficiently undergo total external reflection. The right side of Figure 2.3 gives an equation for estimating the critical angle for an x-ray energy cutoff in glass. The small table shows the cutoff energies for a few different incident angles in glass.

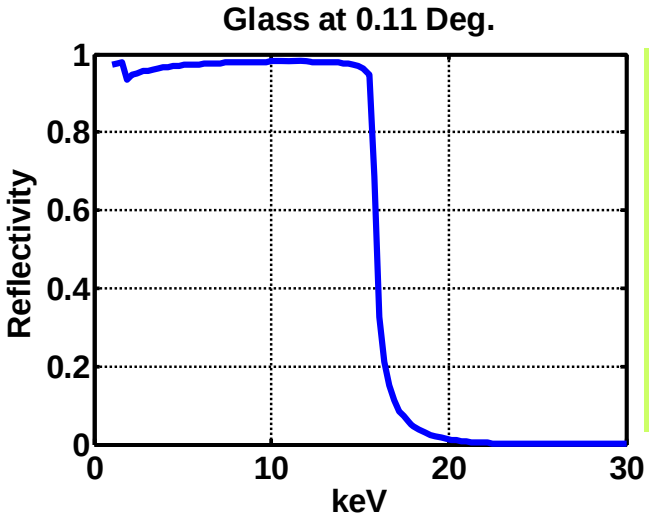

For Glass:

θ_c=32 keV/E_c * milliradians

i.e. 2 mrad (0.11º) at 16 keV
1 mrad (0.06º) at 32 keV
0.5 mrad (.03º) at 64 keV

Figure 2.3 On the left is the calculated reflectivity of a flat glass surface at 2 mrad (0.11º). The reflectivity is close to 100% below 16 keV. To the right is an equation for the critical angle energy cutoff for glass, and a small table of cutoff energies for a few grazing incident angles.

Total external reflection gives a way to redirect x rays. Now the strategy is to reflect all the x rays from a beam into a small focal spot.

2.3 Elliptically Shaped Mirrors

Single-bounce monocapillaries are shaped like a small section of a very eccentric ellipsoid (Figure 2.4). Rays from a point source placed at one foci of an ellipse all go to the opposite foci, when the rays undergo specular reflection. The incident angle equals the reflected angle for specular reflection, '$\theta_{incident}=\theta_{reflected}$'. The ellipsoid shape satisfies the grazing incident requirement needed for total external reflection of x rays [55-57]. This basic premise allows for many potential shapes for optics.

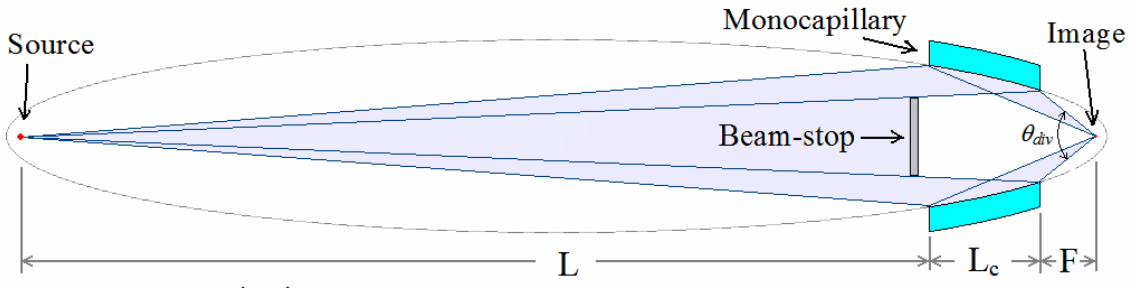

Figure 2.4 A schematic of the full elliptical shape. A portion of that shape is the single-bounce monocapillary optic. Rays are redirected from one foci to the other foci at grazing incident angles. A beam-stop is used to block the portion of the unfocused direct beam from going through the center of the optic (see section 5.3).

The largest grazing incident angle at the tip of the capillary optic sets the maximum divergence of the beam. Equation 2-11 gives the full divergence of the beam from the tip of the capillary optic (Figure 2.5):

$$\theta_{div} = 4\theta_{grazing} \tag{2-11}$$

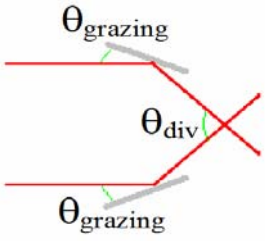

Figure 2.5 The grazing angle and the full divergence at the tip of a capillary optic.

Where 'θ_{div}' is the full capillary divergence and '$\theta_{grazing}$' is the angle between the surface and the x-ray beam. The condition '$\theta_{grazing}=\theta_c$' gives the maximum divergence a single bounce capillary optic can have in order to efficiently reflect x rays up to a given energy. For example, if the capillary optic needs to function at 16 keV, '$\theta_{grazing}$' needs to equal 2 mrad or less. This limits the full divergence of the capillary, 'θ_{div}', to 8 mrad or less.

The basic equation of an ellipse is useful when dealing with single-bounce monocapillaries. Just two parameters define an ellipse's shape, the major axis 'a' and the minor axis 'b' (Figure 2.6). Equation 2-12 is the basic equation for an ellipse in Cartesian coordinates, with 'x_o' and 'y_o' giving the coordinate of the center of the ellipse.

$$\frac{(x-x_o)^2}{a^2}+\frac{(y-y_o)^2}{b^2}=1 \qquad (2\text{-}12)$$

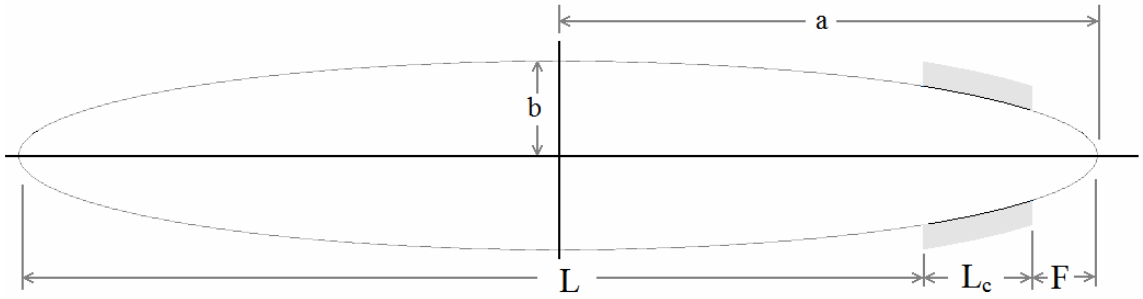

Figure 2.6. A schematic of an ellipse with the major axis and minor axis dimensions labeled. The dimensions used for the single-bounce monocapillary

Equations 2-13 and 2-14 give the major and minor axis of the ellipse in the parameters most often used to describe a single-bounce monocapillary.

$$a \cong \frac{1}{2}\left(L + L_c + F\right) \tag{2-13}$$

$$b \cong \frac{\theta_{div}\sqrt{aF}}{2\sqrt{2}} \tag{2-14}$$

Where 'L' is the distance from the source to the base of the capillary, 'L_c' is the length of the capillary optic, and 'F ' is the distance from the tip of the capillary to the focus. Equation 2-14 holds for only very eccentric ellipse's, where '$a>>b$'; Single-bounce monocapillaries are generally very eccentric ellipsoids, with the major diameter being 0.5 to 15 m and the minor diameter being roughly 0.5 to 3 mm.

Single-bounce capillary x-ray optics are focusing optics, and not imaging optics. Imaging can occur using the ellipsoidal shape in the small area normal to the major axis, near the foci. This region of the ellipsoid is shaped almost like a parabolic mirror. This region of the ellipsoid does not have grazing incident angles, therefore cannot be used for x rays. The region of the ellipsoid that is useful for x-ray optics is between the two

foci (Figure 2.4). For this region of the ellipsoid, point to point focusing of light only works for a point source placed at a foci. An extended source will have an image that is extremely distorted. The source's image is effectively smeared over 720º of rotation. Additionally, the source's image is smeared due to an optic's range of magnifications [56,57].

The two aberrations are a rotational aberration and a magnification aberration[58]. A coordinate system needs to be established in order to understand the rotational aberration (Figure 2.7). Both the source and image reside in a plane with one of the ellipsoid's foci at the center. Positions are defined by a radius 'r_s' and an angle 'θ_s' in the source plane and a radius 'r_i' and an angle 'θ_i' in the image plane. The angle 'ϕ' is the rays' radial position reflected along a section of capillary length 'Δl'. For a full ellipsoid shape, this angle ranges from 0 to 2π. Equations 2-15 and 2-16 give how a point source in the source plane maps into the image plane over the full range of angles 'ϕ' for a small slice of the ellipsoid.

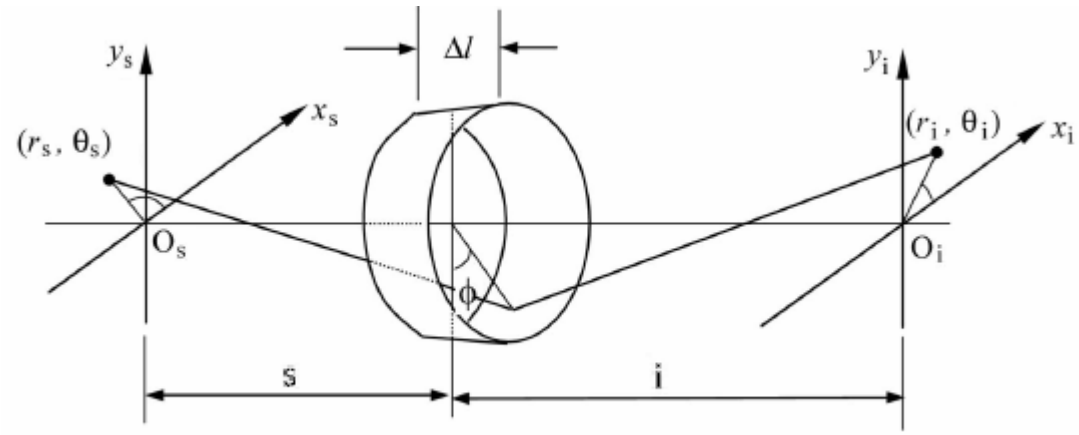

Figure 2.7 This diagram gives the geometry of how a spot in the image plane reflects off of a small section of an ellipsoidal shape to a spot in the image plane. Image taken from refrence [58].

$$r_i = Mr_s \tag{2-15}$$

$$\theta_i = \pi - (\theta_s - 2\phi) \tag{2-16}$$

Where 'M' is the magnification given in equation 2-2. When a point source is at the foci ($r_s = 0$), all the rays will reflect to the other foci ($r_i = 0$). When a point source is put into another region of the source plane, '(r_s, θ_s)', a circle is swept out in the image plane, with 'ϕ' ranging between 0 to π. When the source is bar-shaped, which is very common for synchrotrons, the focal spot in the image plane has circular symmetry, because of the rotational aberration. The second aberration comes from capillary optics that have a length. A good length for an ellipsoidal-shaped capillary is about twice the distance between the capillary tip and the focus [58]. With this length, the capillaries' magnification typically varies by a factor of three between the base and the tip. This means that the magnification varies by the same factor over the length of the entire optic. The length of the optic causes the magnifications to be smeared on the image. In the case of a bar-shaped source that creates a circular spot, the image shows a smear of different sized circular spots as well.

There is a way to change a grazing incident optic into an imaging optic; it is called a Wolter mirror [55,59,60]. These optics consist of a two-bounce grazing incident optic, with one bounce from an ellipsoid and a second bounce from a hyperboloid. Conic section shapes are chosen to closely satisfy the Abbe sine condition [61], which needs to be satisfied for an optic to produce good images.

This is the basic information needed to understand ellipsoidal-shaped single-bounce monocapillary optics. In the next chapter, I will define the tools used to design the capillary shapes needed to best fit a particular x-ray source and a particular experimental application.

Chapter 3 Design of Single-Bounce Monocapillary Optics

All of the work done with single-bounce monocapillary optics hinges on their positive or limiting attributes. There is an ongoing effort to optimize the positive attributes, by expanding the optics' natural advantages in performing various x-ray microbeam experiments. Chapters 5 and 9 discuss optimization of the optics' positive attributes describe the auxiliary equipment needed for the optics, and the experiments performed using the optics at CHESS over the past three years. There is an ongoing effort to minimize the limiting attributes, by improving and developing methods for fabrication. Chapters 6 and 7 describe this aspect of the work, and deal with the current state-of-the-art fabrication of monocapillary optics and future directions for further improving the optics and pulling techniques.

This chapter will define the advantages and limitations of monocapillary optics and will describe the tools used to design the optics. Two examples provide the design process for optics on synchrotron beam lines; one with, and one without additional upstream focusing optics. These two examples will cover most situations that need to be considered when designing single-bounce monocapillary optics for typical synchrotron beam lines.

3.1 Why use a Monocapillary Optic? Its Advantages and Limitations

Why use a microfocusing x-ray optic? To make very small, intense x-ray microbeams. The reason for having x-ray microbeams is twofold; small x-ray beams are excellent for probing microscopic-sized samples or probing micron-sized features in macroscopic-sized samples.

When are microfocusing single-bounce monocapillary optics useful?

- When you need a small beam spot, for microscopic-sized samples between 5 μm to 50 μm, or to resolve 5 μm to 50 μm sized features in macroscopic-sized samples.
- When divergences between 1 to 10 mrad (0.6º to 0.06º) are sufficient for x-ray experiments.

These two criteria hold for many potential sample investigations. Many different types of x-ray experiments benefit from having a small x-ray spot. The differentiating factor for many experiments comes from the amount of divergence the experiment can tolerate. X-ray fluorescence or absorption measurements can handle large beam divergences. Single-bounce monocapillaries are adequate for these types of experiments, at least on synchrotron beam lines. For most x-ray elastic scattering experiments the beam divergence needs to be between 1 to 10 mrad (0.6º to 0.06º). Single-bounce monocapillaries have the same range of divergence, which is a nice natural match. Examples of x-ray diffraction scattering experiments include SAXS, protein crystallography, and powder diffraction. Thus, monocapillary optics suit experiments that need a small beam and a controlled divergence.

What are the advantages and disadvantages of using single-bounce monocapillary optics? I will first list and discuss the positive attributes, then the limiting attributes. The important metrics that define microfocusing optics include spot size, divergence, gain, efficiency, and working length (outlined in section 1.4.2).

3.1.1 Positive Single-Bounce Monocapillary Attributes

The positive attributes:

- They are achromatic.
- They are optically and mechanically robust.
- They are 90% to 99% efficient.
- The divergence and focal length can be designed.

Being achromatic is the most important advantage of the monocapillary optics. This means the focal spot size, the focal spot location, and the divergence of the focused beam do not change with energy. The capillary's focal distance is nearly constant, within ±2 mm, between different synchrotron beam-lines. The reason the image position (focal length) does not change is the source-to-optic length is very long, ranging 1 to 30 meters, compared to the image-to-optic distance, ranging 20 to 150 mm (see section 2.1). These optics focus a 0.01% bandwidth beam as effectively as a 50% bandwidth beam. The reflection efficiency remains almost unchanged over an x-ray energy range, which does not exceed the critical angle. Single-bounce monocapillary optics are unique because they are the only microfocusing optics, with a large focal length, which have a focal size, divergence and focal length independent of x-ray energy. KB mirrors can also do this with two bounces.

Single-bounce monocapillary optics are also optically robust. Optical robustness allows modularity with a wide array of other x-ray optics in a beam. At synchrotrons, a single-bounce monocapillary optic designed for one beam line will very often work at all the other beam lines. They handle x-ray beams with or without upstream focusing optics. They work in both collimated and divergent beams. A monocapillary placed in a divergent beam may have a larger divergence and spot size, but it will produce a focus nonetheless. This robustness, allows them to out perform other micro focusing optics in surprising ways[9].

Single-bounce monocapillary optics are mechanically robust. The optics are strong enough to be handled, and they work in air. The optics are extremely radiation hard, a few of them have spent many weeks to months in a synchrotron beam. The only sign of wear is a discoloration of the glass at the base of the optic. They are small enough to fit into constrained space, which leaves room for other equipment in an experiment. The space in which they fit is most often limited by the hardware used to position the single-bounce monocapillary optics, and not the optics themselves.

Single-bounce monocapillary optics are 90% to 99% efficient[10] [40]. Thus, single-bounce monocapillary optics are generally at the top of the list when efficiency is an important consideration. This means if both the spot size and the divergence of the beam are well matched, a single-bounce monocapillary will always have the highest gain, compared to any other microfocusing optic.

[9] See section 9.9, for an example of a comparison between a monocapillary and KB mirrors done at APS.
[10] This is the efficiency of x-rays which interact with the monocapillary's optical surface. Definitions of efficiency may vary.

Lastly, they have a divergence and focal length that can be designed to fit a particular need an experiment might have. Focal lengths have ranged from 20 to 150 mm, and divergences have ranged from 2 to 10 mrad for the optics. Single-bounce monocapillaries have an additional advantage; their divergence is easily tunable, at the expense of flux, without changing the optics (section 4.3.2).

3.1.2 Limiting Single-Bounce Monocapillary Attributes

The limiting monocapillary attributes are:

- They have profile and slope errors, which limit the spot size to 5 μm or larger, at CHESS with the current technology.
- They are not imaging optics.
- They have finite aperture size of about 1 mm or less and divergence of about 12 mrad or less.

The profile and slope errors are the most severe limits. The spot size is the defining metric for x-ray microfocusing optics. Monocapillaries are theoretically capable of making spot sizes down to a few tens of nanometers [49]. It is the profile and slope errors that keep single-bounce monocapillaries from having spot sizes below 5 μm. Smaller x-ray spots are always on our mind because single-bounce monocapillary optics have this potential for much smaller spots. Because the x-ray spot size is such an important parameter, section 3.1.3 will cover the ideal single-bounce monocapillary, and section 3.1.4 will cover the real single-bounce monocapillary.

Single-bounce monocapillaries are not imaging optics. Again, grazing incident optics can be imaging with a two-bounce Wolter mirror design. Wolter mirrors have been

fabricated by others [59,60]. These optics are complex, therefore we have not attempted to make a two-bounce imaging optic, but they may be attempted in the future. We have pulled a few non-ellipsoidal shapes (section 9.12), and a Wolter mirror may be possible with CHESS's pulling technology (Chapter 6).

Single-bounce monocapillaries have finite aperture size and divergence. This limits the amount of the x-ray beam the optic can collect. The angle of total external reflection sets the largest possible aperture size and divergence, which gets smaller at higher x-ray energies. At 10 keV, the aperture size is about 1 mm or less, and the divergence is 12 mrad or less. This gives a numerical aperture of ~0.006 or smaller. It is quite hard to increase an x-ray optic's numerical aperture—almost all reflective microfocusing x-ray optics have a fabrication or fundamental limit on the size of their numerical apertures, being on the order of $\sim 10^{-3}$ [62]. The aperture size and the divergence could be increased by a factor of two by using a high Z material optical surface, such as rhodium, instead of glass. A multilayer on the reflection surface can also increase the aperture size and divergence, by achieving a larger reflection angle through diffraction effects. Section 7.2 covers the attempts at increasing the aperture size and divergence.

All of the limiting attributes could be improved with either different or better fabrication techniques, but solutions are often hard and time consuming to overcome. Finding ways to improve the optics is always a priority.

3.1.3 Theoretical and Source Constraints for an Ideal Monocapillary

Theoretical limitations, source limitations, and optical surface profile errors limit the spot sizes for single-bounce monocapillary optics. This section will cover the theoretical and source limitations, with an ideal slope error-free optic.

If a single-bounce monocapillary optic is made without any imperfections, what would we have? An ideal single-bounce monocapillary could produce a spot size of a few tens of nanometers, with the smallest theoretical spot size being diffraction-limited:

$$s_i \approx \frac{\lambda}{2NA} = \frac{\lambda}{\theta_{div}} \tag{3-1}$$

Again, 's_i' is the image size, 'λ' is the wavelength of light, and 'NA' is the numerical aperture. An ideal single-bounce monocapillary optic with a divergence of 2 mrad, used at 10 keV, will have a diffraction-limited spot size of ~60 nm. A smaller spot size can be achieved with an optic with a larger divergence. An ideal optic with an 8 mrad divergence will have a diffraction-limited spot size of ~15 nm. Other researchers have more rigorously explored the x-ray diffraction limited spot size, with spot sizes calculated to be on the order of a few tens of nanometers [49,62].

An ideal optic needs an equally as impressive x-ray source to make diffraction-limited spot sizes. A perfect source is a point source. Real sources appear more like a perfect source the smaller the source is and the further away it is observed. What level of perfection must a source have in order to not limit the spot size of a perfect optic? In answering this question I would like to compare two differing sources, the proposed

ERL and D-line at CHESS. Calculations were made using Rong Huang's capillary design program (section 3.2.2).

The ERL is proposed to have a 3 μm source size (in both the vertical and horizontal direction) and a 35 m source to focus distance [63]. The ideal single-bounce monocapillary optic will have a 60 mm focal length and a divergence of 8 mrad. For this very good source, the calculated beam size in Rong Huang's capillary design program, with a perfect single-bounce monocapillary optic would be ~10 nm, which is a little bit below the diffraction limit above, of ~15 nm (the program does not take into account diffraction effects). The ERL source is close to a perfect diffraction-limited source for monocapillary optics. At CHESS, D-line has a 1.5(H)x1.2(V) mm^2 source size and a 13 m source to focus distance. For the same ideal optic, the calculated spot size would be ~8.0 μm. An ideal optic at D-line would only produce a modest improvement over the presently achievable spot size of ~10 to 15 μm of real monocapillary optics. Thus, D-line is not very close to a perfect source, but it does come close to matching the present level of perfection of our optics.

A single-bounce monocapillary optic made without any imperfections could produce a spot on the order of a few tens of nanometers, with the spot size being diffraction-limited from an ERL-type source. Add on top of that the advantage of the optic being 90% to 95% efficient, a perfect single-bounce monocapillary optic would be fantastic, if it can be realized. It would produce higher gains then any other optic. The potential of single-bounce elliptical-shaped optics drives us to further improve the optics to attempt to meet this ideal.

3.1.4 The Limits of a Real Monocapillary

This section defines the shape errors that limit the spot size of real monocapillary optics. There are a number of aspects of this problem to understand not included in this section but are provided in other sections. Ways to measure the limiting distortions are described in sections 4.1, 4.2, and 6.3.3, modeling these distortions are in sections 3.2.2 and 6.4.3, the information about how these distortions may be created during fabrication are in sections 6.3 and 6.4, and ways these distortions could be possibly minimized are in sections 7.1 and 7.2.

All the limitations a single-bounce monocapillary have come from the optic's surface distortions compared to an ideal surface. These distortions increase the optic's x-ray spot size. The distortions are categorized on three length scales: in millimeters, microns, and nanometers, outlined below. The errors are measured in the root mean square (rms) deviations from the ideal surface.

- profile errors (millimeter scale)
    - centerline straightness errors
    - long wavelength errors
    - short wavelength errors
- roughness (micron scale)
- nano-roughness (nm scale)

Profile errors are the largest present limitation of glass single-bounce monocapillaries. These errors come from the optic's fabrication process, or are errors already in the stock glass before fabrication. Slope errors are another slightly different way of representing the profile errors. The slope is the derivative of the profile, and the slope error is the error of the slope compared to the ideal slope. Presently, all the useful optics created

have profile errors on the order of 0.5 to 5 μm rms, and slope errors on the order of 50 to 120 μrad rms.

For our glass monocapillary optics, the profile errors are categorized into three types, centerline straightness errors, long wavelength errors, and short wavelength errors. The straightness variations are a result of a bent or a slightly banana-shaped optic. The straightness limits the optic's performance if the bend over the length of the optic is greater than 1-2 μm. If the optic bends by 5 μm or more, it will not be a good optic. The long wavelength profile errors have amplitudes ranging from 0.1 to 5 μm rms, with wavelengths ranging from 50 to 200 mm. The wavelength is usually longer than the length of the optic. An example of these variations can be seen in the measured of the profile in Figure 3.1. The short wavelength profile errors have amplitudes ranging from

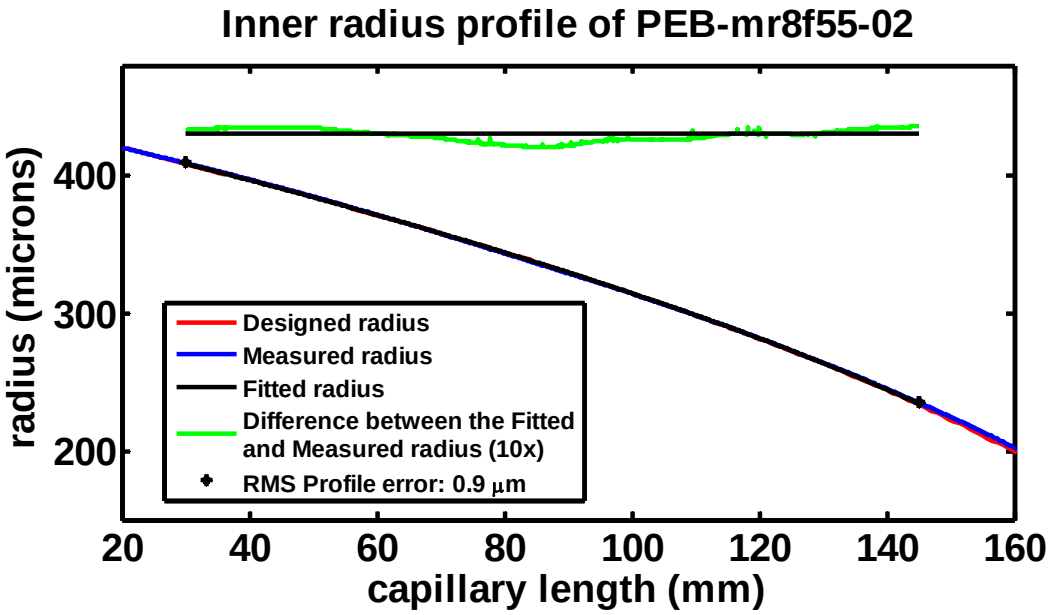

Figure 3.1 The inner radius profile measurement of capillary PEB-mr8f55-02. The graph also shows the difference between the fitted ellipse and the measured profile because the difference in the designed ellipse, measured profile, and fitted ellipse is hard to see *. In this difference, the long wavelength error with a wavelength of ~100 mm can be seen.
*** The spikes in the graph are not real features in the glass, they are errors in measurement.**

0.1 to 1 μm rms with wavelengths ranging from 10 to 30 mm along the length of the optic. The short wavelength errors are most easily seen in the slope profile (Figure 3.2). The short and the long wavelength errors added together make up the total profile error and slope error.

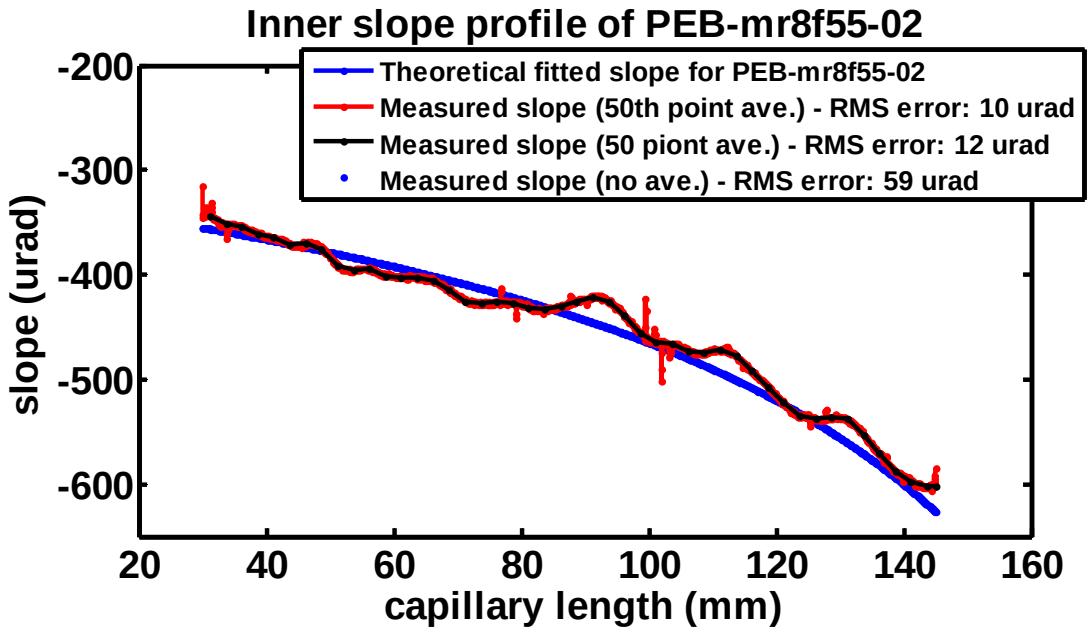

Figure 3.2 The inner slope measurement derived of the profile measurement of capillary PEB-mr8f55-02 in Figure 3.1. The graph shows the slope of the fitted ellipse and the slope of the measured ellipse. This graph shows the short wavelength errors, with a wavelength of ~20 mm as the oscillations in the slope.

The other two categories of errors from the ideal shape are roughness and nano-roughness. A glass surface is naturally very smooth, which translates it to glass having a low roughness. The roughness of glass is measured in height deviations over a surface area of a few square microns. The outer surface of our optics has a roughness of ~ 2-3 nm rms, measured on an optical profilometer. This is not the best roughness that can be achieved on a surface, but it is still very good. It is one of the good reasons to use glass as an x-ray optical surface. The nano-roughness of glass is also known to be

very good, which is the rms height deviations in nanometers over a surface area of a few square nanometers. We have not formally measured the nano-roughness.

What effects do the profile errors have on the single-bounce monocapillary's performance? Figure 3.3 shows a calculation of the effects of slope error on the gain and the spot size for a 4 mrad, 30 mm focal length capillary on four different beam lines. In Figure 3.3, a source-limited optical configuration is represented by an unchanging gain or spot size; i.e. a horizontal line. If the optic is limiting the gain or

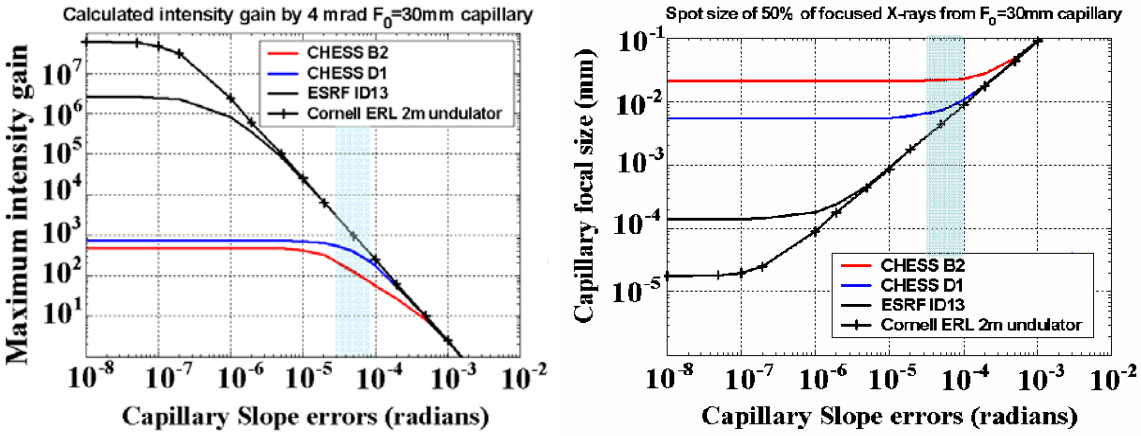

Figure 3.3 These two graphs show the effects of single-bounce monocapillary slope errors on the gain (right) and the spot size (left) in various beam lines. The vertical bar in blue presents slope error quality for single-bounce monocapillaries. Figure taken from reference [58].

spot size, the resulting shape is a sloped line. Again, our present slope errors for single-bounce monocapillaries are about 50 to 120 μrad, which is highlighted in pale blue in Figure 3.3. This shows that presently the optics have a slope error that closely matches the source limitations for both B2 and D1 at CHESS. We are able to acquire beam sizes from about 10 to 20 μm at D1, which is very close to what we expect to get. For the European Synchrotron Radiation Facility (ESRF) ID13 beam line, and ERL beam line, we are far from source limitations. In order to be limited by the source for these beam lines, the slope errors in the single-bounce monocapillaries would need to be improved

by another 2 or 3 orders of magnitude. These small errors in shape sum up the largest limiting feature real single-bounce monocapillaries have. Any improvement in the slope errors can vastly improve the gain and shrink the spot size, when the capillary slope errors are smaller than the angular divergence from the source.

3.2 The Tools for Design of Single-Bounce Monocapillaries

There are a number of methods and tools used to both design and model single-bounce monocapillaries for applications. There are a few shorthand ways to estimate the spot size and gain. However, the most useful tool for designing and modeling the single-bounce monocapillaries is to use Rong Huang's capillary design program, which is available on the internet at the CHESS website[11]. This program is able to estimate the effects of slope errors, and to calculate both the spot size and gain for most sources. Sections 3.3 and 3.4 will show how to apply the shorthand tools and the capillary design program for two very common situations; using single-bounce monocapillaries without upstream focusing optics and with upstream focusing optics. Ray tracing methods are also available to model optics, but are not as easy to use as the capillary design program for single-bounce monocapillaries.

3.2.1 Shorthand Design Tools

The shorthand design tools quickly estimate spot size, gain, and flux, which are quantities that are often wanted when using optics. The simplest way to estimate the spot size 's_i' is using equation 3-1 below (same as equation 2-2).

[11] The website address for the monocapillary design program is at: http://glasscalc.chess.cornell.edu/ImageProf.html.

$$M = \frac{i}{o} = \frac{s_i}{s_o} \tag{3-2}$$

The image distance 'i' is the designed focal spot on the optic, the object distance 'o' is the distance the source is away from the object and the source size 's_o' is the largest size of the source at that location. In most cases, the source size and source-to-optic distance is something that is tabulated for a particular beam line. Using equation 3-2 is adequate for many circumstances, but it can be wrong for sources that are either very large, or for object distances that are rather short, because single-bounce monocapillary optics have a limited field of view (section 3.4.2).

Equation 3-3 can be used to estimate the gain, which compares the cross-sectional area of the capillary with the size of the focal spot. It is good in most circumstances, but can be off for some extreme configurations:

$$G_{\max} \approx \frac{1}{2} \frac{ID_b^{\,2} - ID_t^{\,2}}{s_i^{\,2}} \tag{3-3}$$

Where 'G_{max}' is the maximum gain, 'ID_b' is the capillary's inner diameter at the base, 'ID_t' is the capillary's inner diameter at the tip, and 's_i' is the focal spot size (Figure 3.4). In comparing the capillary's cross sectional area to the spot size area, where does the one half come from in equation 3-3? At first glance you would expect to have a one and not a one half. First, this is how the gain calculated above typically compares to the real gain. The much more rigorous treatment of the problem done in the capillary design program is also close to the measured gain. The gain constant is one in the limit of the capillary having a length 'L_c' which is really short compared to the focal length 'F' (see Figure 3.4). The longer the capillary is, the lower this constant gets. When

you have a capillary length about twice the focal length of the capillary, the gain is multiplied by a factor of one half [12]. If the capillary length is about 10 times the focal length, the gain is multiplied by a factor of about one tenth, etc.

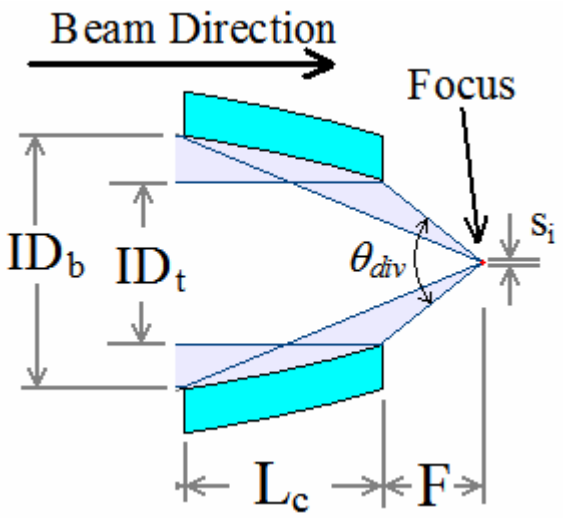

Figure 3.4 A cut-away schematic of a single-bounce monocapillary with the critical dimensions labeled.

Another useful quantity to know is the flux and flux density, which is often measured in photons per second and photons per second per area respectively. The total flux that an optic is focusing is:

$$Flux \propto ID_b^2 - ID_t^2 \tag{3-4}$$

This expression is not very useful by itself, but is quite useful if you want to compare the total flux that two optics can achieve. Sometimes when comparing optics, it is easy to think that the optic with the highest gain is the optic with the highest flux as well.

[12] Almost all of our presently used monocapillaries have this length ratio.

This is not always the case. When comparing optics with ratios of the value above, keep in mind that it only holds if the intensity from the x-ray source is almost completely uniform over the entire inner base diameter of the optic. For many beam lines at CHESS, having a uniform intensity is not always the case, especially if the inner base diameter is about one millimeter, or larger.

3.2.2 Program Designing Tools

The most effective tool we presently have is Rong Huang's capillary design program to both design and simulate single-bounce monocapillary optics. References [41,58] give all the equations used to design this program[13]. This program allows a calculation of the optic's elliptical profile, the expected spot size, the beam profile, and the gain. Rong Huang's capillary design program is in good agreement with what is measured on an x-ray beam line.

For this design program, there are three sets of input: source, capillary optic, and output settings. All input lengths are in units of millimeters and all input angles are in units of mrad. The source inputs are the source's vertical size, horizontal size, and the source's distance from the optic. Most of the capillary optic's inputs are labeled in Figure 3.4. They are the capillary's output divergence 'θ_{div}', with typical values ranging from 2 to 10 mrad, the focal length 'F', ranging from 20 to 150 mm, the optic's length 'L_c', ranging from 40 to 200 mm, and the expected slope error of the optic, ranging from 0.050 to 0.150 mrad for real capillaries. The output scale settings are simply there to match the program parameters to the calculated spot size. The calculated area is the

[13] The website address for the monocapillary design program is at: http://glasscalc.chess.cornell.edu/ImageProf.html.

radius of the area used in the calculation; it should be larger than the calculated spot size by ~2 to 5 times. The number of data points is how many elements this radius is broken into; 200 is a good value. There is an option to select whether or not to include a pinhole-measured spot size. This will give the measured spot size, convoluted with the pinhole. This feature is quite nice when comparing the predicted beam profiles to real pinhole scans, because it gives a profile of what the expected measurement will look like.

Once the inputs have been entered, there are two options for outputs: the capillary inner diameter (ID) profile and the image profile. The capillary ID profile gives the ellipsoidal shape that matches the input parameters. This graph shows if the shape is reasonable to fabricate, by knowing the values of the base and tip inner diameter; 'ID_b' and 'ID_t' shown in Figure 3.4. The image profile gives the distribution of the gain, as a function of position at the focus. This graph gives both the maximum gain 'G_{max}' and the spot size, defined as the FWHM of the peak. From this gain calculation, the flux can be estimated:

$$Flux \propto 2\pi\Delta r \sum_{r=0}^{\infty} rG(r) \tag{3-5}$$

Where 'r' is the radius of the gain curve, '$G(r)$' is the gain at position 'r', and 'Δr' is the step size used in the gain calculation. In order to estimate the flux from the gain curve, you are effectively doing a two dimensional integration of the gain curve. This expression is not very useful by itself, much like equation (3-4), but is useful if you want to compare the total flux that two different optics can achieve. Equation (3-4) and equation (3-5) are close to equivalent when comparing the flux of different capillary optic designs.

Using this program there are a wide array of optical configurations that can be explored, but there are limitations in the program. The program neglects diffraction effects. The source is assumed to be a Gaussian, and not a slit source. The program needs a small source size. It assumes a Gaussian slope error profile on the inner capillary surface. The elliptical shape has to have a major axis 'a' for the capillary to be much larger than the minor axis 'b', i.e. '$a>>b$'. The source-to-optic length has to be much larger than the length of the capillary, i.e. '$L>>L_c$'. This limit has been the most severe limit that the capillary design program has, because it is unable to accurately model close x-ray sources, such as a microfocus x-ray tube. The program starts to break down for sources that are closer than ~100 cm to the optic. Even with that limitation, the capillary design program has been a very good design program, helping to design all the capillaries fabricated for a number of years.

Other methods exist, such as ray tracing programs, for simulating and designing optics. The ray tracing programs can more closely model the effects of slope errors on the capillary surface, non-Gaussian sources, and beam profiles not in the focal plane. Section 6.4.3 gives an example of a ray tracing method used to model the slope errors of the capillary. A disadvantage of the ray tracing methods is they are much harder to set up, requiring much more input, such as a real profile shape. Comparing ray tracing methods to the capillary design program, the capillary program's greatest strength is its simplicity of use and fast calculation speed while still being accurate in modeling the single-bounce monocapillary optics.

There are a few basic strategies for creating good optical designs. When designing an optic, the length of the optic should be about twice the focal length [58]. This has

proven to be a good designing practice for balancing the gain and spot size. Adding length to the optic does increase the gain, but it does so in increasingly smaller and smaller amounts for longer optics. Also, the longer the optic, the more spread out the focus becomes; the intensity outside the FWHM region of the spot greatly increases with an increase in the optic's length [58]. Making the optic's length twice as long as the focal length is a good compromise between maximizing the gain, and keeping most of the x-ray intensity in the focus.

Another strategy is knowing what input variables to control. The divergence on the sample, the focal length, and the optical length are all variables that are controllable in the capillary design. When specifying these inputs, make note that they are very close to the actual fabricated capillary. The slope error however, is a variable that we have very limited control over. Often when designing an optic, we will fabricate a number of optics with that particular design. The optics we use are the straightest and have the smallest slope error. We do not have a very tight control over what the slope error will be, so it is a good idea to error on the side of a larger slope error when designing an optic.

3.3 Monocapillaries without Upstream Focusing Optics

I will now show the tools in the previous section in action, in designing a monocapillary optic for D-line, which does not have any upstream x-ray focusing optics. An example of a project that uses D-line and single-bounce monocapillary optics is confocal XRF (sections 9.4). For confocal XRF, a small spot size and a large flux is wanted. The experiment needs to excite the tin K_α line at 25 keV, with a K edge at 29 keV, therefore

the optic will have to function at 29 keV. For this example, we want an optic which has a 10 μm spot size, with the most x-ray flux possible.

Now that we have formulated what we want, we can use Huang's capillary program to explore designs that maximize the flux, and keep the spot at 10 μm on D-line. For D-line, there are multilayer optics, which select the energy of the beam. Because these optics do not focus the beam, the source parameters at D-line are the source size of the bending magnet, 1.5(H)x1.2(V) mm^2. The optic will be placed 13.3 m from that source in the D1 hutch. Now all the source parameters have been set. Source sizes are often a problem, because we do not know a source size as accurately as we would like for monocapillary optic spot size predictions. For example, D-line also has a tabulated source size of 2.0(H)x0.8(V) [58]. Different literature sources often have different tabulated values for the same source, positions of beam line components, etc., on the same beam line. We often use a best guess since synchrotron source sizes are hard to measure. It is always a source of frustration when trying to model optics.

We now have the three monocapillary parameters to model: the divergence, the slope error, and the focal length. In order to maximize the flux, the divergence will need to be as large as possible. By increasing the divergence we have both a higher flux and a larger gain (Figure 3.5). The optic will have a high limit of 4.5 mrad in divergence, since the optic will need to function at 29 keV (section 2.2). In order to maximize the flux, the optic must go right to the limit of a 4.5 mrad divergence. The FWHM of the spot size remains unchanged when changing the divergence, and when keeping the focal length and the slope errors constant.

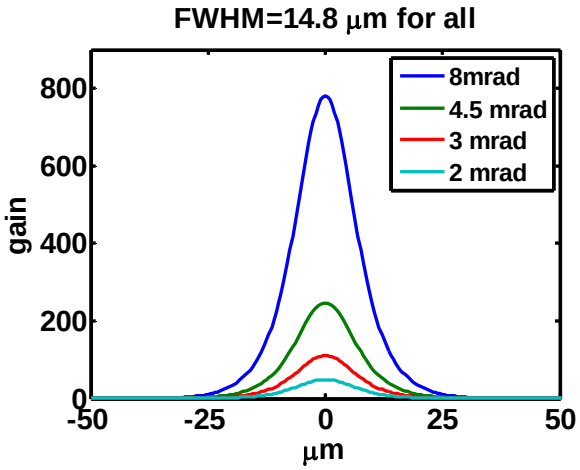

Figure 3.5 This graph shows how changing the designed divergence of a monocapillary on D-line affects the calculated gain and the spot size. The spot size is 14.8 μm for all the different divergences. A larger divergence gives a larger gain and a larger flux. The 8mrad, 4.5 mrad, and 3 mrad capillaries have a flux 16x, 5x, and 2x times larger than the 2 mrad capillary, respectively. The optic design has a 50 mm focal length, 100 mm optic length, and a 0.100 mrad slope error.

In order to minimize the spot size, the slope errors must be as small as possible. By decreasing the slope errors, we have a larger gain and smaller spot size (Figure 3.6). The flux is constant; this is not easily seen in this graph, but can be worked out using equation (3-4) or (3-5). Slope error is a parameter that is not directly controlled, but it can be estimated as shown in the following example. Capillary PEB_mr8f55_02 (8 mrad divergence, 55 mm focus) produced a 13 μm spot size (measured with a 5 μm pinhole) at D-line (Table 4.1 and Figure 5.2). When I input all the source and optical parameters into the capillary design program, we estimate a 0.060 mrad slope error on PEB_mr8f55_02 to simulate the spot size measured with a 5 μm pinhole. I will simply guess a slope error for our design of 0.070 mrad, which is a little larger, but should be achievable. If we are lucky, the actual optic we make will have a slope error smaller than 0.070 mrad.

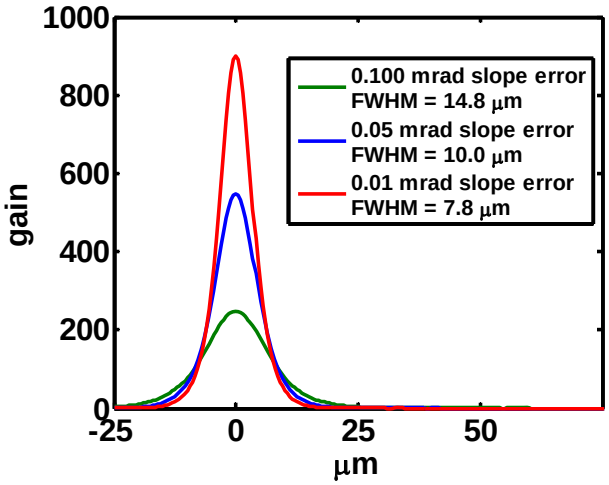

Figure 3.6 This graph shows how changing the slope error of the capillary on D-line affects the calculated gain and spot size. A larger slope error gives a smaller spot size and a higher gain. The total x-ray flux is constant over all three curves, since the optic's shape parameters do not change. The optic design has a 50 mm focal length, 100 mm optic length, and a 4.5 mrad divergence.

The last parameter that we can adjust is the focal length. By increasing the focal length, both the spot size and the flux increase. The gain remains constant (Figure 3.7). Here we are at odds with what we want. We want to maximize the flux, and have a small spot size. This is where the decisions about what is more important are made. Will a 17-18 μm beam spot from the 75 mm focal length optic be acceptable, if the flux is more important? The 75 mm focal length optic can have a flux ~14 times higher than the 20 mm focal length optic. The inner base diameter for the flux maximizing optic is 0.58 mm, so we should not be losing intensity because the optic's inner base diameter is not bigger then the x-ray beam at D1. If the spot size really has to be 10 μm, the calculation gives that the optic's focal length will have to be about 40 mm or less.

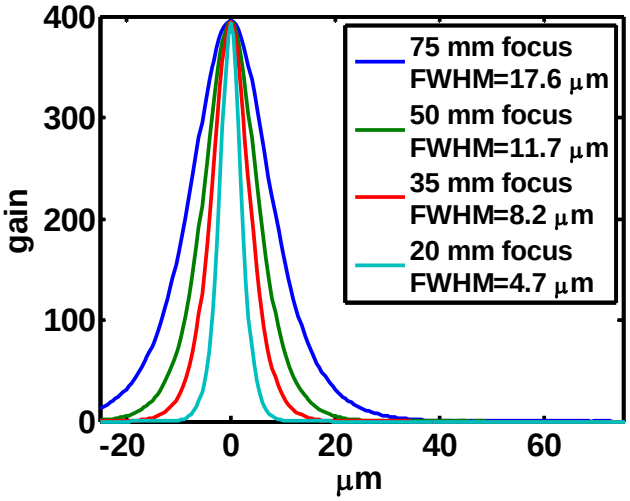

Figure 3.7 This graph shows how changing the focal length of the capillary on D-line affects the calculated gain and spot size. A larger focal length gives a larger spot size and a larger flux. The gain stays constant. The optic's length is twice the focal length. The 75 mm, 50 mm, and 35 mm focal length capillaries have a flux 14x, 6x, and 2x times larger than the 20 mm focal length capillary, respectively. The optic design has a 4.5 mrad divergence, and an assumed 0.070 mrad slope error.

This design example is good because it outlines some of the basic trends when designing an optic. If you increase the divergence, both the gain and flux go up, and the spot size is constant. If you decrease slope errors, the gain increases, the spot size decreases, and the flux is constant. If you increase the focal length, both the flux and the spot size increase, while the gain remains constant.

3.4 Monocapillaries with Upstream Focusing Optics

This next example is more complicated, because there are additional focusing optics in the beamline. This is a real example of a design; this particular design resulted in a series of capillaries, with one capillary named f1b_mr9f20_01 for use at F1 for protein

crystallography and Laue protein crystallography (sections 9.6 and 9.13). A capillary of this same design was sent to the Advanced Photon Source (APS) to test single-bounce monocapillary optics for use in both x-ray micro fluorescence and micro-XANES measurements on the 18ID beam line (section 9.9).

This single-bounce monocapillary optic was designed for F1; for doing protein crystallography. F1 runs at 13.5 keV, and the energy of the beam cannot be changed by more than a few hundred eV for that station. The desired spot size was five microns, with as much flux as possible. The minimum focal length of the optic was 20 mm, to fit a cryo-stream for the crystal samples and a small ion chamber. For many protein crystal samples, the divergence required must be 2 mrad or less, for other samples a larger divergence could be tolerated. We decided early on that in order to maximize the flux, the divergence of the optic would be as large as possible. This decision was made for two reasons, a 2mrad capillary, SF202, had already been made for F1 [64], and the divergence of a single-bounce monocapillary optic can be manipulated to a lower divergence with slits if needed (section 4.3.2).

3.4.1 The Source with Upstream Focusing

In order to design an optic with Huang's capillary program, we need the source size and distance to the optic. With upstream focusing, two basic situations arise. We can place the capillary optic in a location that is upstream from the upstream optic's focus, or downstream from the upstream optic's focus. If the optic is downstream from the focus, the focus is the new x-ray source, and the example of the source without upstream focusing in the previous section is adequate. If the capillary optic is placed on or before

the focus, then we must define an apparent source size at some relevant position upstream from the optic.

The beam line configuration for F1 is somewhat complicated (Figure 3.8). A good place to define the apparent source size is on the last optical element of the beam line, such as an upstream optic, or a slit. The apparent source size will be the x-z cross-sectional area of the x-ray beam on the upstream optic, or the size of the slit. This is the most direct way to define an apparent source size. Functionally, for a convergent beam, the apparent source size can be defined as the cross-sectional area of the beam at any convenient location along the beam path.

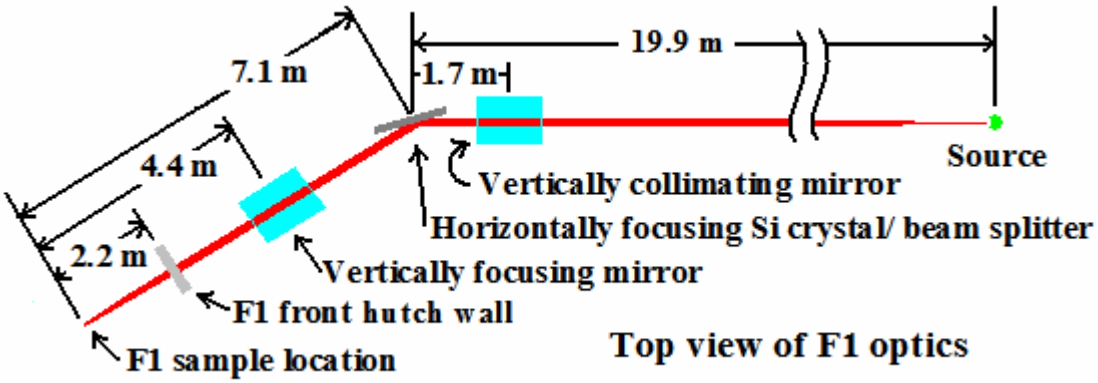

Figure 3.8 A schematic of the upstream optics, and their locations at F1. Different literature sources had different values for the placement of the beam line components; this diagram's values came from some of the CAD drawings of F-line, which I trusted. Other tabulated attributes of F1: Source size: 3.76(H) x 0.944(V) mm FWHM on a 24 pole, 1.2 T wiggler; F1 collects 1 mrad of the wigglers divergence; Flux (200mA)(p/s): 3.0×10^{11} thru a 300 µm collimator; Focus size at the sample position: 2.00(H)x 0.2(V) mm; Focused beam's divergence at the sample position 1.0(H)x0.4(V) mrad.

The easiest way to get an apparent source size is to know the focal spot size, location, and divergence produced with the upstream optics. Also, the apparent source size can be estimated by starting at the synchrotron source, and working through the effects of all the optics. To estimate an apparent source size in both the vertical and horizontal directions we can use:

$$s_e^2 \cong s_s^2 + \left(l_y \theta_d\right)^2 \tag{3-6}$$

Where 's_e' is the estimated beam size, 's_s' is the source or slit size, 'l_y' is the estimated beam size's distance from the source or slit, and 'θ_d' is the beam's divergence (same as equation 1-10). F1 has a focus size of 2.00(H) x 0.2(V) mm^2 and a beam divergence 1.0(H) x 0.4(V) mrad^2, at the sample position. Using equation 3-6, the estimated cross sectional beam is 4.8(H) x 1.8(V) mm^2, 4.4 m upstream of the focus, on the vertically focusing mirror. Now the source parameters are defined.

The optic will be limited to ~9 mrad in divergence, to function at 13.5 keV. The divergence will be set to 9 mrad to maximize the flux. The source is big and close, therefore this configuration is source-limited. Improvements in slope error do not have a dramatic effect on the spot size or gain (Figure 3.9). In order to minimize the spot size, the optic must go to the smallest focal length allowed, which is 20 mm. This results in an optic with a spot size of ~18-19 μm (Figure 3.9). The only option in getting the focal spot smaller for the source we have is to shrink the focal length. Since we cannot go shorter than 20 mm, the only option left is to change the source. A 20 mm focal length, 40 mm optic length, and a 9 mrad divergence was the final design for this single-bounce monocapillary optic.

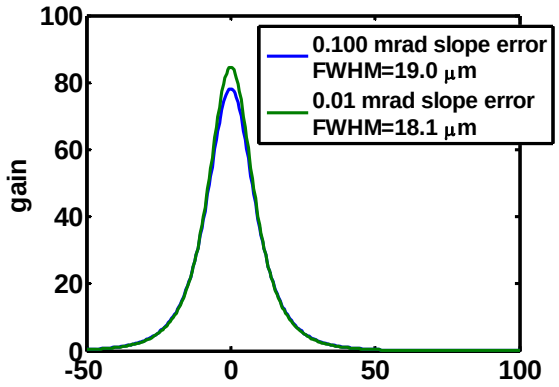

Figure 3.9 This graph shows the effect of changing the slope error of the capillary in the F1 hutch. Changing the slope error does not change the spot size or gain significantly. The optic design has a 20 mm focal length, 40 mm optic length, and a 9 mrad divergence. The source is 4.8(H) x 1.8(V) mm, 4.4 m away.

If the focal length could have been shorter, it would have made a smaller spot. If the focal length was 10 mm, the spot size goes to 11 μm and flux is cut in half, compared to the 20 mm focal length optic. If the focal length is 5 mm, the spot size goes to 6 μm and flux is quartered.

3.4.2 The Apparent Source Size

At this point the optic has been designed, but the spot size of 5 μm has not been achieved. In order to get a smaller spot, the only option left is to change the source size. The source can be made smaller with a set of slits. A slit can fit into the F1 hutch one meter back from the sample location. The estimated cross sectional area of the beam profile at the position of the slits is 2.2(H) x 0.45(V) mm^2, again using equation 3-6. This apparent source (the cross sectional area of the beam) is incorrect, it is not the apparent source size for the capillary optic.

The capillary optic is an aperture itself, thereby limiting what it can collect from the beam to 1.05(H) x 0.51(V) mm^2, one meter back from the optic. This is calculated by knowing the divergence of the beam, which is 1.0(H) x 0.4(V) $mrad^2$, and the inner base diameter of the capillary, which acts as an aperture of 0.31 mm. The area that the capillary optic can collect is calculated by inputting this information into equation 3-6. The apparent source at 1.0 meter away is 1.05(H) x 0.45(V) mm^2, because the capillary optic can only see 1.05 mm of the 2.2 mm beam profile in the horizontal direction.

The capillary design program does not correct for source sizes that are too large for an optic. For this example at F1, a good way to check is to compare the capillary optic's beam profile for the source on the upstream optic at 4.4 m with the apparent source size at 1 m (Figure 3.10). There should be no difference in the capillary optic's beam profile between the two; all that has changed is where the source has been defined. In Figure

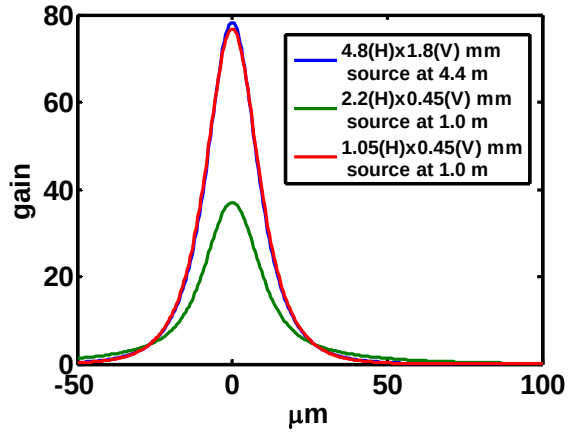

Figure 3.10 This graph shows the capillary optic beam profiles for the real F1 source of 4.8(H) x 1.8(V) mm at 4.4 m, the beam profile of 2.2(H) x 0.45(V) at 1.0 m, and the apparent source size for the capillary optic of 1.05(H) x 0.45(V) mm at 1.0 m. Because the real F1 source and the apparent source size give the same spot size, the apparent source size is correct; the beam profile at 1.0 m is not the correct source size to use. The optic design has a 20 mm focal length, 40 mm optic length, a 9 mrad divergence, and a 0.100 mrad slope error. The spot size is 18 to 19 µm for each curve.

3.10, the capillary optic beam profile for both the real and apparent source size are the same; the apparent source size is the correct apparent source size. The beam profile is not the correct apparent source at one meter, because it does not match the real profile.

The optic's spot size is still ~18-19 μm with the apparent source size of 1.05(H) x 0.51(V) mm^2, one meter back from the optic. With slits at this position, we can now make a smaller source to achieve the smaller spot size. This comes at a cost of flux; when the beam is slit down, the gain the optic produces may increase, but the flux will always go down. Additionally, in the capillary design program, flux comparisons can only be made when changing the optic's parameters. If source parameters are changed, flux comparisons cannot be made using equation 3-5. Since we are closing down slits to make a smaller source, a rough comparison of the flux can be made by taking the ratio of the different slit areas. Figure 3.11 shows the effect different slit settings have

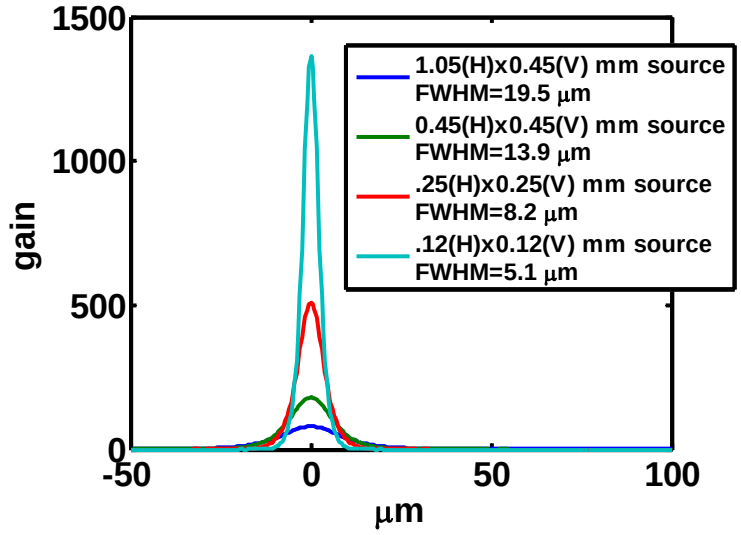

Figure 3.11 This graph shows the effects on the monocapillary optic's spot size and gain when slitting down to a smaller source size one meter from the optic. The optic design has a 20 mm focal length, 40 mm optic length, a 9 mrad divergence, and an assumed 0.070 mrad slope error. The 0.45 mm, 0.25 mm, and 0.12 mm slit settings have a flux of 42%, 13%, and 3%, compared to the flux of the full 1.05x0.45 mm apparent source size.

one meter back; as the slits get smaller, the gain is increased and the spot size decreases. The flux drastically decreases as the slits get smaller. The 0.45 mm, 0.25 mm, and 0.12 mm slit settings have a flux of 42%, 13%, and 3%, compared to the flux of the full 1.05x0.45 mm apparent source size.

3.4.3 Comparisons between the Design and Real Optics

How did this design work out at F1 after the capillary was fabricated? The optics worked out very well! Five optics were pulled, and two of five proved to be very good in their initial evaluations at the G1 hutch. Capillary f1b_mr9f20_01 was the first capillary to produce a 5 μm spot FWHM (gain ~90) in the G1 hutch at CHESS. Only a quarter of the inner surface area was exposed to get the 5 μm spot size. This was the first time CHESS produced a capillary capable of making a 5 μm spot size, and giving the optic the nickname of "the 5 μm capillary". Using the entire inner surface of the glass gave a larger focal spot size of 9 um FWHM (gain ~250) at G1. Figure 4.1 in the next chapter shows the pinhole scan, and a far-field image of this optic measured at G-line.

Capillary f1b_mr9f20_01 was later tested at F1 in April of 2006. The measured spot size was 12 to 14 μm for a slit setting of 0.5(H)x0.5(V) mm^2, and 9 to 12 μm for a slit setting of 0.3(H)x0.23(V) mm^2 (not quite on 0.25(H)x0.25(V) mm^2). This is close to what the predicted values were in Figure 3.11.

We were not able to get a 5 μm spot at F1, mostly because of the source limitations, and not the limitations of the monocapillary optic. Capillary f1b_mr9f20_01, along with the

capillary SF202 (2 mrad, 22 mm focal length), have been put to good use at F1, in many micro-protein crystallography experiments (sections 9.6 and 9.13).

Chapter 4 Evaluation and Performance of Monocapillaries

This chapter finally gets to how single-bounce monocapillaries really behave in the synchrotron x-ray beam. The spot size, gain, flux and the far-field pattern are the major measurements made to evaluate single-bounce monocapillary optics. The spot size and gain are measured by scanning a pinhole across the focus and measuring the intensity of the x-ray beam through the pinhole with an ion chamber. From the spot size, the slope error can be estimated. The total flux through the optic is simply measured with an ion chamber downstream from the optic. The far-field image is viewed on a high quality x-ray fluorescent screen about 25 to 100 cm down stream from the focus. This image contains information regarding the straightness and the slope errors of the optic. Figure 4.1 shows both a pinhole scan and a far-field image from a single-bounce monocapillary optic. Section 4.1 covers the measurement of the spot size, gain, and flux. Section 4.2 will cover the far-field pattern, and how features in the far-field pattern give clues to the quality and slope error of an optic. Section 4.3 will cover how the optics perform on different beam lines, and how slits paired with the optics can modify the divergence from the optic to match the needs of an x-ray experiment.

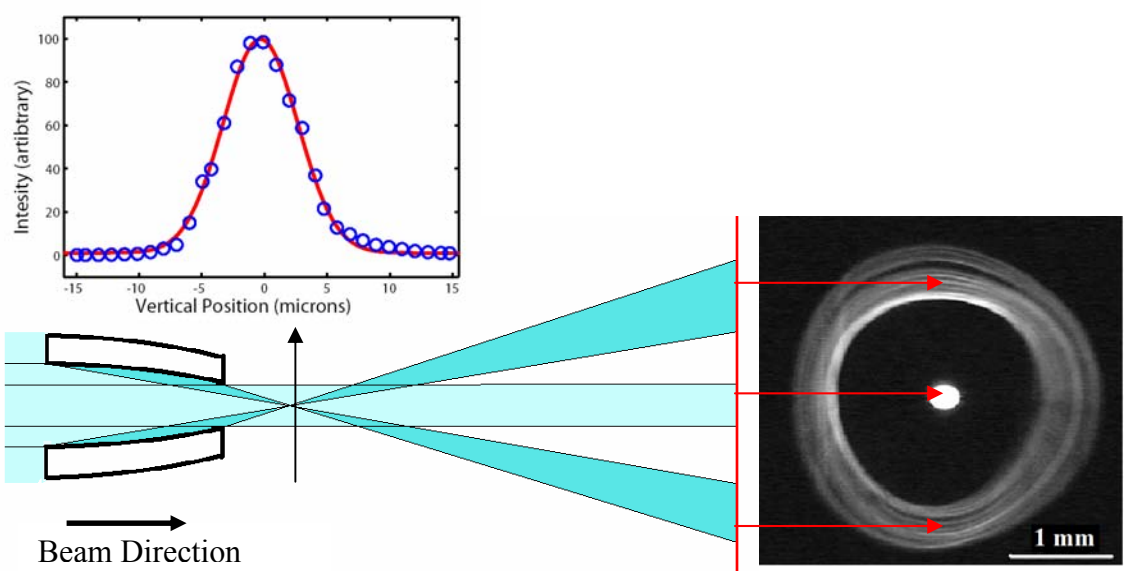

Figure 4.1 A schematic cut away of a single-bounce monocapillary is in the lower left corner. The positions of the reflected rays are in dark blue and positions of the non-reflected rays are in light blue. In the upper left corner shows a pinhole scan across the focus of an optic, with a spot size of 5 µm FWHM. A far-field image is on the right side, in the schematic, the far-field screen is represented by the red line, which is normal to the x-ray beam. Both the scan and the far-field image are from capillary f1b_mr9f20_01.

4.1 Spot Size, Gain and Flux Evaluation

I will first discuss measuring the spot size, and later I will discuss the gain, and flux measurements. At the end of this section, I will compare the measured and predicted spot sizes, gains, and slope errors on some of the good monocapillary optics.

4.1.1 Spot Size and Depth of Field

The spot size is measured with an ion chamber and a small 5 to 10 µm pinhole. The spot size is measured by scanning a pinhole across the focus in both the vertical and horizontal directions perpendicular to the beam at the capillary optic's focal length. An

ion chamber records the intensity of the x-ray beam that goes through the pinhole. The FWHM of this peak defines the measured spot size. The actual spot size is the de-convolution of the measured spot size with the pinhole's size:

$$s_r = \sqrt{s_m^2 - s_{ph}^2} \tag{1-1}$$

Where 's_r' is the de-convoluted or real spot size, 's_m' is the measured spot size, and 's_{ph}' is the pinhole size. De-convoluting the measured spot size to obtain the real spot size becomes more important the closer the real spot size is to the pinhole's size. The measured beam profiles are shaped like the predicted profile curves in the capillary design program (Figure 4.2, in the next section). Again, the capillary design program predicts both the real spot size and the measured spot size.

Positioning of the pinhole needs to have sub-micron resolution in the two directions perpendicular to the beam. Positioning of the pinhole parallel to the beam, along the focal length, is much less critical. When moving away from the focus along the beam path, the focal spot gets larger. When the focal spot grows by √2, this defines the depth of field for the optic. By applying this to the beam profile in equation 1-10, the resulting depth of field the optics is:

$$s_e^2 = \left(\sqrt{2}s_i\right)^2 \cong s_i^2 + \left(l_y\theta_d\right)^2 \tag{4-1}$$

Which is easily reduced to:

$$l_y \cong \pm\frac{s_i}{\theta_d} \tag{4-2}$$

With 'l_y' being the depth of field, 's_i' being the spot size of the optic, 'θ_d' being the divergence of the optic, and 's_e' being the estimated beam profile size away from the focus. Most optics at CHESS have a depth of field ranging from ±1.0 to ±4.0 mm. This means in most cases, the position of the pinhole will be in the focus within 1 mm. Optics with smaller spot sizes or larger divergences have a smaller depth of field. In practice, the actual focal length should be close to the designed focal length, within ± 2 mm, for a good optic. In most instances, the designed and measured focal lengths are right on.

A second method used to measure a focusing optic's spot size is by doing a knife-edge scan across the focal spot. The derivative of the knife-edge scan is the measured spot size. In our experience in measuring spot sizes at CHESS, both work equally as well for measuring the spot size. At CHESS we have preferred using the pinhole scans because it is helpful in both gain and flux measurements.

4.1.2 Gain, Flux, and Flux Density

The gain measurement can be done two different ways. The quickest way to get a value for the gain is to take an ion chamber counts reading while the capillary optic's focus is aligned with a small pinhole. Take the reading again with the optic removed and the pinhole left in place. Subtract the base counts from the ion chamber (counts without an X-ray beam on) from both numbers, and divide the intensity of the optic in the beam by the optic out of the beam (equation 2-5). This is always imprecise, because x-rays going through the pinhole's metal foil contribute to the background count, but it is usually close enough for a quick check.

The gain curve can also be calculated directly from some beam profile scans. In order to calculate the gain from the beam profile scan, the scan has to include a shelf of intensity caused by the direct beam going through the capillary optic. Figure 4.2 shows this shelf of intensity in the both plots. The background, at the edges of the plot, is the x-ray intensity going through the pinhole's metal foil. Next, there is a small jump in the intensity as the pinhole and the direct beam through the monocapillary optic align. The height of the jump corresponds to the intensity of the direct beam. The width of the intensity jump is the same as the tip inner diameter of the capillary optic. The large peak in the center is the intensity from the focused beam. The gain is the ratio between the small jump in intensity and the focused beam. The right plot in Figure 4.2 is the background-corrected gain profile of the same scan, showing that the max gain of the f1b_mr9f20_01 is about 300. The shelf in this plot has a gain of one because it is the intensity from the direct beam.

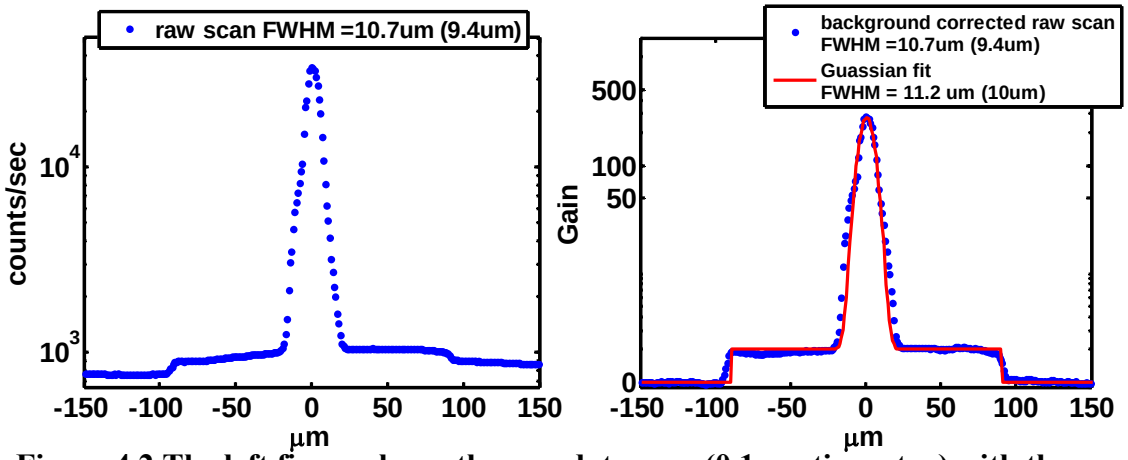

Figure 4.2 The left figure shows the raw data scan (0.1 sec time-step) with the ion chamber (gain 10^8) for capillary f1b_mr9f20_01*. This graph gives the counts as a function of the 5 µm pinhole's position. The right figure shows the same scan, background-corrected and normalized to the direct beam intensity. Intensity is plotted on the log scale to emphasize the pedestal base. The de-convoluted spot sizes are in parentheses in the plot's legends.
***G1's intensity was oscillating with time this particular run. This can be seen in the left plot as the non-flatness in the background. This oscillation was corrected for in the right plot.**

I will now discuss flux measurements. There are two useful flux values; they are the total flux through the optic and flux density at the focus. It is best to make the total flux measurement at the end of a complete capillary lineup, when the slits and capillary beam-stop are in place. The total flux is easily measured with an ion chamber downstream from the optic, without anything else in the beam path between the ion chamber and the optic. The counts per time on the ion chamber can be converted to photons per second if the intensity is measured with one of CHESS's standard short ion chambers. Figure 4.3 gives the conversation between counts/second into

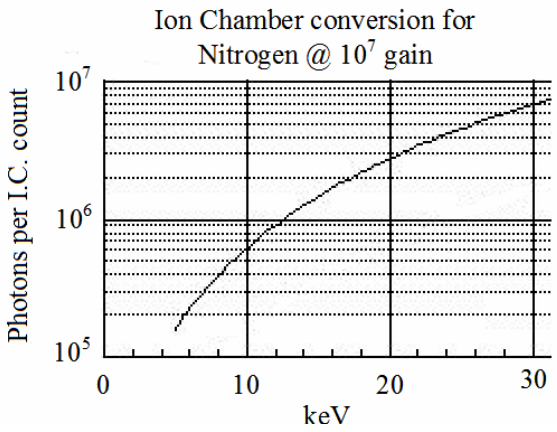

Figure 4.3 The conversion of counts on a CHESS short ion chamber to photons in the X-ray beam at a preamplifier gain of 10^7.

photons/second. If the spot size on the capillary is known, the flux density in the spot can be estimated with:

$$Flux_D \approx \frac{4 \cdot Flux_T}{\pi \cdot s_i^2} \tag{4-3}$$

Where '$Flux_D$' is the flux density, '$Flux_T$' is the total flux through the capillary optic, and 's_i' is the spot size of the capillary optic. The flux density can be also calculated

from beam profile scans as well, if the intensity is measured with one of CHESS's standard short ion chambers:

$$Flux_{D\max} \cong \frac{4 \cdot Flux_{ph}}{\pi \cdot s_{ph}^2} \tag{4-4}$$

Where '$Flux_{Dmax}$' is the maximum flux density, '$Flux_{ph}$' is the flux through the pinhole at the peak of the beam profile scan, and 's_{ph}' is the pinhole size used in the scan. The beam profile scan in Figure 4.2 can be used as an example of the maximum flux density calculation. This scan was taken at G1 with an X-ray beam energy of 10 keV. This makes the flux, in photons per second through the five-micron pinhole:

$$\begin{aligned} Flux_{ph} \cong\ & 3.3\times10^{4}\left[\frac{counts@10^{8}\,gain}{0.1\sec}\right]\cdot 10\left[\frac{0.1\sec}{1\sec}\right]\cdot \\ & 5.5\times10^{5}\left[\frac{photons}{counts@10^{7}\,gain}\right]\cdot\frac{1}{10}\left[\frac{counts@10^{7}\,gain}{counts@10^{8}\,gain}\right] \\ \cong\ & 1.8\times10^{10}\left[\frac{photons}{\sec}\right] \end{aligned} \tag{4-5}$$

Inputting this value into equation 4-4, we get a flux density of 9.2×10^{8} photons/sec/μm^2.

Equation (4-3) and (4-4) are very similar, but in practice they are not quite the same. Equation (4-4) gives the maximum flux density, right at the peak of intensity, and equation (4-3) gives an average flux density over the entire spot size. One word of caution; it is tempting to estimate the total flux from the flux measured through the small pinhole, but this will almost always be off the real value for the total flux. It is always a better idea to measure the total flux, since it is so easy to measure anyway.

4.1.3 Comparison with Predictions and Slope Error Evaluation

With the spot size, gain, and flux measured, we can now go back and see how close the measured values are to the predicted values in the capillary design program. This exercise is valuable for verifying the source parameters and for estimating the slope errors on the optics.

The hardest part for predicting the performance of an optic is getting the source parameters correct. In most cases, the measured spot size is within two or three microns of the predicted spot size. This small difference is not a large problem for the predicted spot size, but it is a problem for estimating the slope error of an optic. Both the source size and slope error parameters can be changed just a small amount to get a measured spot size to match a predicted spot size in the capillary design program. Without knowing the source size exactly, it is hard to know if the slightly larger spot size comes from a slightly larger source size or a slightly larger slope error.

Most of the optics tested in the last three years have been tested at G1, which is a very good example of both what is good and bad in knowing the source parameters. G-line has upstream focusing optics, and it has the advantage of having horizontal cave slits 5.2 meters from the position the capillary is placed in the G1 hutch. This makes it very convenient to set the apparent horizontal size of the beam to a desired size; in testing capillary optics I have always set the horizontal cave slits to a one millimeter opening. The disadvantage is that there are no vertical slits at the same location; the vertical size of the x-ray beam is about one millimeter at this location. The source parameters are almost nailed down, with only the vertical source size not being known exactly. It would be nice to be able to measure the beam's size at this location, but the beam is in a

vacuum chamber at this location, and is therefore inaccessible to measure. Almost all CHESS sources have the same problem, the source size is known, but it is not known to the accuracy I would like. The source sizes at different beam-lines a change a little bit in-between x-ray runs, and in the case of beam-lines with upstream focusing optics, the focusing can be changed. Source sizes in most cases cannot be measured easily to verify its size.

At G1, I have determined that the correct vertical size of the beam 5.2 meters back is about 0.8 mm. This value comes from measuring the spot size for the same optic on different beam lines, and getting the slope errors and source sizes to be self-consistent between the two beam-lines. For example, capillary PEB_mr8f55_02 has been tested at both G1 and D1. For consistency between D1 and G1, the vertical size at G1 has to be 0.8 mm (Table 4.1).

Fortunately, the source sizes do not change much, and the spot size, gain, and flux measurements stay close to predictions. These quantities are much more important for experimental work and are fortunately directly measurable. Even with errors in the source size, the predicted slope errors are still scaleable; an optic with a better slope error will have a smaller spot size in a measurable way. This can be seen in Table 4.1 in comparing capillary PEB605 to PEB_mr8f55_02. Both optics have the same design, and from comparing their performance directly, capillary PEB_mr8f55_02 has a slope error that is ~40 μrad smaller than PEB605. Table 4.1 gives the measured spot sizes, gains, and flux density of optics tested at G1 over the past few years. The table also gives the gain and slope error for the optics, predicted with the capillary design program.

Table 4.1 A table of single bounce monocapillary optics giving the measured gain, counts on a ion chamber through a 5 µm pinhole at G1, and the FWHM spot size in both the vertical and horizontal directions. The de-convoluted spot sizes are in parentheses. From these measurements, other values are predicted, such as the gain, flux density, and estimated slope errors. The name of the optic gives its design; 'mr4f50' is an optic with a 4 mrad divergence and a 50 mm focal length. The measured values for the divergence and focal length are given in parentheses, if different from the designed values. Most predictions use the G1 source parameters of a 1.0(H)x0.8(V) source at 5.2 m.
***D1 source parameters 1.5(H)x1.2(V) at 13.3 m**
**** only a ~1/4 or less of the full optic was used, predicted gain was for the full optic.**
***** did not use a CHESS ion chamber**

	V spot size µm	H spot size µm	max IC cts./0.1s 10^8 gain	Max gain predicted/ measured	flux density at G1 phs/s/µm^2	estimated slope error µrad
PEB605 (mr8f55)	20.3 (19.7)	20.5 (19.9)	3.2×10^4	500/400	9.0×10^8	100
PEB-mr8f55 -02	16.1 (15.3)	16.8 (16.0)	6.5×10^4	800/700	1.8×10^9	60
PEB-mr8f55 -02 at D-line*,**	13.0 (12.0)	14.3 (13.4)	***	1200/~700 **	***	60
f1b-mr9f20-01 (mr7.5f22)	10.7 (9.5)	8.6 (7.0)	3.5×10^4	350/300	9.8×10^8	90-120
f1b-mr9f20-01 quartered**	7.4 (5.5)	7.5 (5.6)	1.4×10^4	350/90**	3.9×10^8	50
f1-mr9f20-02 (mr8f24)	11.9 (10.8)	10.5 (9.2)	3.1×10^4	350/250	8.7×10^8	120
f1-mr9f20-02 quartered**	5.0 (<5)	10.5 (9.2)	0.9×10^4	350/80**	2.5×10^8	50-120
G1c-mr4f50 -09	14.9 (14.0)	18.2 (17.5)	2.3×10^4	180/120	6.4×10^8	60

4.2 Far-Field Patterns

The far-field patterns created by single-bounce monocapillary optics are extremely useful to evaluate monocapillary optics. The primary use for the far-field pattern is to align the optic with the x-ray beam (section 5.5). These images can be used to estimate the optic's slope error deviations. A program has been made which simulates reflections off the inner surface of an optic to make the far-field pattern (section 6.4.3).

From the far-field images, it is immediately evident if the optic is good or bad. For a perfect optic, the aligned far-field pattern would have a central dot from the direct beam, and a uniform circle of intensity around this central beam. Any optic that has slope errors, or is not straight will deviate from this shape in its far-field pattern. In this ring of intensity, the inner part of the ring comes from the base of the optic and the outer part of the ring comes from the tip. Far-field images contain details that give information about straightness, uniformity, and slope errors of the optic. The closer the far-field pattern is to this ideal, the better the optic is. In Figure 4.4, it should be evident which of the optics are better from observing their far-field pattern. I will go through the images in Figure 4.4 and point out some of the details.

Every far-field image in Figure 4.4 has a direct beam spot. This spot is more or less the size of the capillary's tip inner diameter for a low divergence x-ray beam. All the other x rays are reflected from the surface. The optic is aligned when the reflected x rays are centered around the direct beam.

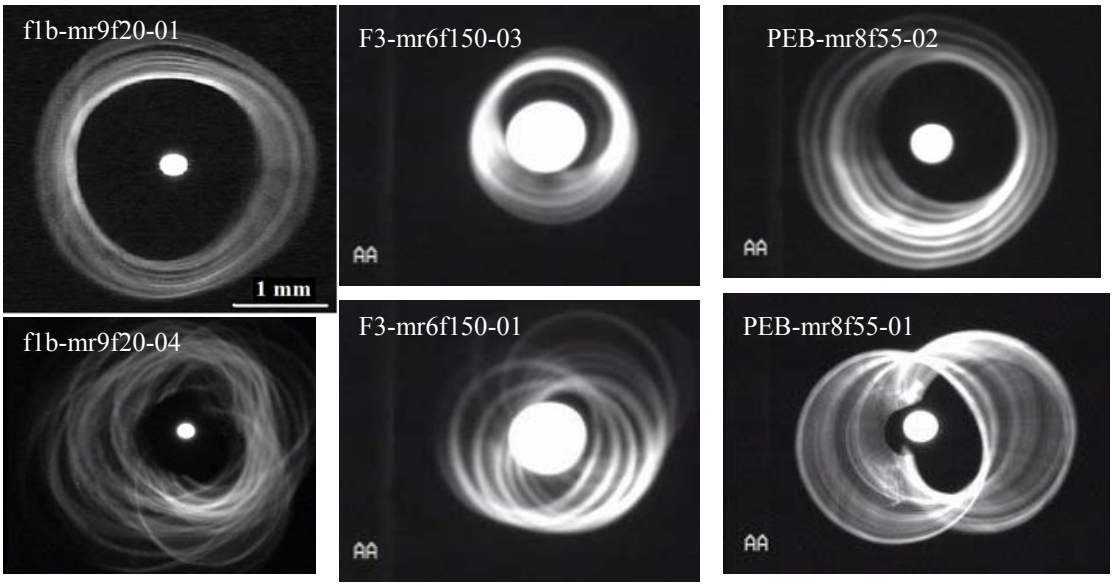

Figure 4.4 This figure shows far-field patterns of both good and bad capillary optics. The names of the optics, which created the far-field patterns, are labeled at the top of each image. The far-field patterns from good optics are on the top row. Below each good far-field image is a far-field image from a bad optic of the same design. The optic designs are 9 mrad, 20 mm focal length, 190 µm tip inner diameter on the left, a 6 mrad, 150 mm focal length, 900 µm tip inner diameter in the center, and a 8 mrad, 55 mm focal length, 470 µm tip inner diameter on the right.

The bottom rows of images come from optics that do not produce a small focal spot. The bottom left image, from capillary f1b-mr9f20-04, shows a far-field pattern with a somewhat random messy pattern. There are many uncorrelated ripples along the capillary's inner surface. This optic was twisted during the pulling process. The bottom center image, from capillary F3-mr6f150-01, has sharp circular rings of intensity, not centered on the direct beam. There are correlated ripples along the length of the inner surface of the optic, evident from the sharp circular rings. These circular rings are not centered on the direct beam, they are swirling around it; this is evidence that the optic is not straight. The bottom left image, from capillary PEB-mr8f55-01 has a diffuse ring of intensity, not centered on the direct beam. The diffuse ring shows that this optic has a smaller amplitude of ripples along the inner surface, but the optic is bent

severely enough that it will not make a focused spot. Each of these images gives clues to the problems each optic has, which prevent it from producing a focal spot.

The top row of far-field patterns come from optics that produce small focal spots. The reflected x rays in these images are closer to the ideal uniform ring that a perfect capillary would produce. These images contain small imperfections that give clues to the slope errors and straightness of the optic.

The top right far-field pattern, from capillary f1b_mr9f20_01, has faint circular rings of intensity within the entire ring of intensity, which arise from a correlated modulation of slope error along the length of the inner surface. The entire ring of reflected intensity is close to uniform in width. This means the optic is straight. Also, the ring of intensity in this image has a subtle triangular shape. The optic is not perfectly round on the inside. This same subtle triangular shape can be seen in the bad optic of the same design in the bottom left corner, suggesting the glass, which was used to make both of the optics, might have a slight triangular shape. The more likely cause is the glass was twisted during the draw; the glass rod this optic was made from twisted by ~90º while being drawn.

The top center far-field pattern, from capillary F3_mr6f150_03, has a slightly egg-shaped ring of intensity, which arises from a small bend along the length of the optic. It also has sharp circular rings of intensity, like the far-field pattern from the optic of the same design below it. This optic has the same correlated ripples along the length of the inner surface of the optic, but they are harder to see because they are all on top of each other, because the optic is straighter.

The top right far-field pattern, from capillary PEB_mr8f55_02, also has a slightly egg-shaped ring of intensity, which arises from a small bend along the length of the optic. It also has sharp circular rings of intensity. The optic also has correlated ripples along the length of the inner surface of the optic. In this far-field pattern, the rings are clear enough to count seven rings of intensity, meaning there are about seven slope error ripples along the length of the optic.

There are some general trends in all the optics above. Every optic, good or bad, has rings of intensity in their far-field patterns; every optic has a slope error modulation along the length of the optic. Additionally, the metrology used to evaluate the optics on the capillary puller consistently shows this same oscillation along the length of the optic (section 6.3.3). The straightness of the optics above is not a surprise. The straight optic is quite short, being only 40 mm long. The bent optics are much longer, 115 and 150 mm. Keeping the optic straight over longer and longer optical lengths becomes progressively harder. Far-field patterns give a quick qualitative look at the quality of the optic.

4.3 Monocapillary Optics on the X-ray Beam Lines

Single-bounce monocapillary optics' major advantage of being achromatic allows them to work well on synchrotron x-ray beam lines. This attribute allows a monocapillary to focus with the same focal length for just about any x-ray beam energy or bandwidth. Because they are achromatic, they are able to work in a beam that is convergent or divergent, discussed in the next section. Another advantage monocapillary optics have is that their divergence can be made smaller with upstream slits, discussed in section

4.3.2. Table 4.2 gives a list of optics available for beam lines, describing their size and functionality.

Table 4.2 A list of optics made at CHESS. The optics on the old puller were made between Oct. 1999 to Dec. 2003. The new puller has been making optics since Nov. 2005. All the new optics where tested at G1 with a 5 µm pinhole, and some of the older ones as well.
***These optics have been especially popular to use at CHESS.**

Capillary Name	Length in mm	Base/Tip IDs in µm	Focal L. in mm	Beam Size in µm	Max. Gain	Div. in mrad
Old capillary puller						
CH015 (multi-bounce, concentrating)	223	25/0.8	<0.1	0.8	100	5.8
BSG2,BSG3	300	400/130	30	18 (not G1)	125	<4
BSG7,BSG301	50	198/125	30	12 (not G1)	75	<4
CHIB714	130	997/558	61	25-29	200	9.5
*BSG644	110	400/226	52	18-22	50	4.3
BSG203,BSG204	40	322/191	21.5	-	-	8
A10,A11	105	211/123	55	14-18	70	2
*Peb605	115	827/469	55	17-23	550	8
*SF202	50	81/44	22	16-18 (F1)	11	2
New capillary puller						
*G1c-mr4f50-09,05,03	100	350/200	50	14-19	120	4
*f1-mr9f20-02	40	310/190	24	10-11	250	7.5
*f1b-mr9f20-01	40	310/195	22	7-10	300	7.5
f1b-mr9f20-06,07,08	40	310/195	23	10-11	250	8
*PEB-mr8f55-02	115	478/822	55	13-20	700	8
F3-mr6f150-03,04	150	1262/900	150	20-40	50	6
F3a-mr6f150-04	150	1260/900	150	25-50	50	6
D1a-mr4f30-01,02	60	195/125	35	8-10	140	4
A2-mr2f55-12,15	100	187/112	50	18-21	50	2
A2a-mr2f45-05	100	187/112	45	22-25	50	2

4.3.1 Effects of a Convergent and Divergent X-Ray Beam

The achromatic monocapillary can function with upstream focusing of the x-ray beam. Upstream optics allow an experiment to use a larger amount of the beam-line's x-ray flux. Monocapillary optics achieve a larger total x-ray flux by using upstream focusing optics to produce convergent beams. The inner base diameter of a capillary acts as an aperture; the larger the total flux density is at the inner base diameter, the larger the total flux is through the monocapillary. The disadvantage of a convergent beam for monocapillary optics is it produces larger spot sizes, and larger divergences.

An upper limit exists to the amount of convergence a capillary optic can accept. The limit of convergence a monocapillary optic can accept is:

$$\theta_{\text{lim}} \cong \frac{ID_b - ID_t}{L_c} \tag{4-6}$$

Where 'θ_{lim}' is the limit of convergence an optic can accept, 'ID_b' is the base inner diameter of the monocapillary, 'ID_t' is the tip inner diameter of the monocapillary, and 'L_c' is the length of the monocapillary. When the convergence of the beam equals the angle 'θ_{lim}', the beam goes through the optic. It cannot get to the inner surface of the optic, therefore it cannot be reflected and focused. Table 4.3 presents how a convergent beam on an optic increases the focal spot size. The table also presents how the optic's maximum divergence scales with the maximum convergence it accepts. The capillary design program estimates the spot sizes for an optic with a 50 mm focal length and a 100 mm optic length.

Table 4.3 The table on the left gives the beam convergence and the resulting calculated spot size. The table on the right gives the limit of beam convergence a capillary can accept, for a given capillary-designed divergence. For both tables the optic has a 50 mm focal length, and a 100 mm length. *source used in left table: (Horizontal divergence)*10 by (Vertical divergence)*10 mm; a source at a distance of 10 meters.

Horizontal divergence (mrad)	Vertical divergence (mrad)	Spot size (μm)
3	1	~120
2	1	~110
1	1	~80
0.5	0.5	~40
0.25	0.25	~20

θ_{div}	θ_{lim}
8 mrad	2.9 mrad
4 mrad	1.5 mrad
2 mrad	0.7 mrad

Convergent and divergent beams also affect the divergence of the single-bounce monocapillary optic. For both converging and divergent beams, the divergence of the optic is a little larger, and the amount of the divergence is increased and can be estimated from the far-field pattern (Figure 4.7 in the next section). If the monocapillary is after the upstream optic's focus, then the beam is diverging. The grazing incident angle of the monocapillary's inner tip surface is increased by:

$$\theta_g \approx \theta_{grazing} + \frac{\theta_T}{2} \tag{4-7}$$

Where 'θ_g' is the highest angle of grazing incidence, and '$\theta_{grazing}$' is the designed angle of grazing incidence (see equation 2-11). 'θ_T' is either the divergence of the synchrotron x-ray beam, if the optic is placed at the focus, or the angle the optic's tip makes with the source position '$\theta_T = ID_t / (L+L_c)$', if placed further downstream from the optic. This effect is mentioned because it can substantially lower the expected high-energy cutoff of the capillary, by increasing the grazing incidence angle.

The effect of convergent and divergent beams can be seen in far-field patterns. In practice, synchrotron x-ray beams have a larger divergence in the horizontal direction. Because of this, the capillary optics usually have a horizontal focal spot size that is slightly larger. The divergence of the synchrotron x-ray beam can also be seen in the far-field images. In the top left image of Figure 4.4, if you look closely, the ring of intensity is slightly smeared out on the left and right sides, while the ring is slightly sharper on the top and bottom. This is from the divergence of the synchrotron x-ray beam, the beam has a smaller divergence in the vertical direction, and a larger divergence in the horizontal direction. For a collimated beam, such as G-line in the G1 hutch, or a divergent beam with the source far away, such as D-line, the far-field pattern looks mostly clear and uniform for a good optic. For example, the far-field images in Figure 4.4 were made with a low synchrotron x-ray beam divergence, of <0.5 mrad or less.

The far-field images in Figure 4.5 had a large horizontal synchrotron x-ray beam divergence of over one mrad. This causes considerable smearing of the far-field image in the horizontal direction, most easily seen in the bar-like smear of the direct beam through the optic in the left image of Figure 4.5. The far-field pattern from the F2 station, which has a horizontally focusing silicon crystal, is especially interesting to look at. The four dots in the direct beam provide evidence that the capillary optic is collecting rays from the four focusing channels or "teeth" through the silicon crystal.

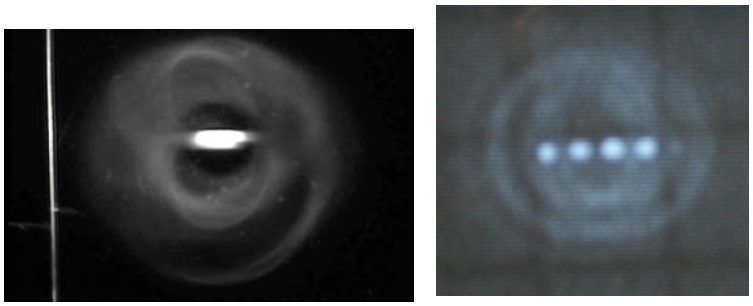

Figure 4.5 This figure shows two far-field patterns from optics with considerable divergence in the beam caused by the focusing optics placed upstream from the capillary. The image on the left is taken at G1 using most of the beam from the sagittal (horizontally) focusing multilayer. The image on the left is taken at F2, which has a sagittal (horizontally) focusing silicon crystal.

4.3.2 Modify the Divergence of Monocapillary Optics

A capillary's divergence can be easily modified with slits a few centimeters upstream of the single-bounce monocapillary. Slits can block part of the inner surface of the optic from the x-ray beam to reduce the apparent divergence of the optic. It takes minutes with slits upstream from the optic to switch between a mode with a higher divergence, higher flux, and lower angular resolution, to a mode with a lower divergence, lower flux, and higher angular resolution. Modifying the divergence of the micro x-ray beam is a huge advantage, and is utilized repeatedly at the CHESS beam-lines. For example, if an experiment needs high resolution in just one dimension, the optic can be manipulated to have a high angular resolution in one direction, to maximize flux, and a low angular resolution in the other, to maximize resolution. This technique has been used in almost all the experimental applications discussed in Chapter 9.

Figure 4.6 outlines the slit technique. The sketch to the left shows a monocapillary with a slit that blocks the beam from hitting one side of the optic. Because one side of the

optic is blocked, the resulting divergence is less than the full divergence of the optic. Only a portion of the full far-field pattern is seen. The divergence of the beam can be estimated from the far-field image, and the equations below (Figure 4.7).

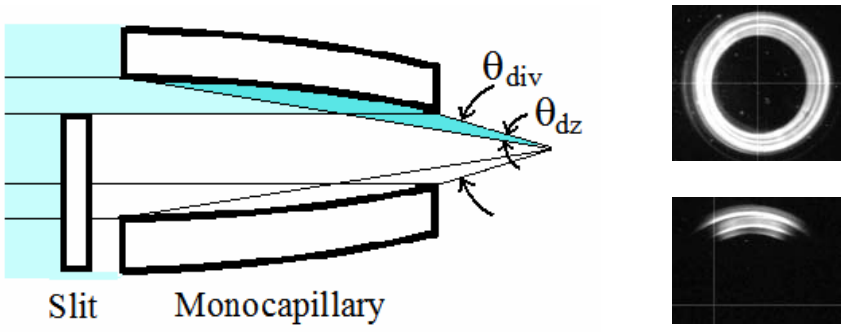

Figure 4.6 On the left is schematic cut away of a single-bounce monocapillary with a slit blocking the direct beam and one side of the optic. On the right are two far-field images of an optic without a slit (upper image) and with a slit (lower image).

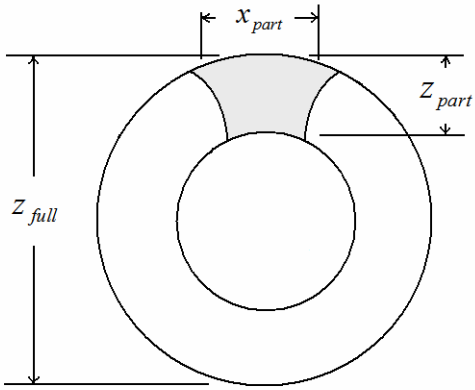

Figure 4.7 A schematic of a slit down far-field image. From the far-field image, the slit down divergence can be measured.

$$\theta_{div} \cong \frac{z_{full}}{y} \tag{4-8}$$

$$\theta_{dz} \approx \frac{z_{part}}{z_{full}}\theta_{div} \qquad \theta_{dx} \approx \frac{x_{part}}{z_{full}}\theta_{div} \tag{4-9}$$

Where 'θ_{dx}' is the divergence of the beam in the horizontal direction, 'θ_{dz}' is the divergence of the beam in the vertical direction, 'θ_{div}' is the full divergence of the optic, 'y' is the distance from the focal spot of the optic to the fluorescent screen, and the 'z' and 'x' distances are labeled in Figure 4.7. If the full divergence is known, the divergence of the slit down beam can easily be estimated by taking the ratio of the full far-field pattern to the remaining part of the pattern.

To demonstrate the advantages of using slits in conjunction with a larger divergent optic, I will compare f1b_mr9f20_01, a 7.5 mrad optic, with SF202, a 2 mrad optic, which are both used for protein crystallography. F1b_mr9f20_01 had an 9 mrad design, but it did not turn out with that divergence (see section 7.1). Figure 4.8 on the left shows the far-field image of capillary f1b_mr9f20_01, with all the distances and the corresponding divergences labeled. A small circle that corresponds to a far-field pattern from a 2 mrad divergence is placed on top of the pattern. A 2 mrad divergence can be created from monocapillary f1b_mr9f20_01, if a wedge of about 1/10 (36º) of the optic is used. The cross-sectional area of the 36º wedge, and the entire cross-sectional area of SF202 are very close to the same (Figure 4.8 upper right). The slit down 7.4 mrad optic and the full 2 mrad optic have the same flux and divergence. A slit setting of 100(H)x60(V) mm^2 can be used to select a similar area (Figure 4.8 lower right), with a divergence and flux that is minutely larger.

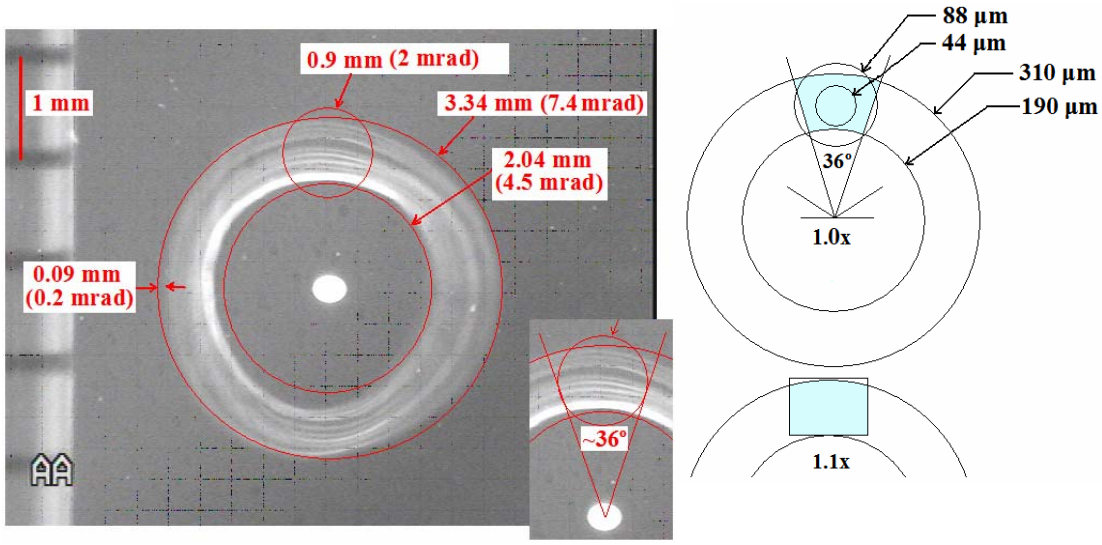

Figure 4.8. The far-field pattern from monocapillary f1b_mr9f20_01 is on the left, with distances and divergences labeled. A 36º section of the optic corresponds to a 2 mrad divergence. A diagram in the upper right is the cross sectional area of both monocapillaries f1b_mr9f20_01 and SF202, defined by their inner tip and base diameters; they have nearly equal cross-sectional areas. Equal areas means the flux is equal. A diagram in the lower right shows a cross-sectional area slit setting on monocapillary f1b_mr9f20_01, which will produce a 2 mrad divergence from the 7.5 mrad the optic.

The larger divergent optic with slits has the advantage. The slits can be adjusted to increase the flux, or increase the angular resolution. If a 45º wedge is used, the flux is 1.25x larger than the SF202 optic, and the divergence is about 2.5 mrad. If a quarter of the inner surface is used, the flux is 2.3x larger, and the divergence is 3 to 4 mrad. If the full f1b_mr9f20_01 optic is used, the flux is 9 times larger than the SF202 optic, at a 7.5 mrad divergence.

There are additional advantages for using a smaller portion of the single-bounce monocapillary optic. Often, a smaller section of the optic will have a localized slope error that is smaller than the slope error for the entire optic. This means that when a

smaller portion of the optic is used, a smaller beam spot can be achieved. At CHESS, monocapillary optics can have their spot size decreased by 50% to 80%, just because the smaller portion of the optic's inner surface is used (Table 4.1). The smallest spot size ever achieved with a single bounce monocapillary optic is 250 nm. To achieve this small spot, one key technique used was only a portion of the inner glass surface was used, which has a minimal local slope error [65]. Using just a portion of the inside of the optic is a real advantage; it allows for a tunable divergence, and produces smaller spot sizes, at the cost of lowering the total flux.

Chapter 5 Auxiliary Equipment for Monocapillary Optics

Single-bounce monocapillary optics, fabricated and extensively used at CHESS, are used in a wide array of experiments. CHESS-made monocapillary optics are used at a few other synchrotrons as well, such as Hasylab and APS (sections 9.9 and 9.14). Auxiliary equipment is used to align and diagnose the monocapillary optics every single time they are used. Over the last few years, monocapillary optics have been popular at CHESS. Commonly, every x-ray synchrotron-running day will have at least one single-bounce monocapillary optic in use at one of the twelve CHESS experimental hutches. A few times in the past three years, three to four monocapillary optics have been used simultaneously in CHESS experimental hutches. When I started working with the capillary optics in the fall of 2004, we had one capillary stage available, and enough other auxiliary equipment to support that stage. It became apparent rather quickly that the auxiliary equipment surrounding the monocapillary optics needed expansion in order to support the demand for x-ray microbeams at CHESS.

Not only did CHESS need more microbeam auxiliary equipment, it needed improved equipment. The equipment did not have the resolution or accuracy required to fully accomplish the needs of many x-ray microbeam experiments. Single-bounce capillary optics have an advantage of being relatively small; this allows them to fit into confined spaces. Improvements in design, resolution, and miniaturization of the auxiliary equipment expand many of the advantages the monocapillary optics already have.

Almost all of the present auxiliary equipment was designed and built over the past three years. I feel that CHESS has just barely reached its needs for microbeam auxiliary equipment in this period.

Below is a list of the basic equipment needed to operate single-bounce monocapillary optics.

- Stages for height, left-right positioning, pitch and yaw angles of the optic and the positioning of other equipment.
- A fluorescent screen for viewing the far-field image for rapid line-up.
- A "hockey puck" beam stop to block the direct beam from the capillary.
- X-ray slits for controlling the divergence and cleaning up the beam profile.
- Small pinholes (5, 10, 25, 50, 100, 200 μm) for spot size measurements, and clean-up apertures.

This chapter discusses the auxiliary equipment needed for monocapillary optics, including their function, improvements, and so forth. Section 5.5 gives a procedure for aligning monocapillary optics in the synchrotron x-ray beam.

5.1 Stages and Motion Controls

Stages and motion controls position the single-bounce monocapillary optic, slits, pinholes, samples, and anything else that needs remote alignment in the x-ray beam. The motion controls need to be remote because the hutch is closed and locked when the x-ray beam is on. There is a convention of labeling directions within CHESS hutches. The '*y*' direction is the direction of the x-ray beam, the '*z*' direction is up and down,

perpendicular to the beam, and the '*x*' direction is left and right, perpendicular to the beam.

We presently have three major setup types used for x-ray microbeam optics. There is a standard capillary setup, a new x-ray microbeam breadboard, and the MacCHESS collimator configuration. A majority of the mechanical drawings for the stages can be found in the appendix, section A.

5.1.1 The Standard Monocapillary Setup

The standard monocapillary setup is adequate for many x-ray microbeam experiments (Figure 5.1 and section A.1 in the appendix). Four motions are needed to align a single-bounce monocapillary optic. Aligning the optic requires positioning in the in the *x* and *z* directions, and the pitch and the yaw angles. The standard monocapillary setup requires standard CHESS x-z stages to position the single-bounce monocapillary into the x-ray beam. The standard monocapillary stage controls the pitch and yaw angles,

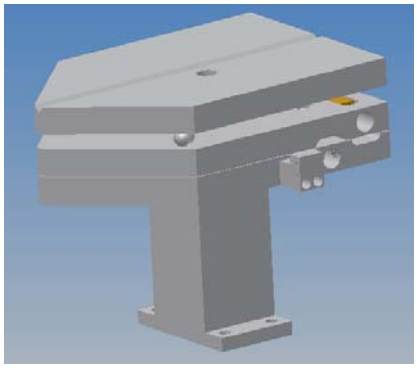

Figure 5.1 The standard capillary stage for controlling the pitch and yaw of the capillary optics. This stage is 15 cm long, 10 cm wide and 5 to 10 cm tall. The monocapillary optic is placed in the V-groove which is along the top surface of the stage.

and mounts on top of standard CHESS x-z stages. The monocapillary stage controls the angle of the optic with a high degree of accuracy, with a resolution of about 10 μrad (0.0005º). Just for reference, a misalignment of about 100 μrad is just visible in the far-field pattern. The two angular motions are controlled with Oriel encoder mike motorized actuators [14].

On the top platform of the monocapillary stage is a V-groove. The monocapillary optic sits in the V-groove. The V-groove has advantages, it accommodates most the monocapillary optics we have, and it helps to align the optic (section 5.5). The V-groove has disadvantage as well, it is prone to misaligning the optic if the monocapillary stage is mistakenly bumped.

The monocapillary stage has adequate resolution to align the optic in the synchrotron beam, it protect the optic fairly well, it has a pointy noise to get it out of the way of other equipment, and it is stable enough for a fair amount of applications. Some disadvantages are that the pitch and yaw angles are not completely independent of each other in the stage's design, and the pitch range is often too limited. Monocapillary optics on the standard monocapillary stage do not reliably stay aligned with monocapillary beam-stops on another CHESS standard x-z stage; the positioning of this equipment is too crude. Often for x-ray microbeam measurements, this monocapillary stage is simply too big to fit with other equipment surrounding it. This motivated the development of a breadboard concept of positioning.

[14] The Oriel® 18212 encoder mike motorized actuators and the Encoder mike controllers 18011 used for this stage are no longer available to buy; Oriel® is now part of Newport®. We have two Newport® CMA-12CCCL motorized actuators and the Newport® Universal Motor Controller/Driver Model ESP300 as a backup for the monocapillary stages. The Newport® motorized actuators also fit the monocapillary stages, are roughly the same size, and have the same travel length of 25 mm. Newport® contact information: www.newport.com (Newport Corporation, 1791 Deere Avenue Irvine, CA 92606)

5.1.2 The X-ray Microbeam Breadboard

There have been two major lessons learned about the stages and the motion controls for x-ray microbeam experiments over the past three years. One, the stages needed better resolution and accuracy. Two, the stages and motors needed to be smaller, in order to get all the needed equipment into a smaller area (section A.2 of the appendix).

The standard CHESS x-z stages have a positional accuracy of about two microns or more. This resolution is adequate for positioning the monocapillary optic into the synchrotron x-ray beam. This resolution is inadequate for positioning samples and pinholes into the micro-focused x-ray beam, especially at the one micron level. CHESS's x-z stages are not repeatable when scanning a 5 μm pinhole through a 5 to 20 μm sized x-ray beam. The non-repeatability of profile scans frustrates the evaluation of the single-bounce monocapillary optics. Additionally, the CHESS stages are too large; it is virtually impossible to get all x-ray microbeam equipment needed for an experiment into the beam.

At CHESS, a new optical breadboard has been built that better matches the resolution and size needs of x-ray microbeam experiments. This breadboard allows higher resolution positioning of more components in a much smaller volume. It has small Newport® stages[15] that allow components such as small ion chambers[16], cleanup

[15] Stages used are Newport® M-561D-YZ and M561D-XYZ ULTRAlign™ Linear Stages. A complete list of parts is given in the appendix section A.2, Newport® contact information: www.newport.com (Newport Corporation, 1791 Deere Avenue Irvine, CA 92606 attn: Scott Giancola scott.giancola@newport.com) Part numbers are in section A.2 of the appendix.

[16] An image of the ion chamber is shown in appendix section A.2. The small ion chambers were built by Basil Blank at PulseRay. Contact information: www.pulseray.com (PulseRay 4583 Route 414, Beaver Dams, NY 14812, Office: 607-654-2070)

apertures (see section 5.4), and a sample viewing microscope[17] to fit into experiments, where they did not fit before (Figure 5.3, 5.4 and section A.2 of the appendix). The x-ray microbeam breadboard has the sub-micron positional resolution. The small Newport® NSA12 actuator controls the stage's position. They have 11 mm of travel with a position resolution of 0.1 μm, which is twenty times better than the standard CHESS x-z stages (Figure 5.2). Multiple motor controllers are controllable through one Ethernet connection, thereby making the entire setup quite mobile from hutch to hutch, which is a needed feature.

There is an important note that should be given about the NSA12 actuators; they are positioned with a stepper motor and are repeatable. We initially tried the PZA12 actuators (also made by Newport®), which are positioned with a piezo motor. They have a lower minimum resolution of ~30 nm, but they have a terrible repeatability over a few hundred μm, without some other positional feedback[18]. Without repeatability, the PZA12 actuator was not a good match for the x-ray microbeam breadboard. The NSA12 actuators have worked out much better because of their repeatability on both the μm and mm size scale without any additional feedback.

There have been additional benefits from having the x-ray microbeam breadboard. It takes less time to set up and align in the experimental hutch. Because all the

[17] For the x-ray microbeam breadboard, we have purchased one microscope lens assembly with a camera (which integrates frames, good for dim signals). The lens assembly parts are given in the appendix section A.2 (along with an image of the lens system). The lens assembly is from Navitar Inc. Contact information: http://navitar.com (Navitar Inc, 200 Commerce Dr. Rochester NY 14623). The AV-STCAM-C Astrovid StelleCam EX color CCD Video Camera is from Adirondack Video Astronomy. Contact information: http://www.astrovid.com (Adirondack Video Astronomy 72 Harrison Avenue, Hudson Falls, NY 12839 USA).) Part numbers are in section A.2 of the appendix.

[18] The extreme non-repeatability issue of the piezo motors was initially unknown to us. Piezo motors (such as the PZA12) need to be run in a closed loop configuration to have repeatability (closed loop means there is an alternate positional feedback mechanism of some sort). Stepper motors (such as the NSA12) have repeatability in an open loop configuration (open loop means there is no positional feedback, the motors can keep track of the position).

components are together, the components on the microbeam breadboard can be assembled and roughly aligned with a small laser pointer ahead of time, thus reducing the aligning and setup during an x-ray experiment. It also has a microscope for looking at samples *in-situ*[16]. Having a microscope image coordinated with x-ray data taken with the x-ray microbeam is a tremendous advantage.

The x-ray microbeam breadboard, with its small stages, increased resolution, modularity, and microscope have been a great benefit and a large step forward in utilizing every advantage we can gain from the auxiliary equipment surrounding x-ray microbeam work. This setup was paramount for the success of μSAXS (section 9.11) and toroidal mirrors (section 9.12). It was also used in the Laue Protein Crystallography project (section 9.13), because of its small size, modularity, and ability to be assembled beforehand. I am sure that it will continue to allow for more aggressive x-ray microbeam setups in the future.

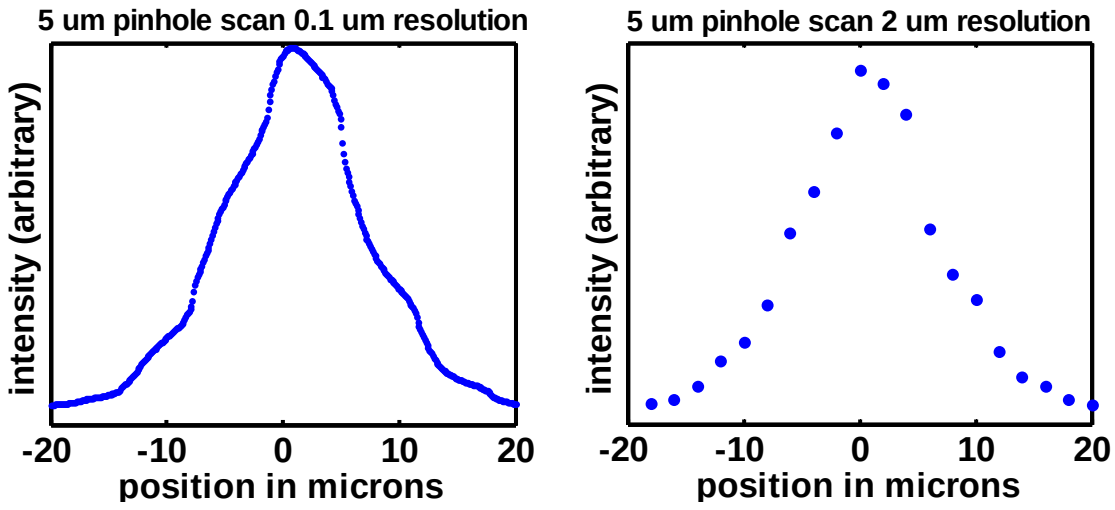

Figure 5.2 Two scans taken with the x-ray microbeam breadboard for monocapillary PEB_mr8f55_02 at the D1 station. The scan on the left is taken at a 0.1 μm step size. The scan on the right is taken at a 2 μm step size, which is near the limit of what the traditional CHESS stages and motors are capable of. The focal spot size is 13 μm (FWHM).

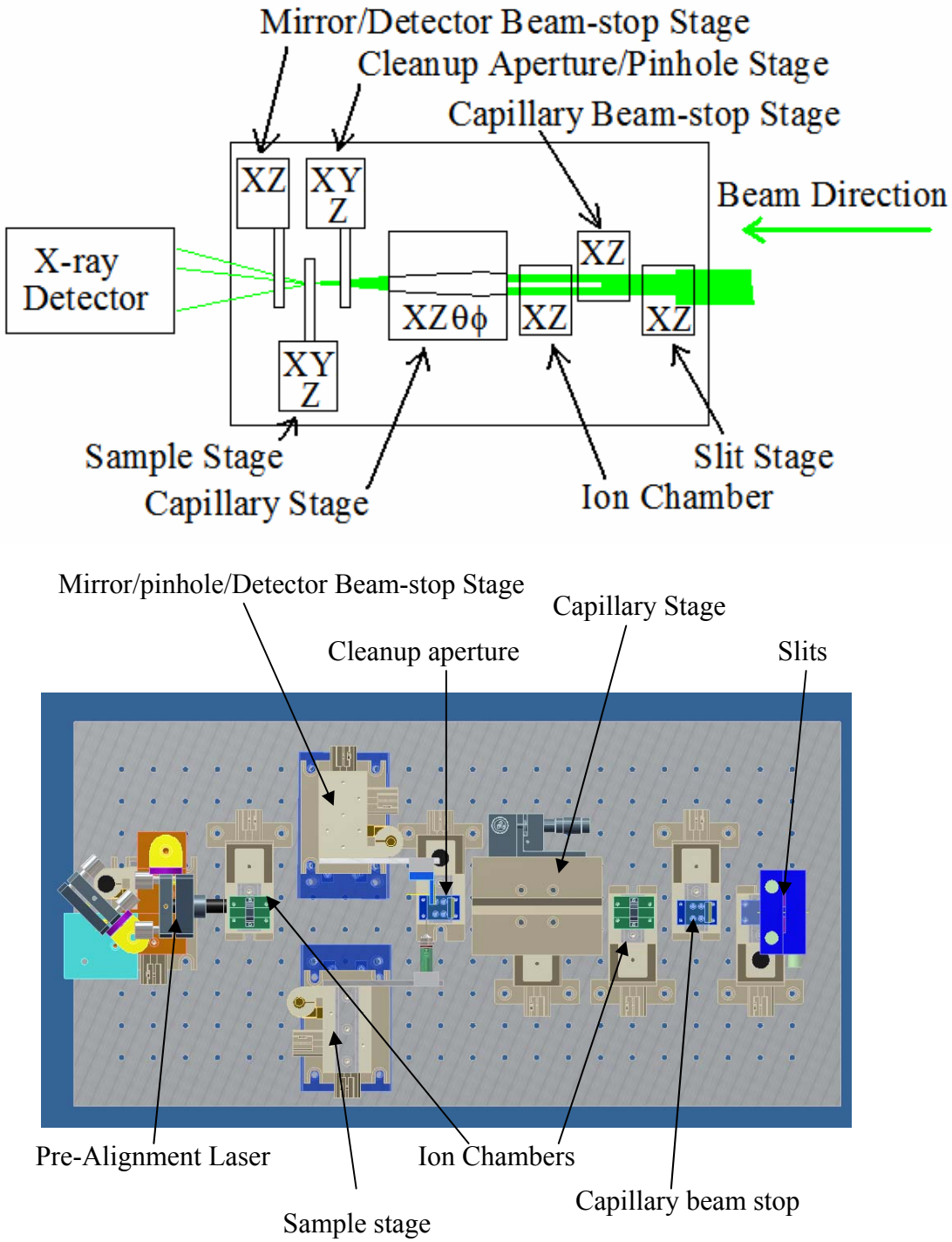

Figure 5.3 The top drawing is a simple schematic of the X-ray microbeam breadboard, with the stages, motions, and functions identified. The bottom drawing is a more complicated schematic of the X-ray microbeam breadboard, with all the stages in place. The small stages allow for placing the needed components in a small space in a variety of ways.

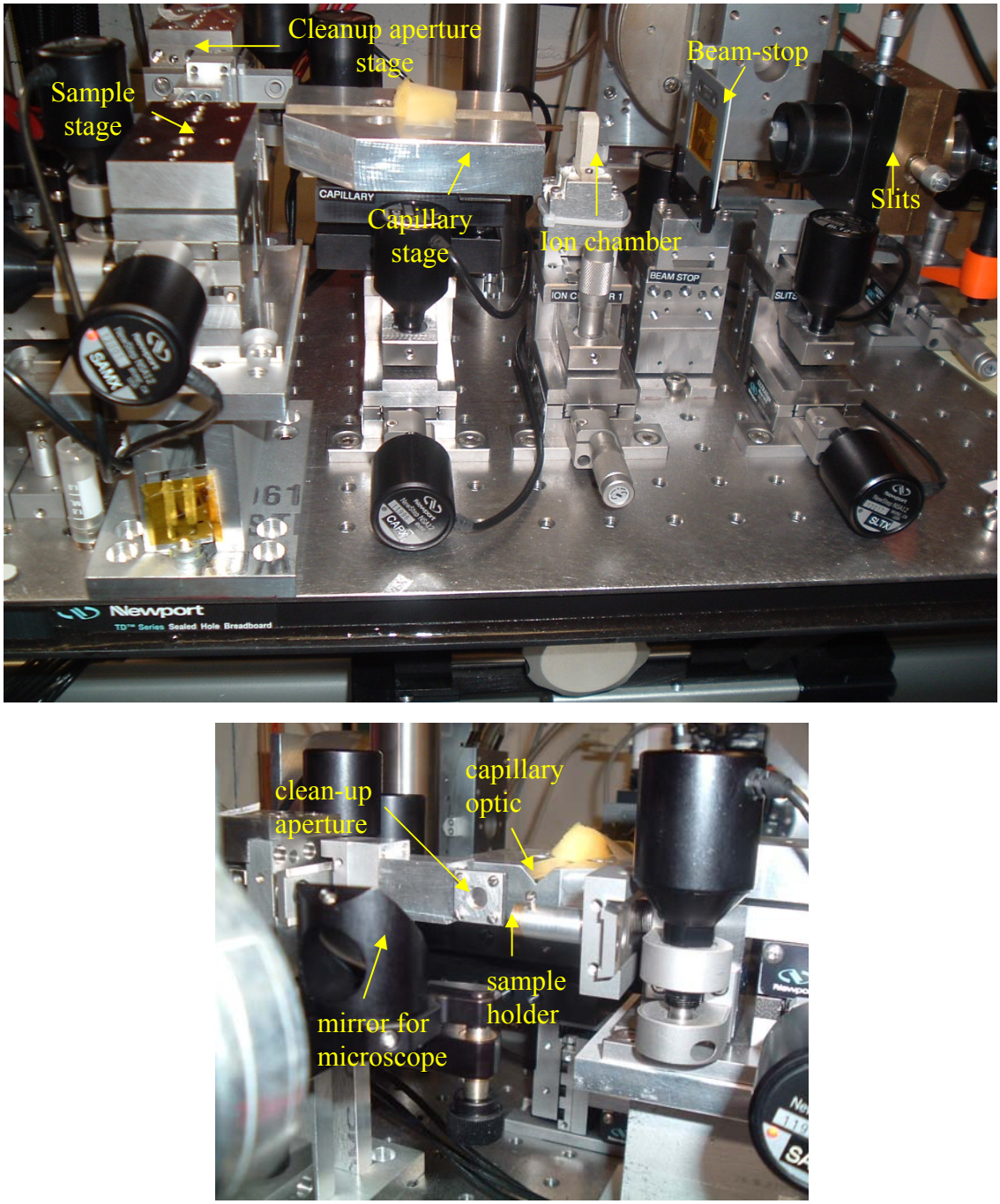

Figure 5.4 The top image shows most of the x-ray microbeam bread setup (for µSAXS section 9.11). The lower image shows a close-up of the sample region, with a single-bounce monocapillary optic in the V-groove, a 200 µm clean-up aperture, the sample, and a mirror for the microscope all within a beam path of ~100 mm (twelve motor motions).

5.1.3 The MacCHESS X-ray Microbeam Setup

MacCHESS is in charge of most of the protein crystallography work done at CHESS (section 9.6). They use collimators for most standard-sized protein crystals, and they use single-bounce monocapillaries for protein micro-crystals. MacCHESS designed mounting hardware which allows switching between the collimator and the single-bounce monocapillary optic. The entire optical table in the hutch is positioned to align both collimators and the single-bounce monocapillary optic. Only minor table adjustments are needed to align the x-ray beam between the collimator and the monocapillary optic. MacCHESS has designed a housing for the monocapillary optics, because they need a highly repeatable process for alignment. The housing fixes the position of the optic with respect to the optical table (Figure 5.5). In addition, hardware has been created to adjust the position of the optic long the focal length, to be able to get the sample at the correct focus position for the optic[19].

There is a disadvantage with this setup. Because the entire table moves to align the optic, other components placed on the optical table, such as slits, are un-aligned as the capillary is aligned. This is not an issue for most protein crystallography users. It is an issue if other components, such as a capillary beam-stop or slits are moved with the optic.

[19] Mechanical drawings of the capillary housing are in the appendix section A.3. All other drawings associated with the monocapillary MacCHESS setup can be found from Mike Cook at MacCHESS.

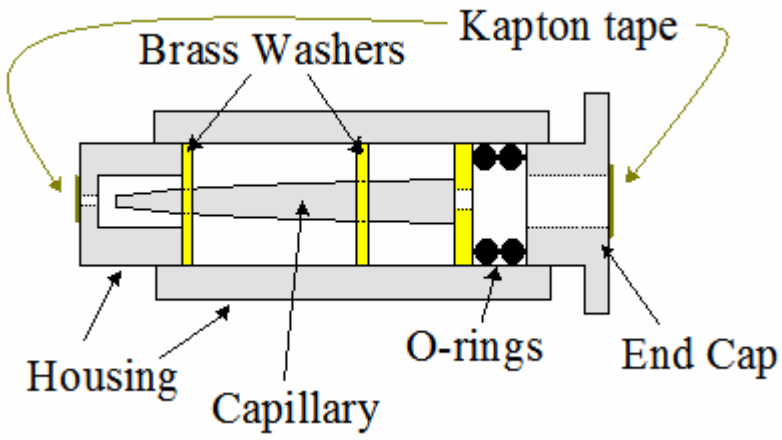

Figure 5.5 A cutaway diagram of the MacCHESS capillary housing designed by Mike Cook. Two brass washers have holes made to fit a particular optic at the ¼ and ¾ positions along the overall length to minimize the bending of the optic due to gravitational sag. They are gently attached to the optic with a small drop of clear fingernail polish or wax. The o-rings hold the optic from moving in the housing. The end cap is gently glued (again with fingernail polish) in place so as to not bend the capillary. Kapton® tape is placed over the openings at both ends of the housing to keep dust out of the monocapillary optic. (Appendix section A.3 has the mechanical drawings)

5.2 Fluorescent Screens

Fluorescent screens are used to view the single-bounce monocapillary optic's far-field patterns. The far-field images are vital for aligning the optic. High-resolution far-field images give vital clues about the optic's quality (section 4.2). Fluorescent screens are made of scintillation materials that fluoresce with visible light where it absorbs x rays. Fluorescent screens used to view far-field patterns include thick phosphor-coated paper, cadmium telluride crystals, and a gadolinium gallium garnet wafer (GGG, $Gd_3Ga_5O_{12}$) (Figure 5.6).

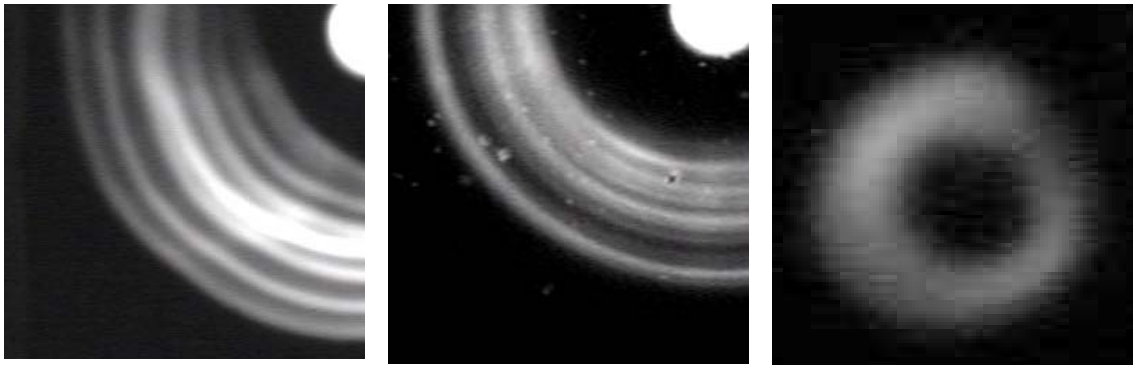

Figure 5.6 Far-field images showing all three screen types. The GGG screen is on the left, the cadmium telluride screen is in the middle, and the thick phosphorous paper is on the right (center spot from the direct beam has been removed with a capillary beam-stop). Only a portion of the GGG and cadmium telluride screen has been shown to highlight the differences.

The thick phosphorus paper[20] is sufficient for aligning the optic, but not much more. They produce a very blurred image, which often is a source of inaccuracy in aligning and diagnosing the x-ray beam. Phosphorus paper is not the ideal fluorescent screen for monocapillary optics, and is only used when the other types of screens are not available.

Cadmium telluride crystals (CdTe) or alternately cadmium tungstate ($CdWO_4$) [21] are good screens for viewing far-field images. They produce clear images, with enough detail to view features within the far-field patterns. They have a number of defects that show up as spots or cracks in the image. Sometimes subtle features seen in the far-field images are not from the x rays, but from the crystal. These problems are relatively minor, but can be annoying when trying to do more quantitative work.

[20] The phosphorus paper used at CHESS originally came from KODAK® about ten years ago. I have been told by Chris Conolly (at CHESS) that it is no longer available from KODAK.

[21] I have not looked for a vendor of cadmium telluride crystals; I have used the cadmium telluride crystals already available at CHESS. Other crystals such as Cadmium tungstate ($CdWO_4$) can work as fluorescent screens as well. Cadmium tungstate crystals can be purchased at Saint-Gobain Crystals. Contact information: www.detectors.saint-gobain.com (Saint-Gobain Crystals 12345 Kinsman Road Newbury, Ohio 44065)

The best fluorescent screen is the gadolinium gallium garnet (GGG, $Gd_3Ga_5O_{12}$) wafer with a homoepitaxial 15 μm GGG layer growth doped with 3 mole % of europium [22]. This screen is excellent; it is very uniform and is virtually free of any visual defects. The uniformity and visual clarity have made it the fluorescent screen of choice, especially when evaluating the far-field images of single-bounce monocapillary optics.

In each case, a video camera, sometimes outfitted with a magnifying lens, views the fluorescent screen. A very advantageous feature the camera needs to have is the ability to integrate frames, which allows for the detection of very dim fluorescent signals[23]. Another example of a camera/fluorescent screen combination is given in Figure 5.7, showing a very small video camera that has been coupled with a cadmium tungstate crystal for viewing the monocapillary far-field image and aligning the optic.

There is a fourth type of fluorescent screen, very thin fluorescent glass fibers[24]. They are primarily used to find the x-ray beam at the single-bounce monocapillary's focus (or find the x-ray beam after a collimator). They can be used to locate the position of the x-ray beam in a microcope's field of view. They are most often used to locate the beam in MacCHESS's protein crystallography experiments. The fibers are mounted exactly

[22] The GGG screens are not easy to come by, we have been trying to get more of them for a number of years. The GGG screen that we have been using for the past few years came from the French academic institute, CEA/Grenoble, which no longer makes the crystals. The original GGG screen was obtain by Sol Gruner (CHESS) from Thiery Martin at the ESRF. Northrop Grumman (Space Technology Division) has attempted to make some GGG crystals for us; they are of an adequate, but lower quality. Contact information: www.st.northropgrumman.com (Northrop Grumman Space Technology, One Space Park,Redondo Beach, CA. 90278) attn: Mark Randles (mark.randles@ngc.com) and Les Albert (les.albert@ngc.com)

[23] see Appendix section A.2 and footnote 17 for camera/microscope information.

[24] Richard Gillilan at CHESS is my source for these fluorescent micro-fibers, which are very commonly used on the MacCHESS beam-lines. He pulls the micro-fibers on his small pulling machine from 700 μm diameter glass fused with terbium oxide (see US patents 3,654,172 (1972) and 5,122,671 (1992)). This glass (called LKH6) was obtained from Collimated Holes Inc., Contact information: www.collimatedholes.com (460 Division Street, Campbell, CA 95008 ,Tel. 408.374.5080)

like the protein samples are, on small magnetic mounts. Because the microbeam breadboard is equipped with a microscope as well, they are useful for aligning the microscope and sample on the x-ray microbeam breadboard as well (section 5.1.2).

Figure 9.7 An image of a small video camera for viewing the x-ray far-field pattern. On the end of the camera is glued a block of clear Lucite (acrylic glass). On the end of the block there is a 10x10x0.24 mm^3 thin cadmium tungstate crystal (see footnote 21). The camera's part number is PC212XS from Super Circuits (www.supercircuits.com).

5.3 Capillary Beam-Stops

Capillary beam-stops block the direct beam going through the single-bounce monocapillary optic. The function of the beam block is to remove the direct beam to achieve a true small spot size (Figure 5.8). For a number of experiments, the direct beam is a source of noise in a signal, producing a signal that is not from the small focus of the optic. The beam block is a short cylinder of material with a high atomic number (high Z material) with a diameter equal to or slightly larger than the inner tip diameter of the monocapillary optic. Materials with a higher atomic number 'Z' are more effective at blocking x-rays than low atomic number 'Z' materials. We have beam-stops made of high atomic number materials such as tungsten, lead, and platinum at

CHESS. Every available monocapillary optic needs a matching monocapillary beam-stop.

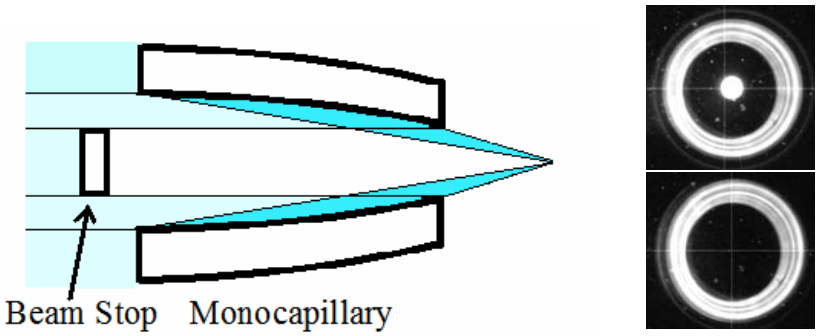

Figure 5.8 On the left is a schematic cut away of a single-bounce monocapillary with a capillary beam-stop blocking the direct beam. On the right are two far-field images, with (lower image) and without (upper image) a beam-stop.

When a beam-stop is used in a convergent beam, the beam-stop must be placed as close to the base of the optic as possible. Additionally, the beam-stop may have to be oversized to fully block the direct beam through the optic. The beam-stops are held in the x-ray beam between two pieces of Kapton® tape, which are mounted in a film holder (Figure 5.9). They are mounted with a wire of the same diameter, this wire is used to find the capillary beam-stop in the x-ray beam. The wire is translated up and down behind the monocapillary optic. The wire is roughly aligned with the optic when it blocks part of the x-ray beam going through the optic, viewed in the far-field image. Then the monocapillary beam-stop stage is translated in the horizontal direction off the end of the wire, which leads to the capillary beam-stop. The beam-stop is aligned when the position of the beam-stop blocks the direct beam, as seen in the far-field image of Figure 5.8. The beam-stop should be placed as close as possible to the base of the monocapillary optic.

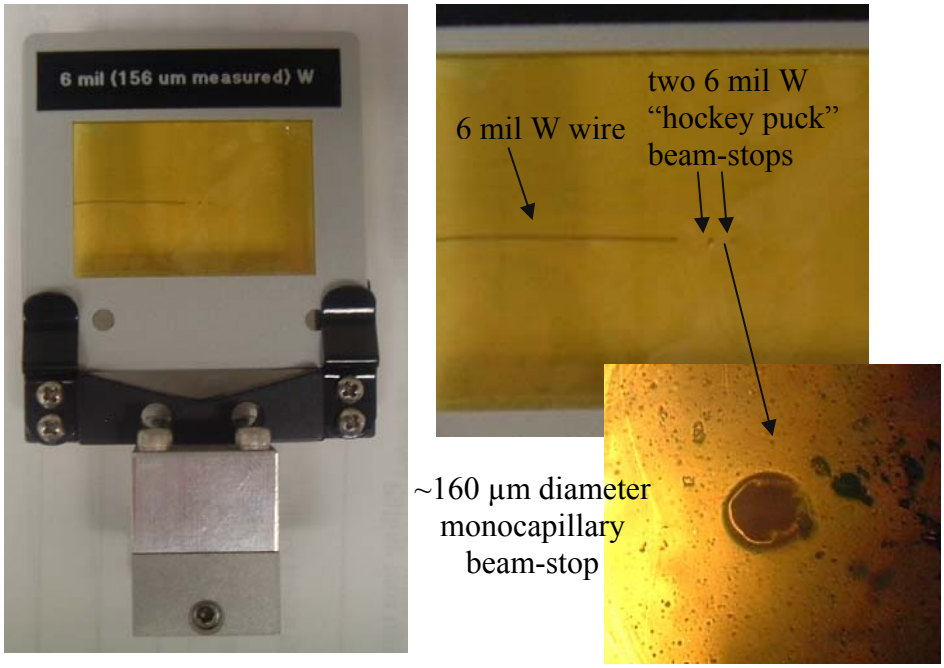

Figure 5.9 An array of images of a monocapillary "hockey puck" beam-stop, going from the film to a microscope image of a ~160 µm (6 mil) diameter beam stop. On each film mount, I have placed 2 to 4 beam stops, with each one looking a little bit different in most cases. This gives a sampling of beam-stops to try if one does not quite block the direct x-ray beam.

5.3.1 Fabrication of Small Beam-Stops

It is useful to know how to make small beam-stops, 100 to 600 µm in diameter and 100 to 300 µm thick. I have included a recipe for recreating them. This method makes several beam-stops of all different sizes at once.

- Get as many different diameters of high Z material (such as tungsten), as needed. The diameter of the wire will be the diameter of the beam-stop. You will be constrained in the diameter size by the selection of wire diameters available.

- Obtain a small copper ¼ inch diameter tube, about 3 to 4 inches long. Fill the copper tube with many strands of different sizes of wire and fill all the gaps between the wires with stycast® 1266 epoxy.
- When the epoxy sets, cut the tube into disks about ¼ inch wide.
- Polish one side of the disk flat on a thin section polishing system. After one side is polished, then the other side can be polished down until you get to the desired thickness [25].
- Dissolve the epoxy in acetone, so you have hundreds of small 'hockey puck' shaped beam-stops.

The beam-stops are then measured, sorted, and mounted on Kapton® (Figure 5.8) tape with help from an Olympus microscope available in the monocapillary pulling area. Beam-stop diameter sizes that we presently have include 115 μm, 140 μm, 156 μm, 178 μm, 210 μm, 254 μm, 310 μm, 340 μm, 480 μm, 508 μm, 635 μm, 910 μm (4, 5, 6, 7, 8, 10, 12, 14, mil etc.). Most of the beam stops are made of tungsten, with a few larger beam-stops made out of platinum and lead-tin solder.

5.4 Slits and Pinholes

Evaluating and modifying the performance of single-bounce monocapillary optics requires slits and pinholes. Both the slits and the pinholes are made out of high atomic number metals, which block x-rays efficiently. Slits have adjustable blades, which allow for a wide selection of opening sizes. CHESS has many slits available, from

[25] There is a thin section polishing system in the Cornell Center for Materials Research at Cornell University, which is traditionally used to thin polish samples. It can work for making monocapillary beam-stops as well. Contact information: John P. Sinnott, (jps39@cornell.edu) Manager, Materials Facility.

remotely positioned slits at G1 to manual Huber® slits. In general, slits cannot be reliably adjusted to opening sizes 100 μm or less.

Pinholes are a better way to implement precision-sized apertures of 200 μm or less. The pinholes available at CHESS range from 5 to 200 μm in size, and are made of 50 to 100 μm thick tungsten foils. For alignment, it is good to have a large 100 to 200 μm pinhole attached to the same mount as a small 5 to 10 μm pinhole. The best pinhole design we presently have is a single 1 cm diameter tungsten foil of 80 μm thickness with an array of six different sized pinholes placed in a 1 mm grid. The pinhole sizes in the array are 100, 50, 25, 15, 10, and 5 μm. This pinhole array was custom made by Lenox Laser[26]. It is excellent for aligning pinholes and for quickly adjusting to different aperture sizes.

5.4.1 Pinhole Alignment

This section lists some instructions for aligning a very small 5 to 10 μm pinhole with a 5 to 20 μm x-ray beam. It is not a procedure, which works every time, but it does point out some general ideas which can help speed up the process.

A pinhole has three directions in space that it can be placed to measure the x-ray beam profile from a single-bounce monocapillary optic. The two directions perpendicular to the beam are labeled '*x*' (left and right) and '*z*' (up and down). The direction along the beam is labeled '*y*', with positive values for '*y*' being in the direction of the beam. The '*y*' direction is associated with the optics focal length measured from the tip of the optic.

[26] Lenox Laser has a number of standard tungsten foil (25 to 50 μm thick) pinholes available. The foil comes in 9.5 diameter discs with the pinhole in the center. Lenox Laser contact information: www.lenoxlaser.com (12530 Manor Rd. Glen Arm MD 21057)

There are some strategies to align the small 5 to 10 μm sized pinhole with the small 5 to 20 μm x-ray beam. The easiest method by far is to place a fluorescent screen or fiber on the pinhole or sample stage, at the focal length of the capillary optic. The beam is found by looking at the fluorescent signal from the x-ray beam with a microscope (see Appendix section A.2 and footnote 17 for camera/microscope information). Next, the fluorescent screen or fiber is replaced with the pinhole, and the pinhole is moved to the same spot using the microscope. This gets the small pinhole close enough to the focus to thread some of the x rays through it. At that point, an ion chamber down stream of the pinhole can be used to fine tune its position. Unfortunately, a microscope is only available on the new, extremely micro-beam friendly, x-ray microbeam breadboard.

Without a microscope, aligning a small pinhole to the small beam is harder. Aligning a small 5 to 10 μm pinhole requires having a larger 100 to 200 μm pinhole on the same mount. The single tungsten wafer with an array of pinholes is an excellent example. The distance in '*x*' and '*z*' between the two pinholes needs to be known.

First, before any pinholes are in the beam, mark the far-field image's direct beam center on the video screen. Place the larger pinhole in the designed focal position. Fine-tuning the '*y*' position can be done later. Next, align a large pinhole with the central x-ray beam through the capillary optic. Semi-randomly scan the large pinhole around until the direct beam through the capillary optic and the pinhole cross. This crossing will show up as a small spot on the far-field screen. Center the large pinhole on the direct beam center marks made previously. When the large pinhole is aligned, the entire far-field image from the monocapillary optic will be visible.

Translate the stage from the large pinhole to the small one. After the translation, a faint small fluorescent spot should be on the far-field screen. The video camera may have to integrate a larger number of frames to see the small faint spot. Center the small pinhole-centering marks made previously. The pinhole alignment is almost complete when a large portion of the far-field ring image can be seen through the small pinhole. The small pinhole alignment is fine-tuned with an ion chamber downstream from the pinhole. Simply maximize the ion chamber reading by translating the small pinhole in the small x-ray beam in micron-sized increments. In many cases, the pinhole alignment is done at this point. At this point the focal length can be verified if desired.

To find the focal length of a monocapillary optic, take a series of maximum intensity measurements in the '*y*' direction in 0.5 to 1.0 mm steps. At each step, realign the small pinhole in the 'x' and '*z*' positions. The axis of the beam and the pinhole stage will not be aligned within 1 or 2 μm over a distance of 1 mm, so realignment of the 'x' and '*z*' positions at each '*y*' position is necessary. The focal length will be at the position if the maximum intensity. Keep in mind that some of the optics have a rather long depth of field, so this maximum may be 1 to 3 mm wide in the '*y*' direction (section 4.1.1).

5.5 Lining up Monocapillary Optics

I have included this section because aligning monocapillary optics happens one or more times every time they are used. Aligning the optic can take hours and hours for the inexperienced. It can take less than fifteen minutes for someone with experience. I hope this procedure will bridge this gap and allow those without experience to be more comfortable using monocapillary optics.

Alignment of the optic centers entirely on the fluorescent screen used to view the far-field images from the optics. Figure 5.10 shows every typical image that has to be seen in order to fully align the monocapillary optic. V-groove alignment is shown in the first column of images, aligning the optic is shown in the second column of images, and slit alignment is shown in the third column of images. The images are labeled in the order of alignment, from *A* to *J*, with a description for what is happening in each image, listed below:

A. Align the synchrotron x-ray beam with the fluorescent screen.

B. Align the V-groove on the capillary stage, adjusted in the *x* and *z* directions, to intersect the beam

C. This is the lengthiest part of the alignment process. Adjust the V-groove's pitch and yaw angles to maximize the rays coming through the groove, so the sides of the V-groove are parallel with the beam. There is a useful method for accomplishing this. Adjust the '*x*' and '*z*' positions so only a small spot of x-rays barely get through the bottom of the V-groove. Adjust yaw angle in the direction that allows more x-rays through the V-groove. The '*x*' and '*z*' positions will likely need readjustment during this process. When the size of the beam gets smaller by adjusting the yaw angle in either direction, the V-groove is close to aligned. Redo this process for the pitch angle. Fine-tuning of the alignment can now be done for both the yaw and pitch angles. Adjust the yaw and pitch angles to view the "bunny ear" x-ray reflections from the surface of the V-groove, as seen in image C of Figure 5.8. Align these reflections symmetrically, and the V-groove is very close to parallel with the direct beam. Note, sometimes the "bunny-ear" reflections are not equal in intensity because the two V-groove surfaces may have a different smoothness.

D. At this point, place the optic into position in the V-groove. Move the '*z*' stage down by one-half of the outer base diameter of the optic. The x-rays should thread though the center of the optic at this point, if the optic has a large inner tip diameter. If the capillary has a smaller inner diameter, the beam may not be able to go through the center of the optic. Adjust the pitch of the stage to roll the tip of the optic up, in order to get the direct beam through the optic. Once the beam goes through the center of the optic, the alignment is much easier to complete. If the direct beam cannot be found, it is a good idea to go back and make sure the alignment of the V-groove was done correctly.

E. Adjust both the pitch and yaw angles to center the reflections from the monocapillary optic on the direct beam.

F. Adjust the '*x*' and '*z*' positions to intersect the beam with the optic. In this image, the optic's inner base diameter is a little larger than the direct x-ray beam, evident from weaker reflections on the top and bottom of the far-field image. In this image, the direct beam is centered on the center of the optic.

G. Adjust the '*x*' and '*z*' positions to intersect the hottest part of the beam with the desired part of the optic. In this image the bottom surface of the optic is centered on the x-ray beam (reflections from the bottom of the optic are on the top of the far-field pattern)

H. Once the optic is aligned to the x-ray beam in the desired way, either a slit or a capillary beam stop is aligned with the optic. In this case, a slit is aligned with the optic. Slit down in the horizontal direction to the desired width and scan the slit horizontally across the optic. In this image a small part of the direct beam and the reflected beam are aligned with the slit.

I. Align the slit as desired. In this case, the silt is aligned with the center and bottom of the optic.

J. Slit down in the vertical direction to pick out the desired portion of the optic. In this case the direct beam is completely blocked by the slit. Sometimes, both the slits and the capillary beam stop are used together. Also, note that the part of the optic selected with the slits is the same part of the optic the direct x-ray beam was aligned with in image G.

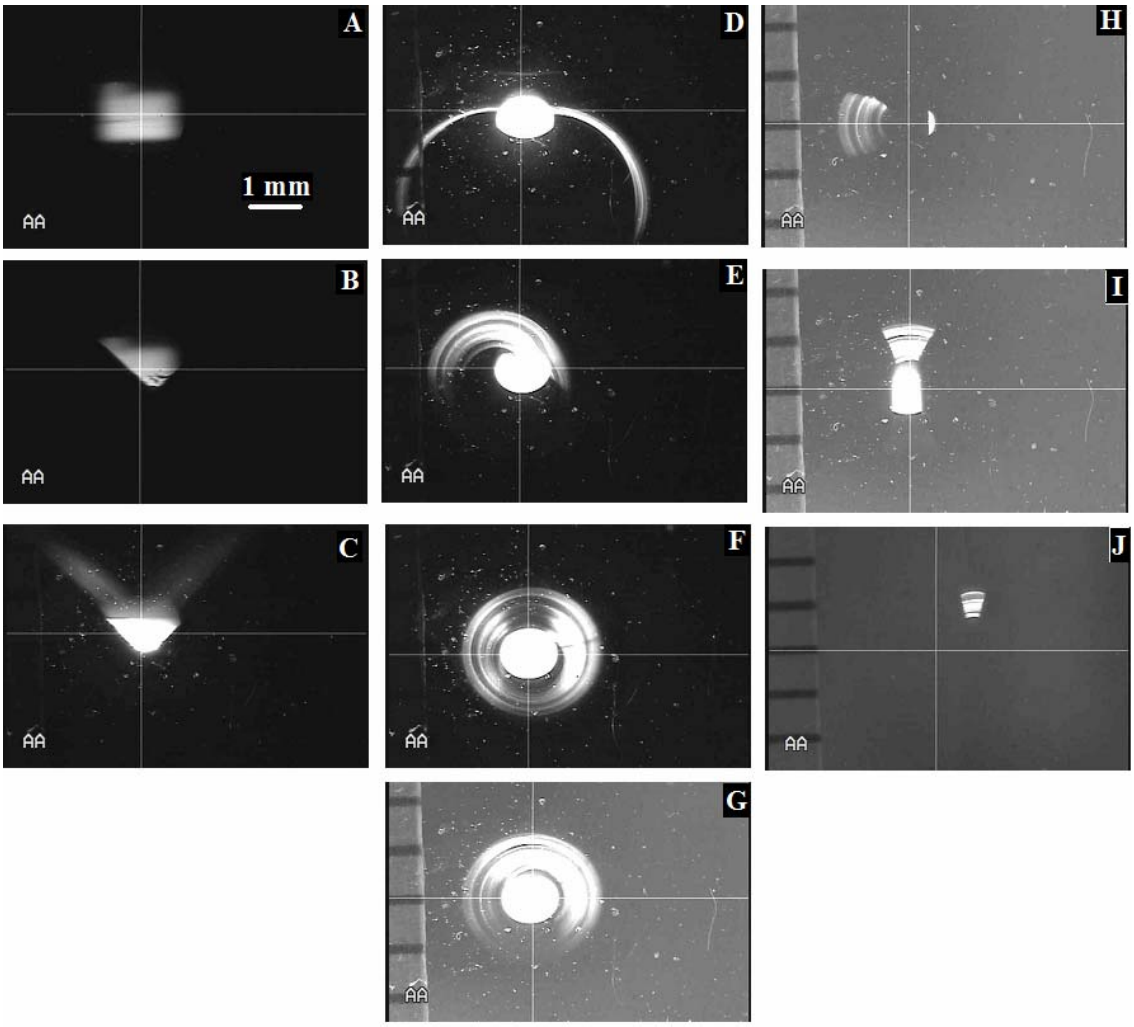

Figure 5.10 An array of far-field images outlining the steps for aligning single-bounce monocapillary optics. Images A to C show the alignment of V-groove that holds the monocapillary optic. Images D to G show the alignment of the capillary optic illuminating the entire inner surface of the optic. Images H to J shows restricting the amount of illumination the monocapillary sees with slits, and eliminating the direct x-ray beam through the optic.

Chapter 6 Fabrication of Monocapillary Optics

This chapter covers the fabrication of single-bounce monocapillaries. The optics are made of hollow glass cylinders, which are softened with a furnace and pulled into the desired ellipsoidal shape on the glass capillary puller. The optics are pulled into a desired shape using the conservation of mass model. This model stipulates that the glass going into the furnace's heat zone equals the glass coming out of the heat zone. This chapter describes the functions of capillary puller, which pulls the glass and performs a preliminarily evaluation on the monocapillary optics.

CHESS is not the only place where single-bounce monocapillaries are made. Single-bounce monocapillaries made of glass are also produced by number of companies. They include: Xradia, Australian X-ray Capillary Optics PTY LTD (AXCO), X-ray, and Institute for Scientific Instruments (IFG). CHESS is unique among all of these companies for two reasons. We produce monocapillary optics on-sight for use at a synchrotron, and we publish our results openly.

Starting with hollow glass cylinders is not the only way to create ellipsoidal shapes out of glass. Single-bounce monocapillaries have also been created by stretching spherical bubbles in glass into ellipsoids [65]. There are other methods capable of creating ellipsoidal shapes in materials other than glass (see discussion in section 7.2).

6.1 Properties of Glass

Single-bounce monocapillaries at CHESS are made of glass, which is an amorphous solid at room temperature. An amorphous solid has no long-range ordering in the positions of atoms within the material. Verification is the process for achieving an amorphous solid. Verification can be achieved by rapid cooling/heating, and/or putting in additives into the material that diminish crystalization. For silicon dioxide, additives such as lime or sodium carbonate help to both reduce the melting point of the silicon dioxide and help in forming amorphous glass. Silicon dioxide based glasses exist in society because the time needed for the material to transition into a crystallized ceramic is exceedingly slow, practically infinite.

Glass has two attributes that are key to the fabrication and function of monocapillary optics. First, glass is naturally very smooth on the micron scale, which is desirable for efficiently reflecting x-rays. Second, glass also lacks an abrupt phase transition from a solid to a liquid, glass gradually changes from a solid to a liquid. This softening of glass allows us to shape the glass into ellipsoids.

The viscosity of glass as a function of temperature gives a wide range of conditions between a molten state of liquid flow to an unyielding solid. Table 6.1 shows a viscosity scale with a description of the various intermediate states between liquid and solid [66]. Because of this slow transition, glass can be heated to the point where it just barely yields to a strain, at a viscosity of about 10^8 Pa•**s**. Many types of glass have a viscosity in this range when the temperature of the glass is 600º to 800º C (Figure 6.1) [67-69].

Table 6.1 A description of materials at various viscosities.

Log_{10} (viscosity,Pa•s)	Description
1	melting point
3	working point (pressing, blowing)
4	flow point
6.6	softening point (Glass deforms visibly under its own weight)
10.5	deformation point (Glass deforms under its own weight on the μm-scale within a few hours.)
11 to 12.3	Glass Transition
12	annealing point (stress relieved in minutes)
14.5	strain point (stress relieved in hours)

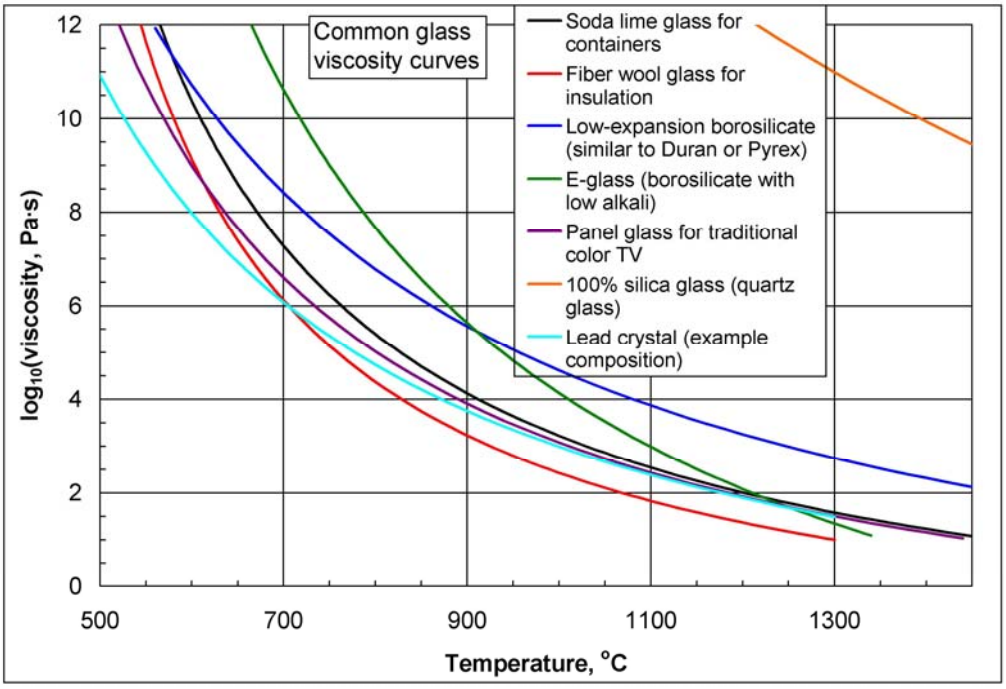

Figure 6.1 A graph of the viscosities of various types of glass as a function of temperature, taken from references [67-69].

Most monocapillary optics are made of borosilicate glass, which has a low thermal expansion rate, and is quite resistant to thermal shock. They can also be made out of high-lead glass, which has the advantage of having a larger critical angle for total external reflection, because of the lead content, but has the disadvantage of having a higher x-ray absorption and creates fluorescent noise from the lead L lines [70]. Table 6.2 gives a small list of different types of glasses, giving the type of glass, density, softening point, and the glass composition [70].

Table 6.2 A list of attributes and glass composition of a few different types of glass [70].

Type		soda lime	Boro-silicate	Boro-silicate	96% Silica	99% Silica	High Lead
Glass code		80	7050	7740	7900	7910	8870
Density (g/cm^3)		2.47	2.25	2.23	2.18	2.18	4.28
Softening point (Cº)		696	703	820	1500	1500	580
Weight percent (%)	SiO_2	73.6	67.3	80.5	96.3	99.5	35
	NaO_2	16	4.6	3.8	0.2	0	0
	K_2O	0.6	1	0.4	0.2	0	7.2
	CaO	5.2	0	0	0	0	0
	MgO	3.6	0.2	0	0	0	0
	PdO	0	0	0	0	0	58
	B_2O_3	0	14.6	12.9	2.9	0	0

The monocapillary optics at CHESS are made from straight cylindrical tubes of borosilicate glass. Table 6.3 gives a number of glass sizes we presently have available for the starting material[27]. The puller heats the glass to the point where it just starts to

[27] Table 6.3 Outlines the most used glass stock we have at CHESS (others are available in very limited quantities). Our most recent suppliers have been Pegisus Glassworks, Fredrick & Dimmock Inc. and Tecnolux Inc. Pegasus Glassworks, Inc. contact information: www. pegasusglassworks.com (Pegasus Glassworks, Inc. 66 Technology Park Rd. Sturbridge, MA 01566, attn: Peter Graves). Fredrick & Dimmock Inc. contact information: www.fdglasss.com (Fredrick & Dimmock Inc. 2127 Wheaton Ave.,

yield under tension, allowing the shape to be modified. The glass puller changes the shape of the cylindrical tubes of glass into an ellipsoid, and a few other shapes as well (section 9.12). The next section describes how shapes are programmed into the glass.

Table 6.3 A list of beginning glass sizes available to pull into monocapillary optics.

Manufacturer	I.D. (mm)	O.D. (mm)	Length (mm)	Quantity
CHI	1.60	3.00	1500	100s
CHI	1.39	3.04	1500	100s
CHI	0.228	2.015	1500	100s
CHI	0.204	2.028	1500	100s
Pegasus	0.90	3.00	1016	43
Pegasus	0.025	1.00	560	100s
Pegasus	0.050	1.00	960	100s
Pegasus	0.46	2.54	1066.8	44
Pegasus	0.48	2.54	1000	42
Pegasus	0.11	2.00	965.2	106
Tecnolux - Simax	2.40	4.00	1500	400
Pegasus	0.50	5.00	1500	19

6.2 Conservation of Mass for the Pulling of Monocapillary Optics

This section describes how the conservation of mass is used to make a desired shape out of glass. A cylindrical glass rod is pulled into a shape that includes a portion of an ellipsoidal shape. The desired ellipsoid shape is cut out and used as a single-bounce monocapillary optic.

Millville, NJ 08332 attn: Bob Geffredi) Tecnolux Inc. contact information: www.tecnolux.com (Tecnolux Inc. 103 14th St. Brooklyn, NY 11215 attn: Joe Paciulla)

The glass that we are drawing optics out of are not quite cylinders, they are tubes of glass; a cylinder with a hole down the center. Conservation of mass holds equally for the tubes of glass with a hole through the center. The ratio of the inner to the outer diameter of the glass drawn stays constant. This has been verified by sectioning and measuring the inner and outer diameter of the glass tube after a draw.

A furnace heats a section of the glass rod, to barely soften the glass. Axial tension stretches the softened glass rod into a rod with a smaller diameter. The stretching process is slow and therefore semi-static; the conservation of mass glass-drawing model is not dynamical. The volume of mass going into the heating zone equals the volume of mass of glass coming out. Dynamically, the ratio of the velocities into and out-of the heat zone sets the ratio of the glass diameters into and out-of the heat zone. If the ratio of the two velocities is constant, the diameter of the resulting small glass rod or fiber will be constant.

To shape the glass into other shapes including ellipsoids, the ratio of the velocities into and out of the heat zone has to precisely change during the draw. As the glass goes through the heat zone, a cylindrical section of the glass stretches into a truncated cone (Figure 6.2).

Equation 6-1 provides the derivation of what the ratio of velocities equal in terms of the radii of the input cylinder and the truncated cone, starting with the conservation of the volume of mass:

$$V_i = V_f$$
$$h_i \pi r_i^2 = \frac{h_f \pi}{3}(r_j^2 + r_j r_{j+1} + r_j^2) \qquad (6\text{-}1)$$
$$\frac{v_i}{v_f} = \frac{(r_j^2 + r_j r_{j+1} + r_{j+1}^2)}{3r_i^2}$$

Where 'V_i' and 'V_f' are the volumes in and out of the heat zone, 'v_i' and 'v_f' are the velocities into and out of the heat zone respectively, 'r_i' and 'h_i' is the radius and height of the cylinder going into the heat zone, and 'r_j', 'r_{j+1}' and 'h_f' are the radii and height of the truncated cone coming out of the heat zone. For the pulling to work, the difference between 'r_j' and 'r_{j+1}' has to be small; drawing glass using this model can not have any abrupt changes. The ratio of velocities in equation 6-1 needs to be changed into the frame of reference of the capillary puller (Figure 6.2 right side). The ratio of

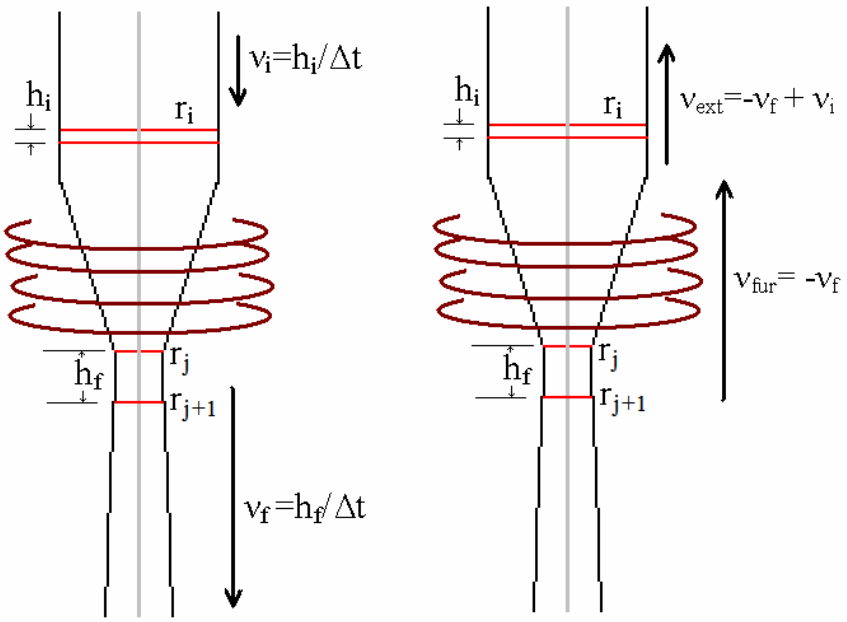

Figure 6.2 Two diagrams of pulling a glass rod into smaller diameter shapes. In the left diagram, the heat zone is stationary. In the right diagram , the reference is changed into the frame the capillary puller uses. The hottest part of the glass, in the furnace, corresponds to the narrowest point on the glass.

velocities is rearranged to give the step size the heat zone makes for a step size in the glass extension:

$$\frac{v_{fur}}{v_{ext}} = \frac{1}{1 - \frac{v_i}{v_f} + s_{fh}} = \frac{\Delta x_{fur}}{\Delta x_{ext}} \tag{6-2}$$

$$\Delta x_{fur}(r_i, r_j, r_{j+1}, \Delta x_{ext}) = \frac{1}{1 - \frac{(r_j^2 + r_j r_{j+1} + r_{j+1}^2)}{3r_i^2} + s_{fh}(r_i, r_j, r_{j+1})} \Delta x_{ext} \tag{6-3}$$

Where 'v_{fur}' and 'Δx_{fur}' are the velocity and step size of the heat zone, 'v_{ext}' and 'Δx_{ext}' are the velocity and step size of the glass extension, and 's_{hz}' is a heat zone height correction term. Using equation 6-3, a table can be created that gives the furnace position, by inputting an array of the desired shape's radii , for a given value of the glass extension. The heat-zone correction term has the form:

$$s_{hz} = \frac{h_{hz}(r_j - r_{j+1})(r_j + r_{j+1} + r_i)}{3h_i r_i^2} \tag{6-4}$$

where 'h_{hz}' is the heat-zone height. This term accounts for the volume of mass changing in the taper of the glass, within the heat zone. Figure 6.3 shows the glass at the beginning and the end of a draw. The volume of mass the heat-zone correction term corrects for the mass outlined is in gray. The heat-zone correction term is derived from how the truncated cone shape of glass in the heat zone changes during the draw. This term only accounts for the volume of this mass, and not where the glass is deposited. This term becomes zero for constant draws and becomes more important the steeper the

slope is. Functionally, the heat zone ranges from 5 to 12 mm, depending on the furnace height.

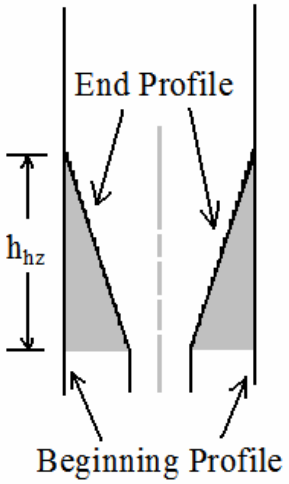

Figure 6.3 A diagram outlining the volume of glass accounted for in the heat-zone term (in gray). The cylinder is the beginning state and the taper at the end is the final state of the draw.

With the equations above, a furnace file is created (Appendix section D). For every extension of the softened glass, this file gives the position the furnace needs to be at in order to achieve the designed shape. The designed shape for monocapillary optics has two parts: an ellipsoid shape and a shape to match into an appropriate starting hollow glass cylinder (Figure 6.4). This shape is designed to have a smooth transition between the beginning glass diameter, and the desired ellipse shape, usually achieved with a spline fit. All transitions must be smooth for the model to hold. Please note that the puller is not constrained to only ellipsoidal shapes, it can make other shapes such as the mini toroidal mirror (section 9.12).

The values for the radius from the desired profile curve are fed into equations 6-2 and 6-3 to generate the relative velocity curve and the glass extension curve. These curves

show how the furnace position and the glass extension relate to each other in order to get the desired profile shape. For the case of a profile with a constant diameter, the velocity curve would be a straight line, and the glass extension curve would have a constant slope. The information in Figure 6.5, on the right side, is the furnace file. It gives the position of the heat-zone, within the furnace, as the glass extends. This is the information the puller needs in order to pull a desired shape into the glass rod.

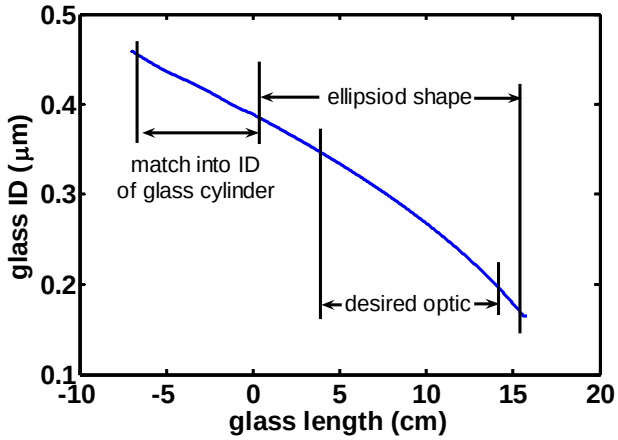

Figure 6.4 A desired profile curve used to create the furnace file for the fabrication of a 4 mrad, 50 mm focal length optic on the capillary puller. This figure outlines the sections of the draw: the section to match into the starting glass, the ellipsoid shaped, and the section of the desired optic.

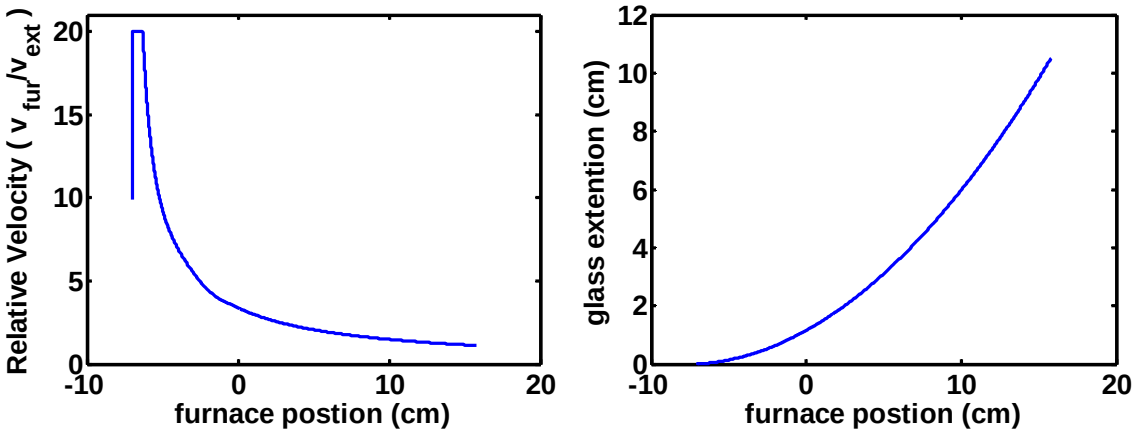

Figure 6.5 A relative velocity curve (left), and a glass extension curve (right) needed to pull glass into the profile shape in Figure 6.4. The relative velocity curve has a maximum value of 20, so that a pull will stay within the distance limits of the puller.

There is one last idea to be aware of when pulling an optic. The maximum achievable slope angle for the pull is:

$$\theta_{\max} = 2\tan^{-1}\left(\frac{ID/2}{h_{hz}}\right) \tag{6-5}$$

'θ_{max}' is the maximum monocapillary divergence angle that can be pulled, '*ID*' is the inner diameter of the glass, and again, 'h_{hz}' is the height of the heat zone. For typical heat zones of 5 to 12 mm, and inner glass diameters of 100 to 1000 μm, the maximum monocapillary divergence possible to pull ranges from 8 to 400 mrad (0.5º to 22º). As the pull gets closer to the maximum possible divergence, the less control the puller has. Pulling near this limit should be avoided if possible. These values have not limited optics we have pulled yet.

6.3 The Monocapillary Puller

The entire process to create a single-bounce monocapillary optic is:

- Design the optic (Chapter 3)
- Create a furnace file (section 6.2)
- Mount glass in puller and measure the initial outer diameter
- Pull the capillary into the desired shape
- Measure the final outer diameter
- Verify the optics performance in the X-ray beam (Chapter 4)

The functions that the capillary puller performs make up a large portion of the complete design to optic process; both measuring the outer diameter of the optic and pulling the optic.

The capillary puller has four main parts/functions:

- A tension stage for maintaining constant tension on the glass during a draw
- Motors for rotating the glass during a draw
- A furnace for heating the glass and a furnace stage for positioning the furnace.
- Optical micrometers for measuring the outer profile after the draw

Figure 6.6 shows each of the major parts of the capillary puller, and Figure 6.7 shows the flow chart of the information shared between the various components. Appendix section B.1 contains a list of parts, and selected mechanical drawings. An outline of the entire drawing process follows: A hollow glass cylinder is mounted in-between the tension stage carriage and the tension gauge with fishing line. When mounting, the glass cylinder is threaded through the center of the furnace, without the glass touching the furnace. The outer diameter of the glass is measured along the length of the glass, with optical micrometers mounted on the furnace stage before the draw. The tension stage keeps an axial tension of 100 to 300 grams on the glass throughout the draw. The rotation motors rotate that glass at about 5 to 20 rotations per minute; this keeps the resulting monocapillary optic straight. The furnace stage starts at a low position on the glass. As the furnace heats the glass, the glass stretches and the tension stage carriage moves up to maintain the constant tension. As the glass extends, the furnace stage also moves up, at a rate specified by the furnace file. During the draw the furnace stage moves faster than the extension stage, and at the end of the draw the furnace is at a high position along the glass. After the draw is complete, the drawn glass's diameter is measured along its length. The diameter measurement is used to evaluate the optic and the puller's performance.

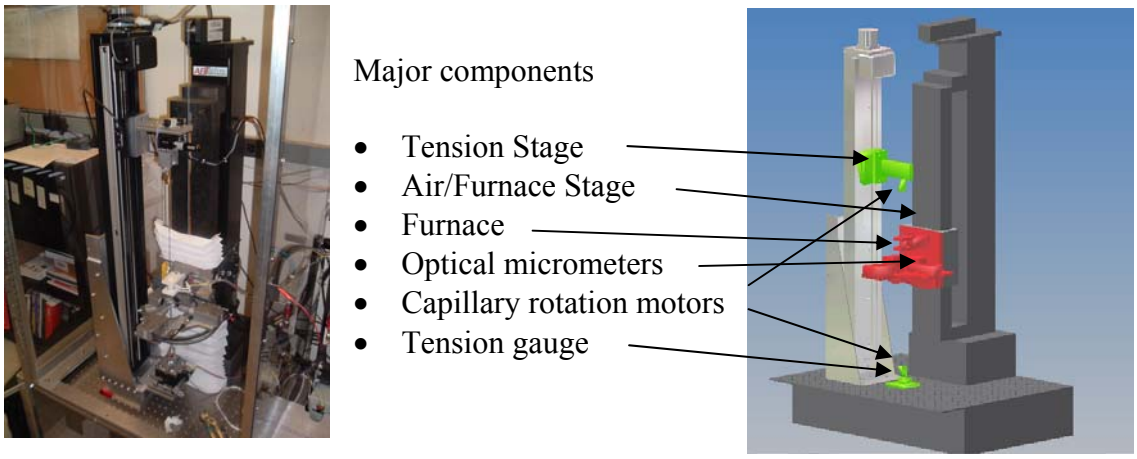

Figure 6.6 On the left is an image of the capillary puller. On the right is a diagram of the puller with the major components color-coded. The tension stage is in silver. The tension gauge, rotation motors, and the tension stage carriage are in green. The air/furnace stage is dark gray. The air stage carriage, the furnace, and the optical micrometers are in red.

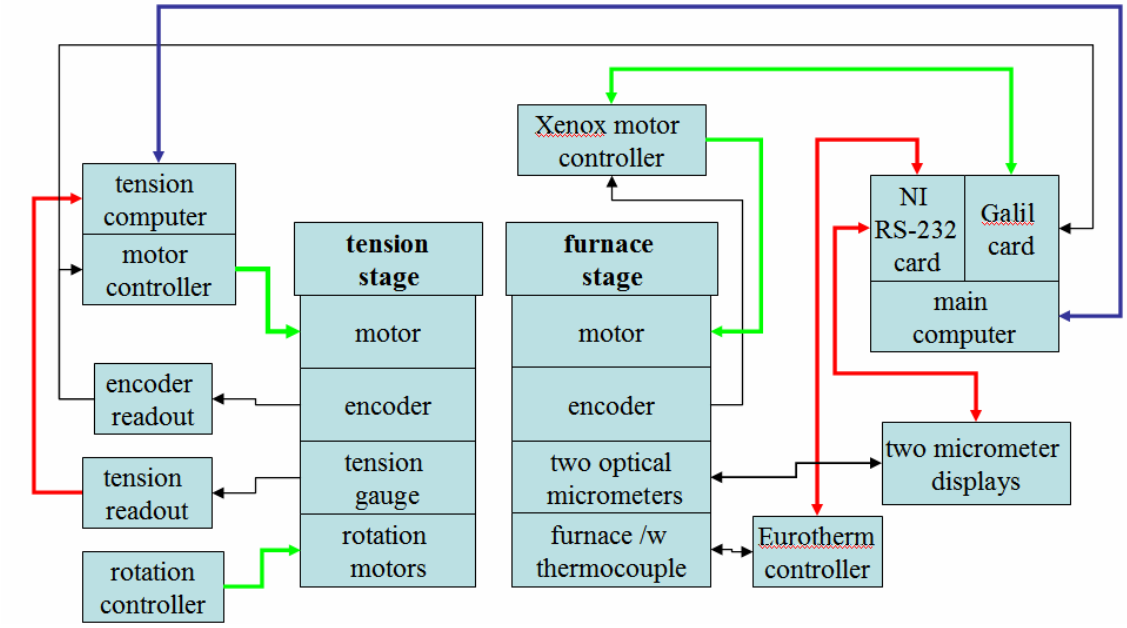

Figure 6.7 This flow diagram shows the flow of commands and information between the various parts. Red lines denote RS-232 connections, green lines for motor commands, the blue line is the Ethernet connection between the two computers and black lines custom cables. The puller is controlled by two computers, a tension stage computer (running the LabVIEW real-time operating system) the main computer (running the LabVIEW main puller program under Windows XP), which gives all the commands and recording all the information during the drawing process.

The capillary puller's resolution and accuracy for each of the functions needs to be high to fabricate and evaluate optics. The new puller has been built in an attempt to make better monocapillary optics (Figure 6.6 and 6.7). It has more control and higher accuracy than the previous monocapillary capillary puller. Most of the effort spent on the new puller has centered on achieving more accuracy and smoother running, in an attempt to reduce the monocapillary optic's profile errors, slope errors, and the centerline profile errors. Table 6.4 outlines some of the improvements in function the new puller has, compared with the old puller. A timeline of milestones for the new puller include: Summer 2004–work begins assembling components and writing the LabVIEW puller program, March 2005–it starts functioning, April 2005–the automatic Matlab monocapillary analysis program is in place, November 2005–the first high quality optic is pulled.

Table 6.4 A table of resolutions and precisions of both the old and new capillary pullers.

	Old Puller	**New Puller**
Glass extension resolution	49 μm /step	0.32 μm /step
Furnace position resolution	6.3 μm /step	0.1 μm /step
Furnace position precision	150 μm over 10 to 20 mm	5 μm over 50 cm
Tension pull variation	0.5 to 2.0 g	0.2 to 1.0 g
Tension gauge resolution	0.5 to 1.0 g	0.1 g
Temperature control	40º to 60º C (over the pull)	0.4º to 1º C
Profile diameter measurement	3 to 5 μm in~5 mm steps (takes hours)	1 μm in 10 to 100 μm steps (takes <30 min)
Computer Software	WinNT w/ Lab Windows	WinXP w/ LabVIEW (software feedback)

Capillary puller's hardware is controlled by the LabVIEW pulling program (Appendix section D). LabVIEW is a graphics-based programming language, which controls the monocapillary pulling process. Figure 6.8 outlines the main functions of the LabVIEW control program. The tension PID loop and the reasons for a separate computer to control the tension are covered in section 6.3.2.

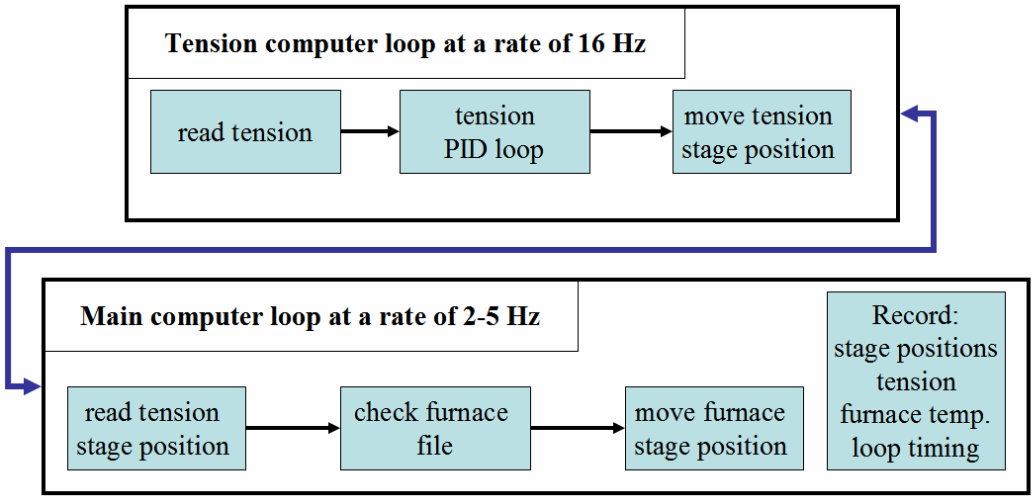

Figure 6.8 This flow diagram shows the main functions of the LabVIEW pulling program. The tension computer (LabVIEW run-time) keeps the tension constant by moving the tension stage, updated at a rate of 16 Hz (limited by the tension readout). The main computer (LabVIEW program under Windows XP) moves the furnace position in reference to the tension stage (dictated by the furnace file, see section 6.2), and displays the pulling operations and records all the pulling variables.

Both before and after the pull, a separate LabVIEW profile measurement program controls the optical micrometers and the furnace stage to scan the outer profile of the glass. Afterward, all the information from the design, the draw, and the profile measurements are evaluated using the Matlab monocapillary analysis program (Figure 6.9, Appendix section D). The optical micrometers and the analysis program are discussed in section 6.3.3.

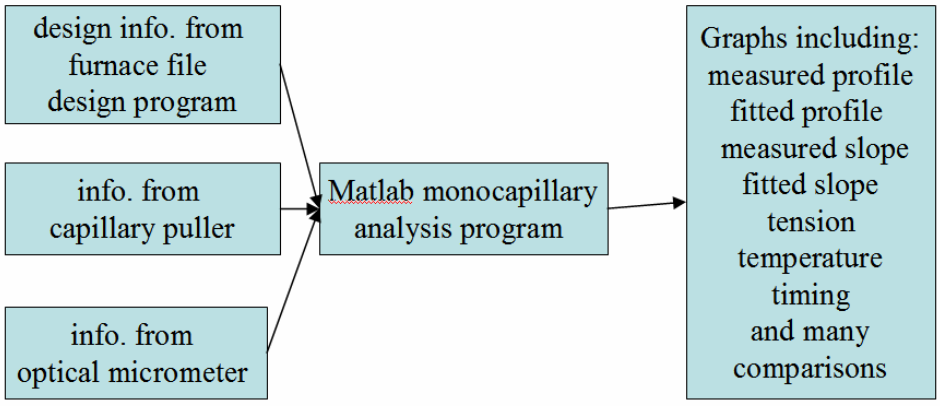

Figure 6.9 An outline of the Matlab analysis program which outputs 20-30 graphs. Graphs include the profile, slope, temperature, tension, motor positions, etc. Additionally, a number of comparison graphs are made in attempt to see how or if timing, tension, and furnace temperature fluctuations affect the drawn glass profile.

We have attempted to improve the monocapillary optics by improving the monocapillary puller. In many of our attempts, we mostly discover ways to make the monocapillary optics worse, not better. The new puller has only been able to produce moderately better optics than the old puller. The entire pulling process is rather an art, with identical draws giving somewhat different optics. If a particular design is needed, it takes about three to six draws to get one good optic. The next few sections emphasize the major parts of the puller giving the progression in function over the past few years.

6.3.1 Tension Feedback and Control

Keeping a constant tension on the glass is a major priority for the glass drawing process. Sudden jumps in tension result in the glass having an undesirable bobble in the profile. The glass is mounted vertically, with stiff non-stretching fishing line[28], between the

[28] Spiderwire®, Teflon® treaded fibers.

tension stage[29] and the tension gauge[30] (section B.2 of the appendix for details). The tension stage moves to keep a constant tension between the tension gauge and the stage.

The LabVIEW pulling program controls the capillary puller's hardware. The LabVIEW pulling program updates the tension stages position using the measured tension as a feedback. The program contains a programmable proportional-integrative-derivative loop (PID) [71]. The constants in the PID loop are manually tuned to attempt to keep the tension as constant as possible. The tension feedback equation for the puller is:

$$X_s = round\left(P_1 \Delta T\left(e^{P_2(\Delta T)} + e^{-P_2(\Delta T)}\right) + D\frac{X_{s-1}}{\Delta t} + I\sum_{n}^{s-1} X_n \Delta t \right) \qquad (6\text{-}6)$$

Where 'X' is the tension stage step size, rounded to an integer number, 'ΔT' is the desired tension minus the measured tension, 'Δt' is the time of the programming loop, both '$P1$' and '$P2$' are proportional gains, 'I' is the integral gain, and 'D' is the derivative gain. The derivative term is most influential on fast changing signals. The tension is not fast changing; the tension is constant so this term has little to no influence. The integrative term is most influential on long-term time scales, and corrects for an accumulated offset.

The proportional term makes the loop highly responsive for large values and minimally responsive for smaller values. In most standard PID equations, there is one proportional

[29] The Velmex stage has 36 inches of travel, with an encoder (one μm resolution), and stepper motor (0.32 μm minimum step size with the Velmex stage),. Contact information: www.velmex.com (Velmex Inc. 7550 State Route 5 and 20 Bloomfield, NY 14469 USA) Part numbers are in section B.1 of the appendix.

[30] We have two tension stages, with a 0 to 150 gram range and a 0 to 5 lbs. range. Contact information: www.transducertechniques.com (Transducer Techniques® 42480 Rio Nedo Temecula, CA 92590) Part numbers are in section B.1 of the appendix.

term. Because glass is a very stiff system, this had to be modified to keep a constant tension on the glass. At room temperature, a one-micron move on the tension stage increases the tension by 2-3 grams across the glass. The stage has a minimum step size of one step (0.33 μm). The step size needs to change by only a few steps in order to keep the tension within one gram. If the '*P1*' term was made much bigger, the tension would be unstable, and be manifested in oscillations around the tension set point.

The single proportional term '*P1*' is too weak for tension differences over ±5 grams. The second term is added to make the proportional term more aggressive for larger tension differences. The present form of the PID loop was created by trial and error; this form of the proportional term worked, therefore it was used. The left graph in Figure 6.10 shows the resulting tension with just the '*P1*' feedback and with both the '*P1*' and '*P2*' feedback during a draw. The two part proportional feedback is better at keeping the tension constant. The steps in the curves were intentional. They show how quickly the program responds to a new set point during a draw.

The proportional terms were not quite enough to get to the desired tension. By closely inspecting the left graph on Figure 6.10, a slight drop in the tension from 100 grams to about 95 grams can be seen about one hundred seconds into the draw. The integrative term corrects for this accumulated offset. In the right graph on Figure 6.10, the tension is held close to 100 grams axially across the glass for both draws.

A number of other influences affect the tension. Figure 6.10 shows the tension during a draw with and without a spring tied into the fishing line. This spring reduced the standard deviation of the tension across the glass by a factor of ten during a draw. Even

though the tension was closer to constant, all the optics pulled with the spring were bad. Every optic's far-field pattern pulled with the spring had swirling patterns (Figure 6.11).

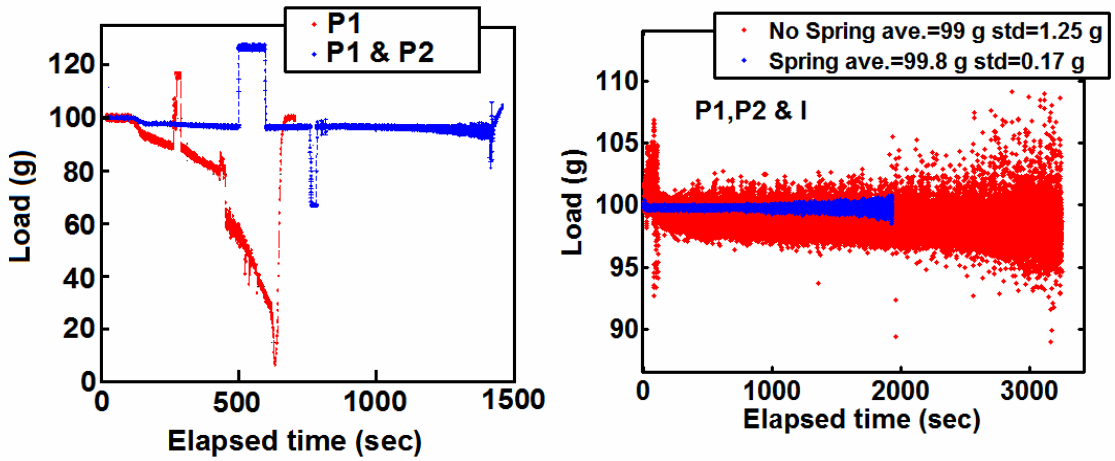

Figure 6.10 The left graph shows how well a draw maintains constant tension with just the 'P1' feedback term, and with both the 'P1' and 'P2' feedback terms. Steps in the curves were intentional to see how quickly the feedback responds. The left graph shows how well a draw maintains constant tension with the full PI loop, both with a small spring in the line with the drawn glass. The draw times change with the furnace temperature.

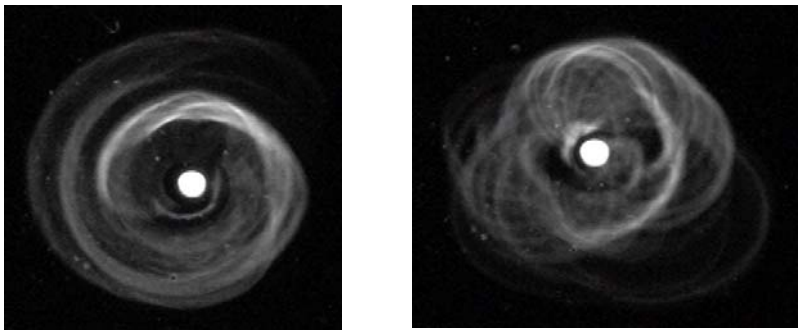

Figure 6.11 Two far-field images from optics pulled in line with a spring on the capillary puller. All the optics pulled with a spring were bad optics and had swirling far-field patterns.

The timing of the programming loop also affects the tension control. Functionality added to the capillary pulling program increases the complexity of the program. More operations, and more hardware inputs, introduce different timing schemes. The different timing schemes increase the time step in the tension loop, which adversely affects the tension control. Also, the Windows XP operating system on the controlling computer causes semi-random 4 to 10 second pauses; these pauses are bad for maintaining a constant tension and the entire pulling process as a whole. These pauses have been very hard to eliminate and have been an extreme source of frustration. To combat these issues, a computer running a LabVIEW Real-Time[31] operating system now controls the tension stage exclusively (Figure 6.7 and 6.8). This has freed the tension stage to run more quickly, while the main capillary program takes care of everything else, such as moving the furnace, and logging all the information from the pull. This has allowed for controlling the tension to a standard deviation of 0.8 to 0.1 grams (Figure 9.12). Before the LabVIEW real-time system, tension had standard deviations of 1 to 3 grams.

Also, the small motors[32] rotate the glass during the draw cause an oscillation in the tension as they spin. Rotating the glass rod keeps the resulting optic straight. The effect on the tension can be up to ±5 grams if the glass rod is slightly bent or if the glass is mounted crookedly. In order to combat this effect, two neck-down regions have been introduced into the pull. The furnace melts the glass rod in a small region above and below the pulling region, to release any strains in the glass and to help align the glass

[31] LabVIEW Real-Time is a computer operating system that allows for software programmable hardware. The operating system eliminates all other unwanted computer functions, doing only what you want the computer to do, allowing very tight control over the timing of operations (unlike the more user friendly windows XP).

[32] The small stepper motors rotate at a rate of about 10 rotations per minute. They have to have a 1 to 256 ratio gear reducer to do this. Contact information: www.micromo.com (phone 1 800 807-9166) Part numbers are in section B.1 of the appendix.

rod within the capillary puller. This helps the tension program hold a more constant tension over the draw of the rotating glass rod.

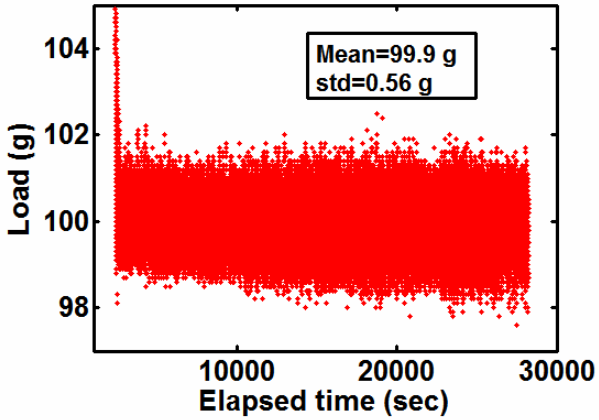

Figure 6.12 The tension for the pull of capillary A2_mr2f55_12 (pulled Oct. 2007) which used the constant tension program on a separate computer with a LabVIEW operating system.

It has taken a considerable amount of time to make the tension as smooth as possible. Having better tension control has not resulted in any large noticeable jumps in reducing profile and slope errors. A constant, smooth tension allows the puller to make some good optics, but we also have good optics pulled with less control on the tension, such as a drop in tension from 100 to 40 g. In general though, we have a much better chance of getting a good optic if the tension is well controlled.

6.3.2 The Furnace and the Heat Zone

The furnace[33] heats the glass and creates the heat zone, which lowers the viscosity of the glass in a small volume. The glass rod is threaded through the center of the furnace and does not make any physical contact with the furnace. The furnace is kept at a

[33] The furnaces we have been making are custom made at CHESS. Drawings are in appendix section B.3.

constant temperature, and the furnace stage[34] is positioned relative to the glass extension.

A number of things help keep the temperature constant within the furnace. The temperature needs to be controlled to under 1º C during the entire draw. For reference, a step in temperature of 10º C makes a large bobble in the glass profile. The furnace controller[35] tunes the furnace to a constant temperature using the furnace controller's internal PID loop. The PID loop uses a thermocouple, running along the inner wall of the furnace, as a feedback sensor. The controller has the ability to self-tune the PID parameters to run at a set temperature. The PID loop has to be tuned before a draw is attempted. This tuning usually needs to be done when the furnace is changed, or the temperature step point changes ±40º C or more due to a different type of glass or a large movement in the feedback thermocouple's position.

Additionally, an end-cap is placed on the top of the furnace. The end-cap allows the furnace to get to a higher temperature and helps to keep the temperature more constant, by limiting air movement through the furnace (the chimney effect). The end cap is a small ceramic plate, which has a hole through the center with a diameter close to the outer diameter of the glass rod. The end-cap is placed around the glass and over the hole at the top of the furnace, through which hot air can rise. It eliminates most of the air gap on the top side of the furnace. The glass rotates in the furnace to keep the glass straight. Rotating the glass rod evens out any slight heating gradients perpendicular to

[34] This stage is an air stage that has a granite rail with an air-cushioned carriage positioned with a linear motor. It has 20 inches of travel with a 0.1 µm resolution. It also has an encoder (0.1 µm resolution). Contact information: www.abtechmfg.com (ABTech, Inc. PO Box 10296, 126 Monadnock Highway, Swanzey, NH USA 03446 Tel: 603-358-6431)

[35] The Furnace is controlled with a Eurotherm 2404 controller. Contact information: www.faberinc.com (Faber Industrial Technologies,1111 Paulison Avenue,Clifton, NJ 07011 Tel: 212-947-4100 NY) Part numbers are in section B.1 of the appendix.

the glass rod along the furnace. All of these things combine to give a constant temperature within the furnace during a draw (Figure 6.13).

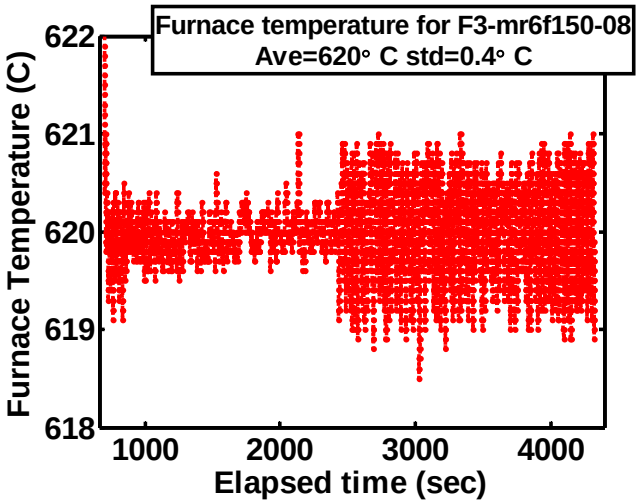

Figure 6.13 A graph of the temperature within the furnace during a one hour draw. The temperature is kept within ±0.5° C. The temperature often has two states of control, which can be seen in this figure. We are not able to control this state change, but it does not noticeably affect the optical profile.

In addition to holding a temperature, the correct drawing temperature has to be found. In a range of 30° C, the glass can go from taking several hours to pull, to becoming too soft to pull. Every time the type of glass changes, the furnace changes, or the thermocouple used for feedback moves, the temperature set point changes. The set point is found by trial and error, within the right range of ±20° C for pulling optics.

The attention will now be turned to the design of the furnace. The furnace that heats the glass is small. The inner diameter of a typical furnace is 0.6 cm and about 3 cm in length (Figure 6.14 see Appendix section B.3 for diagrams). Inside the furnace, an electrical current flowing in a coiled nichrome wire heats the furnace. Changing current in the wire alters the heat load. The entire outer housing of the furnace is made of Macor®, a machinable ceramic. The nichrome wire is wrapped around the furnace's

alumina inner core[36]. Figure 6.14 gives the temperature gradient along the axis of the furnace. A scaled sketch of the furnace is drawn on the graph to reference the temperature gradient with a furnace position.

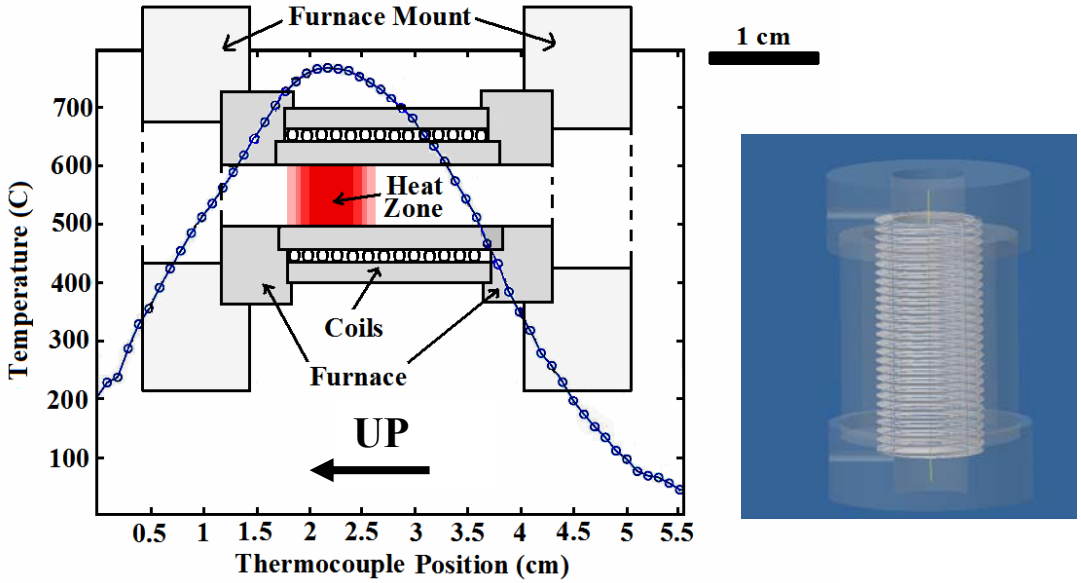

Figure 6.14 On the left is a graph of the temperature profile through the center of the furnace. An on-scale sketch of the furnace is placed on the graph to outline the position of the temperature profile in relation to the furnace position. On the right is a 3D schematic of the furnace.

There is a difference between the heat zone and the furnace gradient. The neck-down region on the glass defies the heat zone (Figure 6.3). The furnace causes this heat zone with an extended temperature gradient much larger than the heat zone. The size of the heat zone greatly affects the profile of the resulting optic. The furnace most often used creates a heat zone on the glass of about 11 to 12 mm in length. The resulting oscillations in the profile, which are most easily seen in the slope error, have a wavelength ranging from 12 to 20 mm (Figure 6.15). Identical pulls were made with a furnace that had half the number of coils. This furnace creates a heat zone of about 6 to 7 mm; about half the size of the regular furnace. The resulting oscillation in the slope

[36] The furnace gets hot enough to damage the inner core, if it is made of Macor®.

error has a wavelength ranging from 8 to 10 mm (Figure 6.16). Additionally, the half furnace created optics with slope errors 30 to 50 μrad higher than the regular furnace.

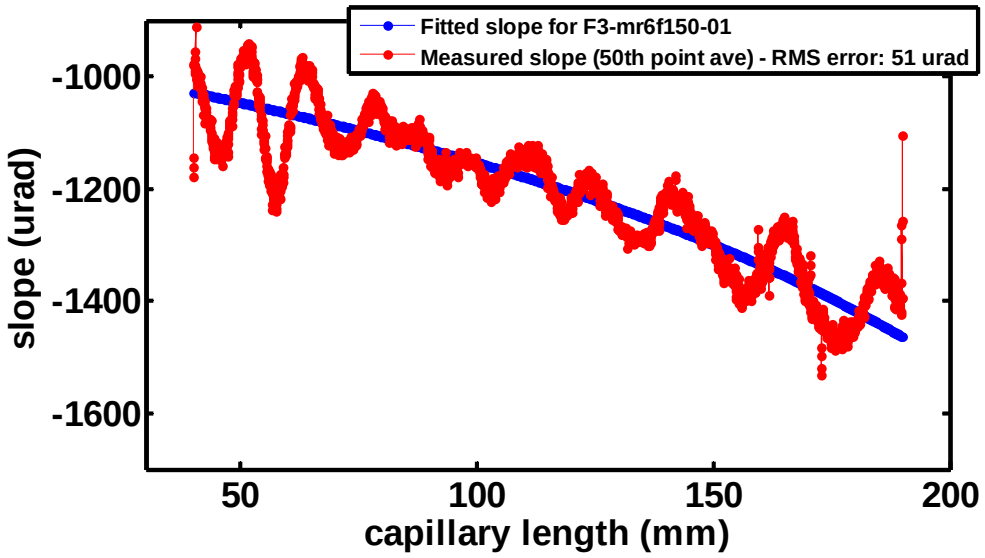

Figure 6.15 The outer diameter slope error of a monocapillary pulled with a regular sized furnace, with a heat zone of about 11 to 12 mm. The slope error wavelength is about 15 mm.

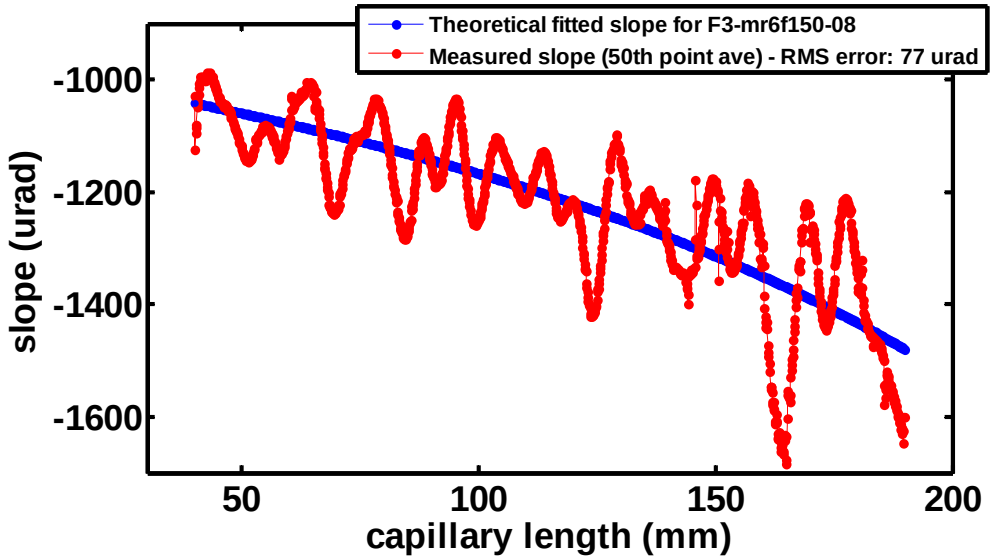

Figure 6.16 The outer diameter slope error of a monocapillary pulled with a half sized furnace heat gradient, with a heat zone of about 5-6 mm. The slope error wavelength is about 7-8 mm.

Of the many parameters explored on the puller, the size of the heat zone is one of the few experiments that produced definitive results. A shorter heat zone created by the furnace always creates a shorter wavelength in the profile error oscillation. The oscillation in the slope error profile is always between one to two times the size of the heat zone. The size of the heat zone strongly affects the short wavelength profile errors. This effect has also shown to be consistent over a range of pull times and pulling temperatures. Specifically, a pull that took less than an hour looked almost identical, with the very same errors in the slope, to a pull that took four hours.

6.3.3 Optical Scans and Metrology

On the same stage the furnace is mounted, two optical micrometers are mounted as well. The optical micrometers measure the outer diameter of the glass along the length of the glass, while the glass is mounted in the puller. This has been a key development for the new capillary puller. It has given new insights in both capillary puller and in monocapillary optics.

Previously, the outer diameters of the monocapillary optics were measured on an Olympus microscope equipped with a digital read-out, manually positioned stage. The optic's diameter was measured in 30 to 40 positions along the length of the monocapillary optic by hand positioning the optic with the stage. This technique took 2-3 hours and was prone to human errors of positioning, entry of data, etc. Also, the diameter measurements were coarse, taken only every 3 to 6 mm, which missed the short wavelength oscillations.

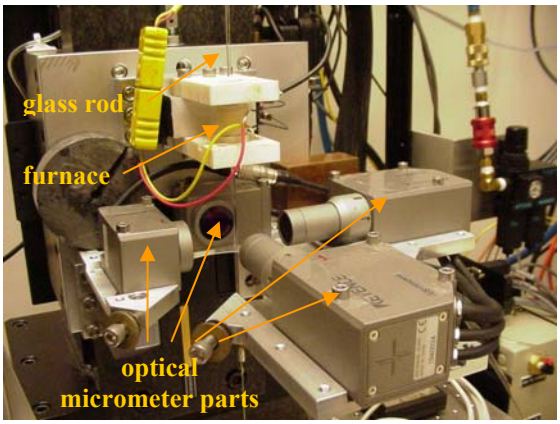

Figure 6.17 An image of the air stage carriage with both the furnace and the optical micrometers attached to it.

We now use the optical micrometers as opposed to the Olympus microscope (Figure 6.17). The Keyence® LS-7010M optical micrometers[37] has a measuring range of 0.04 to 6 mm, a measurement accuracy of ±0.5 μm, and a repeatability of ±0.06 μm. This allows for measuring the outer diameter of the glass rod before and after the pull, along the glass by positioning the furnace stage at a step size of 1 to 10 μm, using the LabVIEW profile measurement program (see Appendix D). The measured outer diameter profile can be used to estimate the inner diameter profile. The pulled inner and outer diameters ratio equals the same inner to outer diameter ratio of the original glass rod. From the profile scan, the profile, slope, and centerline errors of the optic are estimated, down to the level below one micron rms. Figures 3.1, 7.1, and 7.5 show examples of profile scans and Figures 3.2, 6.13, 6.14, and 7.6 show examples of the slope of the glass surface calculated from the profile scan.

Figure 6.18 outlines a simplified explanation of how the optical micrometers function[38]. An object is placed in a collimated beam of green light, casting a shadow on a detector.

[37] Contact information: www.keyence.com (Keyence Corporation of America Corporate Office, 50 Tice Blvd., Woodcliff Lake NJ 07677, Phone: 1-201-930-0099)
[38] Appendix section B.4 gives a more detailed schematic of the optical micrometer's design.

The detector measures the distance from the detector's edge to the shadow's edge, giving both the position and the diameter of the object.

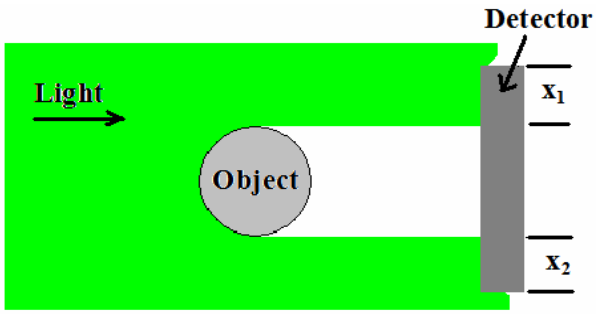

Figure 6.18 A simplified drawing of how the optical micrometer measures distances using the object's shadow.

The raw scans are modified in order to be useful. The Matlab monocapillary analysis program (appendix D) aligns and rotates the raw scans, to match them with the designed profiles, created with the furnace file program. Additionally, the information gathered during the pull, such as the time, temperature, tension, position of the furnace, position of the extension stage, etc, are all aligned and compared with the glass profile. The analysis program displays a series of 20 to 30 output figures, in an effort to find any correlations between a number of pulling variables and the resulting monocapillary optic's profile. A key feature of the analysis program is that it is fully automatic. The user simply clicks one input file, and the program finds all the needed input files, and produces all the figures.

A few problems have arisen in efforts to have accurate profile scans. There are sometimes adverse vibrations on the air stage, upon which the optical micrometers are mounted. A linear motor with magnets every three centimeters positions the air stage. The stage sometimes has vibration problems when driving the linear motor. This tends

to put glitches in some of the profile scans every 3 cm. This same problem may sometimes affect the furnace positioning during a pull as well.

In addition, some small dust particles on the outer surface of the glass sometimes give false diameter readings, resulting in spikes in the measured profile. A few of these spikes can be seen in Figures 6.15 and 6.16. The glass has to be cleaned before scanning to eliminate the most severe problems. Additionally, the analysis program has a reasonable spike-reducing feature that eliminates almost all of spikes still in the scans.

Changing the profile scan into a slope error scan is the last problem that has arisen with the profile scans. Spikes in the profile scan negatively affect the slope error measurements, therefore slope error measurements really need spike-free profiles to be useful. Additionally, the profile can be measured with a repeatability of ±0.06 μm. This sets a limit on the errors in the slope measurement. We usually scan the profiles in 5 to 10 μm step sizes. For a 10 μm step in the profile scan, the slope error due to the repeatability could be as large as 6000 μrad, which is much higher than the range we would like to measure. In order to get around this, we calculate the slope errors averaging 50 points together, and using just every 50^{th} point to calculate the slope. This has helped to get values that are more reasonable for the outer slope errors, and ones that are in approximate agreement with the slope error measurements from x-ray beam experiments, from both far-field and spot size measurements. Both this problem and the solution are not completely verified; it will need some additional effort to fully understand. Section 6.4.1 shows that a non-averaged estimated inner slope error may be adequate for measuring the slope error.

At what level of accuracy are the optical micrometers measuring? This is a question we have had from the beginning, and this question has been partially answered by section 6.3.3. This section discusses a ray-tracing model based on the measured profile, simulating far-field patterns. From these simulations, I believe the optical micrometers are measuring differences in the profile at the level of ~0.2 μm. I have come to trust the optical micrometers; I believe they give very accurate profiles.

Another test compares the optical micrometers to the outer profiles of our optics measured on an optical profilometer[39]. The optical profilometer measured outer profile errors of 0.8 to 1.7 μm rms to the best-fit ellipse, and 2 to 9 μm rms to the designed ellipse. In the test done with the puller's optical micrometers, the outer profile measurements were close to this, measuring 0.8 to 1.1 μm rms, for the best fit ellipse.

In the end, this new method for deducing the shape of the optics has been a very valuable tool. It has helped us quickly assess most of problems with the puller. It has proven to be a good preliminary test of single-bounce monocapillary optics. Most of the information in the next section comes directly from the profile scans.

6.4 Limitations in Fabrication

How well has the new puller performed? Originally, we hoped that the new puller would be able to produce optics with slope errors below the 10 μrad level; that goal has not been reached. The new puller has pulled better optics. One direct comparison of the improvement is between PEB605(old puller) and PEB_mr8f55_02(new puller), which are identically designed optics. PEB_mr8f55_02 produces smaller spot sizes,

[39] Proprietary work-more details cannot be given here.

and has a slope error almost half that of PEB605 (Tables 4.1 and 6.6). The following sections cover our continuing attempts and insights in achieving optics with smaller profile errors, slope errors and centerline straightness errors.

6.4.1 X-ray Test and Puller Test Comparisons

The optical profile scans compared to the x-ray tests of monocapillary optics have given insights into what makes a better optic. Table 6.5 outlines all the optics pulled on the new puller up to January 2008. This table gives an overview of how successful the new puller has been in making good optics. About 16% of the all pulled optics are good. About 32% of the optics that preliminarily look good end up being verified as good optics by the x-ray beam tests.

Table 6.5 The left table summarizes all the pulls performed with the new puller. The right table summarizes the results of all the x-ray optic tests performed at CHESS's G1 station. Not testable optics (at the G1 station) includes 'football capillaries' (section 7.2.2), and the creation of mandrel substrates (section 7.2.1).

	number	percent
Total pulled	141	100%
Not testable optics	20	14%
Untested	5	4%
Bad: not x-ray tested	30	21%
Total tested in x-rays	86	61%

16% of the total pulled optics are good

	number	percent
Total tested in x-rays *	70	100%
Good	22	32%
Marginal	18	26%
Bad*	30	43%

*removed spring errors

Table 6.6 summarizes the general trends between the x-ray tests and the puller metrology. This table is full of information, and that information needs defining in order to read. The x-ray beam test is the defining test for the optic, measuring the spot size, gain, and recording the far-field pattern (sections 4.1 and 4.2). I have divided the optics tested in the beam into three categories, good, marginal, and bad, defined below:

- Good: small x-ray spot and a mostly uniform far-field pattern. These optics I fully trust to use in microbeam x-ray experiments.
- Marginal: moderately larger spot sizes and/or a semi non-uniform far-field pattern. These optics I will only use in microbeam x-ray experiments if I have no other options.
- Bad: very broad or distorted spot sizes and have a non-uniform far-field pattern. These optics I will never use in microbeam x-ray experiments.

Each of these can be broken down into subcategories:

- Bent: they have a 'bent' far-field image, either slightly or severely. Examples of bent far-field images include the center and right far-field patterns in Figure 4.4. They sometimes can be straightened by modifying how they are mounted in a capillary stage's V-groove (section 7.3).
- Bendable: These optics are too flexible and can too easily be straightened or bent. The beginning glass rod needs a larger outer diameter to inner diameter ratio to stiffen the optic.

- Twisted: they have a 'twisted' far-field pattern, either slightly or severely. Examples of twisted far-field images include the left far-field patterns in Figure 4.4 (the left top pattern has a very slight twisted far-field pattern).

There are a few others that are good optics that have an odd design, such as a toroidal mirror, and a few optics pulled from a glass rod with a slightly different inner diameter than specified by the design. There are several bad optics tested that had a spring in line with the glass during pulling[40]. All of these optics are bad (Figure 6.8).

The analysis program that goes with the capillary puller also evaluates the optics. It gives predicted values for the outer diameter profile error, the centerline error and the outer diameter slope error of the optic. Table 6.6 includes these values, which I have also broken down into four categories good, marginal, bad, and null, defined below:

- Good: An outer profile error from 0 to 2 μm rms, an averaged outer slope error from 0 to 70 μrad rms, and a centerline error from 0 to 2 μm rms.
- Marginal: An outer profile error from 2 to 4 μm rms, an averaged outer slope error from 70 to 120 μrad rms, and a centerline error from 2 to 4 μm rms.
- Bad: An outer profile error over 4 μm rms, an averaged outer slope over 120 μrad rms, and a centerline error over 4 μm rms.
- Null: data not available

In addition to the analysis program, I have included whether the optic was rotated during the draw, and whether the glass twisted during the draw. The twist is measured

[40] At the beginning of operation of the new puller, all the monocapillary optics pulled with a spring. This resulted in many bad optics because the spring was not removed until the optics were tested in the X-ray beam, and the source of the error (the spring) was identified.

by aligning two small tape flags on the top and the bottom of the glass rod before the draw, and observing how far the glass twisted during the draw by how far the small flags became unaligned. In the table, the results of the x-ray tests are compared with the results from the puller tests.

Table 6.6 This table shows how the optic's x-ray beam test compared to some of the pulling parameters and the analysis program. In the table heading, g is good, m is marginal, b is bad, n is null, y is yes, and n is no. The numbers represent the number of optics that have that characteristic; the good ratings are highlighted in green, marginal in yellow, and bad in red.

X-ray test evaluation	Total tested in x-rays	profile error g/m/b/null	slope error g/m/b/null	centerline error g/m/b/null	rotated? y/n/null	twisted? y/n/null
good	10	5/5/0/0	7/3/0/0	9/1/0/0	9/1/0	2/8/0
good(bent)	6	5/1/0/0	5/1/0/0	3/2/1/0	5/1/0	1/5/0
good(twisted)	2	2/0/0/0	2/0/0/0	2/0/0/0	2/0/0	1/1/0
good(odd design)	5	5/0/0/0	3/1/1/0	4/0/1/0	5/0/0	0/5/0
marginal(bent)	4	4/0/0/0	2/1/1/0	1/1/2/0	3/1/0	0/4/0
marg.(bendable)	11	6/2/0/3	8/0/0/3	5/3/0/3	10/1/0	0/11/0
marginal(twisted)	3	1/2/0/0	3/0/0/0	3/0/0/0	1/2/0	3/0/0
bad	2	0/0/1/1	0/1/0/1	0/0/0/2	0/0/0/2	0/0/2
bad(bent)	21	10/7/2/2	14/2/3/2	5/3/11/2	10/11/0	1/18/2
bad(twisted)	7	4/1/1/1	3/1/2/1	2/1/3/1	5/2/0	4/3/0
bad(spring)	16	2/6/8/0	9/5/2/0	4/1/2/9	7/0/9	2/3/11
total tested	86					

This table shows what is important to look at when pre-evaluating the optics. First, if both the profile error and the slope error are good, it does not give a strong indication for a good x-ray optic. Almost all the good, marginal, and bad optics have either a good or a marginal profile/slope error. If the profile or slope error is bad, the optic is seldom worth testing. Many of the untested bad optics were easily eliminated by bad slope or profile errors, thus, they never were tested in the x-ray beam to begin with.

The next strong correlation is between the x-ray tested 'bent' optics and whether the optic was rotated during pulling. First, if the optic is not rotated, it has a very good chance of being bent, and most likely will be bent severely. Most of the non-rotated optics are marginal or bad. We have made two good optics that were not rotated during the pull. Both were short, making bending the optic while drawing less of an issue. Rotation is critical for producing good optics.

There is also a good correlation between the x-ray tested 'bent' optics and the centerline error test from the puller metrology. If the optic has a bad measured centerline, it will be bent, and will very likely be a bad, bent optic. This does not catch all the bent optics however. The x-ray beam-line tests found 21 badly bent optics, the centerline test from the puller said 5 to 8 of these optics were good. If the centerline error is above 4 μm rms, the optic will be bent, and most likely be a bad optic.

The next strong correlation is between the x-ray tested 'twisted' optics and whether the optic twisted during the draw. Whenever the optic has a twisted far-field pattern, there is a large chance that the optic twisted during the draw. This holds true for even the good optics in the top column. For example, capillary f1b-mr9f20-01, considered a good optic, shows slight signs of a twist in its far-field pattern (Figure 4.4, top left). In the x-ray test evaluation bad 'twisted' row are three untwisted optics according to the 'twist' notes taken during drawing. I suspect that these are mislabeled; our diligence in testing for twisting was not a high priority in the past year, and all the 'not twisted' optics come from that period. If the glass twists 90º or more during the draw, it will likely result in a marginal or bad optic.

Another very important question is how the slope errors predicted with the optical metrology compare with the evaluated slope errors. For all of the evaluations done on the puller, the outer profile was used for the profile errors and the slope errors. Table 6.6 gives a few of the good optics, listing their x-ray estimated slope errors and the puller estimated slope errors, both on the outside and the inside surface of the optic. I give the outer profile and slope errors for continuity between Tables 6.6 and 6.7. The relation between the inner and the outer profile errors almost scales with the ratio of the outer to inner diameter of the glass used to make a monocapillary optic. For the good optics, the puller estimated a non-averaged inner slope error, and the averaged outer slope error were reasonably close to the x-ray beam-line test's estimated slope error, estimated with the capillary design program.

One interesting feature in the table is the x-ray estimated slope errors get closer to the puller estimated non-average inner slope errors when a smaller section of the optic is used. I believe the slope error measurements may be missing effects such as a bent or twisted optic that affects the entire inner surface of the optic. Using a smaller portion of the optic achieves a smaller localized slope error.

In the end, the optical profile scans have given a large number of insights into the x-ray beam-line tests of monocapillary optics, and vice versa. The profile and slope errors measured with the optical micrometers agree reasonably well with the good, x-ray tested single-bounce monocapillary optics.

Table 6.7 A table comparing the estimated slope errors of the x-ray test with the estimated slope errors from the puller's pre-analysis program, for the outside surface slope, both non-averaged and averaged, and the estimated inside slope, both non-averaged and averaged. The agreement between the x-ray tests and the estimated non-averaged inner slope errors (highlighted in green) is satisfactory. The table also gives the puller's estimated outside and inside profile errors, and its centerline profile error.
*** The spike reduction was not quite adequate in one direction. I trust the smaller values.**
**** Far-field patterns in Figure 4.4**
***** X-ray estimated slope error using just a portion of the inner surface.**
****** The air-stage carriage vibrations caused an error in the centerline measurement one direction.**

	PEB605 (old puller)	PEB-mr8f55-02	f1b-mr9f20-01	f1-mr9f20-02	G1c-mr4f50-09
X-ray rating	good	good (bent)	good	good	good (bent)
X-ray est. slope err. (µrad rms)	100	60	90-120 50***	120 120-50***	60
Puller est. slope err. outside(non-ave. /ave. in µrad rms) inside(non-ave. /ave. in µrad rms)	not tested	440-200* /~45 130-60* /~12	~340 /~60 ~55-70 /~10	340-120 /~45 61-30 /~9	430 /30-40 80 /~8
Puller est. profile err. µm rms outside Inside	not tested	~3.0 0.9	1.2-2.0 0.3	1.5-1.0 0.3-0.2	0.9-2.2 0.2-0.4
Puller est. centerline err. µm rms (in two directions)	not tested	1.1-2.0	0.4-1.0	1.0-none****	1.0-3.6
Far-field comments	straight	slight bend**	slight twist**	slight twist**	slight bend

6.4.2 Effects of Temperature and Tension on Optical Fabrication

How does the furnace temperature and tension affect the quality of the optics? A sudden change in either the tension, such as a 10 gram jump, or the temperature, such as a 10º C jump, will make a noticeable bobble in the profile. When the temperature and the tension are constant, we cannot find any strong effects. Almost all the optics tested were pulled under the conditions of constant tension and furnace temperature described in sections 6.4.1 and 6.4.2. The quality of the optics does not show any strong correlations to changes in these variables.

Even a non-constant temperature or tension can still make a good optic. The old capillary puller ran the furnace under constant current through the heating coil. This resulted in the old puller having the temperature rise smoothly by 40º to 60º C over a pull. The old puller made some good optics under this condition. We have one good optic (SC-mr6f50-08) pulled on the new puller where the tension smoothly dropped from 100 grams to 40 grams over the pull. This gives strong indications the quality of the fabricated optic is weakly linked to the tension or the furnace temperature, as long as the tension and temperature are constant or smoothly varying. I do believe that a constant tension and temperature are the best conditions for making good single-bounce monocapillary optics. I do not believe controlling the furnace temperature and the tension on the glass to higher degrees of accuracy will make optics with significantly smaller slope and profile errors.

The temperature set point seems to have some effect on the quality of the monocapillary optics. Figure 6.19 shows the number of good, marginal and bad optics as a function of the time it took to complete the pull. Effectively, this also shows the temperature of the pull, higher furnace temperatures translate into shorter pull times. This figure shows a preference for good optics with higher temperature pulls, with pull times less than an hour. This is not conclusive; there is also a far fraction of good optics with longer pull times as well.

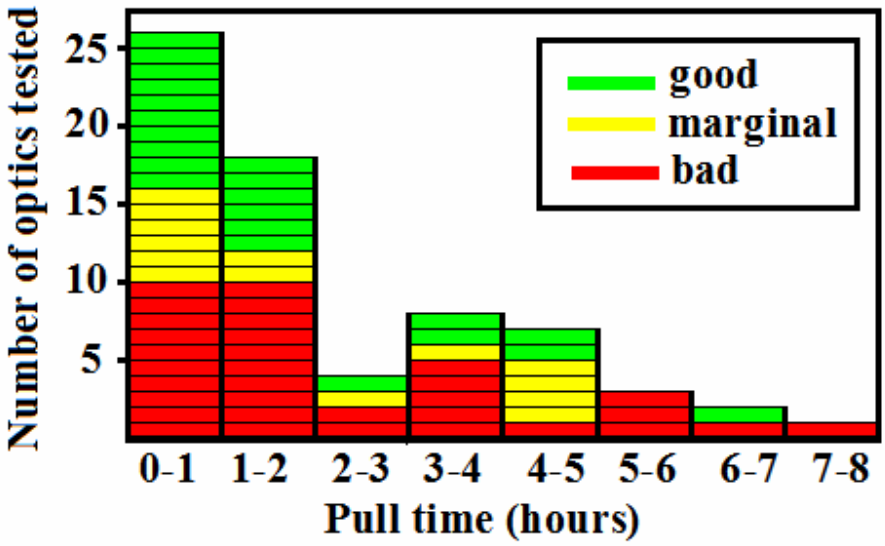

Figure 6.19 A graph of the x-ray tested optics' quality as a function of the time taken to complete the pull. Good optics are in green, marginal in yellow, and bad in red.

6.4.3 Correlating Optical Scans with Far-Field Patterns

The profile and slope error scans have shown to coordinate with the far-field image seen in the x-ray tests. In most far-field images, the reflections make a series of rings. The number of rings in the far-field image has tended to be the same as the number of wavelength humps in the slope error, measured with the capillary puller's optical metrology[41].

A ray tracing simulation was created to simulate far-field images from simulated optical profiles[42] (see Appendix section D). It was also created to give us more insights into how far-field images evolve as a function of distance, and investigate if the slope errors can be quantitatively measured from the far-field images. This program represents a step in that direction. In the program, a perfect ellipse shape is deformed by adding on two small amplitude sine waves. The sine waves mimic the slope and profile error of a real optic. The source is an ideal point source, and rays are made in one millimeter steps along the entire length of the optic. The rays are ordered by color: red ones reflected from the tip, yellow in the middle, and violet from the base, etc, in the predicted far-field map in Figures 7.20 and 7.21.

Capillary PEB_mr8f55_02 was chosen to simulate because its far-field pattern is full of features and spread out. The real optic had an inner profile and slope error of 0.9 μm rms and 60 μrad rms, respectively, measured by the capillary puller's optical metrology. The simulated sine waves chosen produced a profile error of 0.7 μm, and a slope error of 50 μrad, which is a fairly close match[43]. The simulated far-field pattern has features

[41] Compare the bottom graph and the bottom far-field image in Figure 6.20.
[42] Created by Courtney Couvreur, on an RET summer program at CHESS.
[43] Compare the top and bottom graph of Figure 6.20.

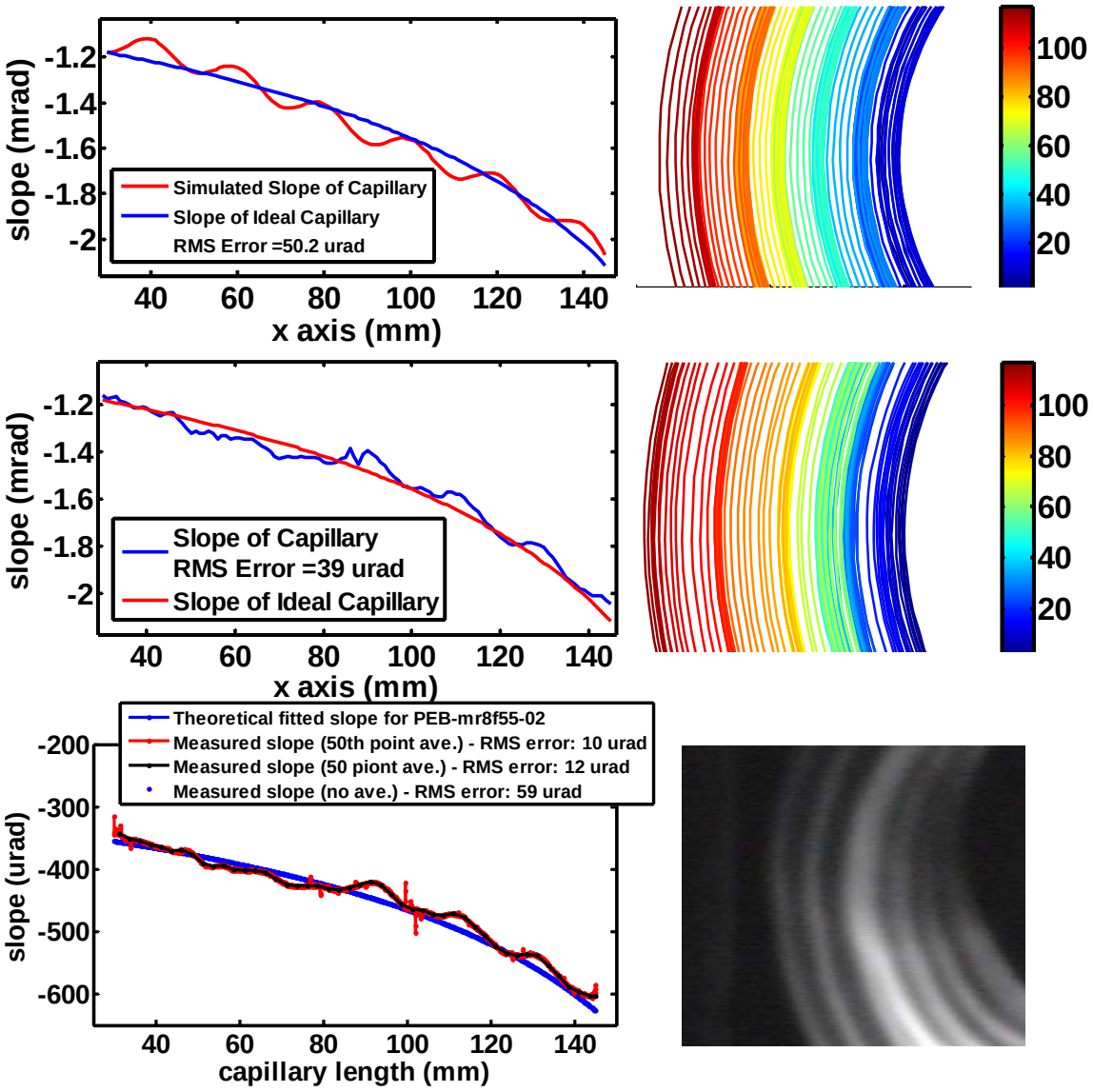

Figure 6.20 This is a series of slope profiles with their corresponding far-field patterns. The top graph and far-field simulation come from two sine wave deviations placed on a perfect ellipse, with a 120 and 20 mm wavelength, and with a 1.0 µm and 0.15 µm amplitude respectively (the long wavelength oscillation is harder to see than the shorter wavelength oscillation). The center graph and far-field simulation come from the measured profile put into the ray tracing simulation. The bottom graph and far-field image are the measured slope profile and the x-ray image of the far-field pattern (The full pattern is in Figure 4.4). For the simulated far-field patterns, only a portion of the far-field is viewed to focus on the details. The color represents x-ray coming from the base (blue) to the tip (red).

that are remarkably similar to the real far-field pattern[44]. The rings of intensity are caused by the smaller wavelength variations of about 20 mm along the inner surface of the optic. In the simulation, if the wavelength of the short oscillation is changed, the number of rings in the far-field pattern matches the number of oscillations along the length of the optic.

In the simulation, the far-field screen position can be shifted to the focal position to give an estimated spot size (Figure 6.21). Each different sine wave error was eliminated in turn to determine which wavelength error on the profile creates the largest effect on the spot size. Table 6.8 gives a synopsis of the calculated spot size results in Figure 6.21.

Table 6.8 A showing the effects of both the long and short wavelength profile errors on the ray tracing program's simulated spot size. Both the long and short wavelength profile errors, contribute equally to the slope error of the optic.
*** Small non-diffraction limited simulated spot size from a point source. The diffraction limited spot size is ~ 16 nm at 10 keV (equation 3-1).**
**** Results for the measured profile curve of PEB-mr8f55-02 in the ray-tracing program. The puller profile gave a 0.9 µm rms profile error and a 60 µrad slope error. The estimated spot size is consistent with measured x-ray spot sizes (Tables 4.1 and 4.2)**

Profile contributions	maximum amplitude µm	wavelength mm	profile error µm rms	slope error µrad rms	estimated spot size µm
ellipse +longwave+shortwave	1.0 & 0.15	120 & 20	0.7	50	20-25
ellipse +longwave	1.0	120	0.7	38	10-15
ellipse +shortwave	0.15	20	0.11	33	10-15
ellipse	0	0	0	0	4 nm*
PEB-mr8f55-02** measured profile	-	-	0.6**	39**	15-20**

[44]Compare the top simulated far-field image and bottom real far-field image in Figure 6.20.

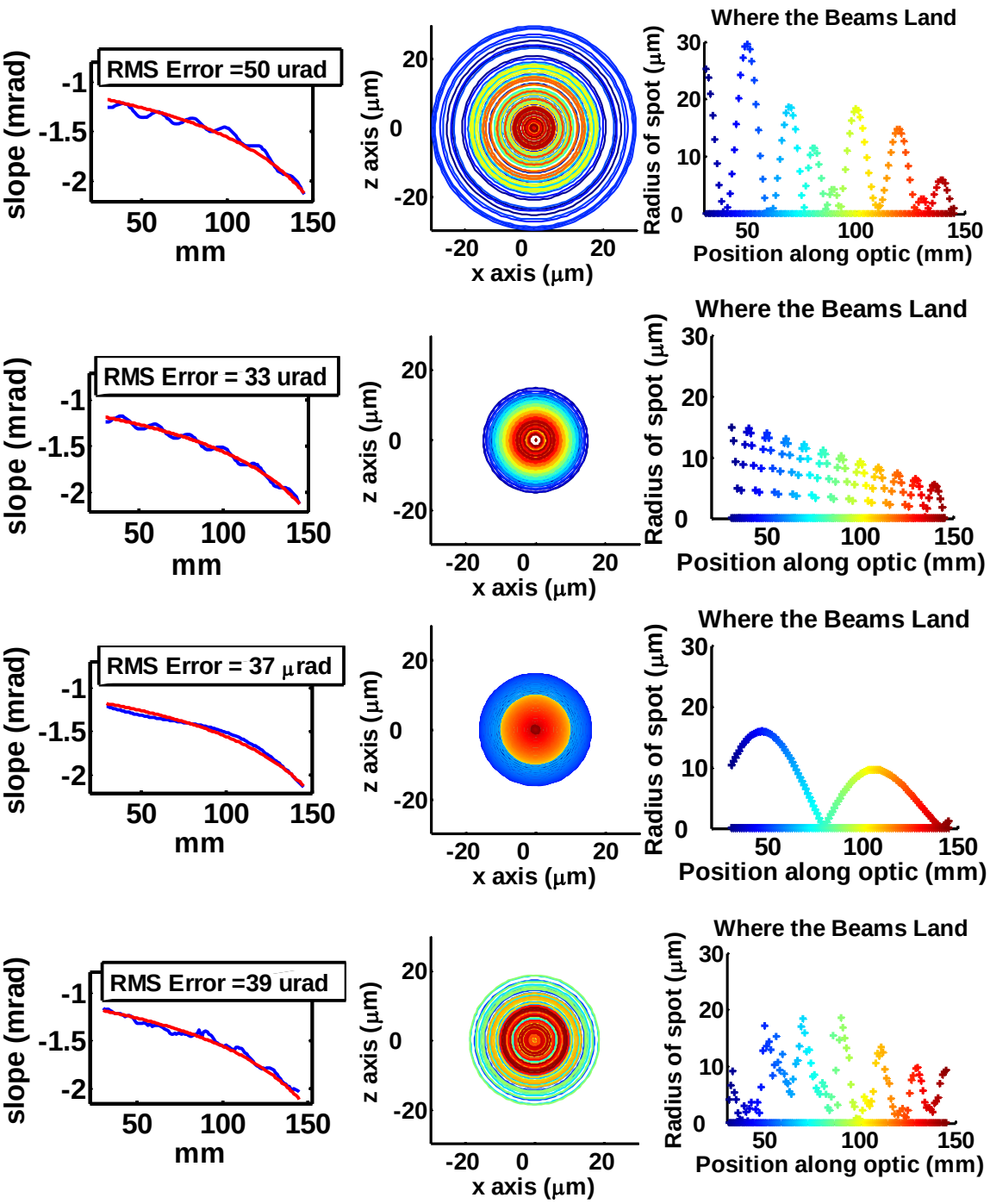

Figure 7.21 This is an array of predicted spot sizes given for different simulated elliptical profiles. The left graphs give the slope of the profile, the center graphs are the simulated spot sizes (all are on the same scale), and the last graphs give the radius of the rays (i.e. spot size) as a function of position along the inner surface of the optic. The top row has both small and long wavelength errors, the second row has just the short wave length errors, the third row has just the long wavelength errors and the bottom row gives the simulation with the profile measured from PEB-mr8f55-02.

Surprisingly, both the long and the short wavelength variations contributed equally to the spot size. Both profile error length scales will need to be reduced to improve the spot size of the optic lower than one μm. In the ray-tracing simulation, slope errors at the base contribute more heavily to increasing the spot size. This can be seen in the spot size simulated images; rays from the base (blue color) are further from the center than rays from the center and the tip of the optic (yellow and red respectively).

Additionally, I took the measured profile from the monocapillary optic PEB-mr8f50-02 and input it into the ray tracing simulation. The simulated far-field pattern has the same features as the real far-field pattern[45]. Remarkably, with the simulated screen shifted to the focal position, the spot size appeared to be about 15 to 20 μm, which is the same as the real optic's measured spot size[46]. This simulation gives an indication of some of the advantages PEB-mr8f55-02 has in order to make a smaller spot size. Having a better slope error on the base, as PEB-mr8f55-02 has, gives a slightly smaller spot size in the simulation. This can be seen in the spot size simulation of PEB-mr8f55-02 in Figure 7.18, with the middle of the optic (in yellow and green) contributing to the spot size as much as the base (in blue).

This simple simulation program gives a number of insights into the function of the optics in the X-ray beam. By manipulating the amplitude and the number of periods of the oscillation error, a number of trends have been found (recapping somewhat).

- There are two major contributions to the profile and slope errors on the optics, a long wavelength (100 to 200 mm) and a short wavelength (5 to 20 mm) variation.

[45] Compare the center simulated far-field image and bottom real far-field image in Figure 6.17.
[46] The last rows in Figure 7.18 and Table 6.7 have the ray tracing simulation information from PEB-mr8f50-02.

- The far-field pattern does not change drastically at further screen distances. This means that deducing the profile and slope error from multiple far-field patterns will be more difficult, but it is still plausible.
- The far-field screen position can be placed right in the focus of the simulated monocapillary optic, to give an estimate on the spot size from the optic.
- By changing the shorter wavelength profile variations, the number of rings in the far-field changes accordingly.
- The short wavelength variations have a low amplitude, on the order of 0.5 to 0.1 μm rms. They are very hard to see in the measured profiles, but easily seen in the slope profile.
- The long wavelength variations have a larger amplitude, 1.0 to 2.0 μm rms, and comprise the bulk of the profile error.
- Both the long and short wavelength errors contribute more or less equally to the slope error and the increase in the focal spot size in this simulation.

This ray-tracing program does not include capabilities for a bent optic, or a twisted optic, or an extended source size. Even without these features, it has granted us a number of insights, and firmly connected the profile scans made with the puller's optical metrology to features seen in the far-field patterns.

Chapter 7 Future Directions Monocapillary Optics

This chapter deals with the untidy edge of single-bounce monocapillary development. What improvements do we want to make? How are we going to make these improvements? The future directions for monocapillary optics hinge on maximizing their positive attributes, and minimizing their limiting attributes. I will list the attributes again, which were discussed in Chapter 3.

The positive monocapillary attributes are:

- They are achromatic.
- They are optically and mechanically robust.
- They are 90% to 99% efficient.
- The divergence and focal length can be designed.

The limiting attributes are:

- They have profile and slope errors, which limit the spot size to 5 μm or larger at CHESS with current technology.
- They are not imaging optics.
- They have a finite aperture size of about 1 mm or less and divergence of about 12 mrad or less.

In my time working with single-bounce monocapillaries, I have spent about half my time trying to maximize their positive attributes, and the other half of my time trying to

minimize their limiting attributes. To take more advantage of the achromatic positive attribute, I made x-ray transmission mirrors, which allow for a very broad, 30% bandwidth of energy (Chapter 8). To take advantage of their optical and mechanical robustness, I created the x-ray microbeam breadboard (section 5.1.2). Both of these efforts have proven to be very successful. To limit their slope error, I helped create a new capillary glass puller (section 6.3). The new puller has increased our understanding of the slope errors, but has fabricated optics with only a modest improvement in the slope error. I have also spent time trying to produce metal or multilayer-surfaced optics to increase the aperture size, using the elliptically-shaped glass as a substrate, discussed in section 7.2 in this chapter. These efforts have not yet been successful.

The following sections outline the directions to pursue in the future. These sections summarize our present knowledge of these future directions. The sections will also discuss why these directions look like promising avenues to explore.

7.1 Improving the Drawing of Glass

There has been a great deal of tinkering around with the capillary puller in an effort to try to minimize both the profile and slope errors of the single-bounce monocapillary optics. This has been going on with different furnace designs, timing of inputs and outputs, smoothing out the puller's operations, etc. These efforts have made improvements, but they have been small incremental improvements. None of the things we have tried in drawing glass have caused large improvements in decreasing profile, slope, and centerline errors so far.

A superior model for glass pulling needs to be completed before there are any more significant changes made to the capillary puller. An accurate dynamical model of pulling glass should give better insights into what parameters, if any, have a larger influence over controlling profile and slope errors. The model we use for pulling, described in section 6.2 is a static, non-dynamical model. Much more complicated dynamical models of the drawing of glass capillaries should provide a good starting place for predicting the features we now see in drawing optics [72-77].

In one paper by A. Yarin et. al., they are specifically modeling hollow drawn fibers [72]. There are known drawing instabilities in glass, even when all the input parameters are constant, such as glass velocities, diameters, etc. Particularly, there is a known instability that causes an oscillation in the diameter of the glass when the glass drawn with an input/output velocity ratio above 22 (equation 6-1). For our draws, the velocity ratios are smaller, on the range of 1 to 12 (section 6.2). If such a model can predict drawing instabilities in straight draws, it may be able to account for or lead into a model which accounts for the small deviations (slope errors) in our glass drawing [78][47].

Armed with a better model of glass pulling, we can decide if our current ideas for an improved puller have merit. We have a few basic thoughts for possible improvements to the puller.

- Change the positional stages to velocity stages. Presently, the stages are positioned, resulting ultimately in a series of short tugs on the glass, at the frequency of the tension feedback loop (10-20 Hz). If the stage's velocity, instead of its position was tuned, it may result in a smoother pull.

[47] Pages 204-218 of Yarin's book (ref. [78]) describe sensitivity to external perturbations in drawing glass, which are present in the stability range of drawing, under a velocity ratio of 22, which is the drawing glass ratio in which single bounce monocapillaries reside.

- Rotate the furnace instead of the glass. Rotation of the glass causes tension vibrations. If the furnace was rotated instead, then these vibrations could be eliminated.
- Try out a CO_2 laser as a more controlled way to heat glass. This may allow more control of the heat-zone during glass drawing.

Again all these points are suggestions, but until a better model of glass drawing is made, which finds the most crucial drawing parameters, it is very hard to say if these major changes will do anything to improve pulling.

We can perform additional tests in the short term to hone our understanding of drawing glass. These tests are in the realm of what we can presently do with the puller, and could give insights into the drawing errors of which we are presently aware.

The size of the heat zone on the glass strongly influences the short wavelength errors (section 6.3.2). Is there a connection between these short wavelength errors, and the heat-zone correction term in our static drawing model? Both the heat-zone correction term, and the shorter wavelength profile errors exist on the same length scale. For example, are the short wavelength errors eliminated or minimized, if we do a straight draw, where the heat-zone correction term goes to zero? In a straight draw, the drawn glass has a constant diameter, or input/output velocity ratio is constant. Doing a series of straight draws should help us recognize if there is a connection between the heat-zone correction term and the short wavelength errors.

Another issue that needs more exploration is how short of a focal length can be pulled using CHESS's current pulling method of a glass cylinder into a ellipsoid. For the shortest focal length optics we have designed, both the divergence and the focal length

have missed the design targets. The 20 mm focal length and a 9-mrad divergence design ended up with optics that had a 22 to25 mm focal length and 7 to 8 mrad divergence. One nice thing about the optical metrology is it finds and predicts this error. It predicted a focal length of 22-23 mm and a divergence of 7.5 to 8 mrad for capillary f1b-mr9f20-01, which is on target for the x-ray measurements (Table 4.2 and Figure 7.1). Other monocapillary optics with a longer focal length, such as the 50 mm, have focal lengths right on the designed target.

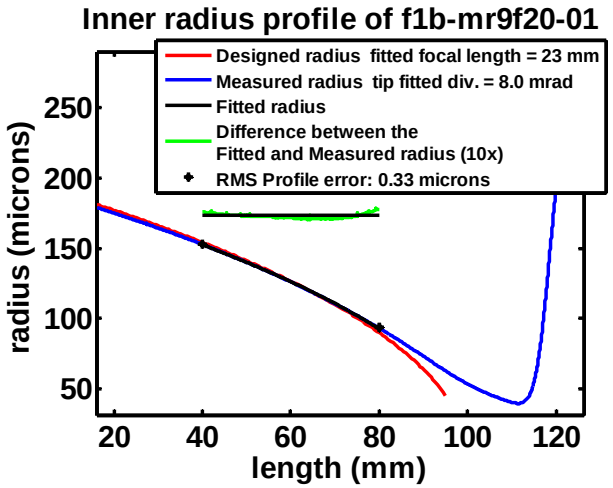

Figure 7.1 The inner profile for monocapillary fb1-mr9f20-01. The predicted focal length and divergence from the profile closely match the measured values in the x-ray beam tests. By close inspection the error in pulling to the design can be seen between the red and blue curves. The red designed profile is slightly steeper than the blue measured profile.

We are not sure why the shorter focal length optics are off the target design. Are we approaching a fabrication limit of the puller (last paragraph in section 6.2)? Do we need to modify our designs of optics with shorter focal lengths to more accurately meet our design target? To answer these questions, we need to draw optics with increasingly shorter focal lengths (15, 10, 5 and 1 mm) to find the shortest focal length monocapillary optic the puller can make. This should give us an idea of how to modify

the design of short focal length optics, to better meet the desired focal length if it is 20 mm or shorter.

7.2 Single-bounce Monocapillary Optics

There are a number of future directions for potentially improving the quality of the single-bounce monocapillaries, and for potentially broadening their experimental applications, outlined below:

- Make metal or multilayer surface optics to obtain a larger aperture size.
- Coat the inner surface of the optics to eliminate the present profile and slope errors.
- Make optics that are appropriate for x-ray tubes.

All of these directions could move the single-bounce monocapillary optics into areas we have not previously explored. It may be possible to make a better monocapillary optic, even if the drawing process cannot be improved.

Our optics may even be able to beat the profile and slope errors right now, if the optics are set up just right. The reason I make this claim is that single-bounce monocapillaries not made at CHESS have already achieved a very small 250 nm spot size [54,65]. These optics are not extremely different than the optics presently used at CHESS.

For these other single-bounce monocapillary optics, there are three basic reasons that they were able to get extremely small spot sizes. One, they first made a small focal spot with a Fresnel zone plate, which created a superiorly small sized x-ray source for the monocapillary optic. Second, they made monocapillary optics with an extremely short

focal length of 2.5 mm[48], which increased the magnification. Third, and probably the most important, they only exposed a very small portion of the optic's inner surface to x-rays, thereby eliminating the effects of the long and short wavelength-sized profile errors. To get the 250 nm spot, only a 5 mm footprint was made on one side of the inner capillary surface [54].

The method of using less of the optical surface to get a smaller spot is a method we use at CHESS as well, but not to this extreme. It is instructive to note that if you inspect our profiles, such as in Figure 3.1 and Figure 3.2, if only a 5-millimeter section of the profile is exposed on one side of the optic, it would virtually eliminate the profile and slope errors that presently limit our optics as well. Using such a small section of the inner surface of the optic would only expose one 'ring' of intensity in the far-field pattern, which we get from using the full optic (Figure 6.17). This method has some severe limitations on the flux throughput, but if the spot size is extremely important, these ideas may work with CHESS optics as well.

7.2.1 Coated Monocapillaries Optics

Other methods exist for making ellipsoidal shapes in materials other than glass. Optics made of metals, such as gold, have a critical angle for total external reflection that is over twice as large as glass. This effectively doubles the numerical aperture and the divergence that the optics produce, at a given energy (Figure7.2). It also quadruples the flux that the optic can collect in a uniform field.

[48] This is the distance from the center of the monocapillary's x-ray-exposed surface to the focal spot.

A few methods of fabrication allow for making metal optics. In these methods, a mandrel with the desired shape is created. In one method, the mandrel is coated with a thin film of metal for the reflection surface, and then coated with another material to provide mechanical structure. The mandrel is removed to leave the desired shape, with a metal-reflecting surface [59,60]. In another method, a mandrel is made from shaping a wire into an ellipsoid shape using an elaborate etching technique, then pressing the wire between two metal plates to imprint the shape. The wire mandrel is then removed, leaving the ellipsoidal shape in the metal plates [79-81].

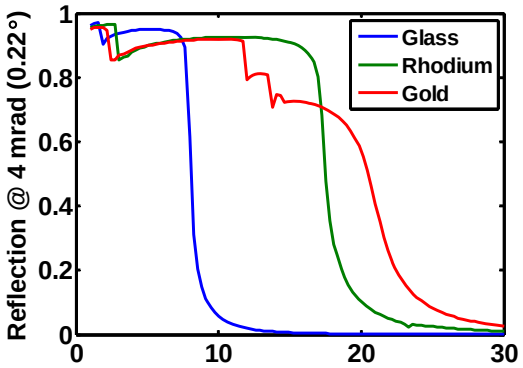

Figure 7.2 The calculated reflectivity of flat glass, rhodium, and gold surfaces at 4 mrad (0.22°). The reflectivity is close to 100% below 8 keV for glass, and 17 keV for rhodium. For gold, the reflectivity is close to 70% below 21 keV. (Compare to Figure 2.3)

The key step in the mandrel technique is getting the required ellipsoidal shape. In that regard, the optics made at CHESS are already halfway there, if the ellipsoidal shapes we make are used for mandrels. We have made one unsuccessful attempt at using glass as a mandrel to make a metal optic. In this attempt, we created three glass mandrels at CHESS with an outer elliptical design for a 55 mm focal length with a 16 mrad divergence. The mandrels were sent to Mel Ulmer, of Northwestern University, where they were coated with gold, then nickel-plated to provide structural support. His group

has worked on a number of x-ray-coated optics, including nested Wolter mirror development for the Chandra x-ray telescope [82,83]. The glass mandrel was dissolved with hydrofluoric acid to leave the desired inner gold-coated ellipsoidal surface shell. With the gold coating, these optics should work up to x-ray energies of 20 keV with a very large total optical divergence or 16 mrad. A glass optic of this design could have only gone up to 8 keV (Figure7.2). Of the three optics created, only one of the optics maintained the inner gold surface, which had a number of imperfections visible by eye. Figure 7.3 shows the far-field pattern from this optic, which was obviously not a good metal single-bounce monocapillary optic.

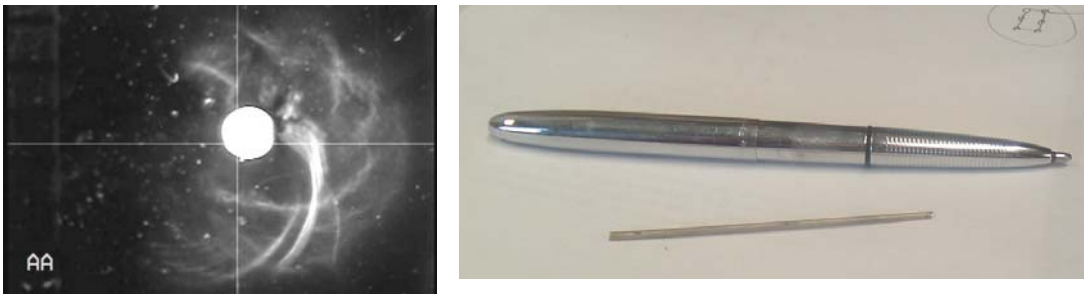

Figure 7.3 On the left is a far-field pattern from the unsuccessful metal optic, taken June 2007 at D1. The optic did not produce a small focal spot, and therefore was unsuccessful. On the right is an image of the metal monocapillary optic with a pen to give the size.

This has been just one attempt of many avenues for using the glass shapes we now produce as substrates for optics. If future attempts at getting a metal optic from a glass mandrel prove to be successful, this idea may be expanded to multilayer coatings. This idea was explored at through a proprietary agreement with a commercial company. They needed the profile errors to be at the 0.15 μm rms level on the outside of the optic before they were willing to attempt to use the shape for multilayers.

There are still other ideas for coating our monocapillary optics. If the optics we now have are cut in half, along the major axis of the optic, we could get to the inner surface of the optic to coat it with other materials, such as a metal. This would limit the optic's full divergence but, in many experiments, only a part of the inner surface is used right now anyway (section 4.3.2).

The ideal optic could be created if we could find a way to tune the coating layer's thickness to correct the optic's profile errors, essentially filling the depressions in the surface to more closely approach an ideal shape. This approach has been used to correct slope errors on KB mirrors [84,85]. Figure 7.4 shows a possible setup that may be able to coat the optics in a way that may correct the present profile and slope errors, using the far-field pattern as feedback for the correction. The largest challenge of this approach is coating evenly over the monocapillary's highly curved sagittal direction, with curvature diameters from 1000 µm down to 50 µm.

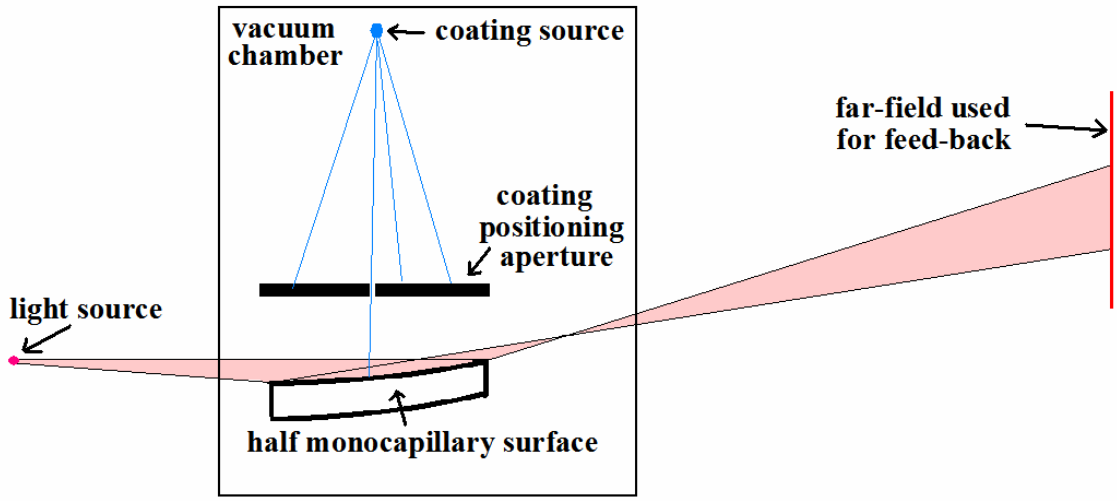

Figure 7.4 A possible configuration for coating the inner surface of an optic. An optic which is cut open could possibly be coated to smooth out the profile and slope errors by positioning an aperture. The far-field image could be used as feedback for the coating. The source of light for the far-field could be an x-ray tube or possibly a laser light source.

7.2.2 Football Monocapillaries

We have discovered that we can make single-bounce monocapillary optics that have a short source-to-focus distance, on the order of 30 cm or less. The very first of these optics was pulled to see if they could be used as a collection optic for confocal x-ray fluorescents (section 9.5). Because the source-to-focus distance is short on these optics, they curve right over the minor diameter of the ellipse, giving them a football shape.

The football monocapillary optics should match well with a microfocusing x-ray tube. A single-bounce monocapillary optic used in conjunction with an x-ray tube is not a new idea. AXCO Inc. has been making single-bounce monocapillary optics for use with rotation anode tubes for a number of years [86]. It would be good to compare the football optics produced at CHESS with other optics presently used to produce micron sized spot x-ray beams for XRD on tube-based systems. Two examples include Bruker™'s Helios Multilayer Graded X-ray Optics® and Rigaku™'s Osmic™ VariMax™ optics. It would be instructive to see if or how football shaped single-bounce monocapillary optics have any advantages over these other x-ray focusing methods.

We have been presently making some football monocapillary optics for micro x-ray tube tests, with source to focus lengths of 30 cm, 25 cm and 20 cm, and a full divergence close to 10 mrad (which should work at Cu K_α line). Figure 7.5 and 7.6 show the puller's optical metrology tests for an optic with a 25 cm source to focus distance (the minor diameter of the optic is 596 μm). For the draw, we were able to pull an optic very close to the design with the best fit minor axis of the resulting ellipse within 1 μm, and the major axis within 3 mm (Figure 7.5).

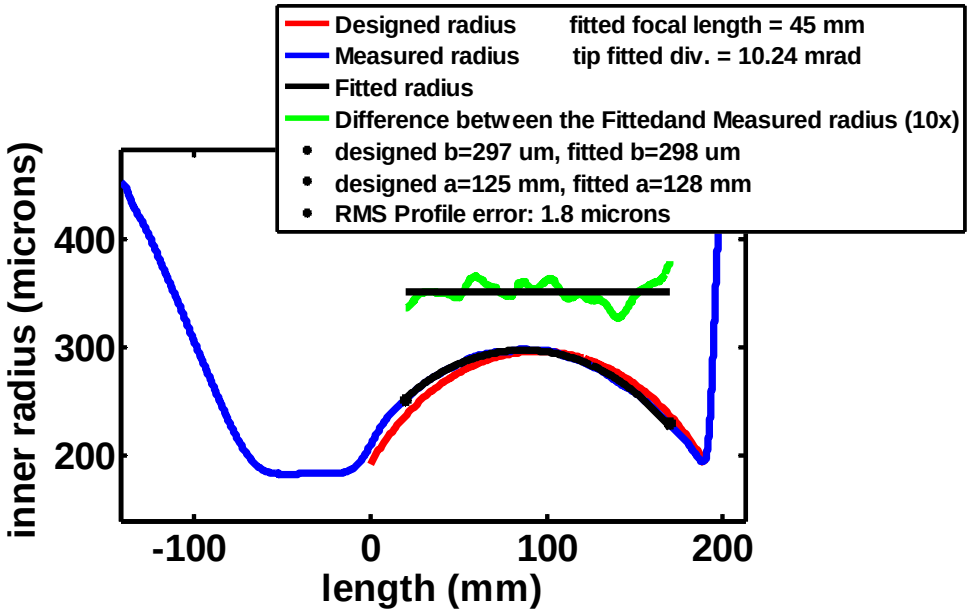

Figure 7.5 The inner profile of a 25 cm source to focus length single-bounce monocapillary optic RK-mr10f50_03. This optic was able to match the design of the optic well. The designed ellipse was meant to have a 1 to 1 symmetric focusing. The optical metrology program missed this a bit, putting the fitted ellipse slightly off center, by about 5 mm.

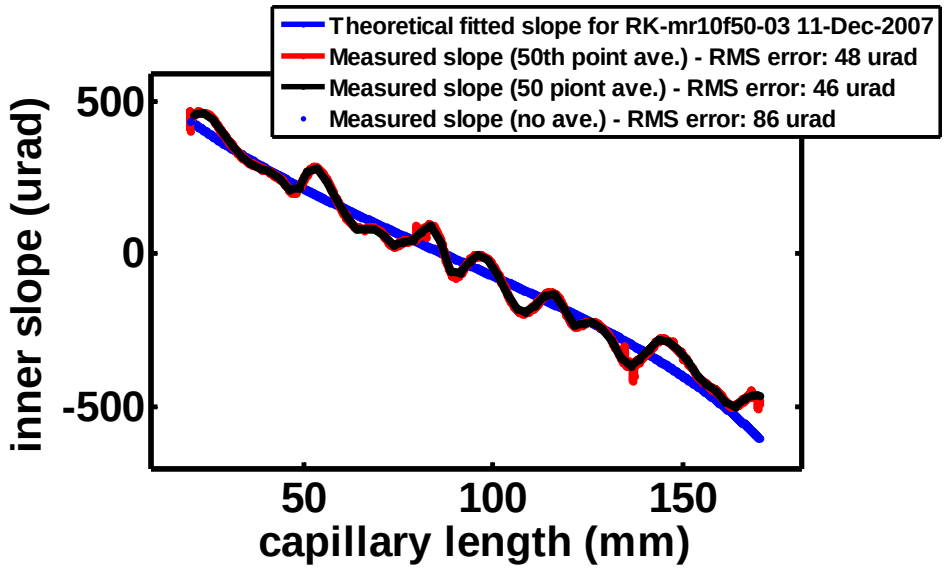

Figure 7.6 The inner slope measurement derived from the profile measurement of capillary RK-mr10f50-03 in Figure 7.5. The graph shows the slope of the fitted ellipse and the slope of the measured ellipse.

This project deals with single-bounce monocapillary optical designs within arenas that we do not have a lot of experience in at CHESS. It may or may not prove to be a promising direction for monocapillary optics to go. The football optics will be more likely to make an increasing impact, if the optics can be made in conjunction with metal and multilayer coatings, discussed in section 7.2.2.

7.3 Auxiliary Equipment Improvements

There are also a few potential improvements that can be made with the monocapillary optics' auxiliary equipment. A few of these ideas have had some preliminary testing, and a few of the others have not, listed below:

- Mount the optic in a housing, which adjusts the straightness, or the optic's centerline.
- Have a mount with an array of capillary beam-stops, for more precise and quick matching of the beam-stop to both the optic and the synchrotron x-ray beam.
- Make an aperture that blocks all the "bad" reflections off the optic, so the optic can achieve smaller spot sizes.

We have known for some time that when the optics are on the beam-lines, they are quite easy to bend. To secure the optic, we gently place the optic in the V-groove then lightly place a sponge on top of it and then tape across the V-groove and the sponge. If the tape is pulled too tight, it results in some bending the monocapillary optic, which can be seen in the far-field pattern. If an optic starts out a little bent, it can often be straightened by manipulating the monocapillary optic in the V-groove, and applying gentle pressure with the sponge.

We have tested this bending dynamically in the x-ray beam as well[49]. A small motor was set up to gently push on the end of a plastic ruler, which pushed on the top of the optic in a specialized V-groove[50]. With this very simple setup, some optics could be bent or straightened by the motor (Figure 7.7). This idea could be further developed by creating a special housing made for the optic to straighten it. The optic could be tuned straight, by looking at the far-field pattern. Then the housing could lock the monocapillary optic into position once the optic is straight.

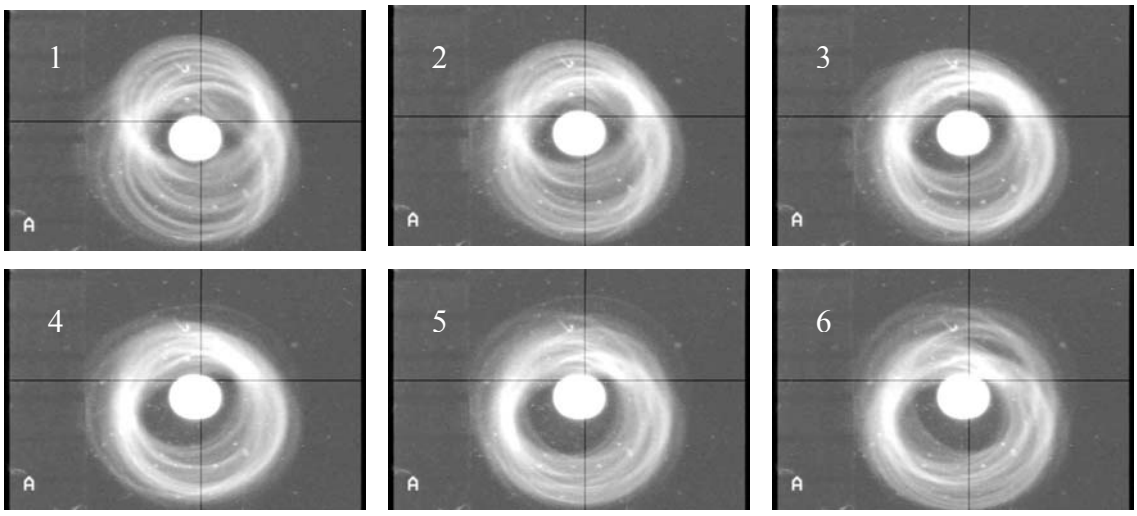

Figure 7.7 A series of far-field images showing a bent monocapillary optic, F3_mr6f150_08, which was dynamically straightened while in the x-ray beam at the F3 station.

If the optics could be fixed this way, a number of bad bent optics we now have could be straightened into serviceable optics. With the optics in such a specialized housing, we could potentially tune out all the centerline errors the monocapillary optics have.

[49] The tests were done at CHESS's F3 station by Heung-Soo Lee, a visiting scientist from the Pohang Accelerator Laboratory in Korea.
[50] See Appendix section A.4 for an image of this monocapillary-bending platform.

Another improvement that could be made is making a capillary beam-stop array, much like the pinhole arrays that we now have. This would allow for more precise and quick matching of the beam-stop to both the optic and the synchrotron x-ray beam. Often the present sizes of beam-stops we now have are a bit too coarse, with beam-stop sizes being either slightly too big or slightly too small. If we could make an array of sizes with 10 to 20 μm steps in the diameter size, we could better match the beam-stop to the optical configuration.

We could also try to make an aperture that blocks all the "bad" reflections off the optic to approach smaller spot sizes with our imperfect optics. These specially shaped apertures would sit in-between the focus and the tip of the optic, and would only allow x-rays that arrive at a very small spot to pass through the aperture. The simplest form of such an aperture would be a pinhole right at the focus, with a diameter size being the size of the focal spot desired. For example, a one-μm pinhole at the focus of a 20 μm spot monocapillary optic would make a one μm spot size. The question is, what shape and size of aperture 10 or 20 mm from the focus will block the same x-rays as the small pinhole at the focus? There could be some shapes, such as a donut shaped aperture, which are able to block some of the "bad" parts of the monocapillaries surface, which leaves only the "good" parts to contribute to a smaller spot size. This is an avenue that has not been explored to see if it could make a difference in the achievable spot size or not.

Chapter 8 Silicon Nitride Transmission X-ray Mirrors

This chapter deals with another type of optic, x-ray transmission mirrors. The chapter will cover both the manufacturing and testing of the optics. Most of this chapter comprises a paper that is now accepted to the Journal of Synchrotron Radiation[87].

The x-ray transmission mirror, in conjunction with the traditional x-ray reflection mirrors allows for a tuneable, broadband x-ray beam. This optic was developed for a Laue protein crystallography project, which needed a large x-ray bandwidth from 10 to 13 keV (section 9.13). In the Laue project, once the larger bandwidth beam was made, a single-bounce monocapillary optic focused the beam down to a small 10 to 15 μm spot. The single-bounce monocapillary can focus this large bandwidth beam because it is achromatic. The transmission x-ray mirror and the single-bounce monocapillary optics complement each other very well.

8.1 Introduction to Transmission X-ray Mirrors

Synchrotrons are magnificent x-ray sources that use an extensive arsenal of x-ray optics to tailor the x-ray beam for a wide sampling of experiments. X-ray transmission mirrors are one type of x-ray optic, which have been used in the past, but not for the last 15 to 20 years, because of mechanical and lifetime limitations. The first transmission mirror optics were made from soap-bubble films, which performed very well as

transmission mirrors [88]. However, the major limitation of the soap bubble transmission mirror was it lasted only a few hours in the x-ray beam. This limitation made them hard to use if the experiment lasted more than a few hours. The bubble transmission mirrors were used in time-resolved Laue diffraction experiments and in wide band-pass x-ray fluorescent experiments [89]. Attempts at producing a better transmission mirror included employing a 0.5 μm thick Mylar film, which was stretched onto a frame [90]. This technique of transmission mirrors also had some limitations; the film was not uniform enough in thickness and lasted for a day or two [91] in the x-ray beam at the Photon Factory. Since that time in the mid 1980's, and to the best of our knowledge, there have not been any further attempts at fabricating a more permanent transmission mirror.

Transmission mirrors are very similar to total external reflection mirrors. The difference is that the transmission mirror is very thin, so the beam that is normally absorbed by the total external reflection mirror is transmitted instead. The total external reflection mirror reflects x-ray energies up to a sharp cut-off energy, which is set by the critical angle for total external reflection. Energies above this cut-off energy are transmitted into the mirror. Total external reflection mirrors make excellent low-pass energy filters because they have a reflection of close to 100% below the cut-off energy, and the reflected energy drops off rapidly above that cut-off energy. For those reasons, total external reflection mirrors are a staple optic used at synchrotron facilities. Transmission mirrors work just the same way, but the beam used is the transmitted beam, thereby switching the functionality into a high-pass filter. In the limit of having a very thin film, the critical energy cut-off is just as sharp as it is for the total reflection mirrors. It is this sharp cut-off energy, in conjunction with changing the cut-off energy

(by changing their angle), which makes them very attractive high-pass filters, compared to absorption filters.

A few critical parameters determine the optical properties of the transmission mirror. The transmission mirror has to be thin, flat, smooth, and uniform in thickness. All of these qualities have to be maintained over a fairly large surface area to allow usable beam sizes. The mirror has to be thin; from 0.5 μm to as thin as possible to minimize the absorption of the film. Another way to minimize the effects of absorption is to have the mirror material made of a low atomic number material. The mirror must be flat so that the angle of incidence does not vary over 5% [89]. At an angle of 0.22º (3.8 mrad) this corresponds to a variation of 0.011º (190 μrad). By comparison, high quality x-ray reflection optics generally have less than a .003º (10 arc second or 50 μrad) variation. The mirror has to be smooth and uniform in thickness. Without a smooth flat and uniform boundary, x-ray mirrors do not work well. A small amount of roughness can be tolerated and may even have some advantages in dampening the amplitude of the Kiessig fringes of the transmitted beam.

8.2 Silicon Nitride Membranes

The most limiting feature of the original transmission mirror was its very short life span in the x-ray beam. One major reason for attempting to make transmission mirrors out of silicon nitride is that this material has proven itself to be a radiation-hard material in x-ray window applications, lasting virtually indefinitely in synchrotron x-ray beams. We have been able to test the life span of the silicon-nitride membrane transmission mirror in two ways. One transmission mirror was in a white x-ray beam at CHESS's B1 bending magnet station for twenty-four hours straight. Another transmission mirror was

used for ten days intermittently in a pink x-ray beam (with a high-energy cut-off at about 13.5 keV) at CHESS's D1 bending magnet station. Both mirrors suffered no degradation over the time that they spent in the x-ray beam. We do not anticipate radiation damage to be a short-term failure mechanism.

The films for the windows were grown by vapor deposition on silicon double sided polished 100 mm diameter wafers. The films grown on the wafers had a thickness of 300 nm, and had a uniform thickness of within 2 % to 5 % over the entire wafer, with the thickness in the middle of the wafer being slightly thinner than the thickness at the edges of the wafer. The roughness of typical silicon nitride films is 1.5 nm rms to well over 2 nm, measured by AFM at the Cornell NanoScale Science and Technology Facility (CNF) [92]. Our films have not been measured with AFM to verify their roughness. Each wafer had three windows 0.6 mm by 85 mm in size. One of the 0.6 mm sides could not be supported by the silicon wafer, to allow the transmitted beam through. Thus, a piece of silicon wafer covered by silicon nitride was glued with epoxy on the top side of the silicon wafer to support the free ends of the silicon nitride windows (Figure 8.1). This unfortunately blocks the reflected beam from the transmission window. Other support methods were tried to allow collection of both the transmitted and reflected beams from the silicon nitride membrane, but they have not yet produced a working transmission mirror.

We wanted to have the membrane as thin as possible. Figure 8.2 shows the predicted transmission curves for membranes of 100 nm, 300 nm, and 500 nm thickness, at 0.22º and with 5 nm rms of roughness [10]. The transmission mirror has a higher transmission efficiency than the aluminum absorber. The transmission mirror also has a desirable sharp change in its energy response curve. The thinner windows have better

transmission properties especially near the cut-off energy. Silicon nitride windows are very strong for their thickness (100 to 1000 μm), but the windows become more fragile when the membrane is thinner or has a larger window size. We tried to make both 100 nm and 300 nm thick windows. For a window size of 0.6 mm by 85 mm, none of the 100 nm films survived the fabrication etching process. The 300 nm thick windows, however, had roughly a 50% survival rate from the fabrication etching process.

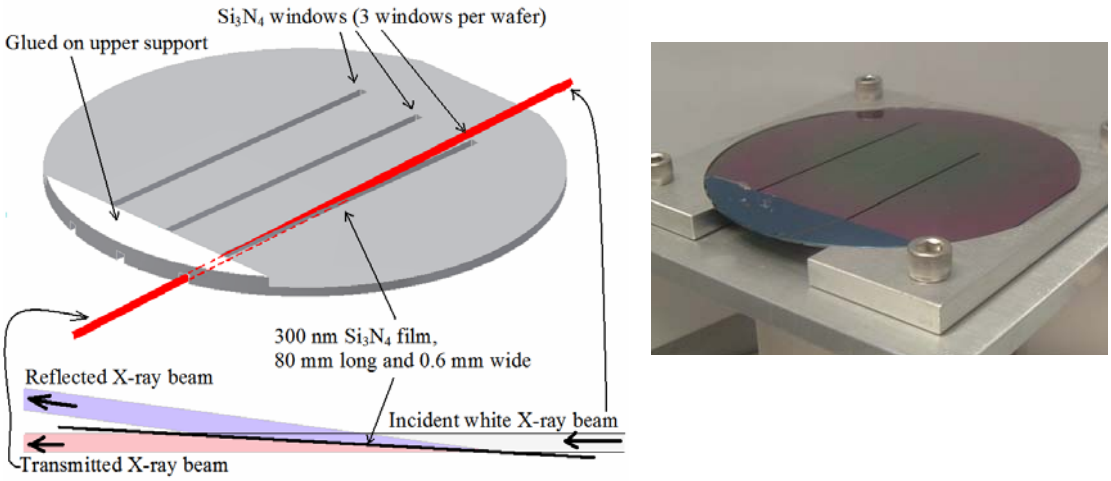

Figure 8.1 On the left is a drawing of silicon nitride transmission mirror windows on a silicon wafer. The wafer holds three transmission mirrors. The upper support blocks the reflected beam. On the right is an image of the silicon nitride transmission mirror. The center silicon nitride membrane is not quite visible. The membranes on either side are broken/gone, therefore the holes through the silicon wafer are visible.

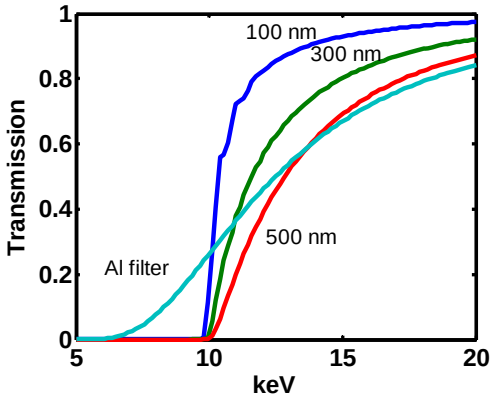

Figure 8.2 Calculated transmission of 100, 300 and 500 nm thick silicon nitride membrane at 0.22° with 5 nm rms roughness on the surfaces. An 200 µm aluminum attenuation filter is also shown for comparison. Calculated at www-crxo.lbl.gov.

8.3 Silicon Nitride Membranes in the White Beam

The silicon nitride transmission mirrors were tested in the B1 station's white beam at CHESS with the full energy spread from a bending magnet with 10 keV critical energy. The only other elements in the beam line were two beryllium windows between an air/vacuum and vacuum/vacuum environment, a few Kapton windows on helium filled flight tubes, and the transmission mirror chamber. The beam was slit down to 0.2 by 0.2 mm, and then was put through the transmission mirror. The x-ray beam traveled 2.25 m in a Helium flight path, then through a 1 mm diameter lead clean up aperture, and finally through a 0.5 mm thick film of Kapton tape. An XFlash® diode detector[51] was used to measure the Compton scattering from the Kapton tape to observe spectrum of the beam. The effects of transmission of windows, flight paths, detector efficiency etc, were normalized by taking a scan with the transmission mirror in the beam, then

[51] X-Flash® SDD Type 1201 from Bruker-AXS (www.bruker-axs.com)

dividing it by a scan taken without the transmission mirror in the beam[52]. Figure 3 shows the observed transmission curves, along with the predicted transmission from two different mirrors. Figure 3a shows the transmission curves for a 300 nm thick silicon nitride membrane at angles from 0.18º to 0.26º in steps of 0.02º, along with the predicted curves, which assume a 5 nm rms roughness. The actual curves track well with the predicted curves. Angles below 0.18º were not reasonable because the beam started to be clipped by the glued-on silicon wafer support. We did not go above 0.26º because the cut-off edge started to be obscured by impure x-ray fluorescent signals from the scattering Kapton tape. Figure 3b is a curve from a second window at 0.22º and 0.24º, which also is well matched to the predicted transmission curves.

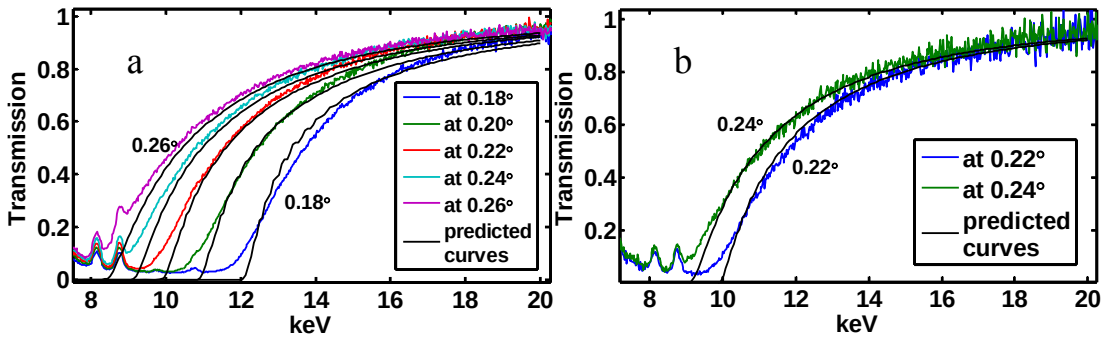

Figure 8.3 The left graph is the transmission of a 300 nm thick silicon nitride film at angles ranging from 0.18º to 0.26º. The right graph is the transmission of a second silicon nitride film at angles 0.22º and 0.24º. The small peaks between 8 and 9 keV in the transmission curves are a result of both copper and zinc fluorescent contamination in the signal that we were unable to eliminate, which most likely originated as trace elements within the Kapton tape.

[52] G-line's GISAXS stage was used to move the transmission mirror in and out of the beam, as well as set its angle. Section C of the appendix shows both the GISAXS stage and the helium chamber which the transmission mirror sits in.

From these transmission curves, we can confirm that the flatness of the silicon nitride membrane is on the order of 0.01º (119 μrad) or below. The consequence of this lack of flatness is that the transmission edge is not as sharp as the predicted sharpness. The observed quality of the transmission mirror transmittance in Figure 3b is slightly better than the transmission mirror in Figure 3a. This can be noticed by observing the match between the predicted and actual transmission curves close to the cut-off energy. Also, to explain the absence of Kiessig fringes in the predicted transmission curves, the mirrors need a roughness of 5 nm rms. The roughness estimated here is based solely on eliminating the Keissig fringes to match the measured transmission curves. The actual roughness may be less, with the Keissig fringes most likely eliminated by a combination of effects, such as a combination of surface roughness of less than 5 nm and the variation in flatness at the level of 0.01º or less. Single oscillations of the Kiessing fringes for a membrane of a 300 nm thickness are on the order of 100 to 150 eV FWHM [10]. Because the fringe energy spacing is close to the resolution of the detector, and the fringe modulation is about 5% or less, we were not able to observe them with the X-flash detector (resolution of 130 eV to 170 eV between 10 and 15 keV respectively). Thus from the fitting work, we estimate that the membranes have a 5 nm rms roughness or less.

We have successfully demonstrated the value of silicon nitride transmission mirrors as a permanent high-pass energy filter for synchrotron applications. They are adequately thin, flat, smooth, and uniform in thickness for working transmission mirrors. They have been able to last in an x-ray beam for several days, and could last a great deal longer. We have used them in conjunction with traditional reflection x-ray mirrors to establish a wide, tunable x-ray band-pass for experiments that need a wide band-pass beam.

8.4 Fabrication of Silicon Nitride Membranes

This section is an outline for making the silicon-nitride x-ray transmission mirror. All of the tools needed to create the silicon-nitride x-ray transmission mirrors are available at the Cornell NanoScale Science and Technology Facility (CNF). I have included a recipe for recreating the silicon nitride membranes.

1. Start with double-sided polished, 500 μm thick, silicon wafers. The reason for using a double-sided wafer is that during the KOH etching, if a single sided wafer is used, it could dissolve the entire wafer because the rough side does not coat quite well enough with silicon nitride to protect the wafer.
2. Before placing the wafers in the LPCVD nitride deposition furnace, they need a MOS cleaning.
3. The double-sided polished wafers are completely coated with silicon nitride in the LPCVD nitride deposition furnace. This process can accommodate up to 25 wafers at a time. The time within the deposition chamber sets the thickness of nitride. A 300 nm film takes about two to three hours to grow. One side of all the wafers will have a close to uniform coating. This will be the side of the silicon nitride windows.
4. A thickness map of the silicon nitride coating can be measured on the FilMetrics film measurement system.
5. After measuring the thickness of the silicon nitride film, a photo-resist spinner is used to deposit photo-resist onto both sides of the wafer. Microposit Surface Coating FSC-M (a photo-resist) can be used for the side with a uniform silicon nitride thickness. This resists primary purpose is to protect that side from damage during the rest of the processing. The non-uniform silicon nitride side is the side where all the etching takes place. Microposit S1813 Photo Resist, (a standard photo-resist), can be used on this side.

6. Before the photo-resist is exposed to UV light, a mask for the desired pattern needs to be made. CNF has programming design tools to design the mask, and a Mann pattern generator to make it. The pattern used for the silicon nitride mirrors is quite simple, it is three straight lines, 15 mm apart, 0.6 mm in width, and a length such that they go over the edge on one side of the wafer and are 15 mm from the other side of the wafer. This mask makes a potential of three membranes per wafer (Figure 8.4).

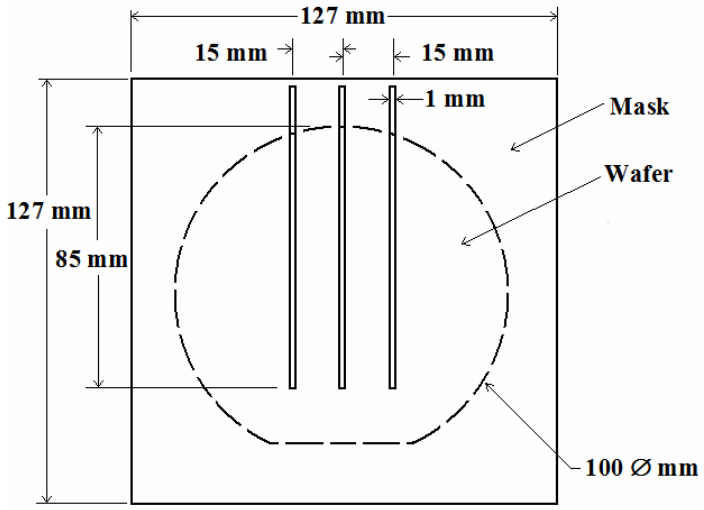

Figure 8.4 This shows a sketch of the mask used to expose the silicon nitride wafers to get three windows out of a single wafer. All the key dimensions labeled.

7. The wafer's S1813 can now be exposed to UV light, using the HTG contact aligner. Once exposed, the resist is developed Hamatech-Steag HMP900 Mask processing system. In the region of the exposure, the resist is gone, down to the silicon nitride. When exposing the wafer, make sure that the mask is aligned parallel with the crystal orientation of the wafer (the wafer is aligned when the lines in the mask are parallel or perpendicular to the flat on silicon wafer).
8. The silicon nitride layer needs to be removed where the photo-resist has been exposed. The silicon nitride layer can be removed in the PlasmaThrem 72 fluorine

based reactive ion etcher. This etching technique etches the remaining photoresist as well, but since the silicon nitride is much thinner, it will etch through the silicon nitride far before it etches through the photo-resist. It is a good idea to etch the wafer 50% to 100% the time estimated for the etch, to make sure and fully etch the nitride layer.

9. The silicon nitride layer needs to be removed where the photo-resist has been exposed. The silicon nitride layer can be removed in the PlasmaThrem 72 fluorine based reactive ion etcher. This etching technique etches the remaining photo-resist as well, but since the silicon nitride is thinner, it will etch through the silicon nitride far before it etches through the photo-resist. It is a good idea to etch the wafer 50% to 100% the time estimated for etching, to make sure and fully etch the nitride layer.
10. The photo-resist covering the rest of the wafer can be removed in the resist hot strip bath.
11. At this point, the small supporting structure needs to be glued on with epoxy[53]. For successful x-ray transmission mirrors, I glue a small piece of wafer on the top side of the wafer (the side of the nitride windows), at the edge of the wafer, over the gaps which the KOH etch takes away (Figure 8.1).
12. At his point, the wafer can be KOH etched. This removes the exposed silicon wafer, and leaves the silicon nitride coated part of the wafer. It will etch though the entire wafer, leaving only the desired silicon nitride membrane. The KOH bath is made by slowly add 600g of the solid KOH to 1.8 L of water, about 100g at a time. This will make a solution with 6 molarity or 25% KOH by weight (please take the appropriate safety precautions). Etching takes about 6 to 7 hours with the KOH bath at ~90º C. When the etch is complete, gently remove the plastic wafer boat, which holds the wafers, from the KOH solution and carefully put them into the

[53] I used stycast® 1266 epoxy.

second glass or plastic beaker filled with water to rinse them. I used Lois Pollack's research area in Clark Hall for the KOH etching. Note, sometimes the support structures glued on to the wafer fall of during the KOH etch, which results in broken nitride membranes.

The final large 0.6x85 mm, 300 nm thick nitride membranes are extremely fragile. Any movement can break them. Handle them with extreme care. There is one last thing that may have to be done. In step 7, the pattern goes right to the edge of the wafer, but some times the exposed pattern does not. In order for the transmission x-ray mirror to function, it has to go right it the edge of the wafer. Most of the time, there seems to be a small sliver of silicon wafer at the end of the window, right on the edge of the wafer. I had to very carefully break out the silver of wafer at the edge after processing. This problem has not been resolved in etching.

By way of acknowledgements, I would like to acknowledge the Cornell NanoScale Science and Technology Facility (CNF) for providing the resources needed to fabricate the silicon nitride membranes, and Kurt Andresen, a former member of Lois Pollack's research group for allowing us to use their laboratory for KOH etching.

Chapter 9 Single-Bounce Monocapillary Experiments

Single-bounce monocapillary optics, made at CHESS, are used in a wide array of experiments at CHESS, and a few other locations. Many projects over the past few years have used the x-ray microbeams produced by monocapillaries. The more the monocapillaries are used, the more they are requested. With some of these projects, the x-ray microbeam was an essential part of the experiment, and could not be accomplished without it, such as in confocal x-ray fluorescence and high-resolution micro x-ray diffraction (sections 9.4 and 9.2). In other experiments, the x-ray microbeam was used to enhance some aspect of the experiment, such as spatial resolution or flux. This pushes the boundaries of what information can be measured from samples, such as in micro-protein crystallography and μSAXS (sections 9.6, 9.7, and 9.11).

In many of these examples, my main responsibility has been to make sure the x-ray microbeam is in place, with the flux, divergence, and spot size optimized for the experimental application. In addition to information collected from samples, each new experimental application has lessons learned in using the single-bounce monocapillaries for x-ray microbeams. Lessons learned include more optimized optical designs for particular applications, and improvements needed in auxiliary equipment. The role single-bounce monocapillaries play in an experiment will be the focus in most of the following sections. The major questions I will address in each section will be:

- Why is a capillary needed?
- Which capillary parameters are important?
- What were the experimental results?
- Conclusions, what did we learn from an optics standpoint?
- What are some avenues for improving the results in follow-up experiments?

The different x-ray microbeam experiments are listed in approximately the order that they started, or I began my involvement in them. The end of each section gives the names of all the others who have been involved in these projects, excluding S. Cornaby and D. Bilderback, who are involved in all of them.

9.1 High Pressure Powder Diffraction

For high-pressure powder diffraction, the single-bounce capillary optic provides an increase in signal and a controlled divergence, which allows the resolving of closely spaced Debye-Scherrer rings. Additionally, the small spot more easily allows for a limited high-pressure sample volume. Small sample volumes are the major motivation for using the x-ray microbeam created with the monocapillary optic, especially in the context of a diamond anvil cell (DAC) where samples are often microscopic in size.

The feasibility of using the capillary optic was checked for high pressure powder diffraction on two known samples: a NIST standard Lanthanum Hexaboride (LaB_6) at atmosphere, and Structure I (cubic) Xenon Clathrate Hydrate ($Xe_8(H_2O)_{46}$) at 1.4 GPa in a diamond anvil cell (DAC) (Figure 9.1). Data was collected with a 50 μm

collimator, which produced a 50 µm spot size on the sample, at a beam energy of 25 keV. The collimator was compared to monocapillary A10 (2 mrad divergence, 55 mm focal length), which produced a 14x18 μm^2 spot (Table 4.2). The diffraction rings of Xenon Hydrate have an exceptionally narrow line-width, which made it a good candidate for evaluating the effect of the capillary's divergence on line-width broadening as observed on a MAR345 area x-ray detector. With the capillary, the diffraction intensity increased by a factor of two. The diffraction peaks' FWHM were only increased by 10% to 20%. Figure 9.1 on the left highlights one narrow peak from LaB_6, where the resolution with the collimator is 1.15 mrad (0.066º), and the resolution with the monocapillary optic is 1.42 mrad (0.081º). The line-widths allow for calculating lattice spacings to approximately one thousandth of an Angstrom (section 1.5.2).

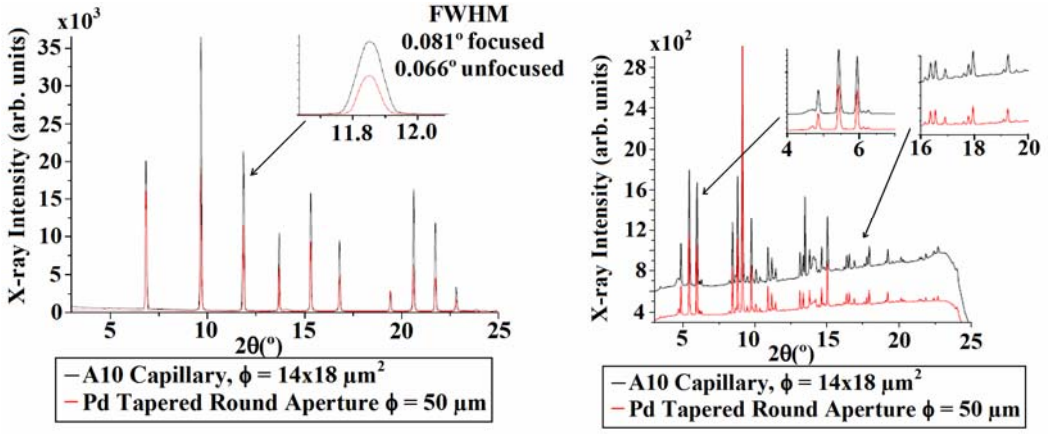

Figure 9.1. The left graph shows the results comparing the A10 capillary modified with upstream slits to a 50 µm aperture on a NIST standard LaB_6 sample at atmospheric pressure. The right graph shows the diffraction pattern from a known sample of Xenon Clathrate Hydrate at 1.4 GPa [94].

For these tests, only a smaller portion of the inside surface of the capillary was used, which further narrow the divergence of the A10 optic (section 4.3.2). The narrow diffraction rings expanded into closely spaced double rings when the entire inner surface of the optic was used, which was undesirable. The closely spaced double rings

resulted from the optic having a different divergence coming from the lower and the upper part of the optic. To eliminate the double rings, a 2 mm thick tungsten blade was positioned downstream from the capillary and blocked the lower portion of the x-ray beam from being focused by the capillary. This eliminated the double ring and improved the angular resolution.

This feasibility study showed that the capillaries provide many advantages for high-pressure work. The advantages of using the optic are, the signal intensity was roughly doubled, the flux per square micron in the sample was increased by a factor of 17, and the spot size in the sample was decreased from 50 μm (with the collimator) to about 16 μm (with the monocapillary optic). The slight disadvantage of using the optic is the line-widths of the peaks were broadened by 10% to 20%. This test showed that the A10 monocapillary optic offers clear advantages in a majority of applications. The use of a collimator is necessary only when the resolution is of greatest importance [93,94].

This experiment was successful; while the high-pressure experiment did not particularly need a monocapillary optic, it did decrease the needed sample size, and increase the flux, at a modest cost of some resolution. It was also the first experiment that took advantage of tuning the divergence with a slit to increase the angular resolution.

This experiment was done at the CHESS A2 station, with A. Kazimirov as the CHESS beam line scientist, with J. Smith and S. Desgreniers as the CHESS users from the University of Ottawa.

9.2 Micro High Resolution X-ray Diffraction

Micro high-resolution X-ray diffraction (μHRXRD) is used to measure lattice strains in small structures. Multiple quantum wells (MQWs) are made from a number of different gallium-based structures using the selective area growth (SAG) technique [95-98]. These structures can be used for devices and components in optoelectronics. Lattice parameter differences due to the differences in composition control the band gaps and other optoelectronic properties of the MQW structure. In a SAG process this control is implemented by adjusting the size of the openings in oxide windows during the growth [99]. High-resolution diffraction is a great structural technique to measure precisely these compositional changes non-destructively. At CHESS, we have used μHRXRD to precisely measure the diffraction peaks in InGaN/GaN and InGaAlAs-based SAG devices [96,97].

For μHRXRD, the single-bounce capillary optic provides an increase in flux on a small sample. The tested structures are typically long and narrow, with structural widths ranging between 2 to 140 μm [96,97]. The x-ray focal spot is placed along the width of the structure. The monocapillary optic provides the increased flux on a small spot that the experiment needs, but the divergence of the optic is much too large for the needed diffraction resolution in the θ-2θ scan direction. In order to increase the angular resolution in that direction, a small two-bounce crystal is placed in-between the tip of the optic and the sample (Figure 9.2 and Figure 9.4).

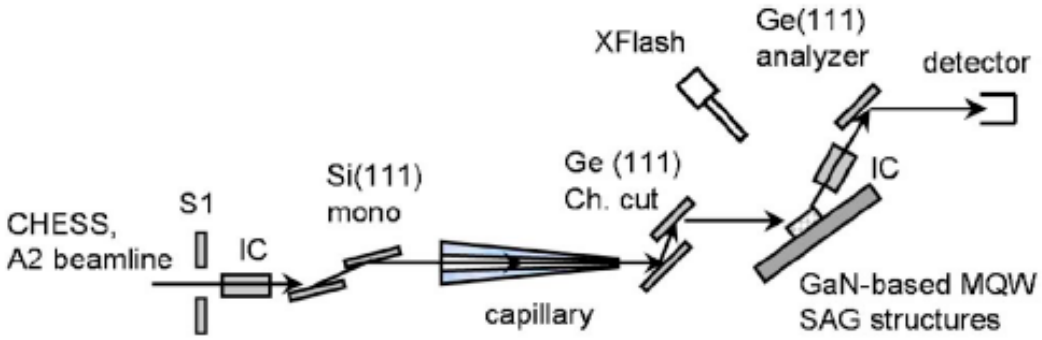

Figure 9.2 This diagram shows all the components used for the μHRXRD experiment at CHESS. It consists of upstream slits, a Si 111 double bounce channel cut to set the energy bandwidth of the beam, a monocapillary optic to make a small x-ray spot, a Ge 111 double bounce channel cut to vertically increase the angular resolution, a X-flash XRF detector to position the small spot on the samples, and a single bounce analyzer crystal and detector to measure the diffraction peaks. The diagram was taken from reference [96].

The monocapillary used is BSG7, which has a 30 mm focal length, a 4 mrad divergence, and produces a spot size of 10 to 12 μm. Using the full optic, the diffraction resolution is 4 mrad (0.22º). The resolution (rocking curve) in the θ-2θ scan direction decreases to 0.06 mrad (0.0036º), by putting a Ge 111 channel cut in-between the monocapillary optic and the sample. The monocapillary optic and crystal channel cut combination creates a small 10 μm sized beam, with a divergence of 0.06 mrad in the θ-2θ scan direction (vertical direction), and approximately a 4 mrad divergence in the horizontal direction. Figure 9.3 shows 2θ scans performed close to the GaN 0002 substrate peak, which includes a series of smaller diffraction peaks from a number of different sized InGaN/GaN MQW devices.

In order for this project to be successful, it needed adequate flux on a small spot, with a very narrow vertical divergence. The single-bounce monocapillary optics in conjunction with the double bounce crystal optics are adequate for measuring the entire

width of the device. To measure strain features within the devices, the monocapillary optic's spot size is too large. Thus, further studies were conducted at the APS 2ID-D beam line using a zone plate to focus the beam down to a 0.25 µm spot size in order to measure strain features within the device, specifically measuring how the strain differed from the edge to the middle of the structure [95].

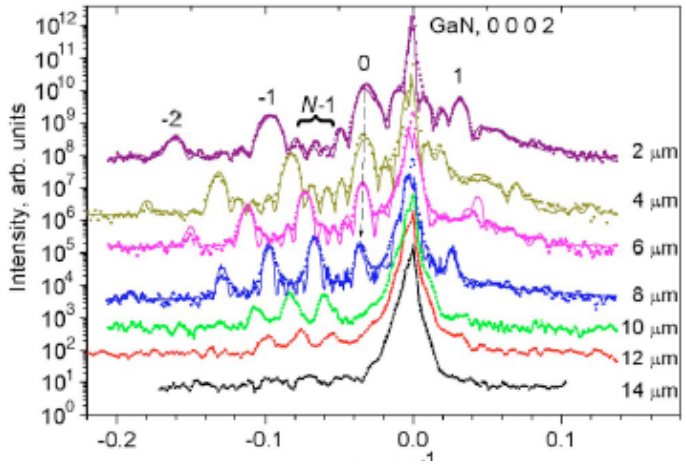

Figure 9.3 These graphs show the x-ray diffraction data taken from an array of InGaN/GaN MQW 6-µm-wide SAG ridges (small dots), and the simulated curves in the solid lines. The ridges have different oxide mask widths, marked next to the curves (2 µm, 4 µm, …). The diffraction curves are vertically offset for clarity. The large peak is from the GaN substrate, a 0002 peak at a Bragg angle of 11.12°. The shift in the 0th order peak shows the change in the MQW's global-strain. The figure was taken from reference [96].

For a monocapillary standpoint, it would have been good to produce a smaller spot size. The spot size was adequate, but not the best. Also, the aligning and positioning of the capillary optic and the capillary beam-stop proved to be cumbersome. The monocapillary optic, small channel cut, and sample, which was mounted in a diffractometer, all had to be within 30 mm. To do this, the monocapillary optic had to be precariously held off the end of the stage (Figure 9.4). During experiments, this precarious positioning was often the cause of frustrations when aligning this very

complicated experiment. Since this time, a new, much more compact capillary stage has been designed specifically to mount on the diffractometer tables, under more constricted space constraints (see Figure A.9 in the appendix). This should alleviate the most severe alignment issues of the monocapillary optic and its beam-stop.

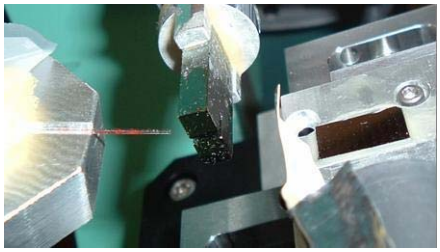

Figure 9.4 An image of the monocapillary optic, Ge 111 channel cut, and the sample for the μHRXRD experiment at A2.

The μHRXRD experiments were done at the CHESS A2 station with A. Kazimirov as the CHESS beamline scientist. The CHESS users were A. Sirenko (TriQuint Semiconductor Inc., and later at the New Jersey Institute of Technology (NJIT)), Sean O'Malley and Peter Bonanno, (NJIT students). Rong Huang, while at CHESS, was involved in this project.

9.3 Scanning Micro X-ray Fluorescence Microscopy

X-ray fluorescence (XRF) can be used for non-destructive spectroscopic techniques. For XRF, the x-ray beam excites a sample, and the elements within the sample fluoresce at characteristic x-ray energies, which allows one to determine the sample's elemental composition. XRF is good at detecting the percentage elements within a sample. XRF is also able to detect elements at parts per million (ppm) conditions, and sometimes

down into the parts per billion (ppb)[54]. XRF is a definitive tool for elemental analysis in all sorts of materials.

Using microbeams for sample excitation broadens XRF's usefulness because of the dramatic increase in spatial resolution. With single-bounce monocapillaries, the micro XRF (μXRF) resolution is the same as the monocapillary optic's spot size. This resolution can be 10 to 50 μm, depending on the monocapillary optic. For XRF, the x-ray spot size and flux are the important parameters; the divergence of the optic is not as important. An example of μXRF at CHESS includes environmental work done on fish ear stones [100]. Fish ear stones grow layers of bone as the fish ages, just like tree rings. X-ray microbeams make it possible to deduce where that fish has been at

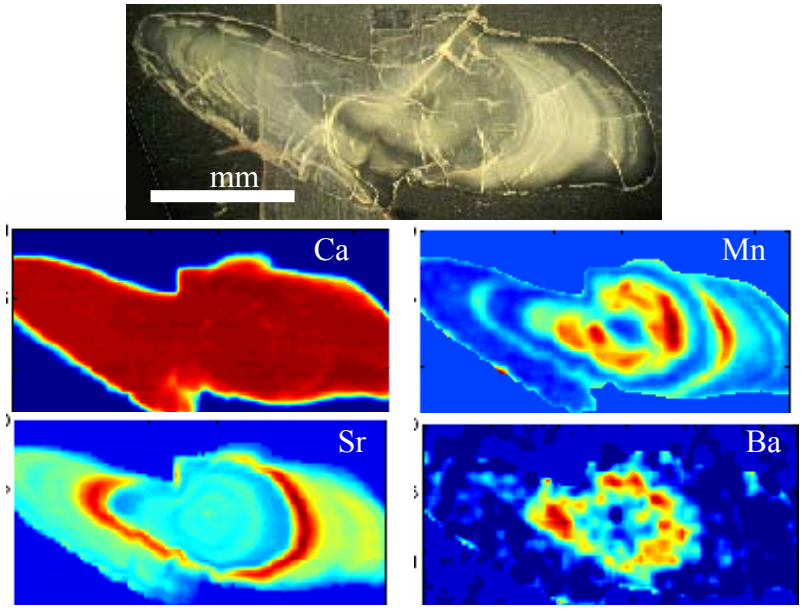

Figure 9.5 An image of a fish ear stone (top) and a array of elemental maps of the fish ear stone labeled by the element, at a resolution of 20 microns. In the strontium map, the red ring is the location of a higher concentration of strontium in a fish ear stone. The Sr ring is consistent with the fish going out to sea. This fish was born in fresh water (center of the stone), went out to sea for the winter (Sr ring), and then returned to a lower estuary (somewhat brackish water).

[54] Parts per billion is not simple because of x-ray fluorescent noise from the x-ray beam path, etc., which gives rise to false signals and artifacts.

different periods of its life by resolving the distribution of different trace elements in the fish ear stones as it aged (Figure 9.5). The fish absorbs different trace elements depending on the trace elements in the water in which it was living at the time. Other examples of samples that have used μXRF at the F3 station include tree rings[55] and soil samples [101][56].

In order to make elemental maps, the small excitation x-ray beam is positioned on the sample and a XRF detector records the spectrum. In order to make a two-dimensional map, the sample is rastered across the small beam, and the detector collects a spectrum for each spot, for 1 to 3 seconds per pixel. It takes several hours to make a μXRF map such as in Figure 9.5. At a resolution of 20 μm, the time needed to create a two dimensional map is about 40 minutes to 2 hours per mm^2. The time required to collect a spectrum presently limits the number of samples viewed with μXRF. This limit is set by the maximum count rate of the detector[57], which has its position set from the sample to maximize its count rate. The best solution for resolving the collection time problem is to increase the number of detectors in a multi-element-array, which would decrease the time it takes to make the map.

A second solution exists for decreasing the data collection time for samples with less stringent spatial requirements. Decreasing the resolution from 20 μm to 40 μm quarters the scan time to the range of 10 to 30 minutes per mm^2. An optic was created to make a larger 40-50 μm spot size[58]. These optics have a 6 mrad divergence and a 150 mm

[55] With John Chiment, Peter Kuniholm, Charles Pearson and Sturt Manning at The Malcolm and Carolyn Wiener Laboratory for Aegean and Near Eastern Dendrochronology.
[56] With Philippe Baveye and Astrid Jacobson from the Laboratory of Geoenvironmental Science and Engineering at Cornell University)
[57] A large 50 mm^2 active area Vortex-90EX® detector. SII Nanotechnology USA Inc. (www.siintusa.com)
[58] Most of the monocapillary optics have a spot size in the range of 10 to 20 μm.

focal length (F3_mr6f150_03,and F3_mr6f150_04, Table 4.2). The divergence was set so the optic could work up to 20 keV. The focal length (150 mm) was made very long for a single-bounce monocapillary optic. They are the longest focal length optics made by far. We chose a long focal length to decrease the magnification and increase the spot size to 40-50 μm. Figure 3.7 (Chapter 3) gives an example of increasing the spot size by increasing the focal length with another optical design. At G1, these long focal length monocapillary optics produced a spot size of 50(H)x25(V) μm^2

For a monocapillary standpoint, it would have been good if we had the option to produce a smaller spot size with the monocapillary. The spot size from an optic determines the best obtainable spatial resolution. Both Chapters 7 and 8 discuss our present attempts at improving the monocapillary optics to attempt to get optics with spot sizes of one μm and smaller. Overall, the single-bounce monocapillaries have been very good for improving the μXRF effort at CHESS.

The μXRF experiments were done at the CHESS F3 station, with D. Dale as the CHESS beam line scientist. The fish ear stone project includes K. Limburg and Ande Lochet as the CHESS user from the College of Environmental Science & Forestry at SUNY of Syracuse. Rong Huang, while at CHESS, was involved in the fish ear stones project.

9.4 Confocal X-ray Fluorescence on Antiquity Paintings

Confocal x-ray fluorescence (CXRF) is a technique used to find the elemental composition of a sample as a function of position, in three dimensions. This technique is capable of unearthing the elemental structures below a sample's surface. At CHESS,

CXRF has been primarily used to resolve different elements in the paint layers of antiquity paintings [102-104]. Because CXRF is a non-destructive technique, the sample does not need to be cut or modified in anyway. This is an advantage for samples which we do not want to modify or destroy, such as valuable museum paintings. In addition to paint layers, the CXRF technique has been used for a number of other studies as well. One such example at another synchrotron includes the three-dimensional placement of uranium in grains of material at nuclear blast sites [105].

CXRF uses x-ray optics to define a small viewable volume in space that the XRF detector can see. By limiting the volume of the detection region with two x-ray optics, the third dimension (the depth) of the sample's elemental composition can be resolved, such as a painting's paint layers. At CHESS, a single-bounce monocapillary is used as the excitation optic and a polycapillary is used as the detector's x-ray fluorescents collection optic. The monocapillary and the polycapillary are set at a right angle to each other. The monocapillary (PEB605) produces a focused beam of 15 to 20 μm, with a depth of field of a few millimeters (section 4.1.1), and an unattenuated flux of $\sim 2\times10^{11}$ photon/sec (on D-line) [102]. Polycapillaries may be designed with a wide range of focal properties. The most critical parameter, focal spot size, is approximately proportional to working distance, and to a lesser extent, the fluorescent x-ray energy. The polycapillary with the smallest spot size at CHESS has a working distance of 2.5 mm and a spot diameter of 15 μm at 8.0 keV. The polycapillary used for the measurements shown in Figure 9.7 has a working distance of 4.5 mm and a focal spot diameter that varies from about 25 μm at 10.5 keV to 67 μm at 4.5 keV, and has a large collection angle of approximately 15º [63,102]. The small spot and the large collection angle make the polycapillary the preferred x-ray optic for collecting florescent x-ray

events. The polycapillary's focus is placed at the monocapillary's focus to define a small detectable volume in space (Figure 9.6).

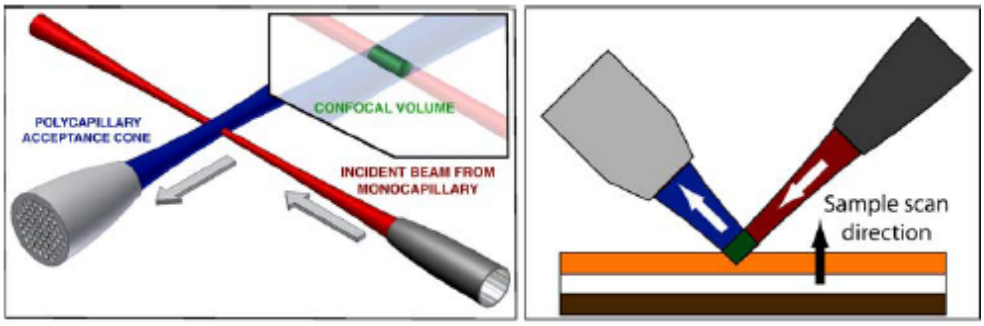

Figure 9.6 The diagram on the left shows how a small detection volume in space is created with both the monocapillary and polycapillary optics. The diagram on the right shows that this small volume can be used to resolve a layered structure. Since the confocal volume is about the same size as the paint layers, the composition of the different layers can be resolved (The confocal volume in green). The diagram was taken from reference [102].

Figure 9.7 shows a test layered paint sample measured using CXRF. This figure shows that the measured positions and thicknesses of this five-layered test sample, along with a cutaway view of the layered sample. The positions can be measured quite well using CXRF, and the thickness of the paint layers can be estimated[59]. The measurement of layer thickness depends primarily on the depth resolution of the instrument, corresponding to the size of the confocal volume projected along the vertical axis of Figure 9.6b. This depth resolution is measured by scanning metallic thin films through the volume. The thicknesses of these films are typically less than 1 μm, much smaller than the depth resolution being measured. Because of the energy dependence of the polycapillary spot size, the CXRF depth resolution also changes as a function of energy. In early tests, this confocal volume resolution changed from 55 μm at 2 keV to about 35 μm above 8 keV [102]. The spot size change, as a function of energy, can be seen in

[59] The thickness estimations are given in Figure 9.7c as the shaded regions of the plot.

Figure 9.7*a*; the streaks caused by the peaks in this image get narrower as the energy is increased, which represents a smaller spot size for the polycapillary, and a smaller confocal volume. More recently a depth resolution of 10 μm has been achieved at 9.7 keV.

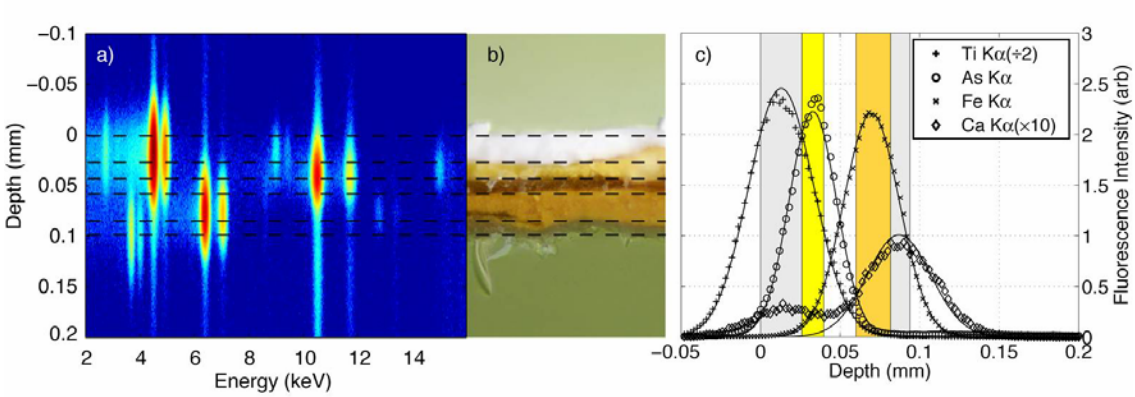

Figure 9.7 This figure consists of three parts showing some CXRF data taken from a test paint sample. Image b) shows the paint layered sample, from top to bottom, that consists of a titanium white (TiO_2) paint layer, orpiment (As_2S_3) , polyvinyl acetate (C,O, and H), iron oxide (Fe_2O_3), Chalk ($CaCO_2$), and the glass substrate. Image a) shows the XRF intensity signal (by color on a logarithmic scale) as a function of both the energy and the depth (the arsenic peak goes into the glass substrate). Graph c) shows the fluorescent peaks from different elements as a function of depth, with the shaded regions representing the best fit on the paint layer's thickness. The diagram was taken from reference [104].

The CXRF technique has been used on a few works of art, including *The Armorer's Shop*, a 17th Flemish oil-on-wood panel by David Teniers the Younger (1638-1687), and a 1918 illustration for the story, "*Mildest Mannered Man*" by Ben Ames Williams (Everybody's Magazine) hidden beneath the 1924 N.C. Wyeth painting "*Family Portrait*" (Brandywine River Museum). The paint layering information gives the art conservationist information about the painting that they could have only obtained by cutting into the work, such as the buried paintings color for "*Mildest Mannered Man*"

by Ben Ames Williams. CXRF has been an excellent tool for the study of paint layers of these antiquity paintings.

For these experiments, the monocapillary optic has worked well. It provides a large x-ray flux in a small spot, which is exactly what is needed. The resolution of CXRF is presently slightly more limited by the polycapillary than the monocapillary.

The CXRF experiments were done at both the CHESS A1 and D1 stations, with A. Woll as the CHESS beam line scientist, with C. Bisulca[1], J. Mass[1,2], M. Cushman[1], N. Ocon[2], and B. Brown[2] as the CHESS users from the University of Delaware[1], and Winterthur Museum, Garden and Library[2], Winterthur, DE.

9.5 Confocal X-ray Fluorescence with a "Football" Monocapillary

This CXRF experiment used a single bounce-monocapillary optic for both the excitation and the collection optic. The motivation for this was we desired to measure the tin K_α line, at 25 keV. The polycapillary that we had at the time did not work very efficiently up to this energy. For this experiment monocapillary BSG644 (4.3 mrad divergence, 52 mm focal length) was used for the excitation optic, with a spot size of about 20 μm. Section 3.3 gives an example of designing a monocapillary optic for exciting the tin K_α line at D line. Monocapillary BSG644 is a close match to this design.

Using a monocapillary as a collection optic has a severe disadvantage compared to the polycapillary optic. The polycapillary can potentially collect x-rays up to 20º, whereas the monocapillary can collect up to 4.5 mrad (0.25º) at 25 keV (Sn K_α). We knew the

polycapillary would be vastly superior as a collection optic at lower fluorescent energies. We did not know how they would compare at higher fluorescent energies, where the polycapillary's efficiency dropped.

Initially during the run, we tried to use a standard monocapillary optic as the collection optic, with a large, greater than one meter, source-to-focus distance. The long source-to-focus distance optic as a collection optic did not work. We decided that the shortest source-to-focus distance monocapillary optic would be a better choice. I made a 4.5 mrad, 50 mm focal length, 140 mm optic length, 300 mm source-to-focus "football" monocapillary optic (section 7.2.2).

This optic was used in the CXRF configuration (Figure 9.8, left). A thin 6 μm lead foil was passed through the confocal volume of the two monocapillaries. An X-Flash® XRF detector observed the fluorescent Pb La fluorescence line at 10.5 keV. At the other foci of the football monocapillary, slits defined the observable volume through the football monocapillary (Figure 9.8, left). As the slits were narrowed, the resolution, or size of the confocal volume became smaller (Figure 9.8, right). By way of comparison, the monocapillary's count rate was down from the polycapillary's rate by an order of a few hundred, which is roughly equivalent to the difference in the collection solid angle between the two optic's.

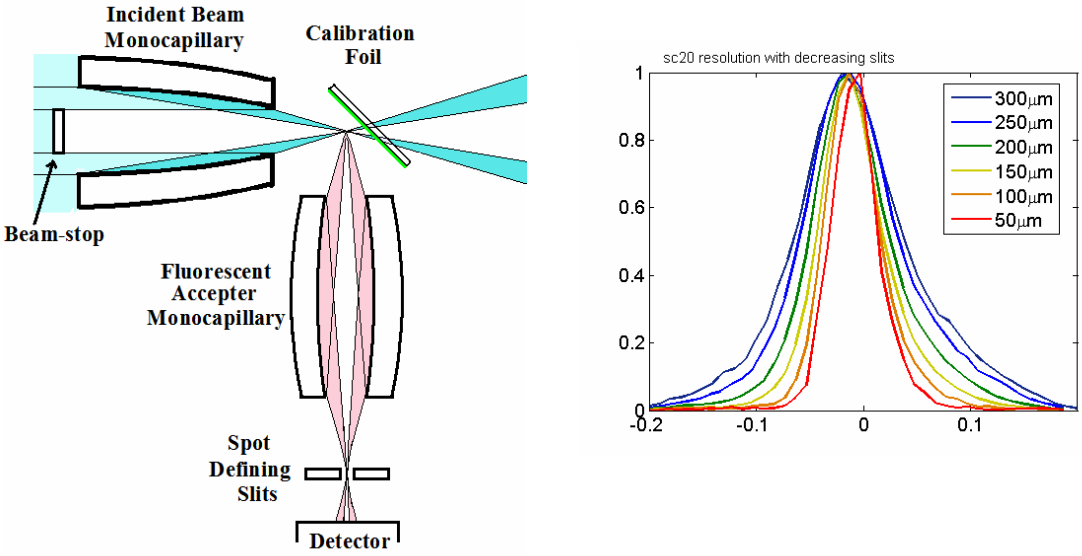

Figure 9.8 The left diagram shows a sketch of the CXRF test done with two monocapillary optics. The confocal volume was measured with an XRF detector, as a thin 6 μm Pb foil was passed through the confocal volume. Spot defining slits at the second foci of the football shaped collection optic controlled the viewable size of the confocal volume. The graph on the right shows the CXRF resolution as a function of the slit sized opening. A resolution of ~120 μm FWHM was achieved with a 300 μm slit setting, and a resolution of ~50 μm FWHM was achieved with a 50 μm slit setting.

Since this initial test, we have not gone back to using a single-bounce monocapillary optic as the collection optic for CXRF. A new polycapillary optic has been acquired which is much more efficient up to 30 keV. Nevertheless, this experiment was successful for a number of reasons. This was the very first optic that we made with a very short source-to-focus distance; it broke some new design territory for CHESS's monocapillary development. The short source-to-focus optics could have a number of potential uses with x-ray tube based sources (section 7.2.2). We have also shown that it is feasible to use the monocapillary optic as the collection optic in CXRF.

Also, this project exemplifies the advantages of having optical fabrication capabilities on site with the synchrotron x-ray source. The "football" shaped optic was created during the run, as a solution to unforeseen problems. Without the fabrication on site, this project would have been unsuccessful.

This experiment was done at CHESS A2 station in cooperation with A. Woll (at CHESS) and C. Bisulca as the user from the University of Delaware. Alex Kazimirov was the CHESS beam line scientist.

9.6 Micro Protein Crystallography

Using single-bounce monocapillaries to provide small beams for small protein crystals has been going on for a number of years at CHESS [40,63,64]. For micro-protein crystallography, the monocapillary provides an increased flux density in a small spot with adequate angular resolution. The ability to collect diffraction data sets from smaller protein crystals is important for crystallography work. Crystallizing proteins is the largest present bottleneck for solving protein structures. Some proteins simply do not crystallize. For other proteins, it is very hard to grow crystals to a size of 100 μm in diameter or more, which are needed for diffraction studies using a collimator. Producing smaller x-ray beams with higher flux densities for crystallographic work is one partial solution to this problem.

All the major parameters of the optic – divergence, flux and spot size – are important for protein crystallography. The optic's divergence has to be small enough that diffraction spots from large unit cells do not overlap. The optic's spot size needs to be about the same size as the crystal, to maximize the flux on the crystal, and to minimize

background scattering from the cryoprotectent surrounding the crystal. The flux density needs to be large enough to get diffraction spots from the small crystal. If the crystal size volume drops by a factor of a thousand (from a 100 μm to 10 μm sized crystal), the x-ray flux needs to grow by this same factor in order to get the same intensity in the diffraction spots. Increasing the flux density increases the radiation damage to the crystal. As the crystal is damaged by radiation, the intensity of the diffraction peaks weakens. The point at where the diffraction intensity is half the original intensity is called the Henderson limit, with a radiation dose of about 2×10^7 Gy (J/kg) [106-108]. There is a delicate balance between increasing the x-ray flux to get diffraction, and destroying the crystal through radiation damage.

The two optics presently used by MacCHESS for micro protein crystallography have already been discussed in sections 3.4.3 and 4.3.2, and the basic setup is discussed in section 5.1.3. Monocapillary f1b-mr9f20-01 is a 7.5 mrad optic with a 22 mm focal length and SF202 is a 2 mrad optic with a 22 mm focal length. At F1, without any upstream slits, both of these optics produce a 15 to 20 μm spot size (section 3.4.3 and [64]). Each optic has its own advantages and limitations. SF202 is adequate for many small crystals, and f1b-mr9f20-01 is available if a higher flux is needed at the cost of a decrease in angular resolution (section 4.3.2). Capillary SF202 also has the advantage of a small tip ID of 44 μm, therefore this optic does not really need a capillary beam-stop, which simplifies alignment. The disadvantage is that it has a somewhat small gain of 10-12 (compared to other monocapillary optics). Capillary f1b-mr9f20-01 can be tuned to a desired divergence. This increases the complexity of the line-up, especially since the slits and the capillary beam-stop are mounted on the optical table in the MacCHESS setup (section 5.1.3).

Microbeams have been used on a number of different crystals at CHESS. Figure 9.9 shows one example pattern from a lysozyme crystal taken with a microbeam created with a monocapillary optic. The microbeam has been used to solve a number of small

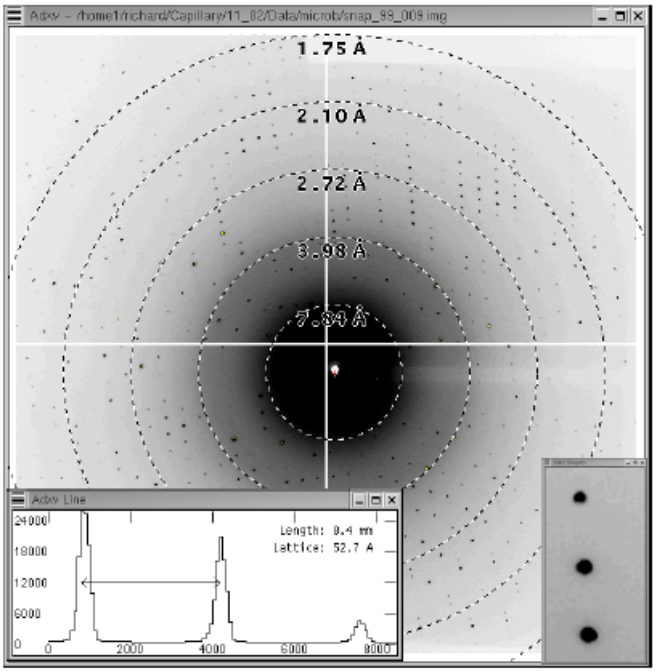

Figure 9.9 Monochromatic diffraction spots from a twenty-second exposure of lysozyme, out to a 1.75 Å resolution with an overall R-sym of 5.6 %, with a 17(H)x14(V) µm spot size. The image was taken from reference [63].

crystals at CHESS, such as a dry mounted < 3 x 20 x 80 μm^3 one-time irreproducible microcrystal (natural product, insect pathogen, possible antibacterial) [109,110]. Using the x-ray microbeam, diffraction spots have been recorded off a crystal as small as 1-2 µm in diameter and 60 µm in length at CHESS's F1 Station. These peptides that form Amyloid fibrils can only be grown as needles 1-2 microns in diameter. These crystals represent a unique challenge to U.S. synchrotron sources due to their extreme small size. With these extremely small crystals, background reduction, including eliminating the background from air scatter, is absolutely needed. MacCHESS has made an enclosed helium box, which surrounds the monocapillary, the protein crystal sample,

and the air path up to the detector beam-stop, to eliminate the air scattering while collection diffraction patterns from these extremely small crystals.

In addition to small crystals, microbeams are sometimes an advantage for some larger crystals and clusters of crystals as well. The small beam can sometimes be used to pick out regions within a larger crystal have better scattering characteristics then the entire crystal or crystal cluster. One example of a large 300- 400 μm crystal using a small beam to find a better quality spot in the crystal is a clathrin terminal domain (TD) + PI3KC2a fragment [111].

For a monocapillary standpoint, again, it would have been good if we had the option to produce a smaller spot size with a higher flux density. In this situation, the upstream optics of both F1 and F2 are more restrictive on the achievable spot size then the monocapillary optic is (section 3.4). Overall, the single-bounce monocapillaries have been very good for the micro protein crystallography efforts at CHESS and MacCHESS.

Micro protein crystallography experiment are done at both the CHESS F1 and F2 stations, with R. Gillilan as the MacCHESS beam line scientist, and M. Cook as a MacCHESS research specialist.

9.7 μSAXS on Time Resolve Protein Folding in Solution

Another technique that can take advantage of having a small micron sized x-ray beam is Small Angle X-ray Scattering (SAXS). SAXS is an x-ray technique used to probe feature sizes in materials ranging roughly from 3 to 300 nm. At CHESS, the time-

resolved protein and RNA folding in-situ experiments were our initiation into combining microbeams with SAXS (μSAXS) [112,113].

The intent of the μSAXS time-resolved studies is to measure the size of either a protein or RNA as it folds over time in a solution. The sample continuously flows down a small, sample-containing capillary. As the sample flows through the capillary, its size changes as it mixes in a buffer solution[60] (Figure 9.10). μSAXS measures the size of the protein or RNA in the solution. The positions of the x-ray microbeam along the flow gives timescale of the size changes (Figure 9.10).

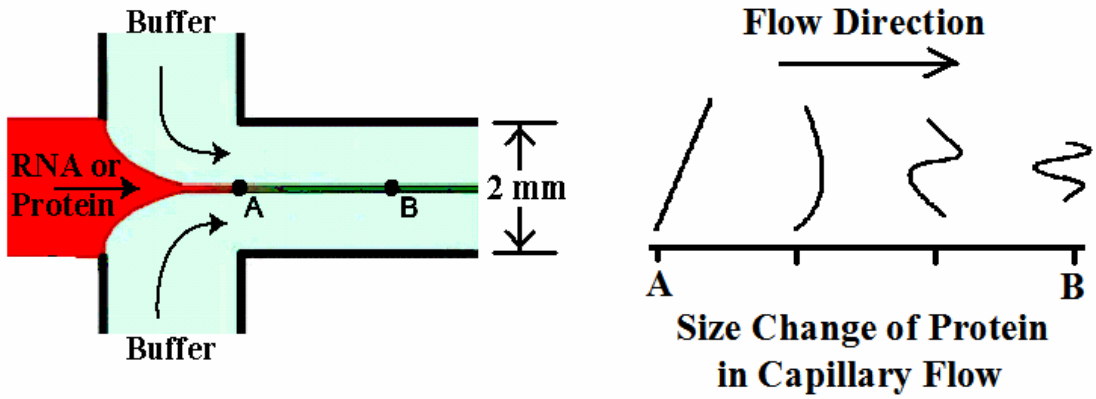

Figure 9.10 The left diagram is of sample cell in which the protein or RNA sample is mixed. As it is mixed, it flows down the tube. At point '*A*' the sample comes in contact with the buffer, and starts to fold, or change shape. At point '*B*' the sample has been in contact with the buffer for a longer period of time, therefore, the amount of folding is more pronounced. The reaction time for the folding is determined by knowing the velocity of the flow, and the distance between points '*A*' and '*B*'. The diagram on the right shows a cartoon of how protein or RNA may change shape as it flows from point '*A*' to point '*B*'.

There are a number of reasons for using an x-ray microbeam for this experiment. The major reason was to increase the time resolution of the experiment. The positional

[60] Light exposure on light-sensitive proteins has been used to start this change as well.

resolution from the x-ray microbeam is small (13 μm); this provides better time resolution because the time resolution is a convolution of beam size and the width of the fluid in the stream. The beam needed a spot size smaller then 0.1 mm, in order to obtain the desired time resolution. We could not get the required intensity with a slit setting less than 100x100 μm^2, to both get a larger signal-to-noise ratio and to conserve the limited sample supply. The x-ray microbeam however, provided a large 60x gain (higher flux density), which allowed for adequate exposure times with a satisfactory signal-to-noise ratio.

Monocapillary BSG644 (4.3 mrad divergence, 52 mm focal length) was used for the feasibility μSAXS study[61]. In this experiment only a small portion of inner surface of the monocapillary was illuminated. This was done for two reasons, to create a beam with a smaller divergence, and to help eliminate parasitic scatter from the optic. The feasibility study measured optical performance, the time resolve information was not collected for this experiment. A comparison was made between the monocapillary optic and 100(H)x100(V) μm^2 slits, at a x-ray energy of 9 keV with a 1.5% energy bandwidth. This setup was tested on a powdered silver stearate calibrant and a solution of heme protein cytochrome c, used at a rate of 0.1 ml per minute in a flow cell (Figure 9.10). The advantages of using the optic was a 30% higher signal intensity in a much smaller spot of 13 μm. This corresponds to a 60x increase in the flux density. There was only a small decrease in angular resolution (Figure 9.11).

[61] Reference [112] comprised this μSAXS microfocusing optics study using a powdered silver stearate calibrant and a solution of heme protein cytochrome c.

For the feasibility study, the flow cell channel was 2 mm and the size of the sample flowing within the center of the cell was 0.6 mm. A 1 mm flow channel with the sample stream about 300 µm wide is presently being used. With the small spot provided by the monocapillary optic, even smaller scale micro-flow cells could be used [114].

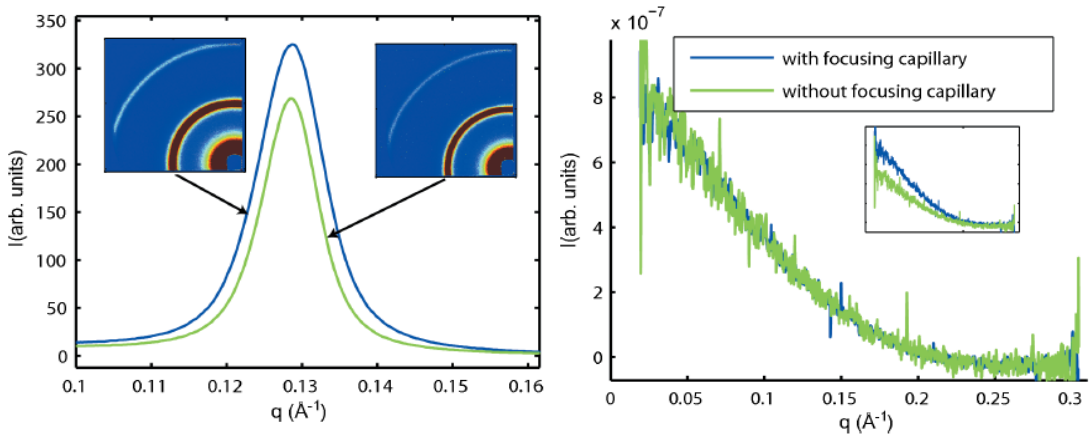

Figure 9.11 The left graph (which includes two µSAXS images) compares the resolution and intensity from the 100x100 µm slits and the monocapillary (with a 13 µm spot size) on a 10 sec. exposures of silver stearate, a calibrant. The FWHM for the silver stearate peak was 0.0046 Å^{-1} for the slits and 0.0053 Å^{-1} with the monocapillary; this angular resolution does not limit the measurements. The right graph compares the resolution and intensity from the 100x100 µm slits and the monocapillary on 60 sec. exposures of heme protein cytochrome c. The unfocused beam has been rescaled upward by 30% to match the intensity from the monocapillary, the inset diagram shows the same graph before scaling. This verifies the information collected from the monocapillary and the slits are not different, therefore the capillary could be successfully used to collect SAXS information. The diagrams were taken from reference [112].

From an optics standpoint, we learn a great deal about make a successful µSAXS experiment from this experiment. This µSAXS experiment is a large reason that I made the x-ray microbeam breadboard a priority (section 5.1.2). The auxiliary equipment needed for this experiment was inadequate. There was not the required room needed to position a small aperture, to block both the parasitic scattering from both the air and the

glass at the monocapillary optic's tip. Getting rid of this unwanted scattering proved to be extremely difficult without a small cleanup, or guard slit aperture after the monocapillary optic. In addition, there was not the required room for a microscope to observe the sample position. Much of the success we have had in our present μSAXS work is a result of the lessons learned from this initial experience at D-line (section 9.11).

The time-resolved folding experiments were done at both the CHESS D1 and G1stations, with both A. Woll and D. Smilgies as the CHESS beam line scientists, and with Jessica Lamb as the main CHESS user from Lois Pollack's group at Cornell University. Others who have been involved from Dr. Pollack's group are K. Andresen, L. Kwok, H.Y. Park, X. Qiu and Suzette Pabit.

9.8 Time-Resolved Powder Diffraction of Reactive Multilayer Foils

In this experiment, extreamly fast phase changes are measured for reactive metal multilayer foils in the time-resolved powder diffraction experiments [115,116]. Reactive multylayer foils are made of exothermic materials, which when ignited, react very quickly to form an alloy (Figure 9.12). The reaction front propagates at a speed of >1 m/s, with a reaction zone ~100 μm in size [115]. The motivation for studing the reactive foils is the brasing or joining of heat sensive materials materials and, scientifically, the opportunity to study phase transformations in the presence of high-heating rates (>1e6 K/s) and large concentration gradients.

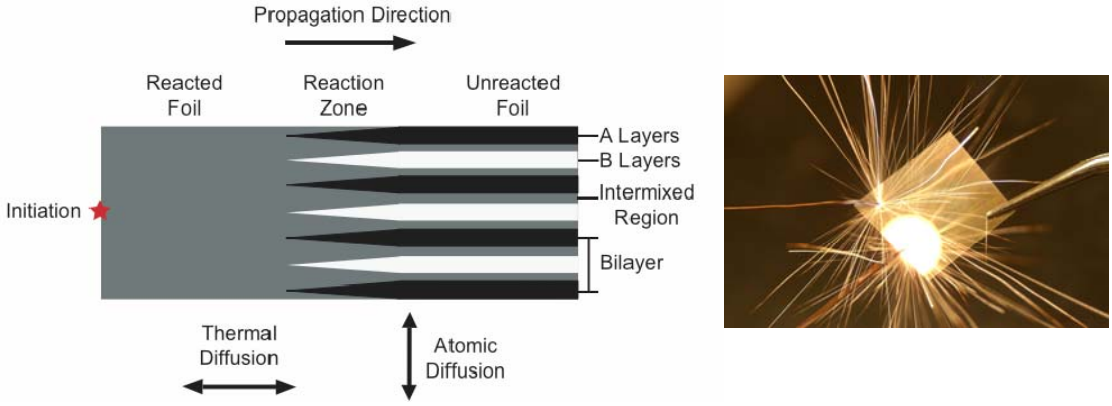

Figure 9.12 The diagram on the left shows a foil during the reaction. Some of the properties of the reaction are the multilayer structure experiences atomic diffusion normal to the multilayer foil, and the reaction propagates from an initiation point. The image on the right shows a quick snap shot of the foil during the reaction. The diagram and image was taken from reference [115].

This *in-situ* experiment requires a very fast area detector, a very high flux x-ray beam in a small spot and a controlled divergence for diffraction. Previously, the phases of this reaction zone were studied by quenching or annealing of the foils, and examining the foils afterward [117]. In order to measure the phases changes of the multilayers *in-situ,* the diffraction powder patterns had to be taken on the microsecond time scale. The pixel array detector recorded the Debye rings. This detector is capable of one microsecond exposures for up to 8 frames [22] (section 1.3) [62]. In order to maximize the flux in a small spot, the upstream optics at the A2 station used a large bandwidth multilayer (1.9%) that focused the 8.2 keV beam. This prefocused beam was focused down further to a 42(H)x 28(V) μm^2 FWHM spot using monocapillary PEB605 (8 mrad, 55 mm focal length). The measured flux of the beam before the monocapillary optic was ~4×10^{13} photons/s. The total flux through the optic was measured to be ~1×10^{13} photons/s. This gives an extremely high flux density of ~9×10^{9} photons/s/μm^2 (~9×10^{15} photons/s/m^2). With this high flux, only about 1×10^{7} photons are left for a

[62] Detector is 15 mm by 13.8 mm with 100x92 pixels (150 µm pixel size).

one-microsecond exposure time, which is roughly equivalent to a one-second exposure with an x-ray tube.

In order for the powder diffraction patterns to be resolved, the pixel array detector had to be positioned to see the appropriate peaks and the monocapillary optic had to have a divergence that allowed the peaks to be resolved. The peak widths of the Debye rings are about 0.08 $Å^{-1}$ (0.6º or 10.4 mrad) wide FWHM (Figure 9.13). The widths of the diffraction peaks are influenced by two effects, the divergence of the monocapillary optic and the bandwidth of the x-ray beam. The width of the peaks caused by the bandwidth of 1.9% at 8.2 keV is about 0.5º (at $\theta_{Bragg} = 21º$). The capillary had a divergence of 8 mrad (0.46º), and contributes that amount to the angular width of the diffraction peaks. Together, they combine for the measured width of ~0.6º FWHM for the integrated diffraction powder peaks (Figure 9.13). The detector was set back from the focal spot by ~20 mm, this gave a peak FWHM of about 1-2 pixels on the detector[63]. The detector captured about 15% of the arc Debye ring's arc [115].

Much like the μSAXS flow cell experiment in section 9.7, the time resolution of the experiment is linked to the position and the spot size of the x-ray beam. The spot needed to be smaller than the estimated reaction zone, which is about 100 μm in size. With the 40 μm spot size and the reaction zone moving ~ 1 m/s, about a 40 μs swath of reaction time is covered by the 40 μm beam in one μs. The pixel array detector was timed with the foil's reaction front to gather diffraction patterns at specific times relative to the reaction front's position.

[63] See section 1.5.1, example 2, for a very similar example of matching the divergence to the detector.

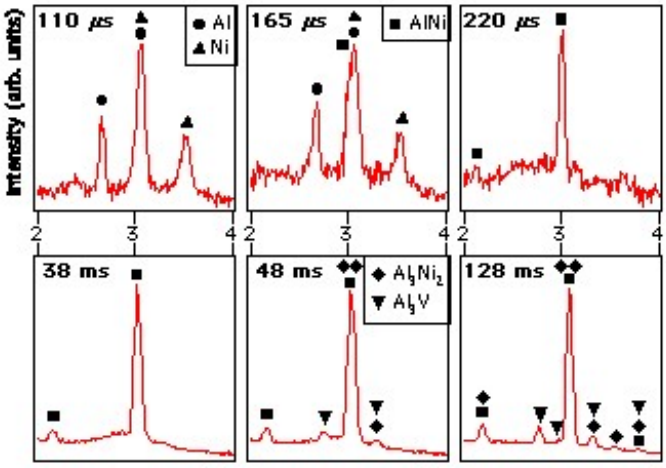

Figure 9.13 Diffraction peaks measured from Al/Ni multilayer foils during and after the reaction. The horizontal axis is in the scattering vector q, ($Å^{-1}$). A 50 μs exposure time was used for the top row of diffraction patterns and a 5 ms exposure time was taken for the bottom row. The timing of the pattern is in the upper left corner of each graph, and each peak of the graph is labeled according to its phase. The diagram was taken from reference [115].

Figure 9.13 shows the diffraction peaks integrated from the Debye rings taken at various times during and after the Al/Ni multilayer foil reaction. From these diffraction patterns the phase changes and the time scale of these changes where measured. The foil's Al and Ni original phases disappear after about 200 μs, afterward an amorphous/liquid phase plus AlNi phase coexist, and it settles into its final Al_3Ni_2 phase after about 50 ms [115,116]. No metastable intermediate phases were observed, as other quenching studies suggested [117]. Zr/Ni foils where also studied, which the reaction temperature always remains below the melting point of both constituents. In contrast, the reaction temperature exceeds the melting point of Al in the Al/Ni foils.

In this experiment all the components were needed to be successful; A2's high flux, the monocapillary's small spot and increased flux density, and the pixel array detector's fast exposure time. This experiment used all the advantages the monocapillary optics

provide fully. The monocapillary optic is achromatic (useful for the 1.9% bandwidth), it can be used with upstream focusing, and had an adequate divergence control for resolving the required diffraction peaks. This experiment provides the highest flux (~1×10^{13} photons/s in 42(H)x 28(V) μm^2 FWHM spot) and flux density (~9×10^{9} photons/s/μm^2) in a small spot that I know of at CHESS.

This experiment was done at the CHESS A1 station, with A. Kazimirov as the CHESS beam line scientist, with L. Koerner and M. Tate taking care of the PAD detector from S. Gruner's Group at Cornell University. The CHESS users are J. Trenkle, T.Weihs, and T. Hufnagel from the Department of Material Science and Engineering at John Hopkins University.

9.9 Monocapillaries at Advanced Photon Source (APS)

Most of the information in this section came from a manuscript in preparation for submission to the Journal of Synchrotron Radiation [118].

In this experiment, we aimed to compare the advantages and disadvantages between a single-bounce monocapillary and a set of 100 mm long KB mirrors on undulator beamline 18ID at the BioCAT sector. The KB mirrors are presently used to make microbeams on this beamline. The monocapillary was tested, in collaboration with Dr. R. Barea (BioCAT) and R. Huang (IMCA-CAT) to see if it was feasible to use monocapillary optics for both μXRF and micro x-ray absorption near edge structure (μXANES) experiments.

The x-ray beam was prefocused with a sagittal focusing double crystal monochomator and a bimorph mirror, to a size of 195(H)x125(V) μm^2 , and a total flux of 1.18×10^{13} photons/s [118,119]. The size of the prefocused spot is energy dependant, ranging from 195(H)x125(V) μm^2 (at 9 keV) to 221(H)x100(V) μm^2 (at 12 keV) FWHM.

The monocapillary used was f1_mr9f20_02, (7.5 mrad divergence , 24 mm focal length, Table 4.2). At G-line, this optic produced a 10.8(H)x9.2(V) μm^2 measured with a 5 μm pinhole using the full optic, and a 5(H)x9.2(V) μm^2, using a quarter of the inner optical surface (section 4.3.2). The monocapillary optic was placed at the focal point of the pre-focusing optics in three different configurations, one with the direct beam aligned with the optic, and others with the direct beam on either the top or bottom side of the optic[64]. With the monocapillary on center, the spot size was 12.3(H)x10.1(V) μm^2 measured with a knife edge fluorescence scans, with a flux of 1.77×10^{12} photons/s at 12 keV and 1.50×10^{12} photons/s at 9 keV. With the monocapillary off center, on the bottom section, the spot size was 10.1(H)x9.1(V) μm^2, with a flux of 3.09×10^{12} photons/s at 12 keV and an flux of 3.30×10^{12} photons/s at 9 keV. This amounts to about 30% of the total flux from the undulator. The signal through the optic was additionally tested to see how the flux changes as the energy is tuned by the upstream optics. The intensity is stable over a ~400 eV range, which is adequate for XANES measurements. Above this range the intensity dropped quickly because the prefocus spot moved off the base of the monocapillary optic while tuning the energy.

[64] With the monocapillary beam-stop in place.

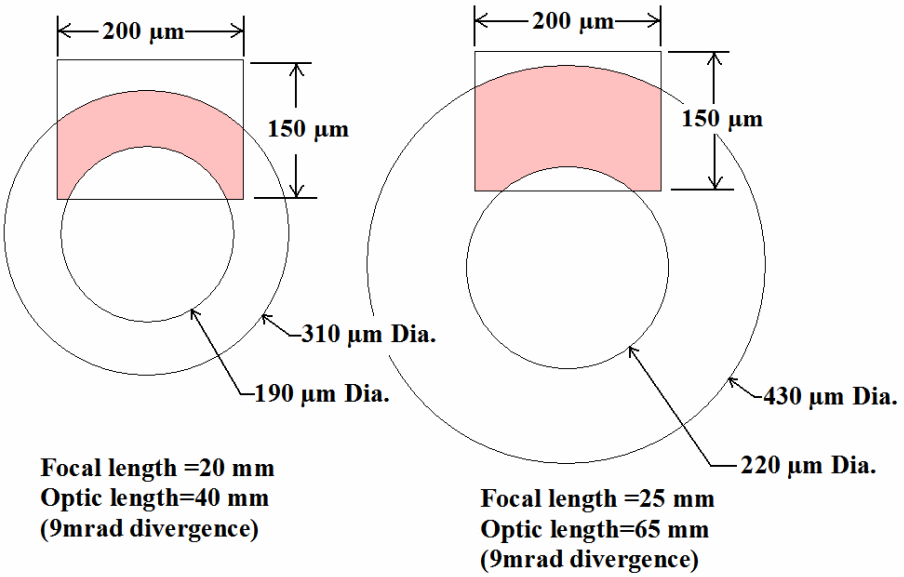

Figure 9.14. The left drawing shows the crossing of the monocapillary f1-mr9f20-02 tip and base ID's with the approximate size of 18ID's prefocused beam. The cross sectional area gathers ~45% (in pink) of the prefocused beam. The right drawing shows the crossing of the alternately designed optic which may have a slightly larger spot size but increases the cross sectional area up to 80%. Such a design may be able to double the total flux.

When the KB mirrors are used, the beam at 18ID is not prefocused. The KB mirrors have an acceptance area of 0.4x0.4 mm^2, therefore most of the incoming beam is wasted. The KB mirrors are able to focus the beam down to a 5 µm size with a total flux of 3.0×10^{11} photons/s at 12 keV. The monocapillary, in conjunction with upstream focusing is able to produce ten times more flux then the current set of KB mirrors [118].

This setup has not yet been completely optimized, from a monocapillary point of view. Another monocapillary optic design may be able to double the flux (see Figure 9.14). Also, a more accurate capillary beam-stop is needed. The current beam-stop is over sized, which blocks part of the capillary's inner surface, thereby reducing the flux (Figure 9.15).

Figure 9.15 Three images showing the far-field patterns from monocapillary f1-mr9f20-02 taken at APS, beamline 18ID. The image on the left shows the entire far-field pattern (compare to f1b-mr9f20-01 in figure 4.4, an optic of the same design). The middle far-field pattern has the beam block in place. The ragged edge at the top of the far-field is due to the slightly oversize, non-ideal beam stop. The figure on the right shows the full far-field pattern after spending time in the undulator beam. Something has changed the optic's surface in that time.

Another observation made was the optic's far-field pattern changed during the tests (Figure 9.15). Possibilities for the odd looking pattern are i) formation of deposits on the monocapillary's surface in the intense x-ray beam ii) changes in the structure of the glass and local bending by heating, or perhaps some other mechanism. At this point, the origin of these distortions are unclear since this has been our first experience with this phenomenon.

Monocapillary optics have only occasionally been used at the 3rd generation synchrotron sources. Because the monocapillaries are achromatic, and have a high reflectivity, they are able to work with upstream focusing. This allows them to have considerable promise for experiments at 3rd generation sources that need a high flux and a small spot.

This experiment was done at the 18ID beamline, by Raul Barrea[1,2], Rong Huang[3] and Tom Iriving[3]. They are from the Biophysics Collaborative Access Team[1], the Dept. of Biological Chemical, and Physical Sciences at the Illinois Institute of Technology[2] and IMCA-CAT at Argonne National Laboratory[3].

9.10 A Study of Fresnel Zone Plates

In this section, I shift to our experience testing Fresnel zone plates at CHESS[65]. I am including this section for two reasons; to compare the functionality of the zone plates to single-bounce monocapillaries, and to show that zone plates are able to image the synchrotron source. The ability to accurately image the source and record its size would be very good for estimating the spot size and the slope errors on the capillary optics (sections 3.3 and 4.1.3). Having a zone plate to image the source is a good reason to have a zone plate.

Both one-dimensional and two-dimensional zone plate lens were tested, all of which resided on a single 18x25x0.6 mm^3 silicon chip (Figure 6.17). Avantes Gmbh, Germany, produced the zone plates. Figure 6.18 shows a cross-sectional diagram of the zone plate with all the critical dimensions labeled. I will cover one zone plate, named '(33) circular'. This zone plate's total thickness 'Tm' is 80 μm, the phase zone profile 'h' is 16 μm, the diameter 'A' is 194 μm, and a width of outer most zone 'dr_n' is 0.4 μm. It has 122 zones, it was designed for the energy range of 11 to 21 keV, and a maximum efficiency 'η_e' of 26% at 14 keV.

[65] Section 1.4.2 includes a number of references for x-ray zone plates.

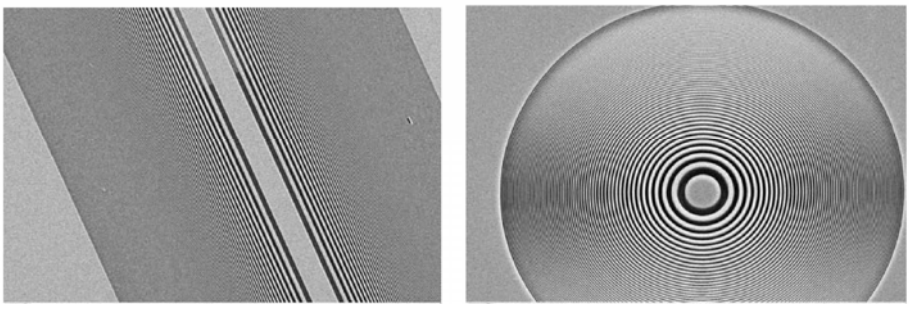

Figure 9.16 An image of both a liner and a circular Fresnel zone plate. The circular zone plate has a 194 μm diameter.

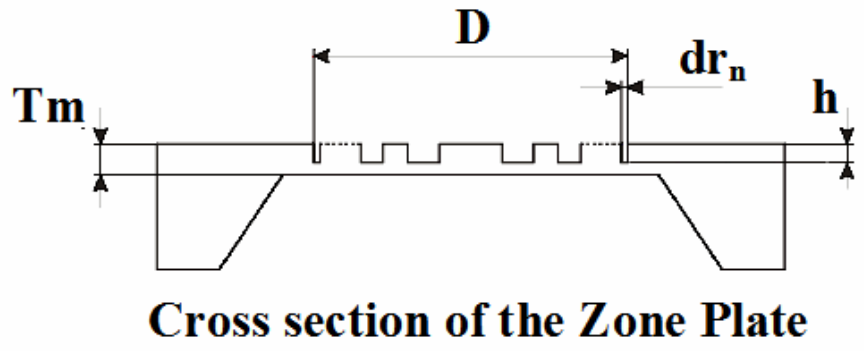

Figure 9.17 A cross-sectional diagram of a Fresnel zone plate with all the critical dimensions labeled.

For the A2 tests, W/B4C multilayers with a d-spacing of 20 Å were used, set to 14.727 keV ($\Delta E/E \approx 0.5\%$). This energy gave a phase shift of ~0.9π for the 16 μm silicon layer phase zone profile of the zone plate (the target value is π for the maximum efficiency). The source size is 2.88(H)x0.32(V) mm^2, and the zone plate was placed 38.6 m from the source in the A2 hutch. Zone plates have a focal length (for the first order focus) and a divergence (or numerical aperture) given by [2]:

$$f \cong \frac{D \cdot dr_n}{\lambda} \tag{9-1}$$

$$NA = \sin(\theta) = \frac{r_n}{F} = \frac{D}{2F} \approx \frac{\theta_{div}}{2} \tag{9-2}$$

Where 'f' is the focal length, 'θ_{div}' is the full divergence angle, and 'θ' is half the full divergence angle ($\theta_{div}=2\theta$), and the other variables are listed above. For zone plates, the focal length and divergence is energy dependant. For the zone plate '*(33) circular*', this gives as focal length of 0.92 m and a divergence of ~ 0.2 mrad at 14.74 keV. Equations 2-1 and 2-2 can be used to find the optic-to-image length and the magnification of the zone plate:

$$i = \frac{f}{1 - \frac{f}{s}} \qquad M = \frac{i}{o} = \frac{s_i}{s_o} \tag{9-3}$$

With 'o' as the object-to-optic distance, 'i' as the image-to-optic distance, 'M' is the magnification, 's_o' is the object size, and 's_i' is the image size. The "thin lens" equation has been rearranged to give the optic-to-image length. The Fresnel zone plate is an imaging optic, unlike single-bounce monocapillaries (section 2.3), therefore the image has the shape of the source. For zone plate '*(33) circular'*, the demagnification is i/o=0.94m/38.6m= 0.024, which gives an estimated image size of 70(H)x8(V) μm^2 for A2. The resolution of the zone plate is [2]:

$$r_{null} = \frac{0.610 \cdot \lambda}{NA} = 1.22 \cdot dr_n \tag{9-4}$$

Where 'r_{null}' is the minimum resolvable feature size of an ideal lens. Since the resolution limit is 0.5 μm for our zone plate, the spot size should not be resolution limited.

In the beam, the Fresnel zone plate had a measured spot size of 70(H)x15(V) μm^2, measured with a 5 μm pinhole (Figure 9.18). The image size suggests that the source is twice as big in the vertical direction than the expected value. This result would need additional testing to verify if the lens is working correctly or if the source at A2 is really twice as big as expected. Also, the measured gain of ~5 is a little bit lower the expected gain of ~7. The estimated gain is calculated with:

$$G \approx \frac{A_Z}{A_i} \eta_e \tag{9-5}$$

Where 'G' is the gain, 'A_z' is the area of the zone plate, 'A_i' is the area of the image and 'η_e' is the zone plate's first order peak efficiency (which is energy dependent).

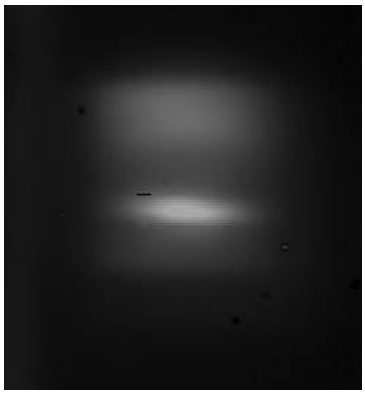

Figure 9.18 This is the zone plate's image of the source at A2, taken with the GGG fluorescent screen. The bright line in the center is the image, the overall square is from the upstream slit setting.

The zone plate may prove to be adequate for measuring source sizes. This particular zone plate would not be extremely useful for other microbeam uses at CHESS. It has a

spot size that is larger and a gain much smaller then most of the single bounce monocapillaries at CHESS.

I investigated some of the commercially available zone plates at Xradia, to find a design which may be more suitable for CHESS beam lines at CHESS's favorite energy of 10 keV. At 10 keV, the width of the outer most zone, 'dr_n', is limited to 0.1 μm [66]. I picked a zone plate diameter of 320 μm, to give a reasonable focal length of 26 cm and to have an area on a similar size to many monocapillary optics, i.e. to have a similar impingent flux on the optic. Diameters of the zone plates at Xradia ranged of 160 to 4000 μm, giving focal lengths of 13 cm to 3.2 m at 10 keV respectively. This alternate zone plate should give a spot size of 19(H)x 4(V), a divergence of ~1.2 mrad, and a gain of ~300 at A2 (assuming a 2.88(H)x0.64(V) mm^2 source size and a 30% efficiency). By inspecting the monocapillary optics in Table 4.2, the spot size, and gain fit well within our present capabilities with the single-bounce monocapillary optics. The major advantage of the zone plate is it has smaller divergence.

In looking at the microbeam experiments talked about in this chapter, the zone plate would not work for Laue Micro Protein Crystallography (section 9.13). For micro protein crystallography (section 9.6), and time resolved powder diffraction, (section 9.8) the monocapillary optic provides more flux than a zone plate could, which is quite critical for these experiments[67]. In μXRF (section 9.14) and CXRF (section 9.14), a zone plate has no clear advantages. If the exitation energy is changed during runing (which is quite common), a monocapillary is much more convenient, since the focal spot does not move. For the μSAXS experiments (sections 9.7 and 9.11) the zone plate may be a better option, since it has a low divergence with a higher gain. A comparison

[66] Values for the estimates come from Xradia's advertised x-ray zone plates (www.xradia.com).
[67] This includes the source size restrictions for the F2 station.

between single-bounce monocapilaries and Fresnel zone plates might be worth the effort in the future. For μHRXRD, a zone plate is an advantage (at APS), because the zone plate is capable of producing a smaller spot size [95].

In conclusion, zone plates could work adequately for some microbeam applications at CHESS but not all of them. The largest advantage at CHESS is the zone plate images the source, which would allow an easy way to monitor and measures source spot size's at CHESS.

The Fresnel zone plate experiment was done at CHESS's A2 station with A. Kazimirov.

9.11 μSAXS and μWAXS

Most of the information in this section will be compiled into a manuscript for submission at some future time [120].

The μSAXS and micro wide-angle x-ray scattering (μWAXS) are a much more recent development in microbeam applications at CHESS using single-bounce monocapillaries. The present set up is a direct result of experiences gained in the μSAXS on time resolved proteins (section 9.7). With the lessons learned there, I pushed for the construction of the x-ray microbeam breadboard, which has all the critical capabilities for μSAXS and μWAXS (section 5.1.2).

SAXS is an x-ray technique used to probe feature sizes in materials ranging roughly from 3 to 300 nm. WAXS is similar to SAXS, but it probes length scales from 0.3 nm to 3 nm. The main difference between the two techniques is in the placement of the

detector and the beam-stop, with the flight paths to match. For WAXS, the detector is much closer to the sample to gather diffraction peaks at larger angles, typically 10 to 15º. In SAXS the beam-stop is placed directly in front of the detector. In WAXS the beam-stop has to be carefully positioned in-between sample and beam-stop, to both allow low scattering angles and to eliminate all powder rings from the beam-stop striking the detector. In SAXS He-filled flight paths are necessary to avoid attenuation of the scattered beam. Ideally in WAXS the sample, the beam-stop, and the flight path are all in helium; however this makes sample changing difficult.

Using microbeams for both SAXS and WAXS broadens the technique's capabilities, real space information can be combined with reciprocal space information. One example using μSAXS, done by Peter Fratzl's group at BESSY II, includes measuring the structures of tissues, such as tendons and bone [121]. These structures are very interesting to study because they are both strong and flexible, which is unique for a material. The microbeam of a diameter of a few microns was needed to isolate the specific structures within the bone and tendon that they were interested in studying. μSAXS was able to isolate specific structures with the small x-ray beam, which in turn provided structural information on the length scales of 10 to 50 nm, and helped them develop a model that explained the physical properties of tendon and bone [122].

μSAXS is challenging to do because the small beam size and the resolution requirements are at odds with each other. The best resolution comes from a parallel beam, and a small beam requires a divergence. The price for μSAXS is always a decrease in the resolution. Hence a good compromise between spatial resolution and scattering resolution has to be identified for each sample. For single-bounce

monocapillaries manipulating the optic's divergence with slits helps to set the required resolution (section 4.3.2). For μSAXS, this is especially important.

In the μSAXS tests we used capillary PEB-mr8f55-02 (8 mrad, 55 mm focal length). The full divergence from this optic is much too large for μSAXS. By judicially placing the slits, about a tenth or less of the full optical surface is used to produce a divergence of 1.9(H)x1.0(V) $mrad^2$, with a spot size of 9.5(H)x13.7(V) μm^2 at the sample position (Figure 9.19). The total flux in the beam was measured to be 1.3×10^{10} photons/s, giving a flux density of ~1.0×10^8 photons/s/μm^2, with a $\Delta E/E \approx 1.7$ % bandwidth from a Mo/B4C 30Å multilayer. Additionally a sample of polyisoprene-block-poly-ethylene

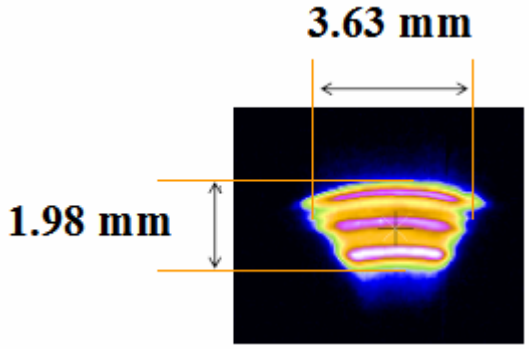

Figure 9.19 This shows an the attenuated x-ray beam profile (far-field image) from capillary PEB-mr8f55-02, slit down, as recorded on the MedOptics CCD (48 μm pixel size in a 1024x1024 array) at a distance of 1900 mm from the focus. The full far-field pattern from this optic can be seen in Figure 4.4. The striped features in the beam profile are caused by the slope errors on the monocapillary optic.

oxide (PI-b-PEO) with aluminosilicate spheres was tested with this setup. The aluminosilicate spheres make a diffraction ring at q=0.148 nm^{-1} (425 Å). This ring was just observable in the μSAXS setup, giving a limit in of resolution size of about 450 Å. In order to put our achievements into perspective, at BESSY II, they have recently publish a paper about a beamline dedicated to μSAXS/μWAXS/μXRF [123]. They have 500 Å resolution, a flux of 2×10^9 ph/sec/10um/100 mA, (multilayer with $\Delta E/E \approx$

1%) over a 16x18 um spot size. Our setup using a monocapillary optic is very comparable, with our setup having about a 2x larger total flux ($\Delta E/E \approx 1.7\%$).

CHESS's μSAXS setup has been used on a number of samples, and I will briefly discuss one of them. For block copolymer polyisoprene-block-poly-ethylene oxide and resol (Pl-b-PEO/resol), the traditional SAXS patterns changed based on the position of the beam on the sample. Pl-b-PEO/resol looked at the inhomogeneous and anisotropic using SAXS. With μSAXS, Pl-b-PEO/resol showed to have homogeneous rings with anisotropic spots (Figure 9.20). Our interpretation is that the homogeneous rings are caused by the lamellar structure of the Pl-b-PEO/resol nano-composite. The anisotropic spots were caused by single-crystalline polyisoprene-block-poly-ethylene oxide (Pl-b-PEO) with a hexagonal morphology. The crystals where found to be about 15 μm in size, by scanning the beam across a few single crystals (Figure 9.21). For this sample, μSAXS helped to separate the scattering of the Pl-b-PEO/resol and the Pl-b-PEO domains, identify the domains sizes, estimate the crystalline inclusion density, and estimate the inclusion sizes [120].

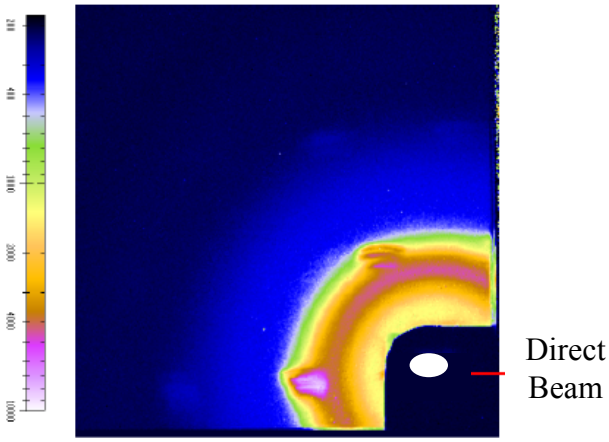

Figure 9.20 A μSAXS images showing a snapshot of the Pl-b-PEO/resol. The ring of intensity is from the lamellar structure and the spots are cause by the small crystals. The direct beam's approximate location is marked with the white dot.

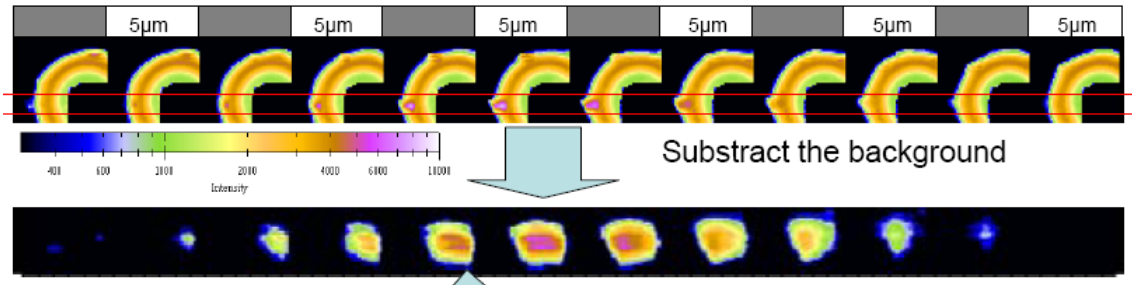

Figure 9.21 The top line of images shows a series of scans, taken at a 5 µm step size, across a Pl-b-PEO crystal. The bottom line is the same image, background subtracted to highlight a single diffraction spot from the crystal. When integrating and plotting these spots, the crystal has shows to have a size of ~18 µm.

For this particular sample, the microbeam was able to resolve two different constituents within the sample. For other samples, such as fine fibers, the smaller beam will provide the needed higher flux density. For flow cells, such as in time resolved protein folding (section 9.7), or in silk formation[68] [124], the small x-ray spot provides a small spot for improved time resolution and small sample volumes.

From a monocapillary optics standpoint, we showed that the monocapillary optic, in conjunction with the new x-ray microbeam breadboard, produces an excellent µSAXS setup. The x-ray microbeam breadboard allowed placement of a 100 µm clean up aperture in between the sample and the optic. This small aperture is absolutely needed to eliminate intense parasitic scattering from the tip of the monocapillary [112]. It also had room for a microscope for observing the sample during the µSAXS experiments. With all of the small components, the setup had ample space for needed miniature equipment. The sample, clean-up aperture and capillary optic were all placed within 55mm of available space, with a combined ten motor motions. A 5µm pinhole could be

[68] A silk flow cell was done with our µSAXS setup with E. Filippidi as the CHESS user in October 2007.

mounted on the sample stage to characterize the focal spot. The positional resolution was excellent, with a 0.1 μm resolution. The x-ray microbeam breadboard has been an excellent tool for the monocapillary x-ray microbeam work (section 5.1.2).

The μSAXS and μWAXS experiments were done at the D1 station with D. Smilgies as the CHESS beam line scientists and Ruipeng Li as a visiting graduate student from the University of Science and Technology of China in Hefei. The Pl-b-PEO/resol sample, and many other samples were provided by M. Kamperman from U. Wiesner's group at the Department of Material Science and Engineering at Cornell University.

9.12 Bifocal Miniature Toroidal X-ray Mirror

Using the glass optical pulling capabilities at CHESS, we have fabricated a bifocal miniature toroidal mirror that horizontally and vertically focuses to two different locations. The toroidal mirror was designed to focus vertically at the sample's position and horizontally at the detector's position. This mirror was made to provide a smaller footprint of beam for grazing incidence wide angle scattering (GIWAXS), while at the same time focusing the beam in the horizontal direction on the detector for better angular resolution in the horizontal direction. No other capillary has been designed to date with a separate horizontal and vertical divergence.

This optic is very similar to the single-bounce monocapillary optics. It is made by the same techniques, and in the far-field, the toroidal mirrors are un-distinguishable from the ellipsoidal shaped optics; the images in Figure 5.8, in section 5.5, come from a toroidal mirror. This miniature toroidal mirror was designed to decouple the sagittal and meridional focusing of the traditional single-bounce monocapillary optic (Figure

9.22). Essentially, the normal ellipsoidal shape is modified by increasing it's inner diameter, changing the sagittal focus, and at the same time not modifying it's meridional curvature, leaving the meridional focus unchanged.

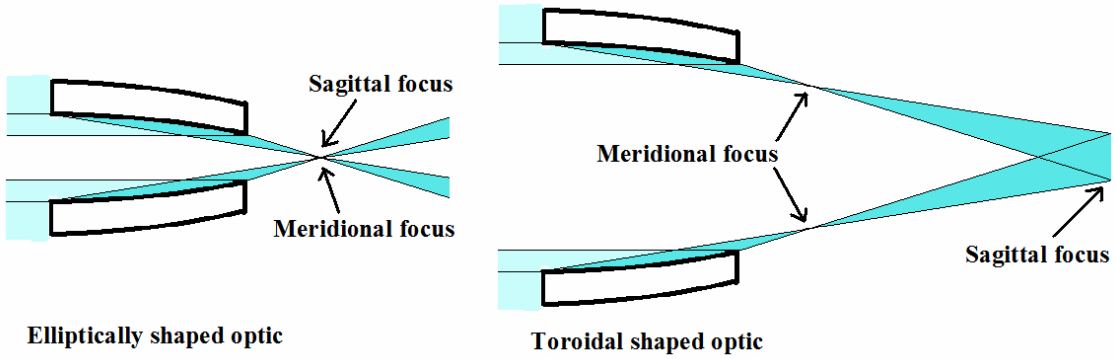

Figure 9.22. This sketch outlines the modification of a ellipsoidal shape (left) to a toroidal shape (right). The diameter of the optic is changed, thereby decoupling, the sagittal and meridional focus. The meridional focus is unchanged, but the sagittal focusing is moved further from the tip of the optic.

Using the entire inner optical surface will not produce horizontal line focus at the sample position and a vertical line focus at the detector position. If the full surface of the optic is exposed to an x-ray beam, a narrow ring of intensity will be at the location of the meridional focus, and a semi large spot will be at the sagittal focus (Figure 9.23, top row of images). In order to have a line focus, only a section of the optic's inner surface is exposed to the x-ray beam. Slits are set upstream of the optic, which blocks most of the optical surface (yet again, see section 4.3.2). Using a subsection of the optical surface produces a vertically focused beam at the meridional focus position, and a horizontally focused beam at the sagittal focus position (Figure 9.23, bottom row of images).

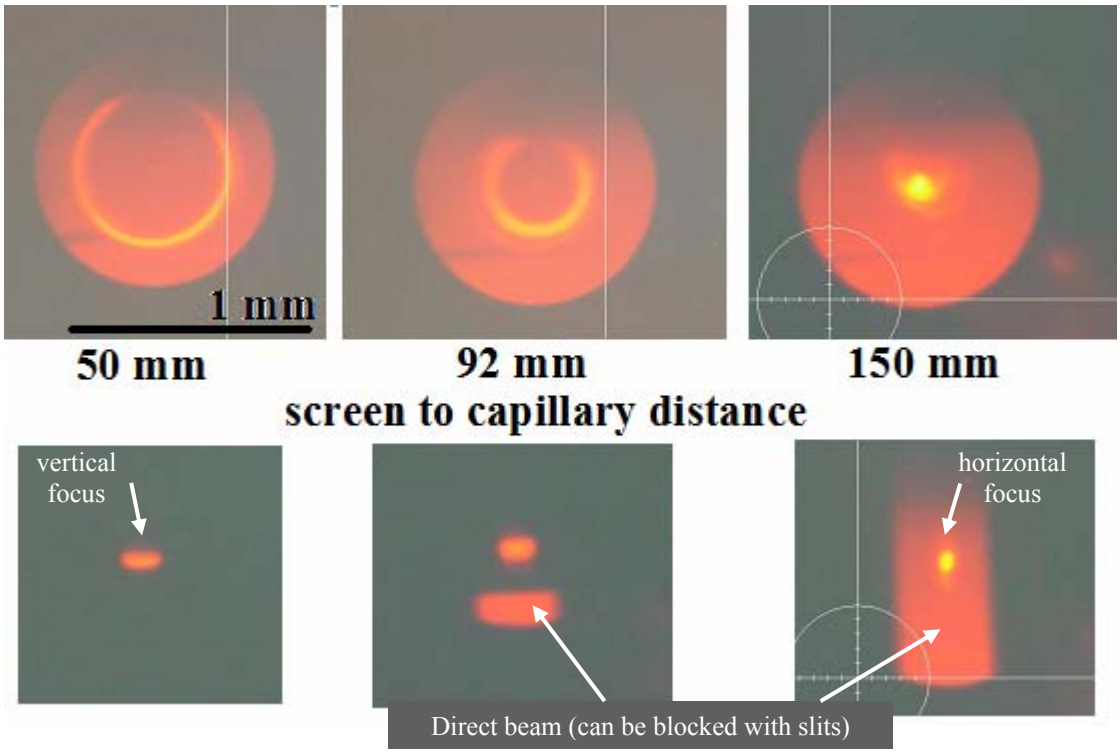

Figure 9.23 This is a set of images taken with the GGG fluorescent screen (section 5.2)and a microscope (section A2) at various distances from the toroidal mirror's tip. The top row of images are from exposing the entire optic, and the bottom images are from the optic using only a section of it's inner surface. The left images are at the meridional focus, the right images are at the sagittal focus, and the center images are between the two. For reference, the background red fluorescence is from the direct beam going through the optic, and has a diameter of 1 mm in the top images.

Of four optics made, two functioned correctly, with TORa-mr7f50-03 being the best. The optic's length was 100 mm with an incident angle of reflection of 1.75 mrad (0.10º) at the tip of the optic. The optic works up to 17 keV. The mirror produced a 120(H)x25(V) μm^2 focus 50 mm from the tip of the optic, and a 44(H)x~70(V) μm^2 focus 150 mm from the tip of the optic at CHESS's D1 station (Figure 9.24). At the vertically focused position (50 mm from the tip), the focus was not exactly a straight line, it curved up on the sides slightly, giving a "smiley" shape. From the center to the edges of the vertical focus, the peak intensity shifted by 20 µm.

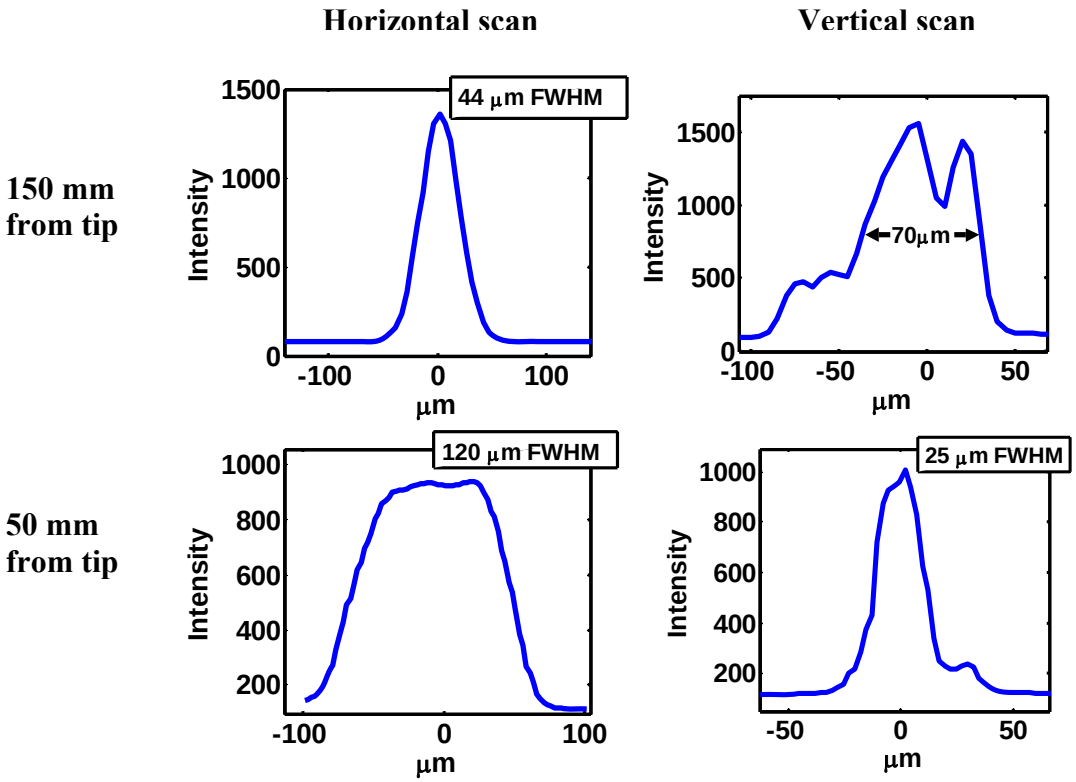

Figure 9.24 This shows the 5 μm pinhole scans across the bifocused beam at 150 mm (sagittal focus) and at 50 mm (meridional focus). The vertical scan of the beam at 150 mm has features, which are primarily caused by the slope errors along the optic, it has a full width of ~130 μm.

In order to design the miniature toroidal mirror, the correct curvatures had to be made on the inner surface of the glass. The curvature of a reflection X-ray mirror in both the sagittal and meridional directions can be calculated from [1]:

$$\rho_{sagittal} = 2 f_v \sin\theta \tag{9-6}$$

$$\rho_{meridional} = \frac{2 f_h}{\sin\theta} \tag{9-7}$$

Where '$\rho_{sagittal}$' and '$\rho_{meridional}$' are the sagittal and meridional radius of curvature, 'f_v' and 'f_h' are the vertical and horizontal focus locations from the optic, and 'θ' is the incident angle. These equations are meant to give the best approximate spherical

curvature to an ellipsoidal shape. We get the correct ellipsoidal shape for the meridional focusing, using Rong Huang's capillary design program for designing ellipsoidal monocapillary shapes [58] (sections 3.2.2 and 6.2). A capillary with a 50 mm focal length, and a 7 mrad tip divergence gives the correct meridional shape (left side of Figure 9.22). At this point, the meridional shape is set, and the sagittal figure will have to conform the best it can to this shape.

There are three 'natural' locations to set the correct sagittal radius; the tip, mid-point and the base of the ellipsoidal/meridional shape. Table 9.1 outlines these three options. When the tip, mid-point, or base are set to the correct diameter for the desired sagittal focal length of 150 mm from the tip, the other locations along the miniature toroidal optic have the incorrect diameter for putting the sagittal focal length at 150 mm from the optic's tip. The last column in Table 9.1 shows where the sagittal focal length ends up for both the base and the tip, when designing the sagittal curvature offset is keyed from the tip, mid-point or base.

This first design of toroidal mirrors is based on the tip having the correct diameter for sagittal focusing, with a diameter offset of 700 μm from the base ellipsoidal shape. This design was picked to get the meridional and sagittal focusing as far apart as possible. For the first attempt, maximizing the distance between the two focal lengths would more definitively show the optics' separation of vertical and horizontal focusing. For this design, the tip focused at 150 mm from the optic's tip and the base focused at 220 mm from the optic's tip. In Figure 9.22, the sagittal-focused spot has a halo of intensity around the central spot, in both the top and bottom image. I believe that this comes from the sagittal mis-focusing from the base of the optic.

Table 9.1 This gives three options for the design of the miniature toroidal mirror, keyed from the tip, middle and base of the optic. The ellipsoidal shape sets the correct shape for meridional focusing. This makes the sagittal focus have a range of focal lengths along the length of the optic, which depends on the chosen design (last column).

	set ID (for ellipse) μm	incident angle (mrad)	sagittal focus length (mm)	ID for sagittal focusing (μm)	ID offset from ellipse shape (μm)	tip-base sagittal focal length (mm)
tip (50 mm to ellipse focus)	350 (at tip)	1.75 (at tip)	150 (at tip)	1050 (at tip)	700	150-220
mid. (100 mm to ellipse focus)	490 (at mid.)	1.23 (at mid.)	200 (at mid.)	984 (at mid.)	494	120-167
base (150 mm to ellipse focus)	610 (at base)	1.03 (at base)	250 (at base)	1030 (at base)	420	110-150

We have tested the optic briefly for GIWAXS, but found a flaw in our thinking: at the sample, the beam is sagittally under-focused, and hence the spot shape has the typical "smiley" shape of sagittal focusing optics. On the sample we had an extended crescent instead of a well-defined short streak, and we did not get the improvement in GIWAXS resolution we had aimed for. Also, the reflections of a test sample on the CCD camera were still smeared out radially, as in an unfocused beam.

The idea may still be revived by noting that the "smiley" shape is only associated with the sagittal focus, but not with the meridional focus. Reversing the focal lengths so that the sagittal focus is on the sample while the meridional focus is on the detector may be a promising approach. In this case we would need to select of sector of the accepted

annulus 90º rotated from the original arrangement. A new design of a glass capillary would be needed to test this idea.

The present bifocal optic can still be very useful for other samples. For instance, diffraction from single fibers or from microfluidic channels could benefit from focusing the beam only in one direction at the sample while maintaining a good resolution in the perpendicular direction.

We demonstrated a unique non-ellipsoidal shaped optic, and the first of its kind we have made at CHESS, with CHESS's monocapillary optic pulling technology. It worked as we expected, giving a separated horizontal and vertical focus. It opens up new optical design space for us to consider when we encounter experimental x-ray microfocusing problems. Again, the microbeam breadboard greatly simplified the testing of this optic. The images in Figure 9.23 were simply taken with the microscope having the GGG fluorescent screen at the sample's position.

The toroidal mirror experiments where done at the D1 station with D. Smilgies.

9.13 Laue Micro-Protein Crystallography

The Laue micro-protein crystallography is an extension of the micro protein crystallography effort discussed in section 9.6. In this section I will address the advantages and limitations of using Laue diffraction for micro-crystallography. I will give a description of the optics used in the experimental setup and give some of the results of the Laue patterns collected from micro-crystals at D1. The appendix section C has a map of the locations of all the equipment used in this experiment.

The Laue micro protein crystallography project is a step in understanding what is needed for getting protein crystallography information from a very intense x-ray beam, such as the Energy Recovery Linac (ERL). Many proteins of biological importance form only microcrystals (10 μm or less). By using a strong, micron-sized X-ray beam, good diffraction can be obtained from a single microcrystal, but radiation damage leads to rapid degradation of diffraction quality with time. To obtain a complete, high quality dataset, multiple crystals must be used for very small crystals. Laue may be able to maximize the diffraction information taken from a single microcrystal.

We have developed this Laue-based wide-bandwidth micro-focus technique for collecting data from a set of identically grown crystals. Diffraction patterns were collected from groups of lysozyme protein crystals, some as small as 10 μm across, mounted on MicroMesh™ Mounts[69], using a "pink beam" at the CHESS D1 station. The bandwidth of the beam was 30%, from 10 to 13 keV. This bandwidth was set with two rhodium-coated mirrors and a silicon nitride x-ray transmission mirror (Chapter 8 and section 9.13.2). The wide bandwidth beam was then focused to a 13 μm spot size with a single-bounce monocapillary optic, which is achromatic, achieving a flux of 4.4×10^{10} photons/s and a flux density of $\sim3.3\times10^{8}$ photons/sec/μm^2 (section 9.13.3). A structure was obtained from a set of 14 Laue images from three lysozyme crystals, using molecular replacement, and refined to an R_{free} under 30% at a resolution of 2.1 Å (section 9.14.4). We believe that this approach will lead to a new avenue for solving protein structures using less then 10 μm sized crystals, in the short term at CHESS as well as in the long term at an ERL source.

[69] These mounts come from Dr. Robert Thorne's group at Cornell University. Contact information: www.mitegen.com (MiTeGen, P. O. Box 3867, Ithaca, NY 14852).

9.13.1 Micro-Crystallography Challenges and the Laue Solutions

The almost universal method for protein crystallography is to take diffraction patterns from the crystal using a monochromatic beam, $\Delta E/E \sim 0.01\%$. A large number of diffraction images are taken of the crystal, rotating the crystal over 60º to 180º. For each image, the crystal is rotated a fraction of a degree (know as an oscillation angle), to fully meet the Laue condition for a number diffraction spots in the image. The diffraction images, if of sufficient quality, can be used to solve for the structure of the protein [15].

Laue diffraction, or wide bandwidth x-ray diffraction, is not a standard method for solving protein structures. Most Laue experiments deal with time-resolved changes in known structures [125-132]. Laue diffraction has not traditionally been used to solve protein structures, but it has the capability [128,132-136]. The reason that Laue is used in time-resolved protein experiments is a wide-bandwidth beam has more flux, and the crystal does not need to be rotated wide-bandwidth beam. The large increase in flux allows for getting diffraction spots more quickly, allowing for better time resolution.

Performing Laue diffraction on protein crystals was first performed at synchrotrons over twenty years ago [89,125]. Very soon afterward the advantage of an increase in flux due to the large bandwidth was used to obtain Laue diffraction from small ~20 μm sized crystals [132]. The potential advantages of using with Laue diffraction for small protein crystals have been known for some time. When the first condensing monocapillary x-ray microbeams where created, they were used to produce Laue

diffraction images [137]. The combination of a wide bandwidth and a micro-focused x-ray beam for obtaining large flux density is ideal for Laue diffraction from small crystals.

Monochromatic micro-beam protein crystallography has a number of challenges to obtain a complete set of diffraction information from increasingly smaller crystals, outlined below:

- Smaller crystals require more flux density to get the same quality of diffraction information. This requires both increasingly better microfocusing optics, with smaller spot sizes, and x-ray sources with a higher spectral brightness.
- Radiation damages crystals, therefore higher flux densities damage crystals more quickly [106-108]. This severely limits the data collection time from small crystal.
- Smaller crystals are more mechanically difficult to place and rotate in very small x-ray beams. Smaller crystals require an increasingly smaller sphere of confusion, which translates into much tighter tolerances on diffractometers.

Using Laue microbeams for protein crystals addressed all of these issues, in some way:

- A wide bandwidth beam increases the x-ray flux. Because the monocapillaries are achromatic, they are able to focus the beam to the same spot size for a net increase in flux density. The increase in the flux density corresponds to the increase in the bandwidth of the beam.
- A wide-bandwidth beam increases the volume of reciprocal space recorded in a single image [133]. Laue may be able to maximize the amount of information collected from a single, very small crystal before it is damaged by radiation.

Laue diffraction from a few crystals may be enough for a complete set of diffraction images to solve the structure.

- Laue does not require rotating the crystal during an exposure, and there are no partial reflections, which are associated with monochromatic protein crystallography [133]. This simplifies the mechanical tolerances on the diffractometer.

Laue diffraction has a number of potential advantages for getting diffraction information from very small crystals, but it does bring along some additional challenges as well.

- With wide-bandwidth x-ray beams, multiple order diffraction spots can be superimposed on each other, especially for low index reflections.
- Laue patterns have an increase in spots and in background noise, due to the wider band-pass x-ray beam. There is a trade off between coverage in reciprocal space and accuracy [133].
- Laue diffraction is sensitive to crystal disorder, such as mosaic spread. Whatever the cause of disorder of the crystal is, it causes elongated diffraction spots which lead to a decrease in resolution [133].
- Lower resolution in Laue patterns equates to a less complete data set.

The first two issues are addressable, by reducing the bandwidth of the x-ray beam, the number of harmonic and spatial overlapping diffraction spots are minimized, likewise with a smaller bandwidth, the background noise can be minimized. The cost of a limiting the bandwidth is lowering the volume of reciprocal space recorded in a single image, and thus limiting the x-ray flux. It was decided that the good compromise between these two conflicting issues was to have an x-ray beam with a ~30%

bandwidth, between 10 keV (λ= 1.24 Å) and 13 keV (λ = 0.95 Å). This gives a fairly wide bandwidth, while at the same time eliminating most of the overlapping diffraction spots. Also, being able to have the bandwidth centered at 12 keV (λ = 1.03Å) has the advantages of limiting absorption correction and reducing thermal damage [128]. This bandwidth equates to a ~3º to ~8º rotation in monochromatic x-ray diffraction, therefore, about 30 to 60 exposures are need to obtain a full set of spots in reciprocal space (a full 180º). The next section discusses how we created the desired wide bandwidth x-ray beam.

9.13.2 Setting the X-ray Spectral Bandwidth

Setting a wide ΔE/E ≈ 30% "pink" bandwidth beam, between 10 keV (λ= 1.24 Å) and 13 keV (λ = 0.95 Å) was not trivial. The full spectrum from the bending magnet at D-line contains energies from a few keV up to 50 keV and higher (Figure 1.3). D-line was chosen because it is capable of having a white x-ray beam (the full synchrotron energy spectrum) in the hutch[70]. Traditionally, setting a large bandwidth in a synchrotron x-ray beam has had two options, a wide bandwidth multilayer or a reflection mirror plus absorption filter combination. The desired 30% bandwidth is too large for multilayers, with a upper limit presently at ΔE/E ≈ 10% (section 1.4.1) [24]. Total external reflection mirrors can provide a relatively sharp low band pass cutoff, which can be tuned by changing the angle of the mirror in the incident beam (Figure 9.25). A tunable cut-off energy is very advantageous. The absorption filter for a high pass filter has a major drawback, it has a very broad energy cutoff, on the order of several keV in the 5 to 20 keV range (Figure 8.2). Not any material can be used. The absorber has to be

[70]CHESS's B1 and B2 hutches can have white beam as well, but are too limited in space for other equipment, such as the large data collection ADSC Quantum 4 CCD area detector.

void of K edges within the desired spectrum, such as aluminum. A sharper low cutoff energy would be much more efficient in suppressing multiple reflections in the Laue diffraction patterns.

In order to achieve a sharper high pass filter, we have created a third option, a reflection mirror, and transmission mirror combination (Figure 9.25 and 9.26). Like the refection mirror, the transmission mirror has a sharp cutoff energy, but it is a high pass filter instead of a low pass filter (Chapter 8). The high pass cut-off can be tuned to the desired cut-off energy by changing the mirror's angle with respect to the x-ray beam (Figure 9.26). Using this new combination of optics, the desired bandwidth for Laue micro-protein crystallography was created.

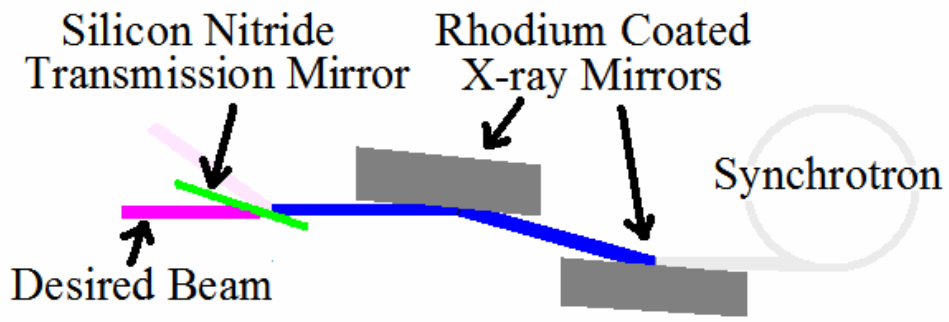

Figure 9.25 A diagram of the setup for both the reflection mirrors and the transmission mirror used to create a tunable large bandwidth beam.

Several years ago, the very first transmission x-ray mirror was created from a soap bubble film, and was used for Laue as well [89]. These mirrors had a very limited life time of a few hours. This created for a non-stable and non-repeatable x-ray optic, which was its fundamental flaw for synchrotron use beyond a proof of the principles. We have now created a long-term stable x-ray transmission mirror made from a 300 nm thick silicon nitride membrane, which is able to make the desired high pass energy cut

off and have stable optical properties over time, during potential periods of weeks to months[71] (Figure 9.26).

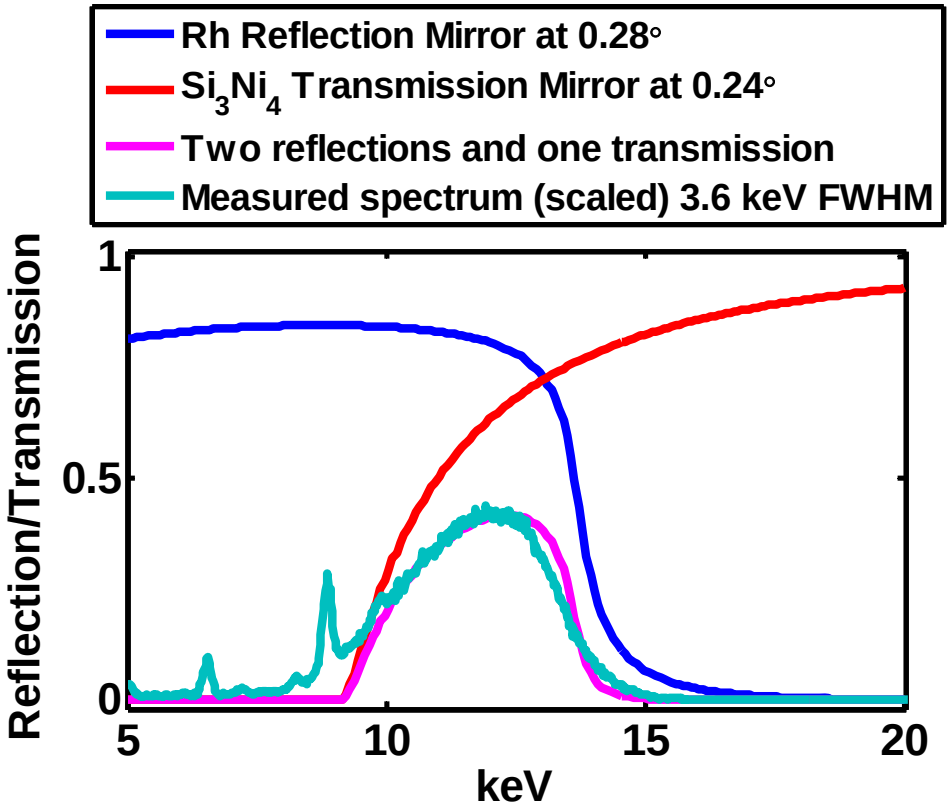

Figure9.26 A graph showing the predicted and actual spectrum of the 30% bandwidth (FWHM) created with two Rh reflection mirrors and one Si_3N_4 transmission mirror combination. The pink curve is calculated, and the blue-green curve is measured. They compare favorably. The bandwidth is peaked at 12 keV (λ=1.24 Å) with the half width values at 9.6 keV (λ=1.29 Å) and 13.4 keV (λ=0.93 Å). In the measured Compton scattered curve, the sharp peaks come from fluorescence within the Kapton tape®; they are not peaks within the bandwidth of the x-ray beam.

The reflection/transmission mirror combination worked well in setting the desired bandwidth of the beam, but the cutoff energy was not quite as sharp as predicted. This is due to the transmission mirror not being perfectly flat; this was expected at some

[71] They have been tested for 24 hours straight in white beam CHESS's B1 station and in pink beam intermittently for two weeks at D1. In both cases, there was no sign of degradation of the transmission mirrors properties.

level from prior experience (see Figure 8.3). An X-Flash diode detector was used to measure the Compton scattering from the Kapton tape to observe spectrum of the beam, before the beam was micro-focused by a single-bounce monocapillary. The Compton spectrum corresponded very well to the lambda curve, which is the energy spectrum curve measured from the Laue diffraction images (Figure 9.27).

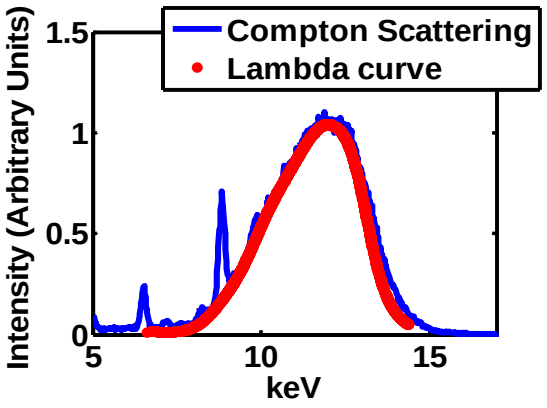

Figure 9.27 shows the measured band pass of the beam collected in two ways, Compton scattering from Kapton® tape, and the lambda curve determined from the Laue diffraction patterns. Both methods agree very well with each other. Again, in the measured Compton scattered curve, the sharp peaks come from impurity fluorescence within the Kapton tape®; they are not peaks within the bandwidth of the x-ray beam.

This first test of the reflection/transmission mirror combination worked very well. By tuning the angles of both the rhodium coated reflection mirrors and the silicon nitride transmission mirror, the desired bandwidth was created. The fragile 300 nm thick transmission mirror was very stable over the week of performing Laue diffraction. This means that the very fragile, 300 nm thick, silicon-nitride transmission mirror is capable of long-term functionality in the x-ray beam.

9.13.3 Micro-Focusing the Wide Bandwidth Beam

Monocapillary f1b-mr9f20-01 (7.5 mrad optic with a 22 mm focal length) was used to focus the wide 30% bandwidth beam between 10 and 13 keV. This optic was chosen for two reasons: i) Monocapillary f1b-mr9f20-01 is mounted in the MacCHESS housing, which is compatible with the F3 protein crystallography table used for the experiment (section 5.1.2). ii) The optic has a large divergence, therefore slits upstream of the monocapillary optic can be used to set an optimized divergence (section 4.3.2).

For the microfocusing there are two competing elements, maximizing the flux density and also having a adequate divergence for the Laue diffraction patterns. Lowering the divergence limits the flux so the divergence of the monocapillary optic was set at a point that just eliminates overlap of the diffraction spots. The diffraction spots in the Laue patterns need to be isolated for proper integration of the x-ray intensity within the spots. Figures 9.28 (overlapping spots) and Figure 9.31 (isolated spots) show two examples of different optical divergence settings. The shape of the diffraction spots in the Laue diffraction images are somewhat distorted because of the increased divergence from the optic. The shape of this distortion is close to the shape of the far-field pattern, used to align the optic (Figure 2.29). The shape of the diffraction spots is not critical for getting the intensity of the spot; the odd shaped spots are acceptable as long as the diffraction spots do not overlap.

Without slitting down the monocapillary optic, having a full 7.5 mrad (0.43º) divergence in both the horizontal and vertical direction, the total flux was ~1.9×10^{11} photons/s in a 16(H)x10(V) μm^2 spot[72] (~1×10^9 photons/s/μm^2). In order to eliminate

[72] There was no capillary beam-stop in the x-ray beam's path for this flux measurement.

the overlapping of diffraction spots in the lysosyme crystals, the divergence of the beam was set to ~ 5(H)x2(V) mrad^2 (0.3º(H)x.0.12º(V)) (Figure 9.29). Using a smaller portion of the optic resulted in a total flux of 4.4×10^{10} photons/s in a 10(H)x13(V) μm^2 spot (~3.4×10^8 photons/s/μm^2).

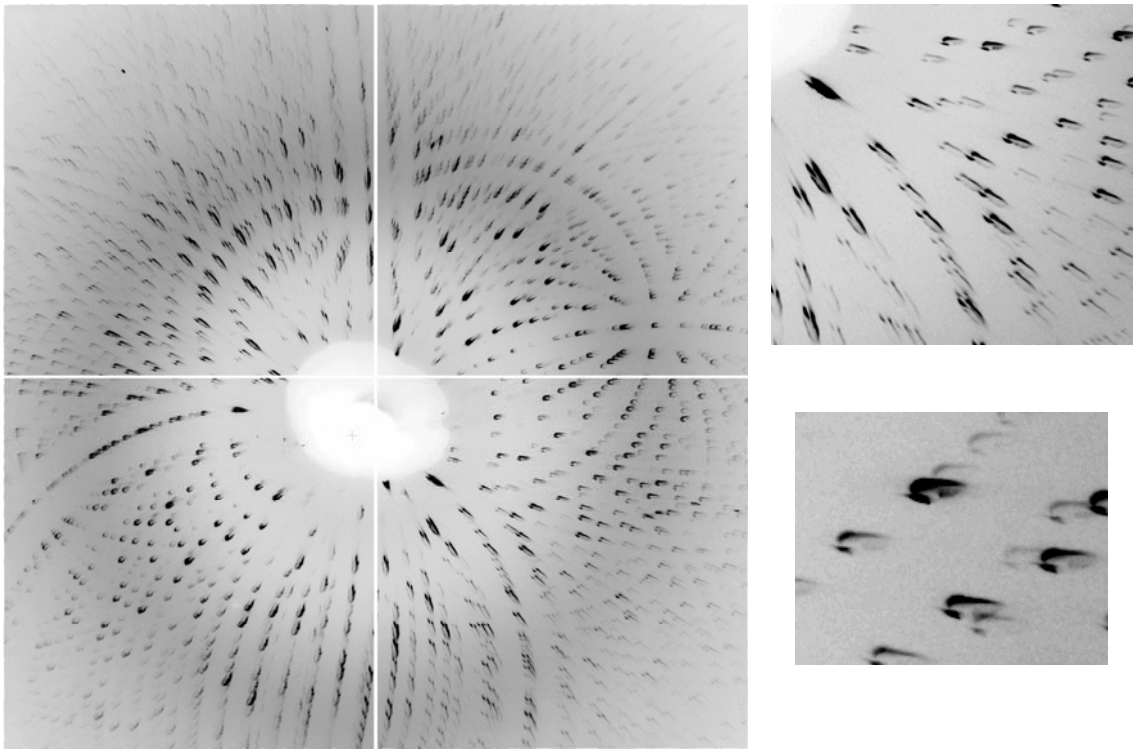

Figure 9.28 This figure shows a Laue diffraction image taken from a small lysozyme crystal, over three size scales. The divergence from the monocapillary was too large, which resulted in the overlapping of diffraction spots, which are undesirable. The odd shape of the spots is a result of the divergence from the monocapillary, they are the same basic shape as the far-field of the optic (see Figure 9.29). These particular spots are approximately half of the full far-field pattern, with a small portion of the direct beam (due to capillary beam-stop misalignment). Using the full divergence from the monocapillary optic would result in having each diffraction spot having a full circle or ellipsoidal shape.

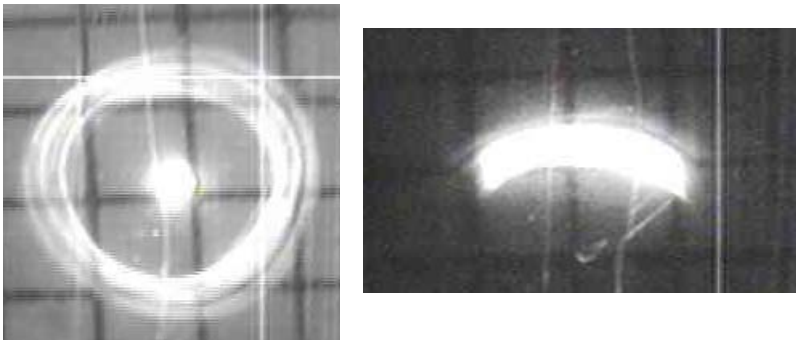

Figure 2.29 On the left is the full far-field image from monocapillary f1b-mr9f20-01 in the wide bandwidth beam (ΔE/E ≈ 30% at 12 keV). On the right is the slit down far-field image from the monocapillary which allowed for isolating the spots in the Laue diffraction imaged. The grid in the image are in one mm squares.

A useful comparison for the total photon flux can be made from the μSAXS setup, which was also performed at D1 (section 9.11). Monocapillary PEB-mr8f55-02 achieved a 1.9(H)x1.0(V) $mrad^2$ divergence in a 9.5(H)x13.7(V) μm^2 spot with a total flux of 1.3×10^{10} photons/s ($\sim1.0\times10^{8}$ photons/s/μm^2) in a ΔE/E ≈ 1.7 % bandwidth. The Laue setup with an adequate divergence had a 3.3x flux over the μSAXS setup. In the

simplest expectations, an 18-fold increase in flux would be expected with an 18-fold increase in bandwidth from ~1.7% to 30%. The difference comes from the amount of x-ray beam each optic can accept. Figure 2.30 shows the cross-sectional area of both monocapillaries f1b-mr9f20-01 (used for Laue at D1) and PEB-mr8f55-02 (used for μSAXS at D1). In this figure, the large square represents the beam size of 300(H)x300(V) μm^2, which is close to the beam size which passed through the transmission mirror to the monocapillary optic. The smaller square represents the approximate slit setting to give the desired divergence. With monocapillary PEB-mr8f55-02, the cross sectional area is close to five times larger. If this optic could have been used, the spot size and divergence would have been adequate for Laue protein

crystallography[73]. The alternate optic would give a five-fold increase in flux, up to an estimated value of ~2×10^{11} photons/s (~1.7×10^{9} photons/s/μm^2). This estimated flux gives the expected 18-fold increase expected from the μSAXS setup, and is consistent with the flux using the full divergence from f1b-mr9f20-01. When the Laue project is performed again, an optic such as PEB-mr8f55-02 would be a better choice for maximizing the flux while maintaining a small spot and an adequate divergence.

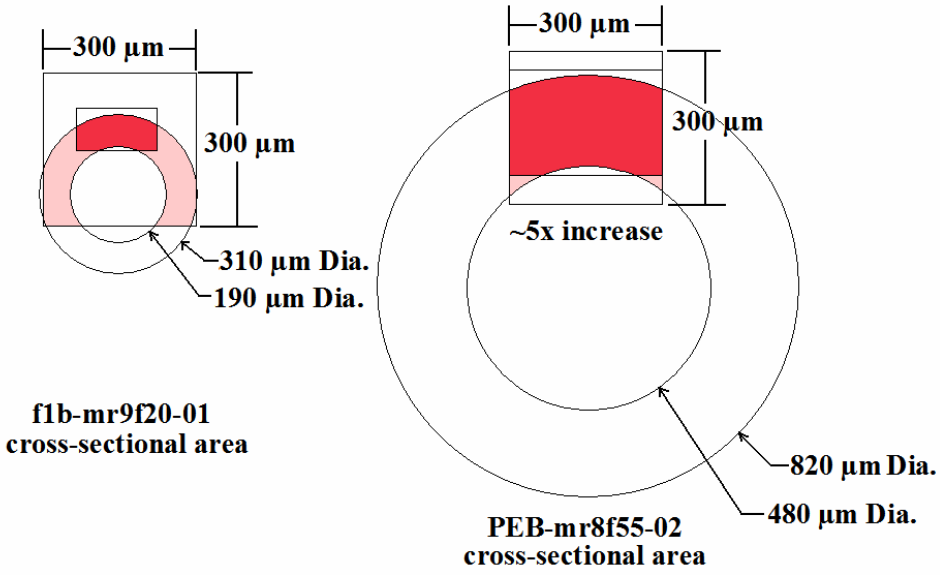

Figure 9.30 This figure shows the cross sectional area of both monocapillary f1b-mr9f20-01 (left) and PEB-mr8f55-02 (right), giving the tip and base inner diameters. The large 300x300 μm square is the size of the beam in the Laue setup, and the dark red shows the approximate cross-sectional area (slit setting) needed to get the appropriate divergence for Laue diffraction. Monocapillary PEB-mr8f55-02 is able to collect most of the beam, with a five-fold increase in cross-sectional area over monocapillary f1b-mr9f20-01.

[73] The μSAXS had a very similar 10(H)x14(V) μm^2 spot size and a smaller divergence of 2(H)x1(V) $mrad^2$.

9.13.4 Collected Laue Patterns

Nine sets of Laue data, mostly 7 frames per set, were collected from a spread of lysozyme microcrystals on a MicroMesh™ Mount (see footnote 69), in a helium enclosure. Crystal dimensions were a few tens of microns. Data was recorded on an ADSC Quantum-4 CCD detector, with exposure times of ten seconds and 10º rotational spacing between images (Figure 9.31). Images were evaluated visually and by preliminary processing, and three datasets were selected for processing. Due to radiation damage, and perhaps to crystals rotating out of the beam, the last few frames of each set were of poorer quality and were not used in the final iteration of processing.

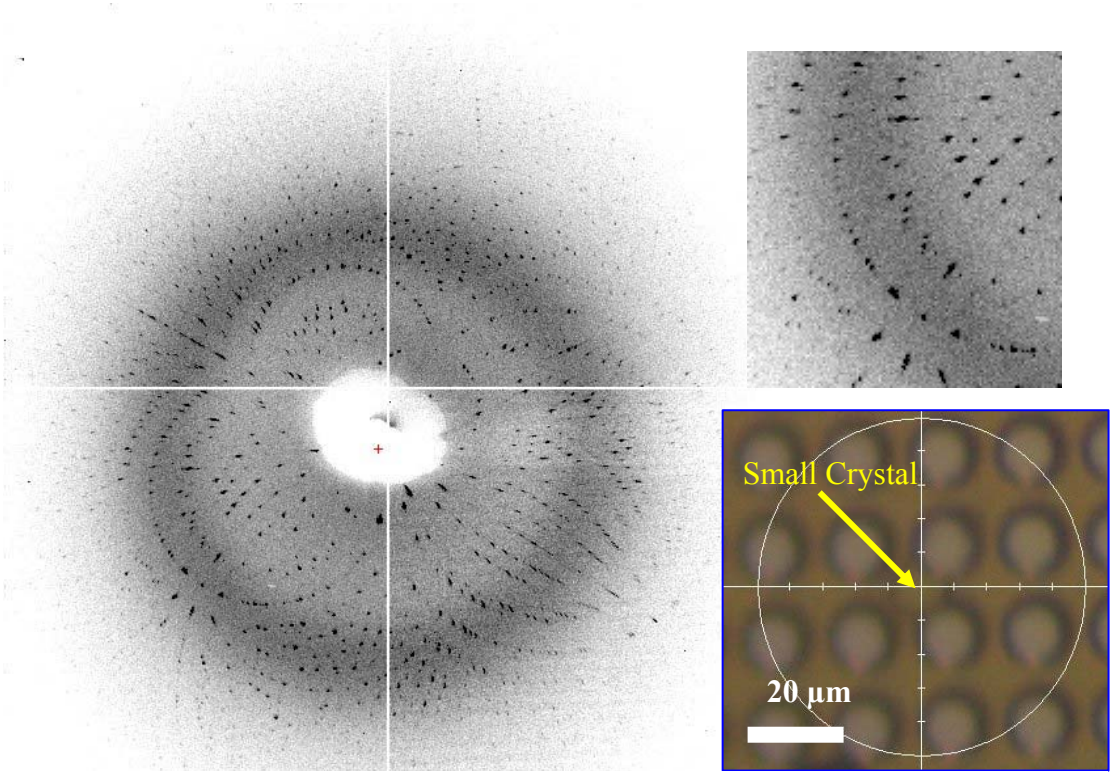

Figure 9.31 This figure shows a Laue diffraction image (5 second exposure) taken from a small ~10µm lysozyme crystal, along with an image of the crystal on the MicroMesh™ Mount for the sample support. The divergence from the monocapillary was adequate, which resulted in isolated of diffraction spots needed for data analysis.

The wavelength range was restricted to exclude regions in which incident X-ray intensity was below about 30% of the peak value. Data were indexed, refined, and integrated with the program LAUGEN, and scaled with lscale, both from the Daresbury Laue processing suite, with local modifications by D. M. Szebenyi. The final dataset, including 14 frames from 3 crystals, was 70% complete over the range 2.0-2.1 Angstroms. From each crystal, about five diffraction images were taken with a total exposure time of ~40-50 seconds. It was used for molecular replacement phasing, with the lysozyme model from Protein Data Bank (PDB) entry 1BWH. The program molrep (from CCP4[74]) easily placed the lysozyme molecule in the unit cell. Two stages of refinement by refmac5 (CCP4) resulted in a satisfactory crystallographic R of 0.22 and R_{free} of 0.28. Table 9.2 gives a summery of this particular test.

Table 9.2 A summary of data taken of three small lysozyme crystals about 20 to 40 µm in size in an helium environment.

Wavelength range(full)	0.86-1.88 Å
Wavelength used	0.92-1.25 Å
Resolution limit	2.1 Å

Frame set	hegrid4	hegrid6	Hegrid9
	1-5	1-4	1-4
RMS positional error(mm) after refinement	0.15-0.29	0.15-027	0.17-0.26
Good singles per frame	2670-3220	2860-3200	2690-3070
I/sig(I)	5.6-9.2	4.8-9.0	6.5-7.4

Rmerge	0.12
Completeness	70%
R after molrep	0.427
R_{free} after refmac	0.221,0.275

[74] The Crystallographic Computing Project #4

For the information in table 9.2, the integration by profile-fitting, box size is 1.0x1.0 mm^2, with a minimum spot separation of 1.0 mm. Spots were rejected if they: were spatially overlapped, contained any overloaded pixels, contained multiple harmonics, or had intensities less than 2 sigma. Scale factors and relative B factors for each frame were refined, as well as an X-ray spectrum modeled with 10 Chebyshev polynomials. Parameters were refined simultaneously.

9.13.5 Laue Conclusions

The wide bandwidth optics in conjunction with the single bounce monocapillary optic worked out very well. They were able to give the desired bandwidth of $\Delta E/E \approx 30\%$ peaked at 12 keV and focus the x-ray beam down to a small ~13 μm size. This gave a large flux density for a bending magnet beam line, with flux densities comparable to wiggler and undulator beam lines[75]. A structure was obtained from three crystals with 14 images. The Laue setup has shown that solving structures from a few small crystals is possible, thereby achieving the goal of this project.

This experiment was done at the CHESS D1 station, with Detlef Smilgies as the CHESS beam line scientist, with D. Schuller, D. M. E. Szebenyi and Quan Hao from MacCHESS.

[75] By taking advantage of the much wider bandwidth, and a 95% efficient achromatic microfocusing optic.

9.14 Other Projects

This last section is more or less a list of projects, and places that we have sent single-bounce monocapillaries. The list gives a few of the other experiments in which the single-bounce monocapillary has been used. Also, the names of others outside of CHESS which have been given monocapillary optics, to give a short record/history of where optics made at CHESS have ended up.

- X-ray Raman scattering in a diamond anvil cell (DAC) at C1 with A. Woll and K. Finkelstein (monocapillary G1c-mr4f50-03).
- Lattice parameters of organic transistors at C1 with A. Amassian, V. A. Pozdin, G. G. Malliaras and K. Finkelstein (monocapillary G1c-mr4f50-03). (see Figure A2.9)
- XSAFS in DAC at B2- (monocapillary BSG625) [63].
- Hasylab beam line "L"-(4 mrad, 50mm focal length, 103 mm long monocapillary optic) [138].
- Dr.Christoph Hermes, European Molecular Biology Laboratory (EMBL)-(monocapillary A10-mr2f55-12)
- Dr. David Sweet, Brokenhaven (RS-mr2f22-02, mounted in MacCHESS housing)
- Dr. I. C. Noyan, Columbia University, NSLS, beamline X20A-(monocapillary A10-mr2f55-15)
- Rigaku/Osmic – football monocapillary optics

Chapter 10 Conclusions

Elliptically shaped single-bounce monocapillary optics are excellent optics for many synchrotron x-ray experiments. They have been used successfully in a diverse number of x-ray microbeam experiments, many of which are covered in Chapter 9. The single-bounce monocapillary optics have spot sizes between 5 and 50 μm, with gains in intensity ranging from 10 to 1000, and divergences ranging from 1 to 10 mrad. At CHESS, all the x-ray microbeams are created with single-bounce monocapillary optics. They have a spot size that is adequate for a large number of different experiments, and they have a divergence range that is a good fit for a very wide array of x-ray diffraction scattering experiments.

At CHESS, we have been able to fabricate these optics with a third generation capillary puller, which has been functional since November 2005. This new puller has been able to pull optics with figure errors of 1.5 to 0.5 μm rms and slope errors of 50 to 120 μrad. The puller allows us to pull optics with a number of different shapes, including the traditional ellipsoidal shapes, "football" ellipsoidal shapes (section 7.2.1), and non-ellipsoidal shapes such as miniature toroidal mirrors as well (section 9.12). Figure 10.1 gives an image of a few monocapillary optics, showing the range of sizes created at CHESS.

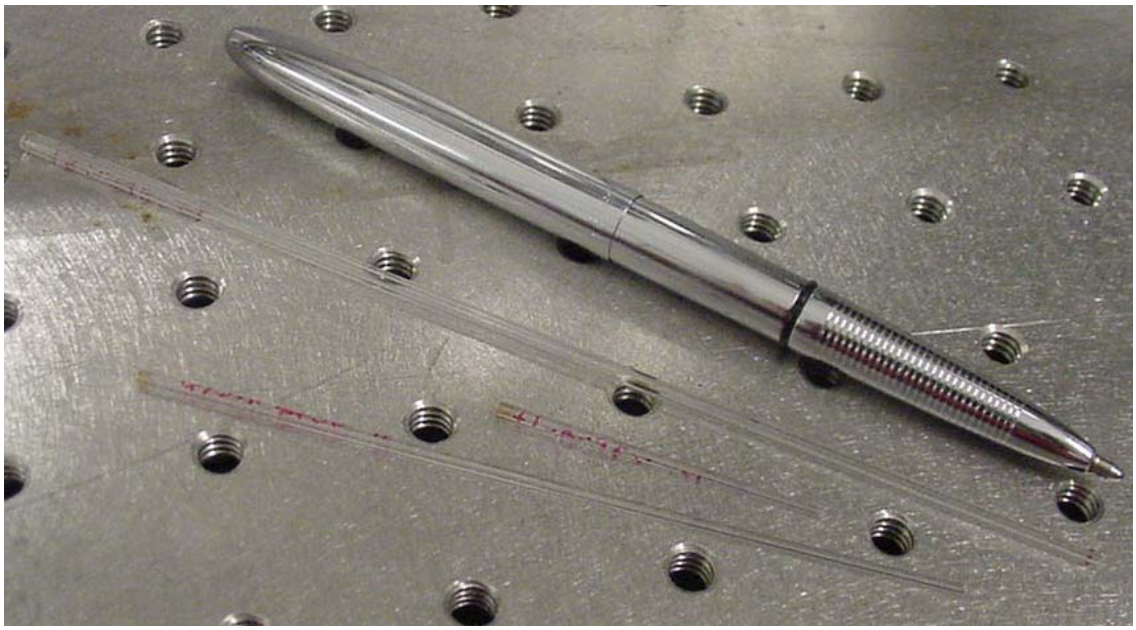

Figure 10.1 This image shows a number of different sized single-bounce ellipsoidal-shaped monocapillary optics fabricated at CHESS. The image is full scale; the pen is shown to give a reference to the size of the optics.

There have been a number of tools created which model the single-bounce monocapillary optics. These include Rong Huang's capillary design program and a ray-tracing program used to model the optics (section 6.4.3). These tools both allow us to design optics for particular uses, and help us understand their functionality. Monocapillary optics have a number of positive attributes and a few limiting attributes. Each of these limitations have potential solutions, discussed in Chapter 7.

The optics will continue to be an asset to CHESS, giving the synchrotron facility at Cornell University the ability to create a variety of x-ray microbeams for multiple purposes.

APPENDIX

A. Stages for Monocapillary Optics

Section A of the appendix covers the auxiliary equipment used with the single-bounce monocapillary optics covered in section 6.3. Section A1 gives the mechanical drawings for the standard monocapillary stages at CHESS. Section A2 gives a list of equipment used to construct the X-ray microbeam breadboard, additional images showing the breadboard, including the μWAXS configuration, the small ion chamber, and the microscope. Section A.3 gives the mechanical drawings for the MacCHESS monocapillary housing. Section A.4 gives an image of the capillary bending platform briefly discussed in section 7.3.

A.1 Standard Monocapillary Stage

The standard monocapillary stage controls two angular motions, the pitch and yaw angles. The stage uses Oriel® 18212 encoder mike motorized actuators to set the two angles (see footnote 14 for motor vendors). Figure A.1 shows two diagrams of how the rotations are achieved. The yaw angle has a ±10º of rotation, which is plenty. The pitch angle is only a few degrees, and is often too limited. I have gotten around this limitation by having a number of different ball bearing sizes (11/32, 3/8, and 13/32 inches in diameter). I mix and match these sizes in order to get into a useful angular range for the standard monocapillary stage.

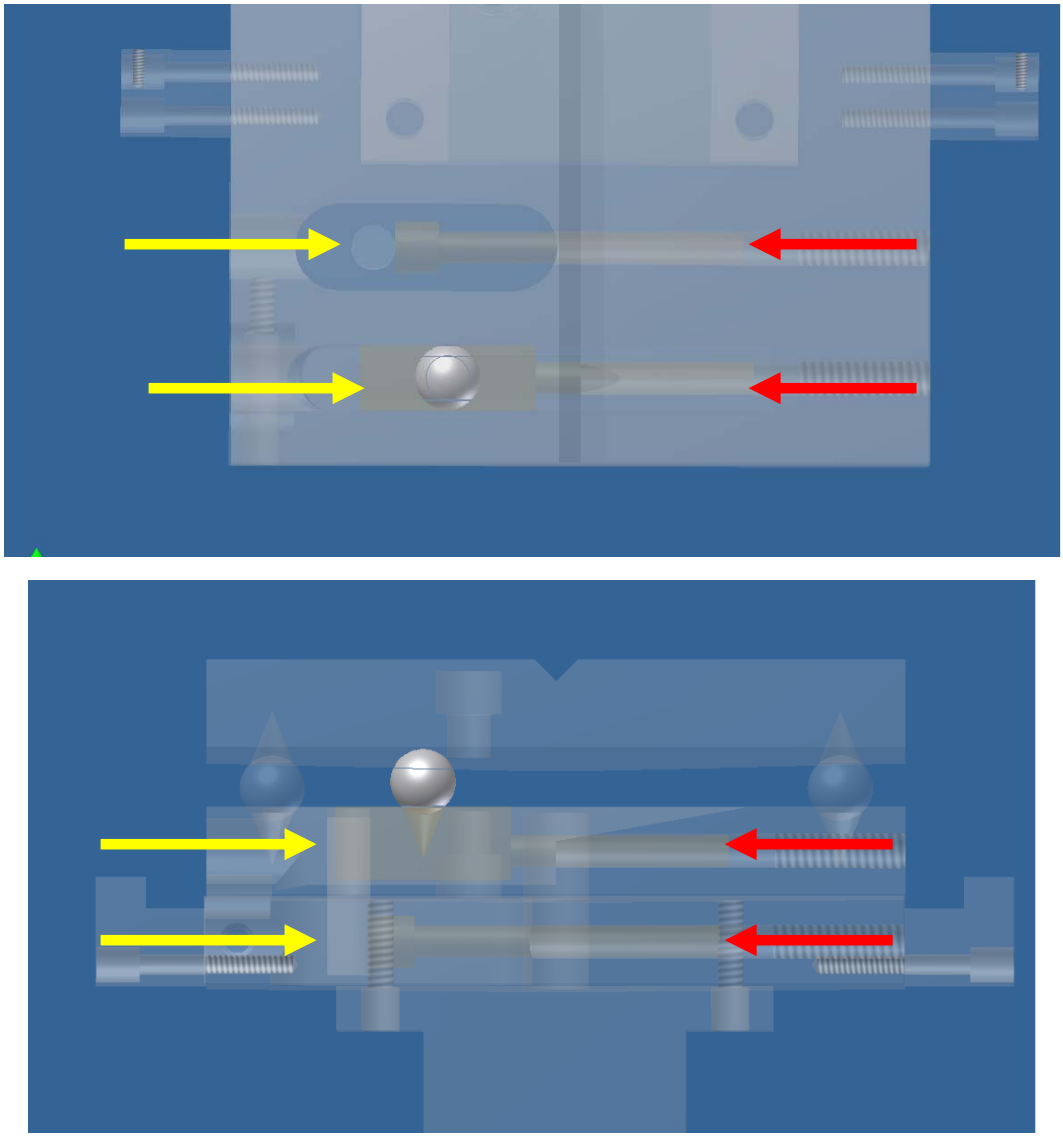

Figure A.1 This figure shows how the two angles are adjusted with motorized actuators. In both the top and bottom picture, the yellow arrows signify the placement of the actuator, and the red arrows signify the placement of a compression spring. The middle platform (of three platforms) swivels in reference to the bottom platform, adjusting the yaw. Between the top platform (with the V-groove) and the middle platform are three ball bearings. The plates are held together with a tension spring. One of the ball bearings is on a wedge at a 10º angle. Positioning of the wedge adjusts the pitch.

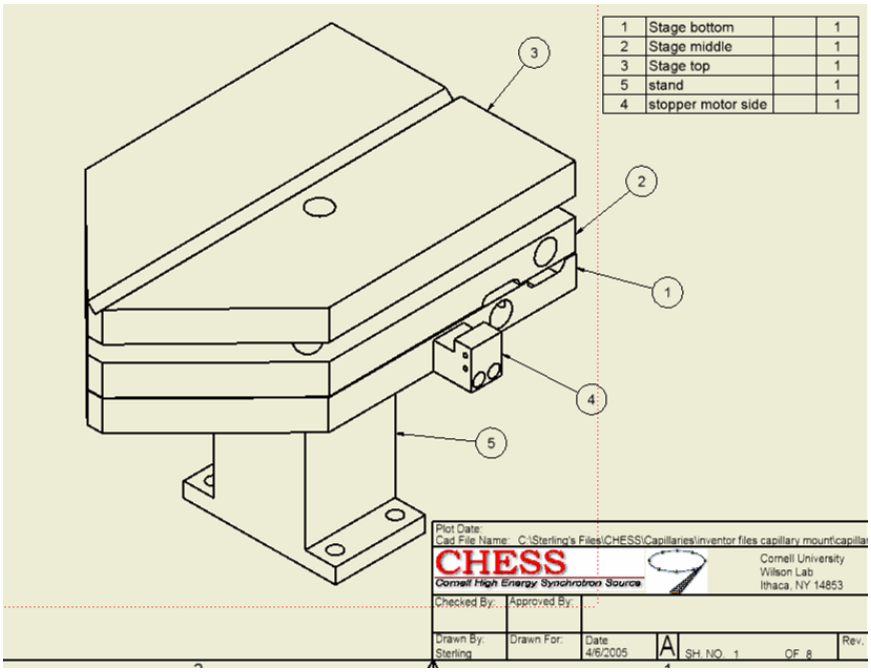

Figure A.2 A drawing of the standard monocapillary stage.

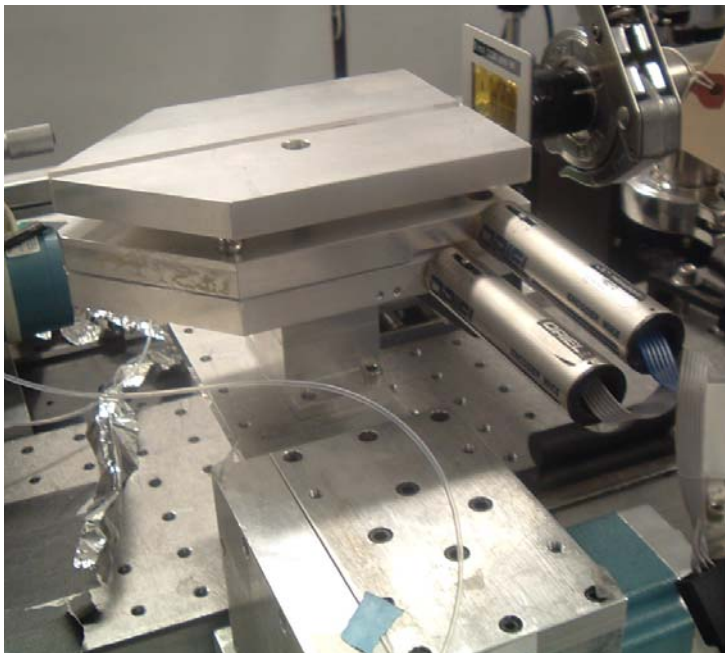

Figure A.3 An image of the standard monocapillary stage.

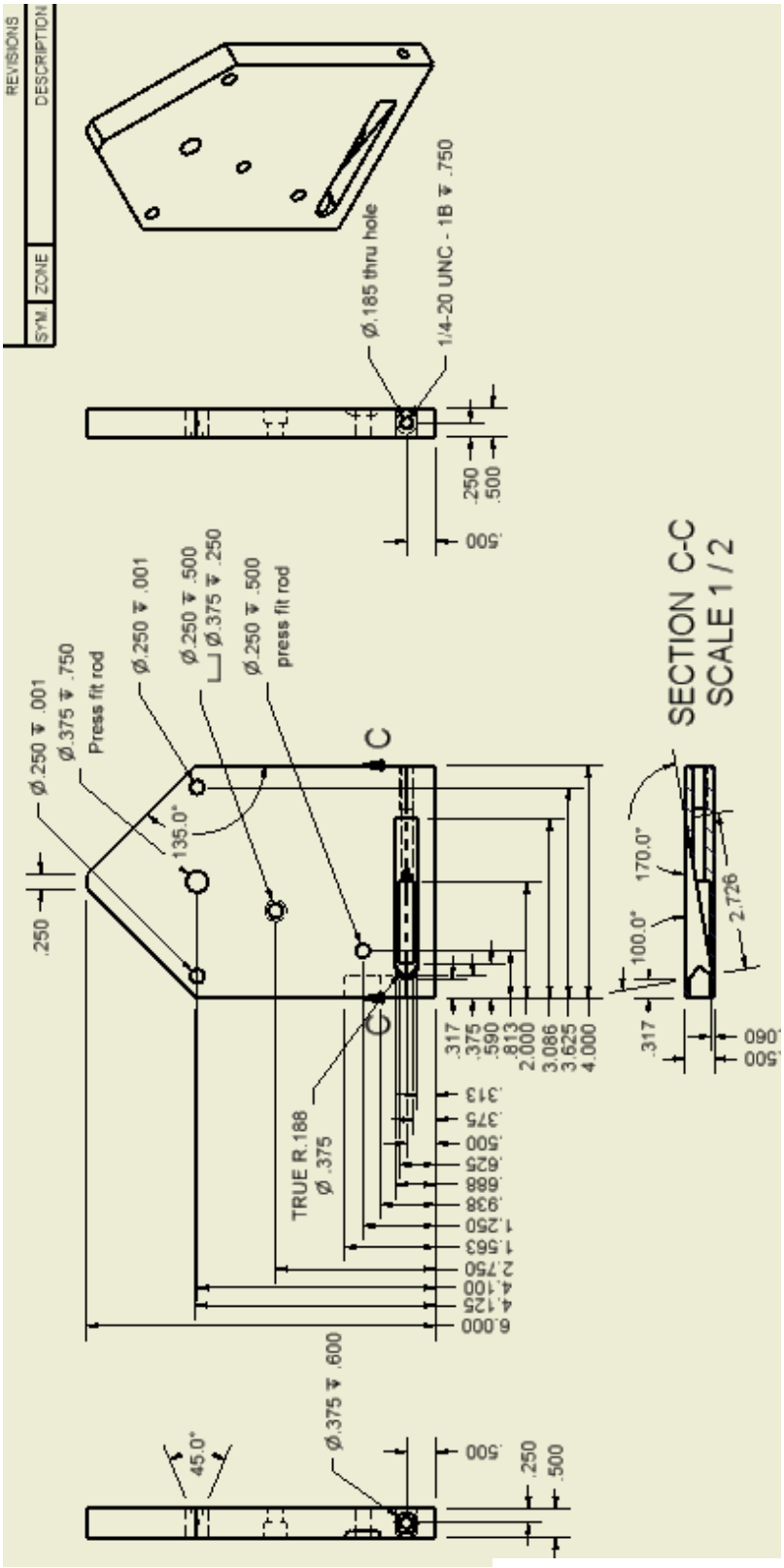

Figure A.4 stage bottom

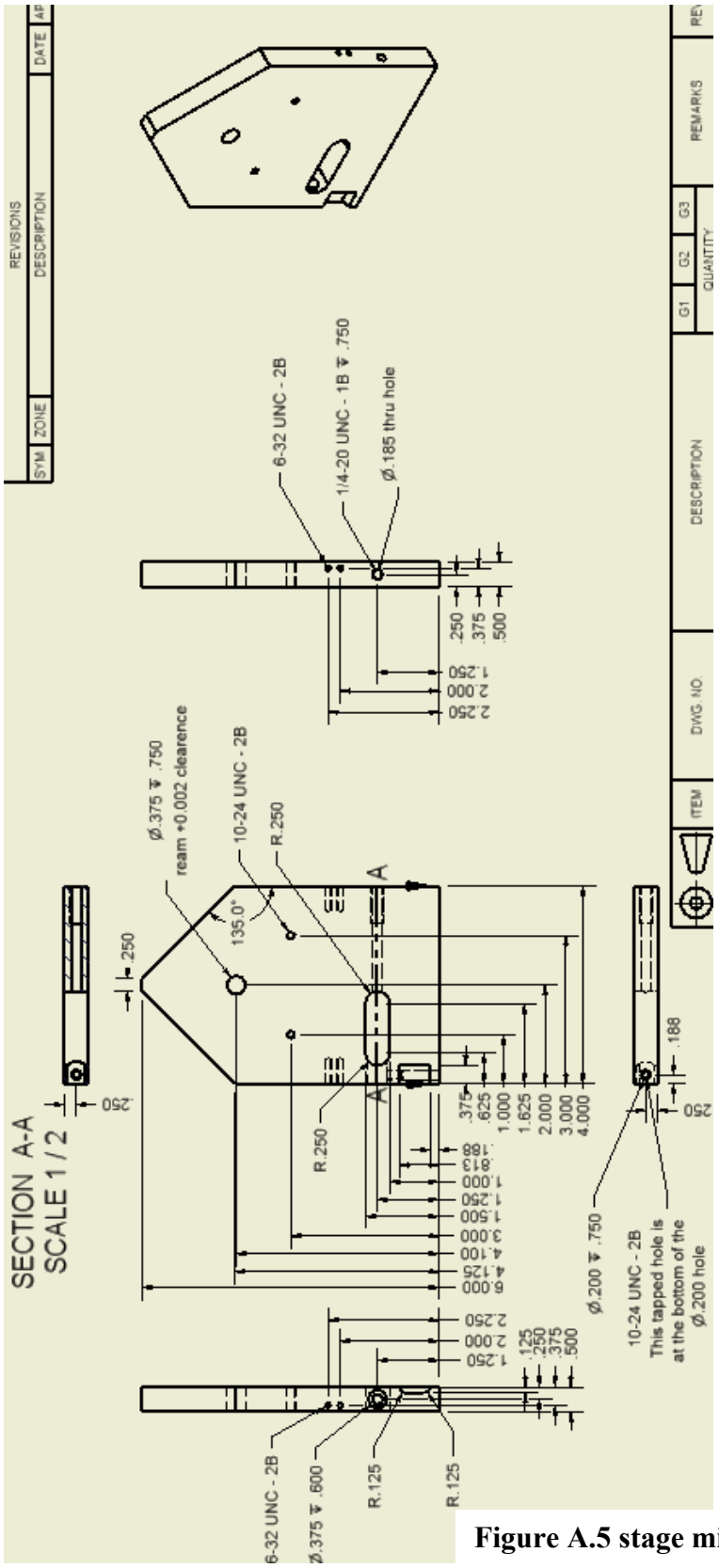

Figure A.5 stage middle

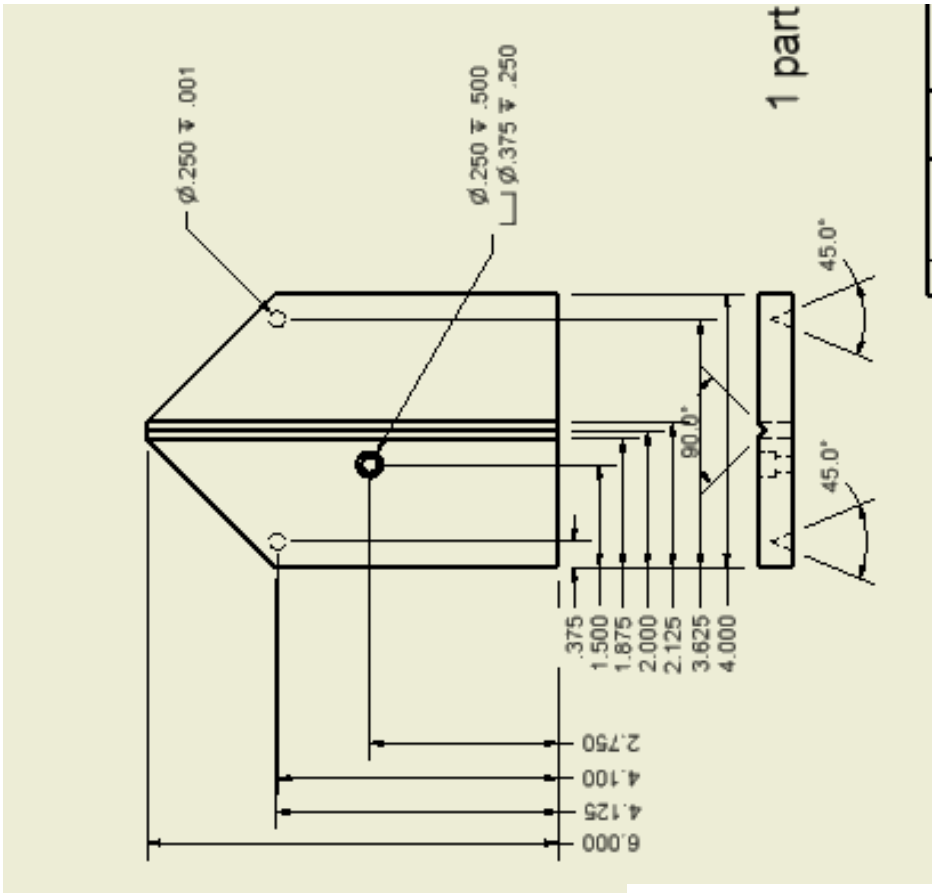

Figure A.6 stage top

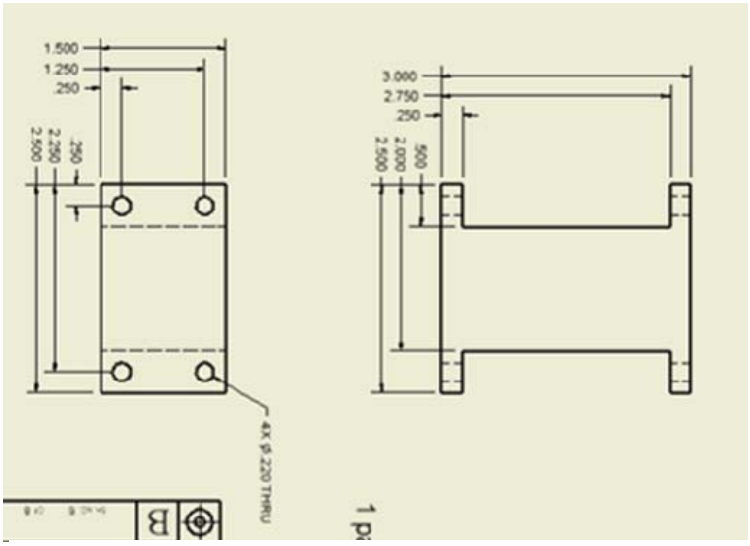

Figure A.7 The Stand (mounts to standard CHESS stages).

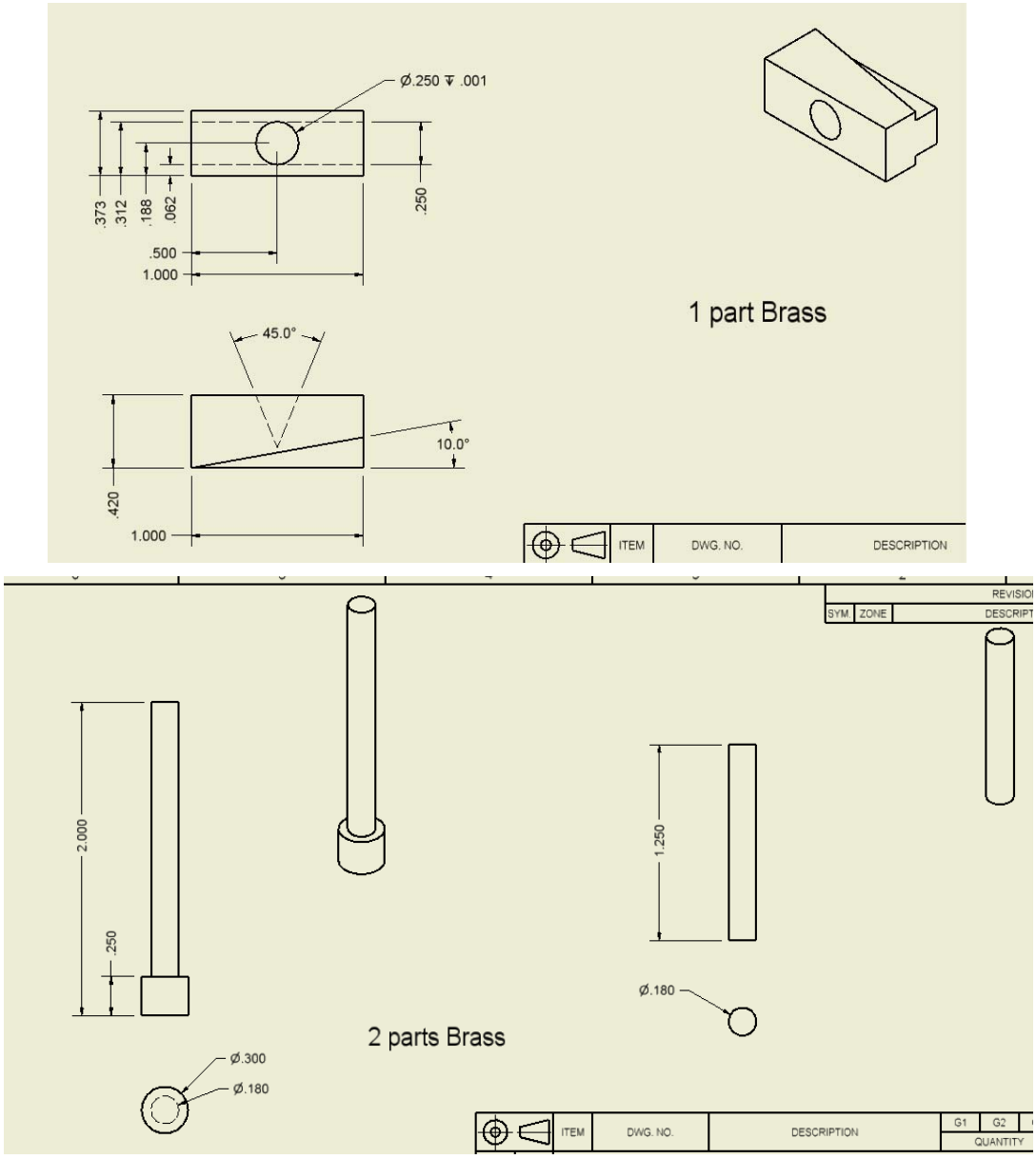

Figure A.8 Internal brass parts (see Figure A1.1).

The standard monocapillary stage is becoming obsolete. Any new capillary stages built should be based on the hardware described in both section 5.1.2 and section A2. We have already built a stand-alone capillary stage based on the Newport® hardware and the NCA12 actuators for use in the constrained space of a four-circle diffractometer (section 9.14, organic transistors project). Figure A1.8 shows this stage in the diffractometer at C1[76]. This stage has all four motions needed (x, z, pitch, and yaw), unlike the older monocapillary stage (pitch, and yaw). Also, it will allow for closer coupling of the monocapillary beam-stop with the monocapillary optic (with one more Newport M-561D-YZ ULTRAlign™ Linear Stage to hold the beam stop).

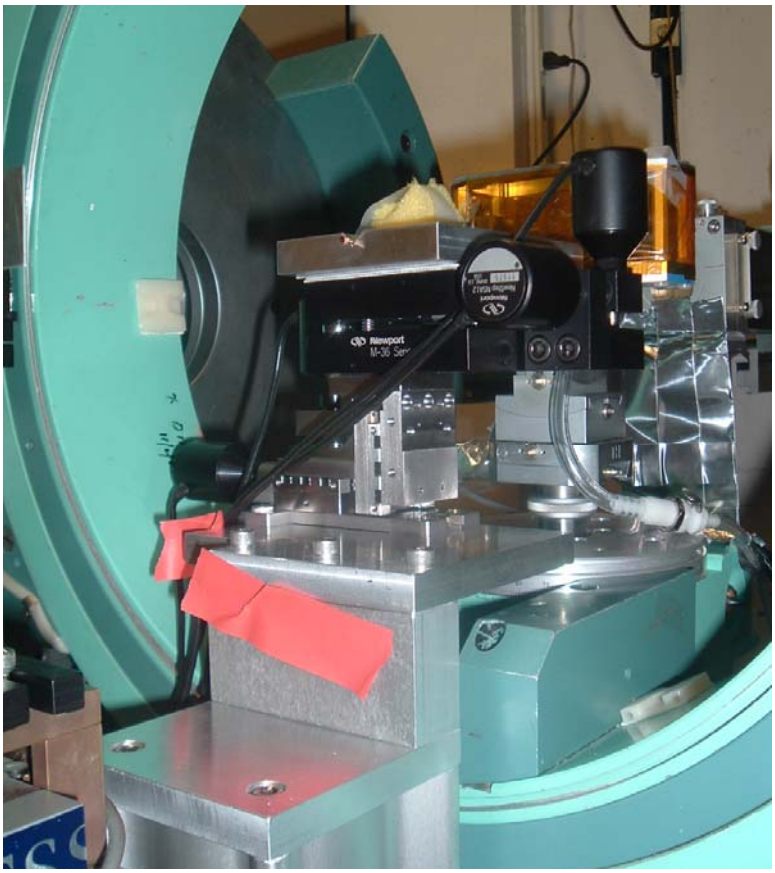

Figure A.9 The new monocapillary stage based on the hardware described in sections 5.1.2 and A2, which replaces the standard monocapillary stage.

[76] The mechanical design was put together by Aaron Lyndaker at CHESS.

A.2 The X-ray Microbeam Breadboard

The assemblies and drawings in this section were done by Tom Krawczyk at CHESS.

Figure A.10 An additional rendition of the X-ray microbeam breadboard. Drawings of a number of parts comprise Figures A2.3 thru A2.7

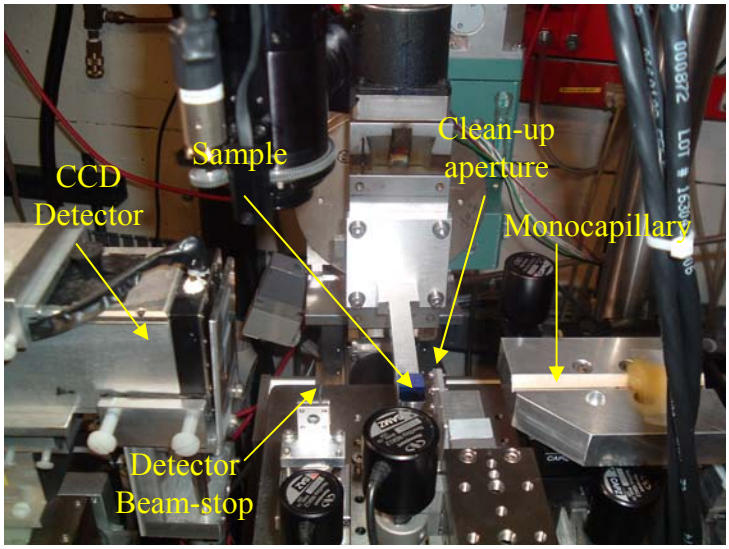

Figure A.11 An image of the x-ray microbeam breadboard modified for WAXS at D1. The samples are placed on a goniometer stage available at D1.

Table A.1 This table gives a list of parts used to construct the x-ray microbeam table, including the microscope. Vendor information is given in the footnotes of section 5.1.2.

Company	**stage and actuator Parts**	**Qty**
Newport	M-561D-YZ ULTRAlign™ Linear Stages	6
Newport	M-561D-XYZ ULTRAlign™ Linear Stages	3
Newport	M-36,Tilt and Rotation Platform, 1 Axis Tilt	1
Newport	NSA12, 11mm travel mini. motorized actuator	21
Newport	NSC200, NewStep handheld motion controller	3
Newport	NSC-SB, NewStep 8-axis switchbox, includes 41791-01, 15769-02 and NSC-CB2	3
Newport	NSC-PS25 Power supply, for up to 4 motors	2
Newport	561-UM Universal module (carriage for small Newport® MRL mini-rails)	8
Newport	NSC-485-322-1 (RS 485 to RS-232 converter)	2
NewportUS (not Newport)	RS232-Ethernet iServer	
PulseRay	Small ion chamber	2
	Microscope Parts	2
Navitar	1-6010 coupler	
Navitar	1-6233 2x Adapter short	
Navitar	1-51200 MRT SS 12x 3MMFF w/CX, Dual pos Hes	1
Navitar	1-50015 2x lens attachment for 12 x	1
Navitar	1-50013 0.75x lens attachment for 12 x	1
Navitar	1-6245 1.0x short adapter	1
Navitar	1-62420 2 phase Micro Mo. Driver Box	1
Navitar	8-62503 24 Vdc 1.05 Amp Power supply	1
Navitar	1-62823 He Manual Controller	1
Navitar	2-50157 Coax Illuminator Assembly	1
Navitar	1-62411 8mm diameter Fiber input for 12x	1
Navitar	2-50157 Coax Illuminator Assembly	1
Navitar	1-62411 8mm diameter Fiber input for 12x	1
Adirondack Video Astronomy	AV-STCAM-C Astrovid StelleCam EX color CCD Video Camera	

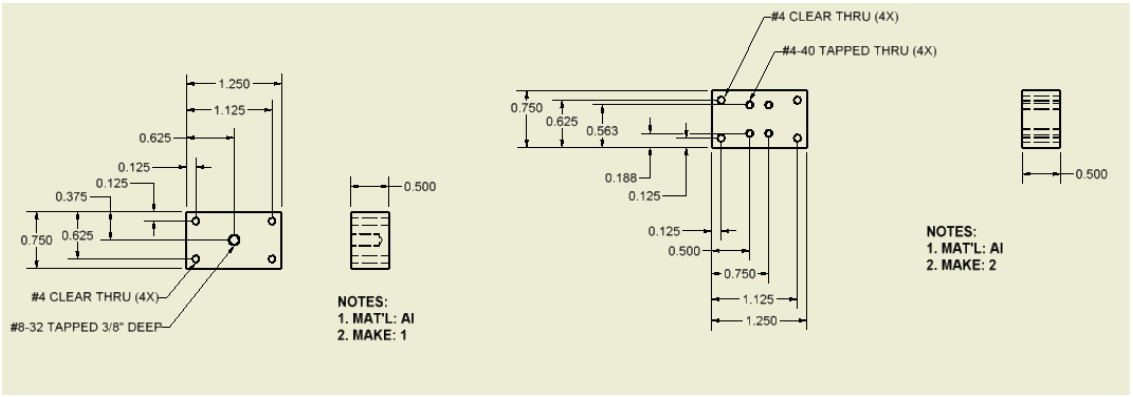

Figure A.12 Drawing for mounts that interface between the 561-UM mini-rail carriages and other components such as pinhole and sample mounts.

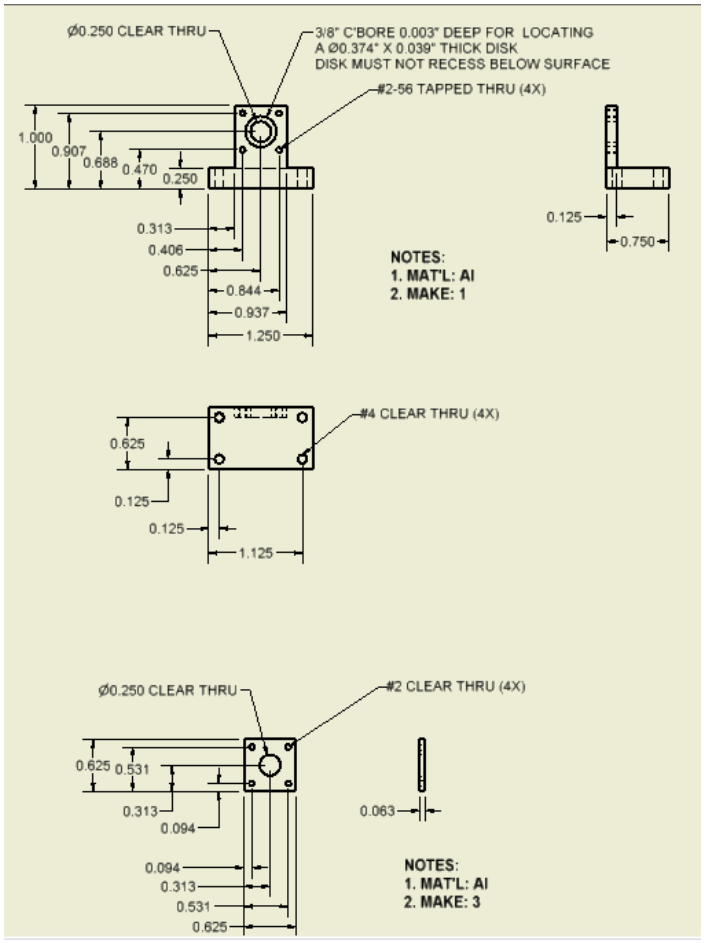

Figure A.13 Drawing for low-profile pinhole mounts.

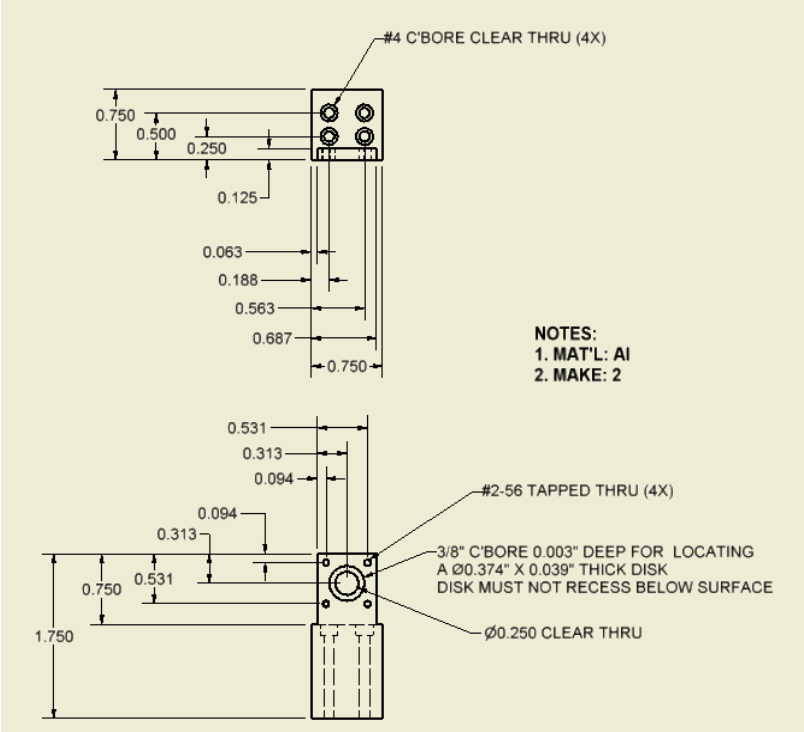

Figure A.14 Drawing for high-profile pinhole mounts.

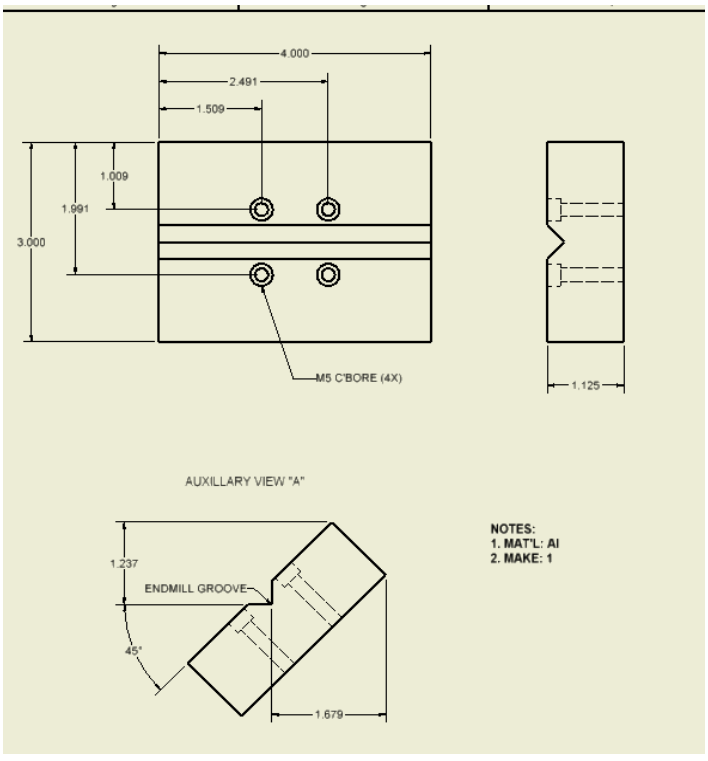

Figure A.15 Drawing for a V-groove for the monocapillary stage. It goes on top of the M-36,Tilt and Rotation Platform.

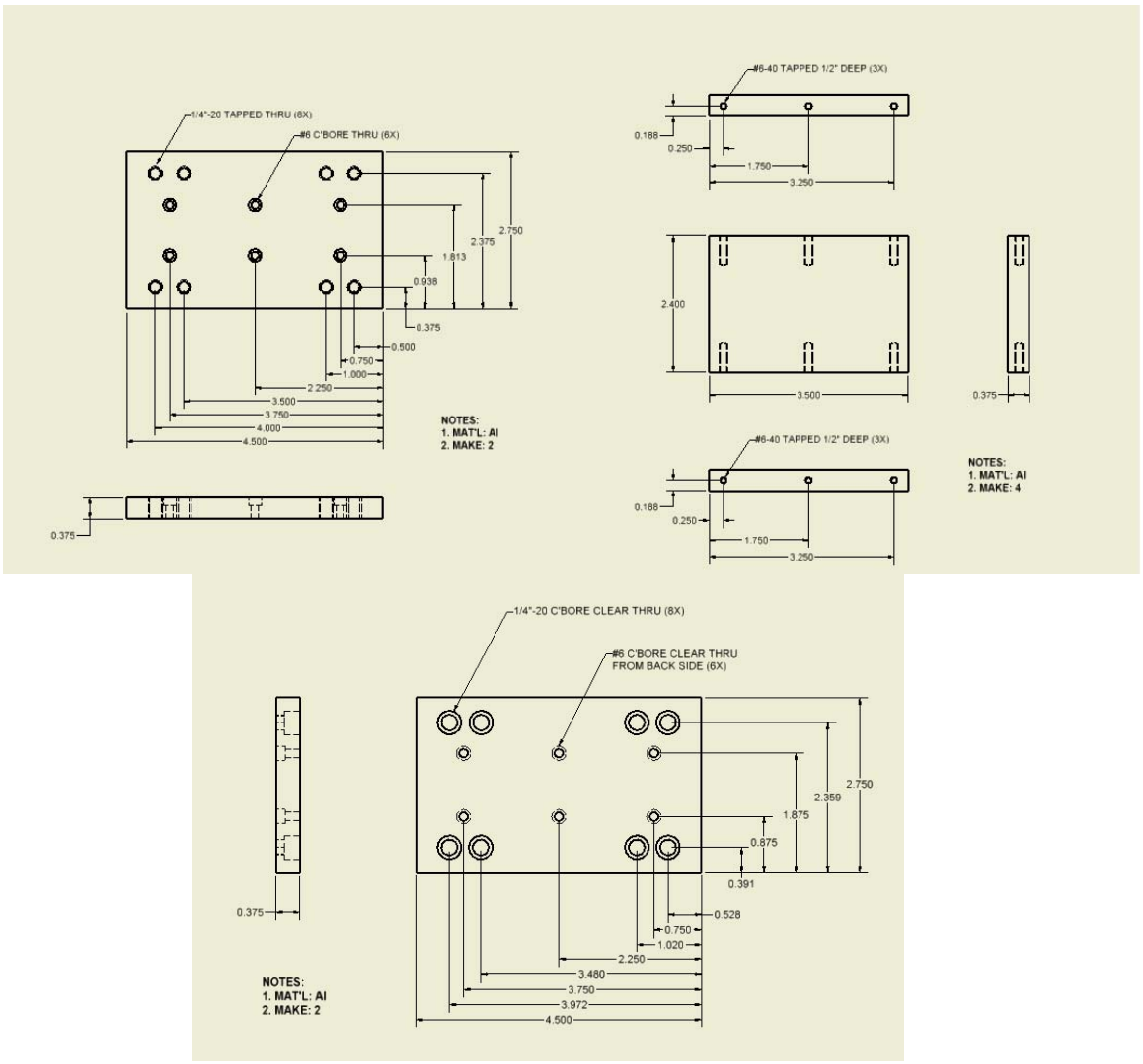

Figure A.16 Drawing for a stand for the M-561D-XYZ ULTRAlign™ Linear Stages.

Figure A.17 An image of the small ion chambers available to use with the x-ray microbeam breadboard.

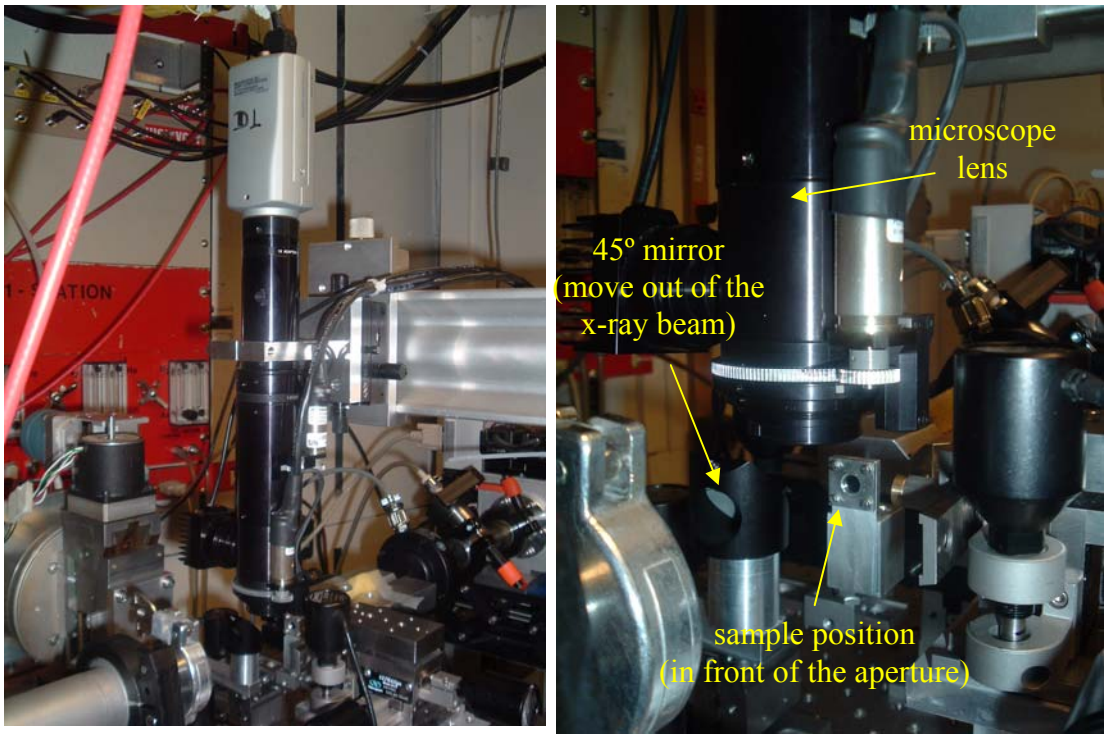

Figure A.18 An image of the microscope used with the x-ray microbeam breadboard. The close up shows a 45º mirror, which can be moved into and out of the x-ray beam path. The mirror allows the microscope to view the sample. The advantage of using a vertical microscope and a mirror at 45º is it makes the sample's x and z positions independent of each other, as viewed by the microscope. We have also used a 45º mirror with a hole in it, which allows the x-ray beam to pass through the mirror. This configuration allows viewing of the sample while in the x-ray beam (for µSAXS).

A.3 The MacCHESS Monocapillary Housing

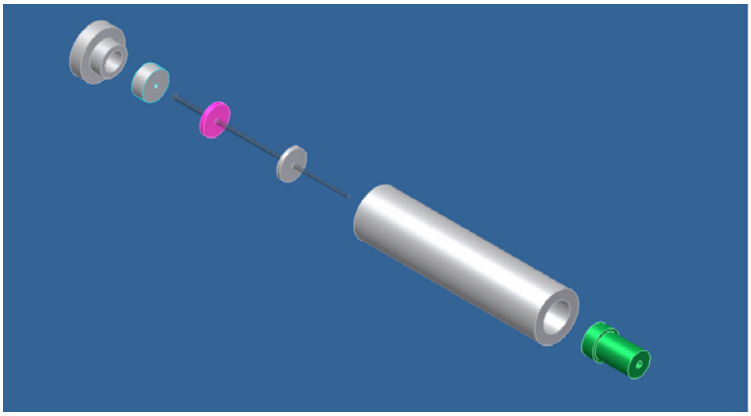

Figure A.19 A blown apart view of the MacCHESS monocapillary housing.

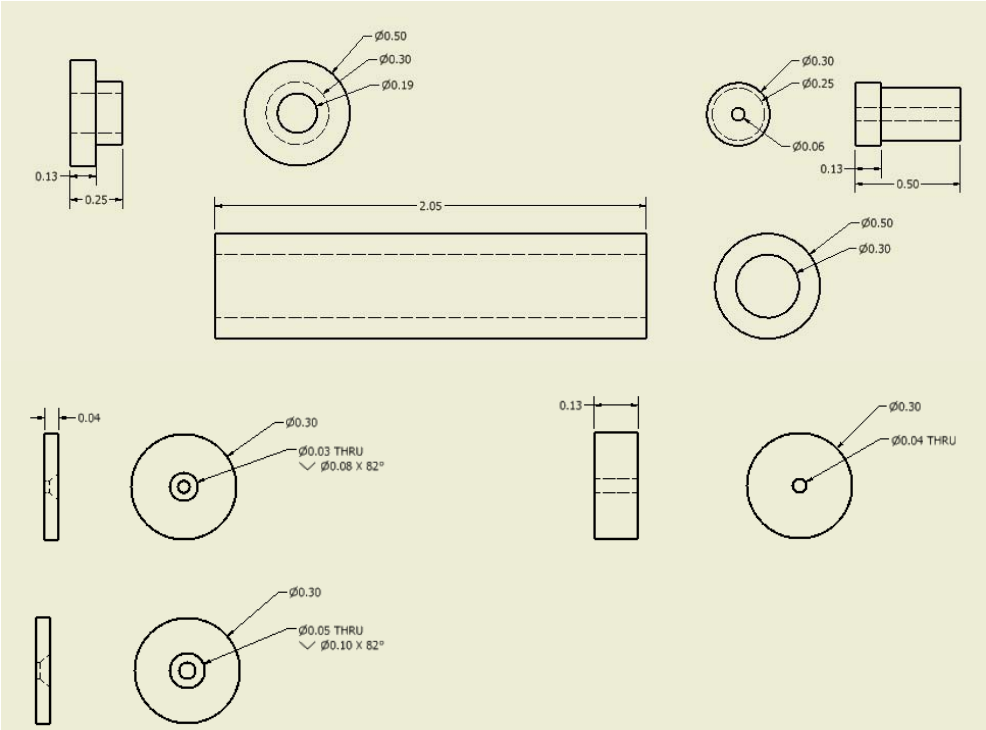

Figure A.20 Drawings of the MacCHESS monocapillary housing parts.

More information about hardware associated with the MacCHESS group can be obtained from Mike Cook at CHESS.

A.4 The Monocapillary Bending Platform

Figure A.21 The monocapillary bending platform used to dynamically bend single-bounce monocapillaries. An actuator (not shown) is put in the bracket on the right, which pushes on the plastic ruler. A monocapillary optic is placed in the V-groove, and a small sponge is placed between the optic and the plastic ruler. As the actuator pushes on the ruler, it in turn pushes on the sponge and then the optic to gently bend it. This is a modified version of the part shown in Figure A.15

B. The Monocapillary Puller

Section B of the appendix covers the monocapillary equipment used to make single-bounce monocapillary optics covered in section 6.3. Section B1 outlines the entire puller, and gives a list of equipment needed to construct it. Section B2 gives some images and mechanical drawings associated with the tension stage (discussed in section 6.3.1). Section B.3 gives an image and mechanical drawings associated with the furnace (discussed in section 6.3.2). Section B.4 gives an image and a diagram of the optical layout of the Keyence optical micrometers (discussed in section 6.3.3).

B.1 The Monocapillary Puller Hardware

Figure B.1 These images show the puller (left) and the puller's electronics rack (right). The parts are labeled on the images and listed on the next page.

List of parts labeled in Figure B.1

1. PZA12 actuator positioning motors for aligning the glass capillary in the puller. (the actuators are non-essential, but we have them available (see section 5.1.2))
2. top rotational motor on top
3. tension stage
4. furnace stage
5. furnace
6. optical micrometer #1
7. optical micrometer #2
8. bottom rotational motor
9. tension gauge

A. tension computer running LabVIEW real-time
B. monitored/display for optical micrometer #1
C. monitored/display for optical micrometer #2
D. PZA12 actuator switch box
E. tension display/readout
F. rotation motors controls
G. encoder readout for tension stage
H. main computer
I. Xenox motor controller
J. monitor and keyboard
K. furnace controller

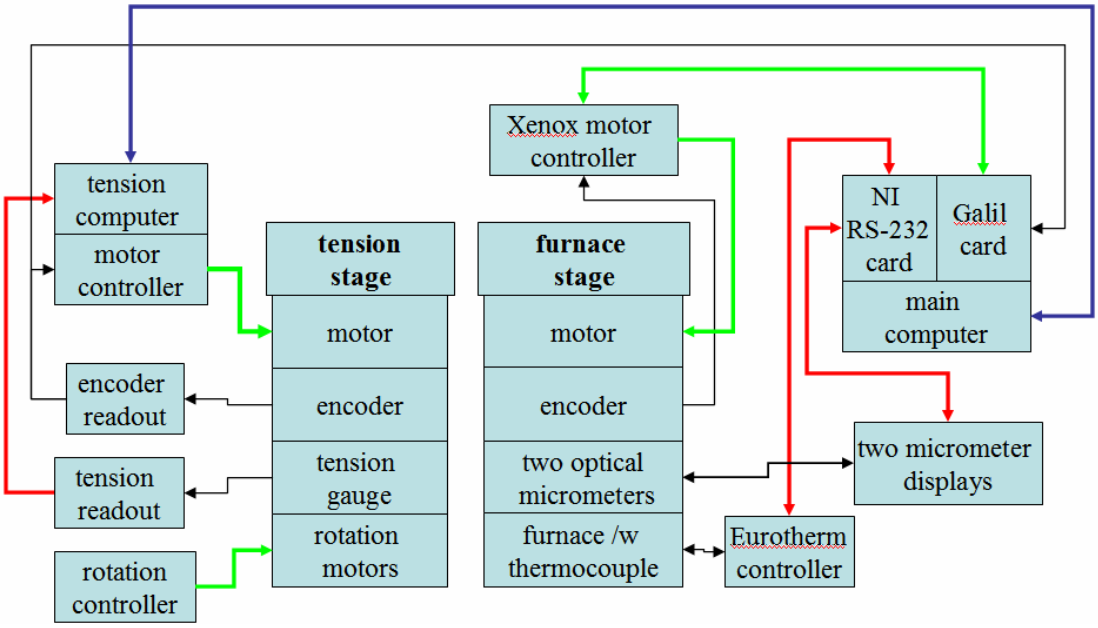

Figure B.2 This diagram shows the flow of commands and information between the various parts (same as Figure 6.7). Red lines denote RS-232 connections, green lines are motor commands, blue lines are Ethernet connections and black lines are custom cables. This figure is shown again because it outlines the functions of the components in Figure B.1. Also, Table B.1 lists the puller parts in one column according to their function in this flow diagram.

Table B.1 This table gives a list of parts used to construct the monocapillary puller. Vendor information is given in the footnotes of section 6.3.

Company	Description	Puller part (in Figure B.2)	Qty
National Instruments	PCI-8430/8 - 8 serial port concentrator	NI RS-232 card main computer	1
National Instruments	185196-01 - Serial Cable, 68 POS SCSI to 8 DB-9, 1 m (RS-232)	cable	1
National Instruments	PCI-7344 4-axis motor controller	tension motor controller	1
National Instruments	SH-68-C68 VHDCI-68-pin D-connector cable	cable	1
National Instruments	UMI-7764 Connector box	Labview RT motor controller	1
Galil, Inc	DMC-1840 - PCI Bus 4-axis controller	Galil card main computer	1
Galil, Inc	ICM-1900-LAEN-OPTO Interconnect module	cable/ connector	1
Galil, Inc	Cable-100-2M 100-pin 2 meter cable	cable	1
Galil, Inc	WSDK Servo tuning software	-	1
Zeller Electric	XLS-230-18 - Copley Xenus Digital Servo Amplifier	motor controller	1
Faber Industrial Technologies	2404/CP/VH/XX/XX/XX/ XX/XX/XX/XX/ENG Eurotherm 2404 controller	furnace controller	1
Transducer Techniques	DPM-3 Digital Panel Meter	tension display	1
Transducer Techniques	GSO-150 150g load cell	tension gauge	1
Transducer Techniques	MDB-5 5lb load cell	tension gauge	1

Table B.1 (Continued) This table gives a list of parts used to construct the monocapillary puller. Vendor information is given in the footnotes of section 6.3.

Company	Description	Puller part (in Figure B.2)	Qty
Keyence Corp.	LS-7010M laser head	optical micrometer	2
Keyence Corp.	LS-7501 Digital readout	Micrometer display	2
Keyence Corp.	LS-11 Power supply	-	1
Keyence Corp.	LS-C3AM Cable	cable	2
Keyence Corp.	LS-C3A Cable	cable	2
US Digital	MD1 motor controller	rotation controller	3
US Digital	PS-320 Power supply	-	1
Micro Mo Electronics	AD CM M3 ARSAPE motor driver	rotational motor	2
Micro Mo Electronics	Stepper motor (Am 1020-A-.25-8-09+10\1k256:1)	rotational motor	2
Centent Co.	Centent CN1073 oscillator	rotation controller	1
Oriental Motor Co.	PK266-03A 2-phase stepping motor	tension motor	1
Velmex, Inc	MB4036P40J-S4-BK-AR Unislide with Encoder and readout	tension encoder	1
AB Tech	Granite stand and linear motor	furnace stage	1

B.2 Tension Stage Components

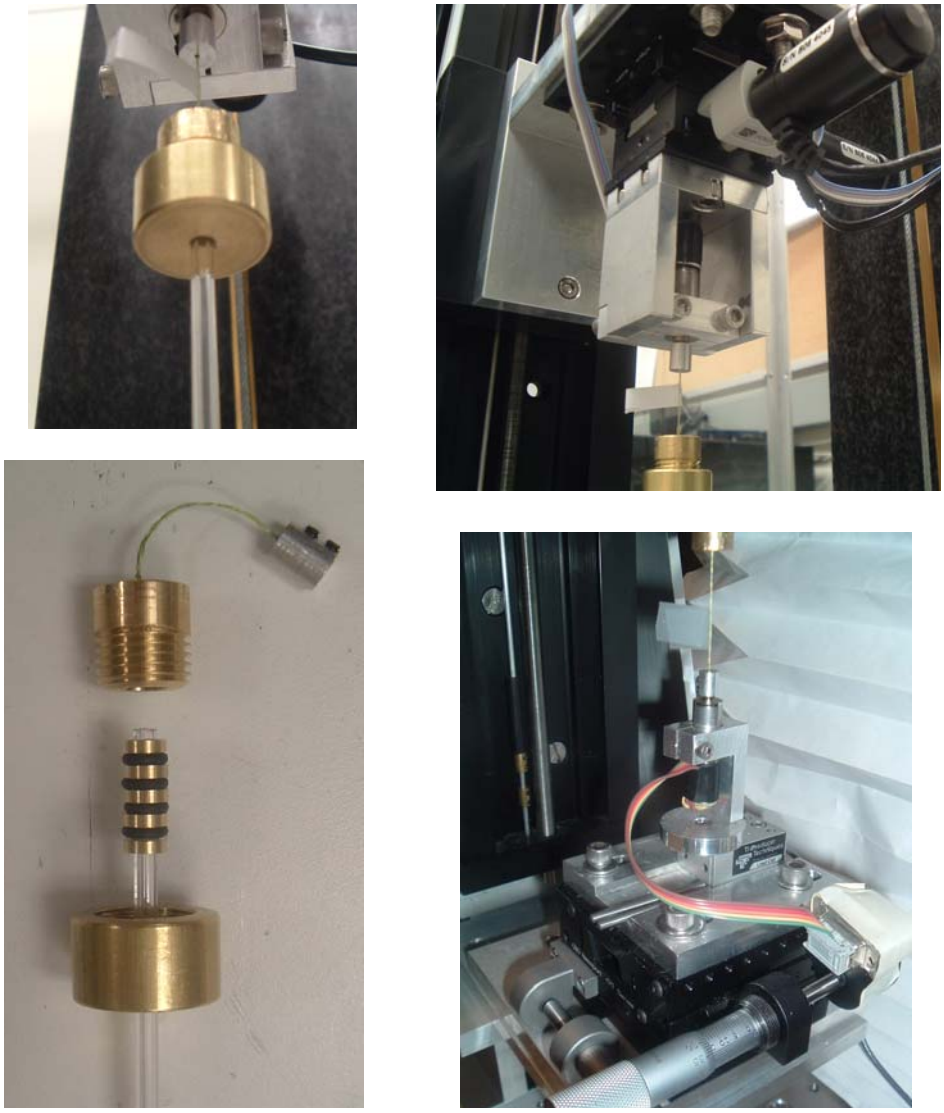

Figure B.3 This shows an image of the glass connector used to attach the glass into the puller (top and bottom left), the top rotation motor (top right), bottom rotation motor (bottom right), and strain gauge (also bottom right). Each size of glass (see Table 6.3) needs two glass connectors to match for connecting the glass into the puller. There is a series of washers and viton® o-rings placed along the end of the glass rod (bottom left image). The two ends of the glass connector are screwed together, smashing the o-rings, which in turn grip the glass rod (top left image). They are presently made out of brass; in the future they will be made out of graphite to make the glass connector lighter. The viton® o-rings are used because normal o-rings may melt.

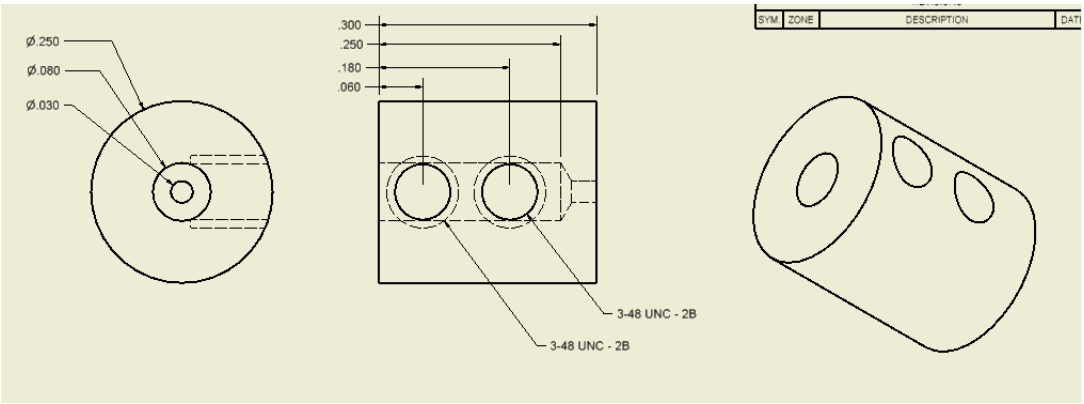

Figure B.4 A mechanical drawing of the connector between the shaft on the rotation motor and the SpiderWire® fishing line. An image of this connector can be seen in Figure B.3 in the bottom left image.

B.3 Furnace Components

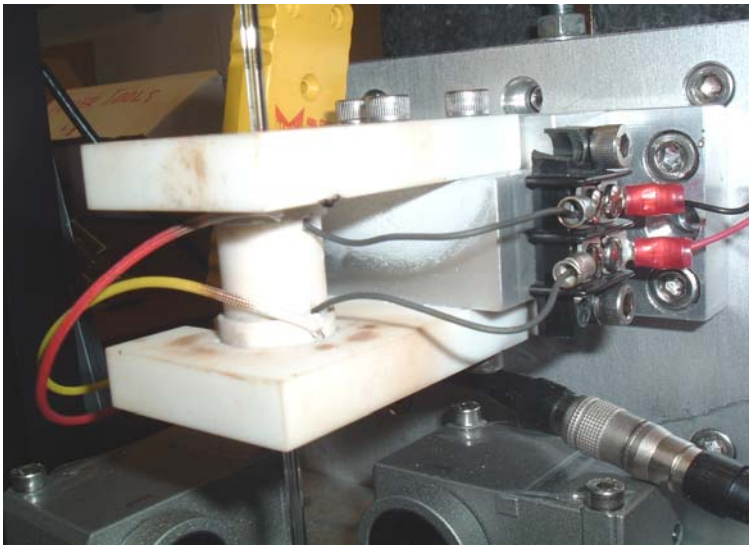

Figure B.5 An image of the furnace mounted on the furnace stage's carriage. The nichrome heating coil wires can be seen coming out of the furnace (gray), along with the thermocouple wires (red and yellow) for feedback.

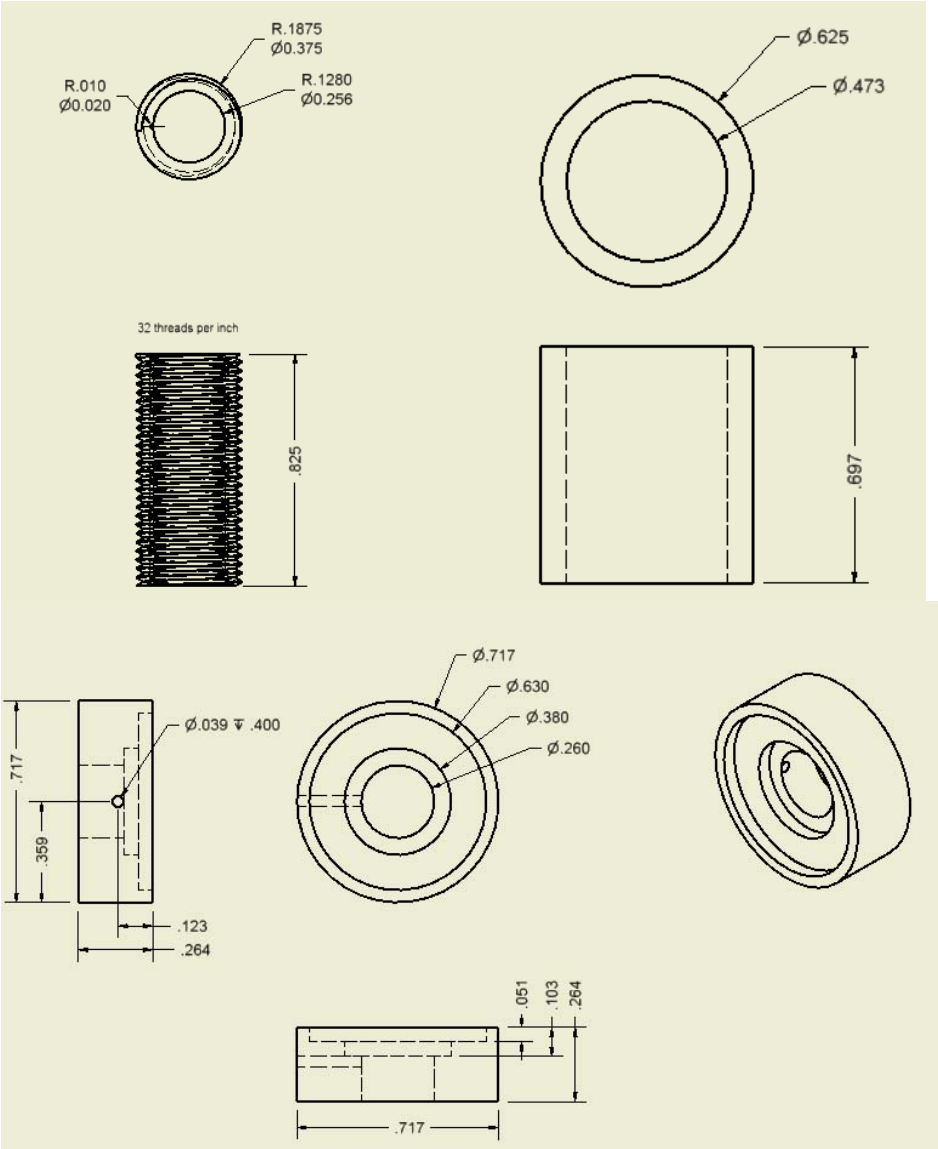

Figure B.6 The mechanical drawings of the furnace parts. All the parts are made out of macor, except for the inner core, (the threaded part in the drawing) which is made of alumina. When building the furnace, the nichrome wire (wire gauge sizes ranging from 28 to 36) is wrapped around the threading on the alumina, then cemented into place using high temperature stove and gasket cement (available at hardware stores). The rest of the housing is placed and cemented into place afterward.

B.4 Optical Scan Components

Figure B.7 An image of the two Keyence optical micrometers used to measure the glass profile both before and after the pull.

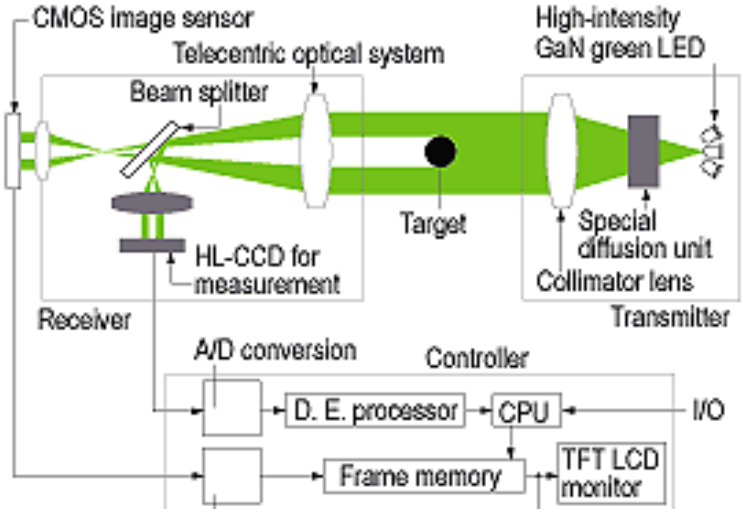

Figure B.8 A detailed functional diagram of the Keyence optical micrometers. (see Figure 6.18).

C. Transmission mirror and the Laue Setup

Section C of the appendix covers the hardware used with the x-ray transmission mirror that is used for the experiments in both Chapter 8 and section 9.13. This section also gives a diagram and list of the equipment used in the Laue Micro-Protein Crystallography experiment discussed in section 9.13.

Figure C.1 An image of the x-ray transmission mirror chamber attached to G-line's GISAXS stage. The x-ray transmission mirror chamber is filled with helium to keep the transmission mirror clean in the white x-ray beam. G-line's GISAXS stage had all the motions (left-right, up-down, pitch and yaw) needed in order to correctly position the x-ray transmission mirror into the beam.

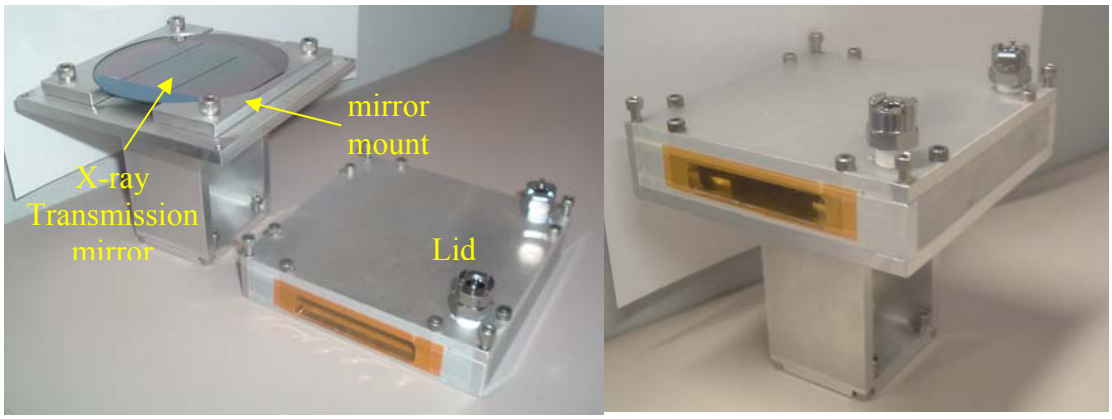

Figure C.2 Two images of the x-ray transmission mirror chamber, opened (left) and closed (right). The chamber is simply and aluminum box with two Kapton tape windows on each end to let the x-ray beam in and out. The lid of the chamber was designed be fully removed, to not get in the way when placing the fragile transmission mirror into the chamber. Also, a transmission mirror mount (Figure C.3) holds the transmission mirror within the chamber.

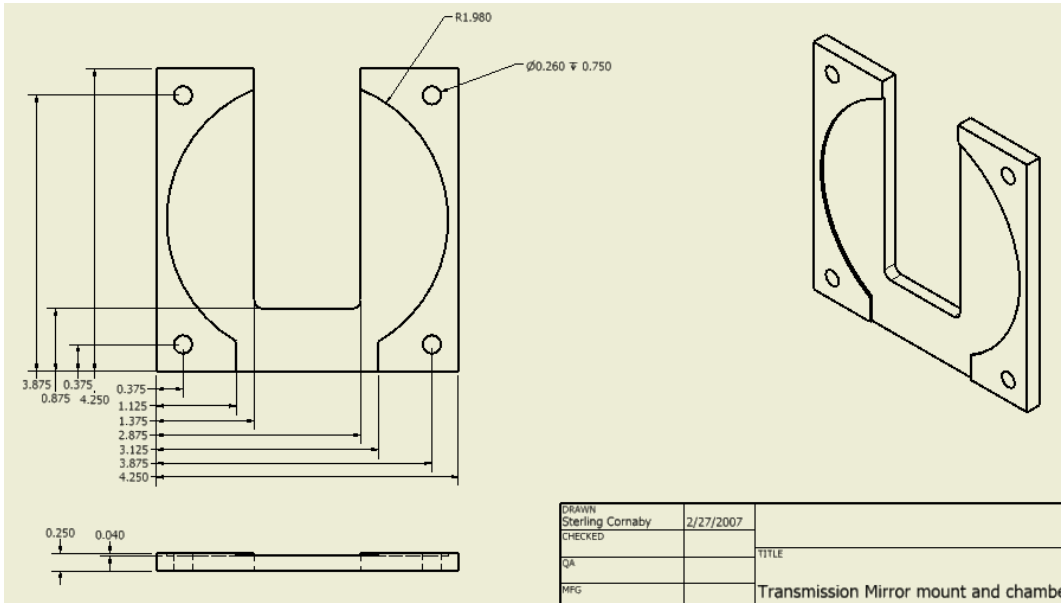

Figure C.3 A mechanical drawing of the transmission mirror mount (image in Figure C.2). This aluminum piece holds the transmission mirror within the chamber. The silicon wafer with the silicon nitride membranes simply sits in the round recess of the mount. The center cutaway allows the transmitted x-ray beam through the transmission mirror to exit the x-ray transmission mirror chamber.

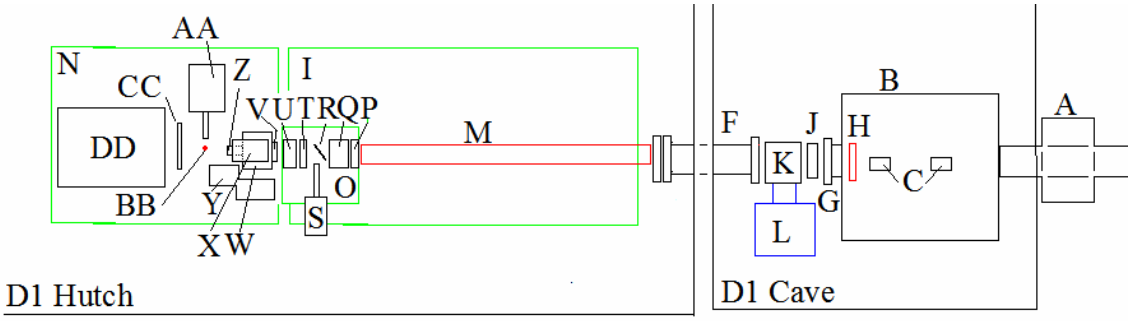

Figure C.4 A schematic of all the equipment used in the Laue Micro-protein experiment (section 9.14). The equipment used required a complete overhaul of D-line, from the D1 hutch into the D1 cave. The parts are labeled and listed below.

A. D1 upstream white beam slits set to 0.5(H)x0.5(V) mm^2
B. Optics helium box in D1 cave
C. The two Rh coated 1x4 $inch^2$ mirrors
D. nothing
E. nothing
F. Flight path through wall.
G. Beryllium window (not moved)
H. White beam safety block, moved to let the white x-ray beam into the hutch
I. D1 2' by 3' table
J. Huber slits to define beam size on transmission mirror, set to 0.3(H)x0.3(V) mm^2 (On I.)
K. Transmission mirror and chamber
L. G1's GISAXS stage to align transmission mirror
M. Flight path (On I.)
N. F3 MacCHESS crystallography table
O. The X-ray micro-beam breadboard (section 5.1.2 and A.2) (On I.)
P. Slits for monocapillary, and to clean up beam from transmission mirror (On O.)
Q. Ion chamber (On O.)
R. Kapton tape recording the bandwidth of the beam (On O.)
S. X-Flash® SDD Type 1201 detector for recording Compton scattering (On I.)
T. Capillary beam-stop (On O.)
U. Slow heavy shutter (On O.)
V. Fast Uniblitz D1 shutter (On W.)
W. F3 crystallography collimator/capillary optics mount. (On N.)
X. Sample positioning MacCHESS microscope (On W.)
Y. Cold cryo-stream (On N.)
Z. MacCHESS mounted monocapillary using the f1_mr9f20_02 monocapillary in the MacCHESS housing (the 5 um capillary) (On W)
AA. Protein crystal sample stage (On N.)

BB. Protein crystal samples (On AA)
CC. Detector beam-stop (On N.)
DD. Quantum 4 CCD area detector (On N.)

During running, two more components were added, a laser pointer and the MacCHESS helium chamber. A laser pointer (Figure 5.3) was set between the flight path (M) and the slits (P). When the x-ray beam was aligned with all the components on the x-ray microbeam table (O), the laser was then aligned with the slits (P) and the heavy shutter (U), making the laser beam have the same path as the x-ray beam. The laser beam was then used to position the F3 MacCHESS crystallography table (N). This vastly simplified the alignment of the F3 crystallography table.

The helium box was added the last few days of the run to eliminate the background x-ray scattering from the air surrounding the protein samples (section 9.6).

D. Monocapillary Optics Programs and Files

All the available programs and drawings associated with the monocapillary puller project are on the D Appendix disk, which may or may not be attached to this copy of the dissertation. An outline of what is on the disk is below:

- Mechanical drawings (Autodesk Inventor formats)
    - Standard capillary stage parts (by S. Cornaby, sections 5.1.1 and A.1)
    - Glass monocapillary puller parts (by S. Cornaby, sections 6.3 and B)
    - X-ray Microbeam breadboard parts (by T. Krawczyk, sections 5.1.2 and A.2)
    - MacCHESS monocapillary housing (by M. Cook, sections 5.1.3 and A.3)

    - Transmission mirror chamber (by S. Cornaby Chapter 8, sections 9.14 and section C)
- LabVIEW programs
    - Furnace file creator (by A. Mauer, section 6.2)
    - All puller operations programs (by S. Cornaby and T. Szebenyi, section 6.3)
- Matlab programs
    - Monocapillary analysis program (by S. Cornaby and T. Szebenyi, section 6.2)
    - Ray tracing program (by C. Couvreur and S. Cornaby, section 6.4.3)

REFERENCES

[1] Jens Als-Nielson and Des McMorrow, *Elements of Modern X-Ray Physics*. (John Wiley & Sons Ltd, New York, 2001).

[2] David Attwood, *Soft X-Rays and Extreme Ultraviolent Radation: Principles and Applications*. (Cambridge University Press, New York, 1999).

[3] Z. Chang, A. Rundquist, H. Wang, I. Christov, H. C. Kapteyn, and M. M. Murnane, "Temporal phase control of soft-x-ray harmonic emission," Phys Rev A **58** (1), R30-R33 (1998).

[4] J. J. Rocca, "Table-top soft x-ray lasers," Rev Sci Instrum **70** (10), 3799-3827 (1999).

[5] Personal communications with Boris Verman of Osmic/Rigaku Oct. 2007.

[6] ed. Albert C. Thompson and Douglas Vaughan, *Center for X-ray Optics Advanced Light Source X-ray Data Booklet*. (Lawrence Berkeley National Laboratory, University of Califorina, Berkeley, 2001), second ed.

[7] E. Sato, Y. Hayasi, R. Germer, E. Tanaka, H. Mori, T. Kawai, T. Inoue, A. Ogawa, S. Sato, T. Ichimaru, K. Takayama, J. Onagawa, and H. Ido, "Monochromatic flash x-ray generator utilizing a disk-cathode silver tube," Optical Engineering **44** (9), - (2005).

[8] J. P. Blewett, "Synchrotron radiation - Early history," J Synchrotron Radiat **5**, 135-139 (1998).

[9] I. H. Munro, "Synchrotron radiation research in the UK," J Synchrotron Radiat **4**, 344-358 (1997).

[10] B.L. Henke, E.M. Gullikson, and J.C. Davis, "On the Web at http://www-cxro.lbl.gov/index.php?content=/tools.html " (1995-2007).

[11] Manual Sanchez del Rio and Roger J. Dejus., "XOP X-ray Oriented Programs http://www.esrf.eu/computing/scientific/xop2.1/intro.html," (2003).

[12] A. Grigoriev, D. H. Do, P. G. Evans, B. Adams, E. Landahl, and E. M. Dufresne, "Synchronizing fast electrically driven phenomena with synchrotron x-ray probes," Review of Scientific Instruments **78** (2), - (2007).

[13] K. D. Finkelstein, I. V. Bazarov, A. Liepe, Q. Shen, D. Bilderback, S. Gruner, and A. Kazimirov, "Energy recovery LINAC: A next generation source for

inelastic X-ray scattering," Journal of Physics and Chemistry of Solids **66** (12), 2310-2312 (2005).

[14] B. L. Henke, E. M. Gullikson, and J. C. Davis, "X-Ray Interactions - Photoabsorption, Scattering, Transmission, and Reflection at E=50-30,000 Ev, Z=1-92," Atomic Data and Nuclear Data Tables **54** (2), 181-342 (1993).

[15] J. Drenth, *Principles in Protein X-ray Crystallography*. (Springer, 1999), Second ed.

[16] T. J. Davis, D. Gao, T. E. Gureyev, A. W. Stevenson, and S. W. Wilkins, "Phase-Contrast Imaging of Weakly Absorbing Materials Using Hard X-Rays," Nature **373** (6515), 595-598 (1995).

[17] Q. Shen, "Solving the phase problem using reference-beam X-ray diffraction," Physical Review Letters **80** (15), 3268-3271 (1998).

[18] Glenn F. Knoll, *Radiation Detection and Measurement*. (John Wiley & Sons, 2000), Third ed.

[19] James R. Janesick, *Scientific Charge-Coupled Devices*. . (SPIE Publications, 2001).

[20] S. Cornaby, A. Reyes-Mena, H. K. Pew, P. W. Moody, T. Hughes, A. Stradling, D. C. Turner, and L. V. Knight, "An XRD/XRF instrument for the microanalysis of rocks and minerals," Meas Sci Technol **12** (6), 676-683 (2001).

[21] S. M. Gruner, M. W. Tate, and E. F. Eikenberry, "Charge-coupled device area x-ray detectors," Rev Sci Instrum **73** (8), 2815-2842 (2002).

[22] G. Rossi, M. Renzi, E. F. Eikenberry, M. W. Tate, D. Bilderback, E. Fontes, R. Wixted, S. Barna, and S. M. Gruner, "Tests of a prototype pixel array detector for microsecond time-resolved X-ray diffraction," J Synchrotron Radiat **6**, 1096-1105 (1999).

[23] K. D. Finkelstein, S. Rosenblatt, and P. Cottle, "X-ray optics fabricated by deep reactive ion etching (invited)," Rev Sci Instrum **73** (3), 1464-1468 (2002).

[24] A. Kazimirov, D. M. Smilgies, Q. Shen, X. H. Xiao, Q. Hao, E. Fontes, D. H. Bilderback, S. M. Gruner, Y. Platonov, and V. V. Martynov, "Multilayer X-ray optics at CHESS," J Synchrotron Radiat **13**, 204-210 (2006).

[25] W. B. Yun, P. J. Viccaro, B. Lai, and J. Chrzas, "Coherent Hard X-Ray Focusing Optics and Applications," Rev Sci Instrum **63** (1), 582-585 (1992).

[26] A. C. Thompson, K. L. Chapman, G. E. Ice, C. J. Sparks, W. Yun, B. Lai, D. Legnini, P. J. Vicarro, M. L. Rivers, D. H. Bilderback, and D. J. Thiel, "Focusing Optics for a Synchrotron-Based X-Ray Microprobe," Nucl Instrum Meth A **319** (1-3), 320-325 (1992).

[27] B. Lai, W. B. Yun, D. Legnini, Y. Xiao, J. Chrzas, P. J. Viccaro, V. White, S. Bajikar, D. Denton, F. Cerrina, E. Difabrizio, M. Gentili, L. Grella, and M. Baciocchi, "Hard X-Ray Phase Zone Plate Fabricated by Lithographic Techniques," Appl Phys Lett **61** (16), 1877-1879 (1992).

[28] K. Saitoh, K. Inagawa, K. Kohra, C. Hayashi, A. Iida, and N. Kato, "Fabrication and Characterization of Multilayer Zone Plate for Hard X-Rays," Japanese Journal of Applied Physics Part 2-Letters **27** (11), L2131-L2133 (1988).

[29] C. Liu, R. Conley, A. T. Macrander, J. Maser, H. C. Kang, and G. B. Stephenson, "A multilayer nanostructure for linear zone-plate applications," Thin Solid Films **515** (2), 654-657 (2006).

[30] C. G. Schroer, "Focusing hard x rays to nanometer dimensions using Fresnel zone plates," Physical Review B **74** (3), - (2006).

[31] H. Rarback, D. Shu, S. C. Feng, H. Ade, J. Kirz, I. Mcnulty, D. P. Kern, T. H. P. Chang, Y. Vladimirsky, N. Iskander, D. Attwood, K. Mcquaid, and S. Rothman, "Scanning-X-Ray Microscope with 75-Nm Resolution," Rev Sci Instrum **59** (1), 52-59 (1988).

[32] M. A. Kumakhov, "Channeling of Photons and New X-Ray Optics," Nuclear Instruments & Methods in Physics Research Section B-Beam Interactions with Materials and Atoms **48** (1-4), 283-286 (1990).

[33] D. H. Bilderback, D. J. Thiel, R. Pahl, and K. E. Brister, "X-Ray Applications with Glass-Capillary Optics," J Synchrotron Radiat **1**, 37-42 (1994).

[34] Q. F. Xiao and S. V. Poturaev, "Polycapillary-Based X-Ray Optics," Nucl Instrum Meth A **347** (1-3), 376-383 (1994).

[35] N. Gao, I. Y. Ponomarev, Q. F. Xiao, W. M. Gibson, and D. A. Carpenter, "Monolithic polycapillary focusing optics and their applications in microbeam x-ray fluorescence," Appl Phys Lett **69** (11), 1529-1531 (1996).

[36] E. A. Stern, Z. Kalman, A. Lewis, and K. Lieberman, "Simple Method for Focusing X-Rays Using Tapered Capillaries," Applied Optics **27** (24), 5135-5139 (1988).

[37] D. J. Thiel, D. H. Bilderback, and A. Lewis, "Production of Intense Micrometer-Sized X-Ray-Beams with Tapered Glass Monocapillaries," Rev Sci Instrum **64** (10), 2872-2878 (1993).

[38] S. A. Hoffman, D. J. Thiel, and D. H. Bilderback, "Developments in Tapered Monocapillary and Polycapillary Glass X-Ray Concentrators," Nucl Instrum Meth A **347** (1-3), 384-389 (1994).

[39] D. X. Balaic, K. A. Nugent, Z. Barnea, R. Garrett, and S. W. Wilkins, "Focusing of X-Rays by Total External Reflection from a Paraboloidally Tapered Glass-Capillary," J Synchrotron Radiat **2**, 296-299 (1995).

[40] D. H. Bilderback and R. Huang, "X-ray tests of microfocusing mono-capillary optic for protein crystallography," Nucl Instrum Meth A **467**, 970-973 (2001).

[41] R. Huang and D. H. Bilderback, "Simulation of microfocused image size from a one-bounce glass capillary," Nucl Instrum Meth A **467**, 978-981 (2001).

[42] A. Snigirev, V. Kohn, I. Snigireva, and B. Lengeler, "A compound refractive lens for focusing high-energy X-rays," Nature **384** (6604), 49-51 (1996).

[43] C. G. Schroer, M. Kuhlmann, U. T. Hunger, T. F. Gunzler, O. Kurapova, S. Feste, F. Frehse, B. Lengeler, M. Drakopoulos, A. Somogyi, A. S. Simionovici, A. Snigirev, I. Snigireva, C. Schug, and W. H. Schroder, "Nanofocusing parabolic refractive x-ray lenses," Appl Phys Lett **82** (9), 1485-1487 (2003).

[44] K. Evans-Lutterodt, J. M. Ablett, A. Stein, C. C. Kao, D. M. Tennant, F. Klemens, A. Taylor, C. Jacobsen, P. L. Gammel, H. Huggins, S. Ustin, G. Bogart, and L. Ocola, "Single-element elliptical hard x-ray micro-optics," Optics Express **11** (8), 919-926 (2003).

[45] S. Suehiro, H. Miyaji, and H. Hayashi, "Refractive Lens for X-Ray Focus," Nature **352** (6334), 385-386 (1991).

[46] P. Kirkpatrick and A. V. Baez, "Formation of Optical Images by X-Rays," Journal of the Optical Society of America **38** (9), 766-774 (1948).

[47] O. Hignette, P. Cloetens, G. Rostaing, P. Bernard, and C. Morawe, "Efficient sub 100 nm focusing of hard x rays," Rev Sci Instrum **76** (6), - (2005).

[48] F. Pfeiffer, C. David, M. Burghammer, C. Riekel, and T. Salditt, "Two-dimensional x-ray waveguides and point sources," Science **297** (5579), 230-234 (2002).

[49] C. Bergemann, H. Keymeulen, and J. F. van der Veen, "Focusing X-ray beams to nanometer dimensions," Physical Review Letters **91** (20), - (2003).

[50] C. Ollinger, C. Fuhse, A. Jarre, and T. Salditt, "Two-dimensional X-ray waveguides on a grating," Physica B-Condensed Matter **357** (1-2), 53-56 (2005).

[51] H. C. Kang, J. Maser, G. B. Stephenson, C. Liu, R. Conley, A. T. Macrander, and S. Vogt, "Nanometer linear focusing of hard x rays by a multilayer Laue lens," Physical Review Letters **96** (12), - (2006).

[52] W. Jark, F. Perennes, and M. Matteucci, "On the feasibility of large-aperture Fresnel lenses for the microfocusing of hard X-rays," J Synchrotron Radiat **13**, 239-252 (2006).

[53] A. Snigirev, "The Recent Development of Bragg-Fresnel Crystal Optics - Experiments and Applications at the Esrf (Invited)," Rev Sci Instrum **66** (2), 2053-2058 (1995).

[54] A. Snigirev, A. Bjeoumikhov, A. Erko, I. Snigireva, M. Grigoriev, V. Yunkin, M. Erko, and S. Bjeoumikhova, "Two-step hard X-ray focusing combining Fresnel zone plate and single-bounce ellipsoidal capillary," J Synchrotron Radiat **14**, 326-330 (2007).

[55] Hans Wolter, "Spiegelsysteme streifenden Einfalls als abbildende Optiken für Röntgenstrahlen," Annalen der Physik **445** (1-2), 94-114 (1952).

[56] J. A. Howell and P. Horowitz, "Ellipsoidal and Bent Cylindrical Condensing Mirrors for Synchrotron Radiation," Nuclear Instruments & Methods **125** (2), 225-230 (1975).

[57] J. Voss, C. Kunz, A. Moewes, and I. Storjohann, "Grazing-Incidence Optics for Soft-X-Ray Microscopy," Rev Sci Instrum **63** (1), 569-573 (1992).

[58] R. Huang and D. H. Bilderback, "Single-bounce monocapillaries for focusing synchrotron radiation: modeling, measurements and theoretical limits," J Synchrotron Radiat **13**, 74-84 (2006).

[59] M. Hasegawa, H. Taira, T. Harada, S. Aoki, and K. Ninomiya, "Fabrication of Wolter-Type X-Ray Focusing Mirror Using Epoxy-Resin," Rev Sci Instrum **65** (8), 2568-2573 (1994).

[60] H. Takano, S. Aoki, M. Kumegawa, N. Watanabe, T. Ohhigashi, T. Aota, K. Yamamoto, H. Yokosuka, R. Tanoue, Y. Tsujita, and M. Ando, "X-ray scattering microscope with a Wolter mirror," Rev Sci Instrum **73** (7), 2629-2633 (2002).

[61] J. E. Harvey, A. Krywonos, P. L. Thompson, and T. T. Saha, "Grazing-incidence hyperboloid-hyperboloid designs for wide-field x-ray imaging applications," Applied Optics **40** (1), 136-144 (2001).

[62] C. M. Kewish, L. Assoufid, A. T. Macrander, and J. Qian, "Wave-optical simulation of hard-x-ray nanofocusing by precisely figured elliptical mirrors," Applied Optics **46** (11), 2010-2021 (2007).

[63] Donald H. Bilderback, Alexander Kazimirov, Richard Gillilan, Sterling Cornaby, Arthur Woll, Chang-Sheng Zha, and Rong Huang, "Optimizing Monocapillary Optics for Synchrotron X-ray Diffraction, Fluorescence Imaging, and Spectroscopy Applications," AIP Conference Proceedings **879**, 758-763 (2007).

[64] Rong Huang and Donald H Bilderback, "Secondary Focusing for Micro-Diffraction Using One-Bounce Capillaries," Eighth International Conference on Synchrotron Radiation Instrumentation, AIP Confrence Proceedings, 712-715 (2004).

[65] A. Snigirev, A. Bjeoumikhov, A. Erko, I. Snigireva, M. Grigoriev, V. Yunkin, M. Erko, and S. Bjeoumikhova, "Submicrometer hard X-ray focusing using a single-bounce ellipsoidal capillary combined with a Fresnel zone plate," J Synchrotron Radiat **14**, 227-228 (2007).

[66] Werner Vogel, *Glass Chemistry*. (Springer-Verlag Berlin and Heidelberg GmbH & Co K., 1994), 2nd revised edition ed.

[67] A. Fluegel, "Glass Viscosity Calculation Based on a Global Statistical Modeling Approach," Glass Technol.: Europ. J. Glass Sci. Technol. A **vol. 48** (no. 1), p 13-30 (2007).

[68] SciGlass 6.7 (2006).

[69] Thomas P. Seward III and Terese Vascott (Editors), *High Temperature Glass Melt Property Database for Process Modeling*. (The American Ceramic Society, Westerville, Ohio, 2005).

[70] Optical Society of America, *Handbook of Optics Vol. III*. (McGraw-Hill Professional, 2000).

[71] George Ellis, *Control System Design Guide, Using Your Computer to Understand and Diagnose Feedback Controllers* (Elsevier Academic Press, 2004), Third ed.

[72] A. L. Yarin, P. Gospodinov, and V. I. Roussinov, "Stability Loss and Sensitivity in Hollow-Fiber Drawing," Physics of Fluids **6** (4), 1454-1463 (1994).

[73] P. Gospodinov and A. L. Yarin, "Draw resonance of optical microcapillaries in non-isothermal drawing," International Journal of Multiphase Flow **23** (5), 967-976 (1997).

[74] A. L. Yarin, P. Gospodinov, O. Gottlieb, and M. D. Graham, "Newtonian glass fiber drawing: Chaotic variation of the cross-sectional radius," Physics of Fluids **11** (11), 3201-3208 (1999).

[75] H. M. Reeve and A. M. Mescher, "Effect of unsteady natural convection on the diameter of drawn polymer optical fiber," Optics Express **11** (15), 1770-1779 (2003).

[76] J. S. Lee, H. W. Jung, J. C. Hyun, and L. E. Scriven, "Simple indicator of draw resonance instability in melt spinning processes," Aiche Journal **51** (10), 2869-2874 (2005).

[77] J. J. Wylie, H. X. Huang, and R. M. Miura, "Thermal instability in drawing viscous threads," Journal of Fluid Mechanics **570**, 1-16 (2007).

[78] A.L. Yarin, *Free Liquid Jets and Films: Hydrodynamics and Rheology* (Longman Scientific & Technical and Wiley & Sons, Harlow, New York 1993).

[79] R. Mroczka, G. Zukocinski, and A. Kuczumow, "Investigations of X-ray metallic capillaries," Journal of Alloys and Compounds **401** (1-2), 108-117 (2005).

[80] Gregory Hirsch, "Metal Monocapillary Optics Produced by Hydraulic Pressing," Eighth International Conference on Synchrotron Radiation Instrumentation, AIP Confrence Proceedings, 728-731 (2004).

[81] G. Hirsch, "Metal capillary optics: novel fabrication methods and characterization," X-Ray Spectrom **32** (3), 229-238 (2003).

[82] M. P. Ulmer, R. Altkorn, M. E. Graham, A. Madan, and Y. S. Chu, "Production and performance of multilayer-coated conical x-ray mirrors," Applied Optics **42** (34), 6945-6952 (2003).

[83] M. P. Ulmer, R. Haidle, R. Altkorn, P. Georgopoulos, B. Rodricks, and P. Z. Takacs, "Fabrication and Characterization of Replicated and Lacquer-Coated Grazing-Incidence Optics for X-Ray Astronomy," Optical Engineering **30** (8), 1150-1154 (1991).

[84] G. E. Ice, C. R. Hubbard, B. C. Larson, J. W. L. Pang, J. D. Budai, S. Spooner, S. C. Vogel, R. B. Rogge, J. H. Fox, and R. L. Donaberger, "High-performance Kirkpatrick-Baez supermirrors for neutron milli- and micro-beams," Materials Science and Engineering a-Structural Materials Properties Microstructure and Processing **437** (1), 120-125 (2006).

[85] C. Liu, L. Assoufid, R. Conley, A. T. Macrander, G. E. Ice, and Z. J. Tischler, "Profile coating and its application for Kirkpatrick-Baez mirrors," Optical Engineering **42** (12), 3622-3628 (2003).

[86] P. A. Lynch, A. W. Stevenson, D. Liang, D. Parry, S. Wilkins, and N. Tamura, "A laboratory based system for Laue micro x-ray diffraction," Rev Sci Instrum **78** (2), - (2007).

[87] Sterling Cornaby and Donald H. Bilderback, "Silicon Nitride Transmission X-ray Mirrors," J Synchrotron Radiat (Accepted March 2008).

[88] B. M. Lairson and D. H. Bilderback, "Transmission-X-Ray Mirror - a New Optical-Element," Nucl Instrum Methods **195** (1-2), 79-83 (1982).

[89] D. H. Bilderback, K. Moffat, and D. M. E. Szebenyi, "Time-Resolved Laue Diffraction from Protein Crystals - Instrumental Considerations," Nuclear Instruments & Methods in Physics Research Section a-Accelerators Spectrometers Detectors and Associated Equipment **222** (1-2), 245-251 (1984).

[90] A. Iida, T. Matsushita, and Y. Gohshi, "Synchrotron Radiation Excited X-Ray-Fluorescence Analysis Using Wide Band Pass Monochromators," Nuclear Instruments & Methods in Physics Research Section a-Accelerators Spectrometers Detectors and Associated Equipment **235** (3), 597-602 (1985).

[91] Personal communications with T. Matsushita of the Photon Factory, (2007).

[92] Personal communications with R. Ilic at CNF, (2008).

[93] S. Desgreniers, L. Beaulieu, and I. Lepage, "Pressure-induced structural changes in ZnS," Physical Review B **61**, 8726 (2000).

[94] Personal communications with with J. Smith and S. Desgreniers, (June 2005 and Feb. 2007).

[95] A. A. Sirenko, A. Kazimirov, A. Ougazzaden, S. M. O'Malley, D. H. Bilderback, Z. H. Cai, B. Lai, R. Huang, V. K. Gupta, M. Chien, and S. N. G. Chu, "Strain relaxation and surface migration effects in InGaAlAs and InGaAsP selective-area-grown ridge waveguides," Appl Phys Lett **88** (8), - (2006).

[96] A. A. Sirenko, A. Kazimirov, S. Cornaby, D. H. Bilderback, B. Neubert, P. Bruckner, F. Scholz, V. Shneidman, and A. Ougazzaden, "Microbeam high angular resolution x-ray diffraction in InGaN/GaN selective-area-grown ridge structures," Appl Phys Lett **89** (18), - (2006).

[97] A. A. Sirenko, A. Kazimirov, R. Huang, D. H. Bilderback, S. O'Malley, V. Gupta, K. Bacher, L. J. P. Ketelsen, and A. Ougazzaden, "Microbeam high-resolution x-ray diffraction in strained InGaAlAs-based multiple quantum well laser structures grown selectively on masked InP substrates," Journal of Applied Physics **97** (6), - (2005).

[98] A. A. Sirenko, C. L. Reynolds, L. J. Peticolas, A. Ougazzaden, A. Kazimirov, R. Huang, E. Fontes, and D. Bilderback, "Micro-X-ray fluorescence and micro-photoluminescence in InGaAsP and InGaAs layers obtained by selective area growth," Journal of Crystal Growth **253** (1-4), 38-45 (2003).

[99] T. Takeuchi, H. Amano, and I. Akasaki, "Theoretical Study of Orientation Dependence of Piezoelectric Effects in Wurtzite Strained GaInN/GaN Heterostructures and Quantum Wells " Jpn. J. Appl. Phys. **39**, 413-416 (2000).

[100] K. Limburg, R. Huang, and D. Bilderback, "Fish otolith trace element maps: new approaches with microbeam X-ray fluorescence," submitted to the journal of Limnology and Oceanography: Methods (2005).

[101] A. R. Jacobson, S. Dousset, F. Andreux, and P. C. Baveye, "Electron microprobe and synchrotron X-ray fluorescence mapping of the heterogeneous distribution of copper in high-copper vineyard soils," Environmental Science & Technology **41** (18), 6343-6349 (2007).

[102] A. R. Woll, J. Mass, C. Bisulca, R. Huang, D. H. Bilderback, S. Gruner, and N. Gao, "Development of confocal X-ray fluorescence (XRF) microscopy at the Cornell high energy synchrotron source," Appl Phys a-Mater **83** (2), 235-238 (2006).

[103] A. R. Woll, D. H. Bilderback, S. Gruner, N. Gao, R. Huang, C. Bisulca, and J. Mass, "Confocal X-ray Fluorescence (XRF) Microscopy: A New Technique for the Nondestructive Compositional Depth Profiling of Paintings," Materials Research Society Symposium Proceedings **852** (2005).

[104] Arthur Woll, "Science meets art: Confocal X-ray Fluorescene Microscope at CHESS," CHESS News Magazine (2005).

[105] M. A. Denecke, K. Janssens, K. Proost, J. Rothe, and U. Noseck, "Confocal micrometer-scale X-ray fluorescence and X-ray absorption fine structure studies

of uranium speciation in a tertiary sediment from a waste disposal natural analogue site," Environmental Science & Technology **39** (7), 2049-2058 (2005).

[106] R. Henderson, "Cryoprotection of Protein Crystals against Radiation-Damage in Electron and X-Ray-Diffraction," Proceedings of the Royal Society of London Series B-Biological Sciences **241** (1300), 6-8 (1990).

[107] C. Nave and E. F. Garman, "Towards an understanding of radiation damage in cryocooled macromolecular crystals," J Synchrotron Radiat **12**, 257-260 (2005).

[108] C. Nave and M. A. Hill, "Will reduced radiation damage occur with very small crystals?," J Synchrotron Radiat **12**, 299-303 (2005).

[109] Stuart B. Krasnoff, Ivan Keresztes, Richard E. Gillilan, Doletha M.E. Szebenyi, Bruno G.G. Donzelli, Alice C.L. Churchill, and Donna M. Gibson, "Serinocylins A and B, Cyclic Heptapeptides from Metarhizium anisopliae," Journal of Natural Products **70** (12), 1919-1924 (2007).

[110] Nicle Hofer, Olga Kolaj, Hui Li, Vadim Cherezov, Richard Gillilan, J. Gerard Wall, and Martin Caffrey, "Crystallization and preliminary X-ray diffraction analysis of a soluble domain of the putative zinc transporter CzrB from Thermus thermophilus," Acta Crystallographica Section F **63**, 673-677 (2007).

[111] Ferguson group University of Pennsylvania (2007).

[112] J. S. Lamb, S. Cornaby, K. Andresen, L. Kwok, H. Y. Park, X. Y. Qiu, D. M. Smilgies, D. H. Bilderback, and L. Pollack, "Focusing capillary optics for use in solution small-angle X-ray scattering," J Appl Crystallogr **40**, 193-195 (2007).

[113] Sterling Cornaby, Thomas Szebenyi, Rong Huang, and Donald H Bilderback, "Design of Single-Bounce Monocapillary X-ray Optics," Advances in X-ray Analysis **50** (2006).

[114] L Pollack, M W Tate, N C Darnton, J B Knight, S M Gruner, W A Eaton, and R H Austin., "Compactness of the denatured state of a fast-folding protein measured by submillisecond small angle x-ray scattering," Proceedings of the National Academy of Sciences of the United States of America **96**, 10115-10117 (1999).

[115] L J Koerner, J C Trenkle, M W Tate, S M Gruner, T P Weihs, and T C Hufnagel, "X-ray Diffraction Studies of Rapidly Propagating Reaction Fronts Using a Pixel Array Detector," CHESS User's Meeting (June 2006).

[116] J Trenkle, L Koerner, M Tate, S Gruner, T Weihs, and T Hufnagel, "In-situ x-ray diffraction of phase transformations in nanostructured reactive multilayer

foils," Fifth International Conference on Synchrotron Radiation in Materials Science **SRMS5-123** (2006).

[117] K. J. Blobaum, D. Van Heerden, A. J. Gavens, and T. P. Weihs, "Al/Ni formation reactions: characterization of the metastable Al9Ni2 phase and analysis of its formation " Acta Materialia **51** (13), 3871-3884 (2003).

[118] Raul A Barrea, Rong Huang, Sterling Cornaby, Don Bilderback, and Tom Irving, "High Flux Hard X-ray Microprobe Using a Double Focused Undulator Beam and a Single-bounced Monocapillary," J Synchrotron Radiat (to be submitted in 2008).

[119] R. Fischetti, S. Stepanov, G. Rosenbaum, R. Barrea, D. Gore, R. Heurich, E. Kondrashkina, A.J. Kropf, S. Wang, Ke Zhang, T.C. Irving, and G.B. Bunker, "The BioCAT undulator beamline 18ID: a facility for biological non-crystalline diffraction and X-ray absorption spectroscopy at the Advanced Photon Source," J Synchrotron Radiat **11**, 399-405 (2004).

[120] Ruipeng Li, Sterling Cornaby, Marleen Kamperman, and Detlef Smilgies, "micro-SAXS on Pl-b-PEO/resol and the Pl-b-PEO domains," (to be published).

[121] O. Paris, I. Zizak, H. Lichtenegger, P. Roschger, K. Klaushofer, and P. Fratzl, "Analysis of the hierarchical structure of biological tissues by scanning X-ray scattering using a micro-beam," Cellular and Molecular Biology **46** (5), 993-1004 (2000).

[122] P. Fratzl and R. Weinkamer, "Nature's hierarchical materials," Progress in Materials Science **52** (8), 1263-1334 (2007).

[123] O. Paris, C. H. Li, S. Siegel, G. Weseloh, F. Emmerling, H. Riesemeier, A. Erko, and P. Fratzl, "A new experimental station for simultaneous X-ray microbeam scanning for small- and wide-angle scattering and fluorescence at BESSY II," J Appl Crystallogr **40**, S466-S470 (2007).

[124] L. J. Kaufman, C. P. Brangwynne, K. E. Kasza, E. Filippidi, V. D. Gordon, T. S. Deisboeck, and D. A. Weitz, "Glioma expansion in collagen I matrices: Analyzing collagen concentration-dependent growth and motility patterns," Biophysical Journal **89** (1), 635-650 (2005).

[125] K. Moffat, D. Szebenyi, and D. Bilderback, "X-Ray Laue Diffraction from Protein Crystals," Science **223** (4643), 1423-1425 (1984).

[126] D. Bourgeois, F. Schotte, M. Brunori, and B. Vallone, "Time-resolved methods in biophysics. 6. Time-resolved Laue crystallography as a tool to investigate

photo-activated protein dynamics," Photochemical & Photobiological Sciences **6** (10), 1047-1056 (2007).

[127] F. Schotte, J. Soman, J. S. Olson, M. Wulff, and P. A. Anfinrud, "Picosecond time-resolved X-ray crystallography: probing protein function in real time," Journal of Structural Biology **147** (3), 235-246 (2004).

[128] Z. Ren, D. Bourgeois, J. R. Helliwell, K. Moffat, V. Srajer, and B. L. Stoddard, "Laue crystallography: coming of age," J Synchrotron Radiat **6**, 891-917 (1999).

[129] B. L. Stoddard, B. E. Cohen, M. Brubaker, A. D. Mesecar, and D. E. Koshland, "Millisecond Laue structures of an enzyme-product complex using photocaged substrate analogs," Nature Structural Biology **5** (10), 891-897 (1998).

[130] D. M. E. Szebenyi, D. H. Bilderback, A. Legrand, K. Moffat, W. Schildkamp, B. S. Temple, and T. Y. Teng, "Quantitative-Analysis of Laue Diffraction Patterns Recorded with a 120 Ps Exposure from an X-Ray Undulator," J Appl Crystallogr **25**, 414-423 (1992).

[131] K. Moffat and J. R. Helliwell, "The Laue Method and Its Use in Time-Resolved Crystallography," Topics in Current Chemistry **151**, 61-74 (1989).

[132] B. Hedman, K. O. Hodgson, J. R. Helliwell, R. Liddington, and M. Z. Papiz, "Protein Microcrystal Diffraction and the Effects of Radiation-Damage with Ultra-High-Flux Synchrotron Radiation," Proceedings of the National Academy of Sciences of the United States of America **82** (22), 7604-7607 (1985).

[133] K. Moffat, "Laue diffraction," Macromolecular Crystallography, Pt B **277**, 433-447 (1997).

[134] P. D. Carr, I. M. Dodd, and M. M. Harding, "The Determination of Unit-Cell Parameters from a Laue Diffraction Pattern," J Appl Crystallogr **26**, 384-387 (1993).

[135] J. R. Helliwell, J. Habash, D. W. J. Cruickshank, M. M. Harding, T. J. Greenhough, J. W. Campbell, I. J. Clifton, M. Elder, P. A. Machin, M. Z. Papiz, and S. Zurek, "The Recording and Analysis of Synchrotron X-Radiation Laue Diffraction Photographs," J Appl Crystallogr **22**, 483-497 (1989).

[136] Z. Ren and K. Moffat, "Quantitative-Analysis of Synchrotron Laue Diffraction Patterns in Macromolecular Crystallography," J Appl Crystallogr **28**, 461-481 (1995).

[137] D. H. Bilderback, S. A. Hoffman, and D. J. Thiel, "Nanometer Spatial-Resolution Achieved in Hard X-Ray-Imaging and Laue Diffraction Experiments," Science **263** (5144), 201-203 (1994).

[138] G. Falkenberg, K. Rickers, D. Bilderback, and R. Huang (APS), Hasylab Annual report 2004.